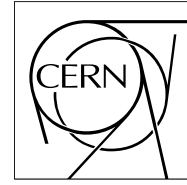


The Compact Muon Solenoid Experiment

CMS Note

Mailing address: CMS CERN, CH-1211 GENEVA 23, Switzerland



April 1998

Discovery potential for supersymmetry in CMS

For the CMS Collaboration

S. Abdullin^a, Ž. Antunović^b, F. Charles^c, D. Denegri^d, U. Dydak^e, M. Dželalija^b,
 V. Genchev^f, D. Graham^g, I. Iashvili^{h,i}, A. Kharchilava^{h,i}, R. Kinnunen^j,
 S. Kunori^k, K. Mazumdar^l, C. Raccaⁱ, L. Rurua^{h,e}, N. Stepanov^a, J. Womersley^m

Abstract

This work summarizes and puts in an overall perspective studies done within CMS concerning the discovery potential for squarks and gluinos, sleptons, charginos and neutralinos, SUSY dark matter, lightest Higgs, sparticle mass determination methods and the detector design optimisation in view of SUSY searches. It represents the status of our understanding of these subjects as of Summer 1997.

As a benchmark model we used the minimal supergravity-inspired supersymmetric standard model (mSUGRA) with a stable LSP. Discovery of supersymmetry at the LHC should be relatively straightforward. It may occur through the observation of a large excesses of events in missing E_T plus jets, or with one or more isolated leptons. An excess of trilepton events or of isolated dileptons with missing E_T , exhibiting a characteristic signature in the l^+l^- invariant mass distribution could also be the first manifestation of SUSY production. Squarks and gluinos can be discovered for masses in excess of 2 TeV. Charginos and neutralinos can be discovered from an excess of events in dilepton or trilepton final states. Inclusive searches can give early indications from their copious production in squark and gluino cascade decays. Indirect evidence for sleptons can be obtained also from inclusive dilepton studies. Isolation requirements and a jet veto would allow detection of both, the direct chargino/neutralino production and of directly-produced sleptons. Squark and gluino production may also represent a copious source of Higgs bosons through cascade decays. The lightest SUSY Higgs $h \rightarrow b\bar{b}$ may be reconstructed with a signal/background ratio of order 1 thanks to hard cuts on E_T^{miss} justified by escaping LSP's. The lightest supersymmetric particle of SUSY models with conserved R -parity represents a very good candidate for the cosmological dark matter. The region of parameter space where this is true is well-covered by our searches, at least for $\tan\beta = 2$.

If supersymmetry exists at electroweak scale it could hardly escape detection in CMS, and the study of supersymmetry will form a central part of our physics program.

- ^a *Institute for Theoretical and Experimental Physics, Moscow, Russia*
- ^b *University of Split, Split, Croatia*
- ^c *Université de Haute Alsace, Mulhouse, France*
- ^d *Centre d'Etudes Nucleaire de Saclay, Gif-sur-Yvette, France*
- ^e *Institut für Hochenergiephysik, Wien, Austria*
- ^f *Institute for Nuclear Research and Nuclear Energy, Sofia, Bulgaria*
- ^g *Imperial College, University of London, London, United Kingdom*
- ^h *Institute of Physics, Georgian Academy of Sciences, Tbilisi, Georgia*
- ⁱ *Institut de Recherches Subatomiques, Strasbourg, France*
- ^j *Helsinki Institute of Physics, Helsinki, Finland*
- ^k *University of Maryland, College Park, USA*
- ^l *Tata Institute of Fundamental Research-EHEP, Bombay, India*
- ^m *Fermi National Accelerator Laboratory, Batavia, USA*

Contents

1	Introduction	1
2	SUSY model employed	2
2.1	Charginos and neutralinos	2
2.2	Sleptons	4
2.3	Gluinos and squarks	7
3	Experimental signatures considered	26
4	Detector issues	27
4.1	CMS detector optimisation for SUSY studies	27
4.2	HCAL optimisation and tail catcher	28
4.3	The role of the tracker in SUSY searches	30
4.4	Lepton isolation	30
4.5	Tagging of b -jets in CMS	31
4.6	CMSJET – an approximate description of detector response	31
5	$Leptons + jets + E_T^{miss}$ channel – search for gluinos and squarks	47
6	Search for next-to-lightest neutralino	65
6.1	Inclusive 2 $leptons + E_T^{miss} + (jets)$ channel	65
6.2	Inclusive 3 $leptons$ channel	66
6.3	Inclusive 3 $leptons + E_T^{miss}$ channel	68
7	Exclusive 2 $leptons + no jets + E_T^{miss}$ channel – search for sleptons	81
8	Exclusive 3 $leptons + no jets + E_T^{miss}$ channel – search for chargino/neutralino pair production	95
9	Possibility of observing $h \rightarrow b\bar{b}$ in squark and gluino decays	108
10	Sensitivity to sparticle masses and model parameters	123
10.1	Establishing the SUSY mass scale	123
10.2	Constraints from $\tilde{\chi}_2^0$ leptonic decays	123
10.3	Determination of the squark mass	126
10.4	Sensitivity to model parameters in $3l + no jets + E_T^{miss}$ final states	127
10.5	Sensitivity to model parameters in inclusive $l^+l^- + E_T^{miss} + jets$ final states	130
11	Summary and conclusions	146

1 Introduction

There are strong arguments that the Standard Model (SM), despite its phenomenological successes [1], is only a low energy effective theory of spin-1/2 matter fermions interacting via spin-1 gauge bosons. A good candidate for “new physics” is the Supersymmetric (SUSY) extension of the SM which in its minimal version (MSSM) doubles the number of known particles, introducing scalar and fermion partners to ordinary fermions and bosons and relating their couplings. This scheme provides the necessary cancellation of quadratic divergences which appear in loop corrections to the masses provided the masses of super-partners are of the order of electroweak (EW) scale, i.e. ~ 0.1 to 1 TeV.

One of the main motivations of the experiments at the Large Hadron Collider (LHC) is to search for SUSY particles (“sparticles”). Previous studies [2] have shown that at the LHC the observation of an excess in event rates of specific final states over the SM expectations would signal the production of SUSY particles. The present study is based on a more precise description of the Compact Muon Solenoid (CMS) detector and covers a wider spectrum of physics channels. The primary goal is to understand the experimental limiting factors for SUSY studies and contribute to the detector optimisation while its design is not entirely frozen. The emphasis is put on leptonic channels, which are as interesting in terms of discovery potential, if not more, as the classical *multi-jets* + E_T^{miss} signature. The latter is more sensitive to instrumental backgrounds which can be fully understood only once the cracks, dead areas and volumes of diminished instrumental response due to detector services, mechanical supports are fully specified and evaluated. Another motivation for this study was the need to evaluate the discovery potential of an LHC detector in terms of accessible sparticle spectrum, sparticle mass reach, possibilities to determine the SUSY model scenario at work and possibilities to determine sparticle masses and model parameters in comparison and competition with a future e^+e^- collider and dedicated SUSY (WIMP) dark matter search experiments [3].

This work summarizes and puts in an overall perspective specific studies done within CMS concerning the observability and discovery potential for squarks and gluinos [4, 5], sleptons [6, 7], charginos and neutralinos [8, 9, 10], SUSY dark matter [11], the lightest Higgs [12], sparticle mass determination methods [9, 10, 7], detector design optimisation in view of SUSY searches [13], etc., and represents the status of our understanding of these subjects as of summer 1997.

We discuss the specific SUSY model employed in section 2 and the experimental signatures investigated in section 3. Detector issues and simulations of detector response are described in section 4. Searches for SUSY in *lepton(s) + jets* + E_T^{miss} final states from strongly interacting particle production are discussed in section 5 followed by inclusive searches for the next-to-lightest neutralino in section 6. Exclusive *2 leptons + no jets* + E_T^{miss} and exclusive *3 leptons + no jets* + (E_T^{miss}) channels are discussed in sections 7 and 8. Possibilities to observe $h \rightarrow b\bar{b}$ in squark and gluino decays are discussed in section 9. The methods to measure sparticle masses and restrict model parameters are addressed in section 10. Results and conclusions are summarized in section 11.

The potential of CMS to study the Higgs sector of SUSY has been extensively discussed elsewhere [14] and we do not address this problem here. Obtained results are based on two-loop level calculations [15]. To summarize, in the search of the various MSSM Higgs bosons, most of the m_A , $\tan\beta$ parameter space will be explored through at least one channel, provided an integrated luminosity of $L_{int} = 10^5 \text{ pb}^{-1}$ is available. A difficulty

still exists in the region of $120 \text{ GeV} \lesssim m_A \lesssim 240 \text{ GeV}$ and $2 \lesssim \tan\beta \lesssim 10$, which would require $L_{int} = 6 \div 10 \times 10^5 \text{ pb}^{-1}$ to be fully explored (though section 9 indicates that the Higgs sector may also be detectable in the decays of other SUSY particles).

2 SUSY model employed

Since the phenomenological implications of SUSY are model-dependent, the discovery potential of a detector has to be studied resorting to some particular model, preferably with a limited number of free parameters. This implies some loss of “generality”, but ensures tractable predictions. Once the possibilities and problems have been well understood within a defined scheme it is easier to evaluate its generality.

We have chosen to make the investigation in the minimal Super Gravity constrained version of the MSSM (mSUGRA) [16] as implemented in ISAJET [17]. This mSUGRA scheme has a limited number of parameters, has well established and simple mass relations, and is implemented in event generators, besides having definite phenomenological/theoretical attractiveness and plausibility. In the mSUGRA model only five extra parameters, which are not present in the SM, need to be specified: the universal scalar m_0 and gaugino $m_{1/2}$ masses, the SUSY breaking universal trilinear coupling A_0 , the ratio of the vacuum expectation values of the Higgs fields $\tan\beta$ and the sign of the Higgsino mixing parameter $\text{sign}(\mu)$. The first three parameters are fixed at the gauge coupling unification scale and the sparticle spectrum at the EW scale are then obtained via renormalization group equations [18].

Throughout this study except for cases specially mentioned we largely limit ourselves to the set:

$$\tan\beta = 2, \quad A_0 = 0, \quad \mu < 0, \quad (1)$$

and also consider five representative parameter space points suggested by theorists, and listed in Table 1.1.

Table 1.1: Representative mSUGRA points suggested by theorists.

Point	m_0 (GeV)	$m_{1/2}$ (GeV)	A_0 (GeV)	$\tan\beta$	μ
1	100	300	300	2.1	> 0
2	400	400	0	2	> 0
3	400	400	0	10	> 0
4	200	100	0	2	< 0
5	800	200	0	10	> 0

In the following we discuss the mass relations among sparticles in mSUGRA, display isomass curves in terms of model parameters, discuss production mechanisms and decay modes accessible to experimental observations.

2.1 Charginos and neutralinos

The mixing of the fermionic partners of the electroweak gauge and Higgs bosons, the gauginos and the Higgsinos, gives rise to the physical mass eigenstates called the charginos

($\tilde{\chi}_{1,2}^\pm$) and neutralinos ($\tilde{\chi}_{1,2,3,4}^0$). They are among the lightest expected SUSY particles and therefore present particular interest. The two lightest neutralinos and the lightest chargino ($\tilde{\chi}_1^0$, $\tilde{\chi}_2^0$, $\tilde{\chi}_1^\pm$) have as their largest mixing component the gauginos, and their masses are determined by the common gaugino mass, $m_{1/2}$. Within mSUGRA:

$$M_{\tilde{\chi}_1^0} \approx 0.45 m_{1/2} \quad (2)$$

$$M_{\tilde{\chi}_2^0} \approx M_{\tilde{\chi}_1^\pm} \approx 2 M_{\tilde{\chi}_1^0} \quad (3)$$

$$M_{\tilde{\chi}_2^0} \approx (0.25 \div 0.35) M_{\tilde{g}} \quad (4)$$

Figure 2.1 shows the isomass contours of ($\tilde{\chi}_1^0$, $\tilde{\chi}_2^0$, $\tilde{\chi}_1^\pm$) and of ($\tilde{\chi}_3^0$, $\tilde{\chi}_4^0$, $\tilde{\chi}_2^\pm$) in the $(m_0, m_{1/2})$ plane. We remind the reader that in most of parameter space and in the more plausible scenarios the lightest neutralino, $\tilde{\chi}_1^0$, is the Lightest Supersymmetric Particle (LSP) and as such is particularly interesting as it is one of the most plausible cosmic dark matter candidates particle physics provides.

The lightest chargino $\tilde{\chi}_1^\pm$ has several leptonic decay modes, giving an isolated lepton and missing energy due to the undetectable neutrino and LSP ($\tilde{\chi}_1^0$ in mSUGRA):

$$\left. \begin{aligned} &\bullet \tilde{\chi}_1^\pm \longrightarrow \tilde{\chi}_1^0 l^\pm \nu && \text{three-body decay} \\ &\bullet \tilde{\chi}_1^\pm \longrightarrow \tilde{l}_L^\pm \nu \\ &\quad \quad \quad \hookrightarrow \tilde{\chi}_1^0 l^\pm \\ &\bullet \tilde{\chi}_1^\pm \longrightarrow \tilde{\nu}_L l^\pm \\ &\quad \quad \quad \hookrightarrow \tilde{\chi}_1^0 \nu \\ &\bullet \tilde{\chi}_1^\pm \longrightarrow \tilde{\chi}_1^0 W^\pm \\ &\quad \quad \quad \hookrightarrow l^\pm \nu \end{aligned} \right\} \quad \text{two-body decays}$$

Figure 2.2 shows the branching ratios for the above listed $\tilde{\chi}_1^\pm$ decay channels as a function of $(m_0, m_{1/2})$. One can see that in different regions these different leptonic decay modes are complementary, amounting to a larger than 20% branching in the entire $(m_0, m_{1/2})$ plane (for $l = e, \mu$). Three-body decays are open in the region $m_{1/2} \lesssim 200$ GeV and $m_{1/2} \gtrsim 0.5 m_0$, whereas in the rest of parameter space the two-body decays are dominant.

Leptonic decays of $\tilde{\chi}_2^0$ give two isolated leptons and missing energy ($\tilde{\chi}_1^0$):

$$\left. \begin{aligned} &\bullet \tilde{\chi}_2^0 \longrightarrow \tilde{\chi}_1^0 l^+ l^- \\ &\bullet \tilde{\chi}_2^0 \longrightarrow \tilde{\chi}_1^\pm l^\mp \nu \\ &\quad \quad \quad \hookrightarrow \tilde{\chi}_1^0 l^\pm \nu \end{aligned} \right\} \quad \text{three-body decays}$$

$$\bullet \tilde{\chi}_2^0 \longrightarrow \tilde{l}_{L,R}^\pm l^\mp \quad \text{two-body decay}$$

$$\quad \quad \quad \hookrightarrow \tilde{\chi}_1^0 l^\pm$$

Figure 2.3 shows the $\tilde{\chi}_2^0$ leptonic branching ratios as a function of $(m_0, m_{1/2})$. Like the $\tilde{\chi}_1^\pm$ case, the three-body decay branching ratios are sizable at $m_{1/2} \lesssim 200$ GeV and $m_{1/2} \gtrsim 0.5 m_0$. Beyond $m_{1/2} \simeq 200$ GeV, the three-body decay of $\tilde{\chi}_2^0$ is suppressed due to the opening up of the channels $\tilde{\chi}_2^0 \rightarrow \tilde{\chi}_1^0 h$ and $\tilde{\chi}_2^0 \rightarrow \tilde{\chi}_1^0 Z$ (“spoiler” modes). The two-body decay branchings are significant if $m_0 \lesssim 0.5 m_{1/2}$.

In hadronic collisions, the charginos and neutralinos can be produced directly via a Drell-Yan mechanism or, more abundantly, through the cascade decays of strongly interacting sparticles. There is also the possibility of associated production $\tilde{\chi}_i^\pm/\tilde{\chi}_j^0 + \tilde{g}/\tilde{q}$. There are 21 different reactions (8 $\tilde{\chi}_i^\pm\tilde{\chi}_j^0$, 3 $\tilde{\chi}_i^\pm\tilde{\chi}_j^\pm$ and 10 $\tilde{\chi}_i^0\tilde{\chi}_j^0$) for direct chargino-neutralino pair production among which $\tilde{\chi}_1^\pm\tilde{\chi}_2^0$ production followed by leptonic decays of $\tilde{\chi}_1^\pm$ and $\tilde{\chi}_2^0$ is most easy from the detection point of view, yielding a 3 *leptons* + *no jets* + E_T^{miss} event topology.

Figure 2.4 shows the cross-section times branching ratio, $\sigma \times B(3l + invisible)$, where σ is the $\tilde{\chi}_1^\pm\tilde{\chi}_2^0$ direct production cross-section and $B(3l + invisible)$ is the convolution of all the leptonic decays of $\tilde{\chi}_1^\pm$ and $\tilde{\chi}_2^0$ listed above. Within a relatively small region of $m_{1/2}$ and for $m_0 \gtrsim 400$ GeV, the $\sigma \times B(3l + invisible)$ drops by several orders of magnitude and vanishes at $m_{1/2} \simeq 200$ GeV. For $m_0 \lesssim 400$ GeV the slope is less sharp thanks to the presence of two-body decay modes.

Probabilities for production of $\tilde{\chi}_1^\pm$ and $\tilde{\chi}_2^0$ from gluinos and squarks are shown in Figs. 2.5a and 2.5b for $\tan\beta = 2$, $\mu < 0$. One sees that these two sources of charginos and neutralinos are complementary in $(m_0, m_{1/2})$ parameter space. This abundant production of $\tilde{\chi}_2^0$ from strongly interacting sparticles over the whole $(m_0, m_{1/2})$ plane has very useful experimental implications, which will be discussed in detail later in this paper. The convolution of the $\tilde{\chi}_2^0$ indirect production cross-section with its leptonic decay branching ratio is shown in Fig. 2.5d. Clearly, over a large portion of the $(m_0, m_{1/2})$ plane, one expects rather large rates of same-flavor opposite-sign dileptons originating from $\tilde{\chi}_2^0$.

Similarly to the $\tilde{\chi}_2^0$, the lightest chargino $\tilde{\chi}_1^\pm$ is predominantly produced from strongly interacting sparticles, as illustrated in Figs. 2.6a,b. Moreover, the leptonic decay branching of the $\tilde{\chi}_1^\pm$ always exceeds 0.1 per lepton flavor (Fig. 2.6c). For low values of m_0 , in the region where decay to sleptons are kinematically allowed, the $\tilde{\chi}_1^\pm$ decays to a lepton with a probability close to 1.

Figure 2.7 shows the sum of $\tilde{\chi}_2^0 \rightarrow \tilde{\chi}_1^0 l^+ l^-$ and $\tilde{\chi}_2^0 \rightarrow \tilde{l} l \rightarrow \tilde{\chi}_1^0 l^+ l^-$ branching ratios for larger values of $\tan\beta = 10$ and 35 for both signs of μ . These branchings to e^+e^- or $\mu^+\mu^-$ are smaller than at $\tan\beta = 2$ shown in Fig. 2.5c.

2.2 Sleptons

The SUSY partners of ordinary leptons are scalars. Left and right-handed charged sleptons are not mass-degenerate. The slepton masses are determined by m_0 and $m_{1/2}$ [18]:

$$m_{\tilde{l}_R}^2 = m_0^2 + 0.15m_{1/2}^2 - \sin^2\theta_W M_Z^2 \cos 2\beta \quad (5)$$

$$m_{\tilde{l}_L}^2 = m_0^2 + 0.52m_{1/2}^2 - 1/2(1 - 2\sin^2\theta_W)M_Z^2 \cos 2\beta \quad (6)$$

$$m_{\tilde{\nu}}^2 = m_0^2 + 0.52m_{1/2}^2 + 1/2M_Z^2 \cos 2\beta \quad (7)$$

Asymptotically, for $m_{1/2} \rightarrow 0$ the slepton mass is determined by m_0 . Charged left sleptons are the heaviest. The mass dependence on $m_{1/2}$ for left (L) sleptons is stronger than for right ones (R), hence the left-right slepton mass splitting increases with $m_{1/2}$. Figure 2.8a shows slepton isomass contours in the $(m_0, m_{1/2})$ plane.

Since $\tilde{\chi}_1^\pm, \tilde{\chi}_2^0$ isomass contours (see Fig. 2.1) are approximately straight lines of constant $m_{1/2}$, as one moves up a slepton isomass curve, the $\tilde{\chi}_2^0$ mass increases and eventually

becomes higher than that of the slepton. Thus we may identify two domains in the $(m_0, m_{1/2})$ parameter plane: one is where left sleptons are more massive than $\tilde{\chi}_1^\pm, \tilde{\chi}_2^0$ ($m_0 \gtrsim 0.45 \cdot m_{1/2}$, domain I), and the other, where they are lighter ($m_0 \lesssim 0.45 \cdot m_{1/2}$, domain II). These mass relations, shown Fig. 2.8b are responsible for distinct contributions to slepton production and decay mechanisms. In domain I sleptons can be produced only through a Drell-Yan mechanism (*direct* slepton production), via $q\bar{q}$ annihilation with neutral or charged gauge boson exchange in the s-channel. Pairs with the same “handedness” can be produced, namely, $\tilde{l}_L\tilde{l}_L, \tilde{l}_R\tilde{l}_R, \tilde{\nu}\tilde{\nu}, \tilde{\nu}_l\tilde{l}_L$. In this part of parameter space both direct and cascade decays of sleptons to LSP are possible:

i) the left sleptons can decay to charginos and neutralinos via the following decays:

$$\tilde{l}_L^\pm \rightarrow l^\pm + \tilde{\chi}_{1,2}^0$$

$$\tilde{l}_L^\pm \rightarrow \nu_l + \tilde{\chi}_1^\pm$$

$$\tilde{\nu}_l \rightarrow \nu_l + \tilde{\chi}_{1,2}^0$$

$$\tilde{\nu}_l \rightarrow l^\pm + \tilde{\chi}_1^\mp$$

ii) for right sleptons, only decays to neutralinos are possible; they dominantly decay directly to the LSP:

$$\tilde{l}_R^- \rightarrow l^- + \tilde{\chi}_1^0$$

If decays to the second neutralino or lightest chargino are kinematically allowed, the decay to the LSP can proceed through several decay paths (cascade decays) with missing energy and/or isolated leptons in final state:

$$\tilde{\chi}_2^0 \rightarrow \tilde{\chi}_1^0 + l^+l^-$$

$$\tilde{\chi}_2^0 \rightarrow \tilde{\chi}_1^0 + \nu\bar{\nu}$$

$$\tilde{\chi}_2^0 \rightarrow \tilde{\chi}_1^0 + Z^0$$

$$\tilde{\chi}_1^\pm \rightarrow \tilde{\chi}_1^0 + l^\pm + \nu$$

$$\tilde{\chi}_1^\pm \rightarrow \tilde{\chi}_1^0 + W^\pm$$

In domain II *indirect* slepton production, from directly or indirectly produced charginos/neutralinos is also possible:

$$\tilde{\chi}_2^0 \rightarrow \tilde{l}_{L,R}^\pm l^\mp$$

$$\tilde{\chi}_2^0 \rightarrow \tilde{\nu}_l \bar{\nu}_l$$

$$\tilde{\chi}_1^\pm \rightarrow \tilde{\nu}_l l^\pm$$

$$\tilde{\chi}_1^\pm \rightarrow \tilde{l}_L^\pm \nu_l$$

When allowed, *indirect* \tilde{l} production arising from decays of strongly produced \tilde{g}, \tilde{q} to $\tilde{\chi}_2^0$ or $\tilde{\chi}_1^\pm$, is the predominant production mode. With increasing $m_{1/2}$ along a slepton isomass curve, the fraction of direct decays into the LSP increases as the mass difference between sleptons and charginos-neutralinos decreases, until in domain II sleptons can only directly decay to the LSP. Sneutrinos in this domain thus decay totally invisibly, i.e. no component $(\nu, \tilde{\chi}_1^0)$ from sneutrino decay can be directly detected. The slepton production and decay features described above give rise to several characteristic experimental signatures:

- *two leptons + E_T^{miss} + no jets* event topology arises from direct charged slepton pair $\tilde{l}_L\tilde{l}_L, \tilde{l}_R\tilde{l}_R$ production, followed by direct decays to the LSP. The same signature is

found in $\tilde{\nu}\tilde{\nu}$ production when one of the sneutrinos decays invisibly and the other has a cascade decay with two leptons in final state. This signature can also be found when sleptons are produced among decay products of directly or indirectly produced charginos-neutralinos. In the case of indirectly produced sleptons there are the following differences compared with direct production: i) single production is also possible, for example in $\tilde{\chi}_1^\pm\tilde{\chi}_2^0$ production followed by decay of the $\tilde{\chi}_2^0$ to a slepton; ii) a $\tilde{\nu}_l\tilde{l}_L$ pair can be produced from direct $\tilde{\chi}_1^\pm\tilde{\chi}_1^\mp$; iii) left handed sleptons production is favored;

- *three leptons + E_T^{miss} + no jets* final states are expected only from $\tilde{\nu}_l\tilde{l}_L$ production followed by cascade decays to LSP;
- *four leptons + E_T^{miss} + no jets* comes from $\tilde{l}_L\tilde{l}_L$, $\tilde{\nu}\tilde{\nu}$, $\tilde{\nu}_l\tilde{l}_L$ production followed by cascade decays to LSP.

The last two topologies can also be found when sleptons are produced in the decay of directly produced charginos-neutralinos.

- Indirect slepton production from gluinos and squarks through charginos, neutralinos (domain II), leads to a *two (or more) leptons + E_T^{miss} + jets* signature. This production has the largest cross-section because of the strongly interacting \tilde{g} and \tilde{q} , and again sleptons can be singly produced.

The largest contribution to the two leptons with no jets final state in charged slepton pair production comes from their direct decays to the LSP, $\tilde{l}_L \rightarrow l \tilde{\chi}_1^0$. However, with decreasing $m_{1/2}$ along an isomass curve the fraction of slepton direct decays to LSP decreases as shown in Fig. 2.9a. Figure 2.9b The $\sigma(\tilde{l}_L\tilde{l}_L) \times B(2l + invisible)$ for directly produced left sleptons and Fig. 2.9c shows the same for right sleptons: $\sigma(\tilde{l}_R\tilde{l}_R) \times B(2l + invisible)$. As right sleptons decay directly into LSP's the cross-section times branching ratio is constant along an isomass curve. One can see that the topological cross-section $\sigma(\tilde{l}_R\tilde{l}_R) \times B(2l + invisible)$ is larger than $\sigma(\tilde{l}_L\tilde{l}_L) \times B(2l + invisible)$ in almost the entire $(m_0, m_{1/2})$ plane.

For sneutrino pair production, the main contribution to the 2 leptons and no jets topology comes from one sneutrino decaying directly to the LSP and the second to $\tilde{\chi}_1^\pm$ or $\tilde{\chi}_2^0$ followed by their leptonic decays. The sneutrino decay branching ratios are shown in Figs. 2.10a-c. The $\sigma(\tilde{\nu}\tilde{\nu}) \times B(2l + invisible)$, shown in Fig. 2.10d, is limited along the $m_{1/2}$ axis by the $\tilde{\chi}_1^\pm$, $\tilde{\chi}_2^0$ leptonic decay branching ratios (see Figs. 2.1 and 2.2), and along the m_0 axis by the sneutrino production cross-section.

Figure 2.11 shows the total cross-section times branching ratio for *two lepton + E_T^{miss} + no jets* event topology arising from all possible combinations of directly produced slepton pairs, $\tilde{l}_L\tilde{l}_L$, $\tilde{l}_R\tilde{l}_R$, $\tilde{\nu}\tilde{\nu}$. It drops rapidly with increasing m_0 and $m_{1/2}$, from a maximum value of the order of a few pb down to a few fb for $m_0 \sim m_{1/2} \sim 500$ GeV. In almost the entire $(m_0, m_{1/2})$ parameter plane slepton pair production is dominated by right sleptons.

To illustrate the additional contribution from $\tilde{\chi}_1^\pm\tilde{\chi}_1^\mp$ direct production and the potential contribution from $\tilde{\chi}_1^\pm\tilde{\chi}_2^0$ to the *two same-flavor opposite-sign leptons + E_T^{miss} + no jets* event topology, we show $\sigma(\tilde{\chi}_1^\pm\tilde{\chi}_1^\mp) \times B(\tilde{\chi}_1^\pm\tilde{\chi}_1^\mp \rightarrow l^+l^- + invisible)$, $\sigma(\tilde{\chi}_1^\pm\tilde{\chi}_2^0) \times B(\tilde{\chi}_2^0 \rightarrow \tilde{l}_L^\pm + l^\mp)$ and $\sigma(\tilde{\chi}_1^\pm\tilde{\chi}_2^0) \times B(\tilde{\chi}_2^0 \rightarrow \tilde{l}_R^\pm + l^\mp)$ in Figs. 2.12a, b and c, respectively. One can see that the contribution from electroweak indirectly produced sleptons is not negligible, and in some areas of the $(m_0, m_{1/2})$ parameters space is even higher than for direct production.

Indirect slepton production from strongly produced \tilde{g}, \tilde{q} is larger still, when allowed, but is (almost) always accompanied by jets in the final state, so will not contribute unless the jets somehow escape detection.

2.3 Gluinos and squarks

In mSUGRA the gluino mass is determined mainly by $m_{1/2}$ [18]:

$$M_{\tilde{g}} \approx 2.5m_{1/2} \quad (8)$$

The five squark flavors ($\tilde{d}, \tilde{u}, \tilde{s}, \tilde{c}, \tilde{b}$) with their left and right chiral states are assumed to be mass degenerate, giving altogether ten degenerate squark flavors with:

$$M_{\tilde{q}} \approx \sqrt{m_0^2 + 6m_{1/2}^2} \quad (9)$$

The \tilde{t}_L and \tilde{t}_R are however treated differently. Through their mixing they give rise to two mass eigenstates \tilde{t}_1 and \tilde{t}_2 with \tilde{t}_1 most often significantly lighter than all other \tilde{q} states, which requires a separate discussion in terms of both, production and decay. Mixing also introduces a small non-degeneracy among the \tilde{b}_1 and \tilde{b}_2 states, but this is usually neglected compared to behavior of the stop system.

At LHC energies, the total SUSY particle production cross-section is dominated by strongly interacting gluinos and squarks, which through their cascade decays, (Figs. 2.13 and 2.14) can produce many jets and leptons, with missing energy due to at least 2 escaping LSPs and possibly neutrinos. Figure 2.15 shows the total squark/gluino production cross-section contours versus m_0 and $m_{1/2}$. Figure 2.16 shows the $(m_0, m_{1/2})$ parameter space subdivided into several domains corresponding to the characteristic kinematic configurations of gluino and squark events and the predominant sources of lepton production. Isomass contours for squarks, gluinos, light and pseudoscalar Higgses are also shown in Fig. 2.16 for $\tan\beta = 2$, $A_0 = 0$, $\mu < 0$, with h masses calculated at the two-loop radiative correction level.

The first domain is characterised by $m_{\tilde{g}} > m_{\tilde{q}}$ and $m_{\tilde{\chi}_2^0} > m_{\tilde{l}}$. This means that gluinos decay to quark-squark pairs but the contribution from gluino production to the total squark/gluino cross-section is small compared to the squarks. Both the $\tilde{\chi}_2^0$ and $\tilde{\chi}_1^\pm$ in this domain decay via sleptons (see Figs. 2.2 and 2.3) giving rise to a significant number of leptons in the final state. This region extends to higher values of m_0 at fixed $m_{1/2}$ than just two-body decays of $\tilde{\chi}_2^0$ and $\tilde{\chi}_1^\pm$ to sleptons, since the three-body decays (e.g. $\tilde{\chi}_2^0 \rightarrow \tilde{\chi}_1^0 l^+ l^-$) still remain even when two-body modes $\tilde{\chi}_2^0 \rightarrow \tilde{\chi}_1^0 h$ and $\tilde{\chi}_1^\pm \rightarrow \tilde{\chi}_1^0 W^\pm$ are open.

In the second domain of the $(m_0, m_{1/2})$ plane, the gluino mass is still somewhat larger than the squark masses, so that gluinos still decay into quark-squark pairs. The yield of stop-top final states is however higher than in the first domain since the contribution of the $\tilde{g}\tilde{g}$ process in the total \tilde{g}/\tilde{q} production cross-section is larger and the $\tilde{g} \rightarrow \tilde{t}t$ branching ratio is also higher. This results in an increase of the jet multiplicity and in a higher fraction of b -jets in the final state. The $\tilde{\chi}_2^0$ and $\tilde{\chi}_1^\pm$ are now lighter than the sleptons, and they decay to LSP + h/W^\pm , respectively, which means a reduced yield of isolated leptons when compared to the first domain.

In the third characteristic region of the $(m_0, m_{1/2})$ plane, the gluino mass is smaller than the mass of squarks, except for \tilde{t}_1 and \tilde{b}_L , and hence the stop-top final state dominates in overall production. The cross section for $\tilde{q}\tilde{q}$ is significantly smaller than that for $\tilde{g}\tilde{g}$.

All this gives rise to a significant jet multiplicity in the event and some increase of the yield of isolated leptons, as a result of $t \rightarrow Wb \rightarrow l\nu b$ decays, and an enrichment in the fraction of b -jets. Compared with the previous domain, nothing changes from the point of view of the $\tilde{\chi}_2^0$ and $\tilde{\chi}_1^\pm$ decays.

The fourth domain is characterised by very massive squarks compared to gluinos, thus $\tilde{g}\tilde{g}$ production dominates and the gluino decays predominantly via three-body final states (mainly LSP + $t\bar{t}$). This increases further the jet (and b -jet) multiplicity of the event. Again the decays of the $\tilde{\chi}_2^0$ and $\tilde{\chi}_1^\pm$ are the same as in domains 2 and 3.

There is a fifth domain which has approximately the shape of a band along the m_0 axis, under domains 2-4, for $m_{1/2} \leq 180 - 190$ GeV. In this region the masses of $\tilde{\chi}_1^\pm$ and $\tilde{\chi}_2^0$ are smaller than $\tilde{\chi}_1^0 + W$ and $\tilde{\chi}_1^0 + h$, respectively, and smaller than the slepton and sneutrino masses, thus 3-body decays of $\tilde{\chi}_2^0$ ($\rightarrow \tilde{\chi}_1^0 \tilde{q}\tilde{q}/\tilde{\chi}_1^0 l^+ l^-$) and $\tilde{\chi}_1^\pm$ ($\rightarrow \tilde{\chi}_1^0 \tilde{q}\tilde{q}'/\tilde{\chi}_1^0 l^\pm \nu$) take place. However, the yield of leptons does not differ significantly from that of domain 1.

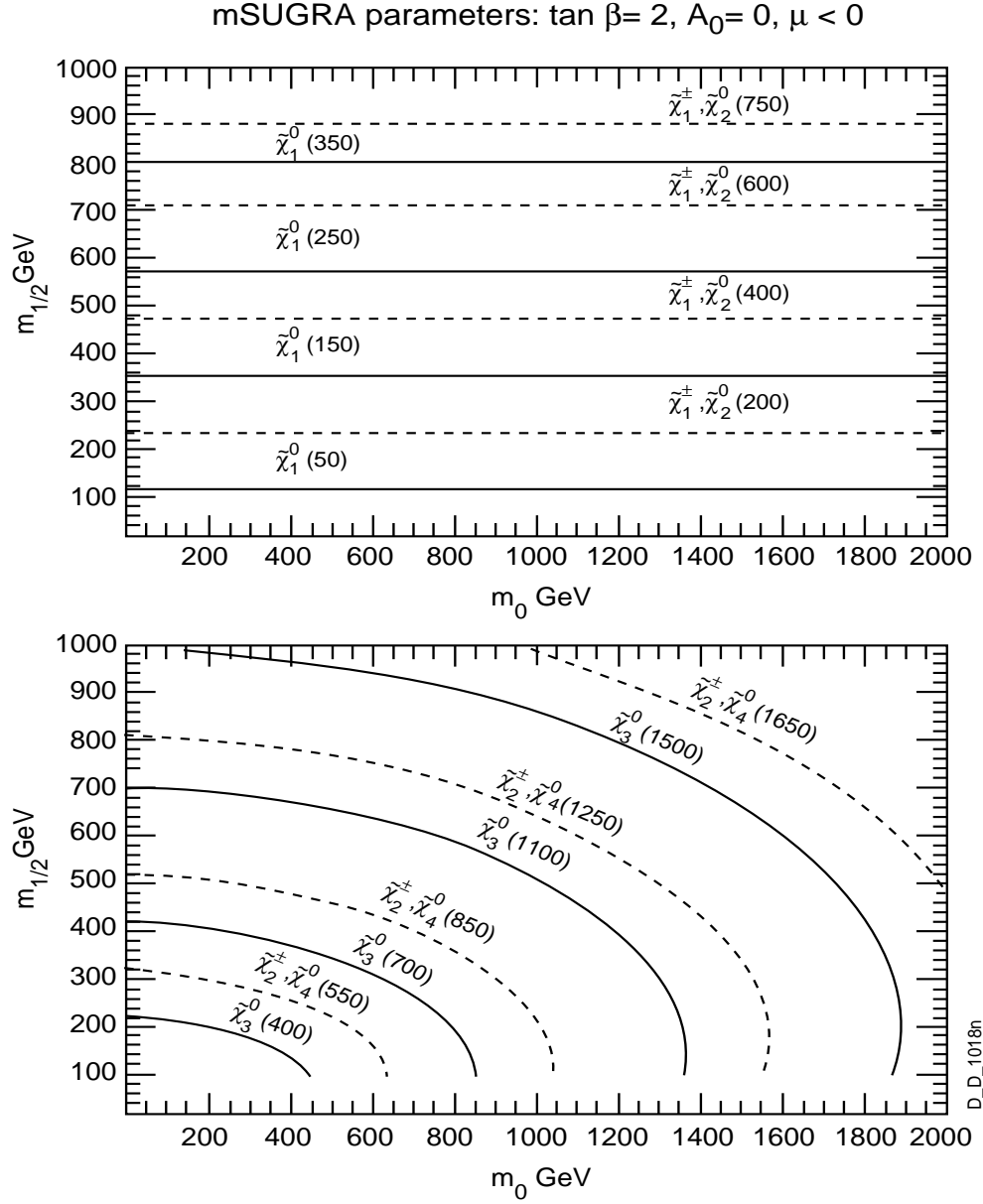


Figure 2.1: Isomass contours for: a) light ($\tilde{\chi}_1^\pm$, $\tilde{\chi}_1^0$, $\tilde{\chi}_2^0$) and b) heavy ($\tilde{\chi}_2^\pm$, $\tilde{\chi}_3^0$, $\tilde{\chi}_4^0$) charginos/neutralinos.

mSUGRA parameters: $\tan\beta = 2$, $A_0 = 0$, $\mu < 0$

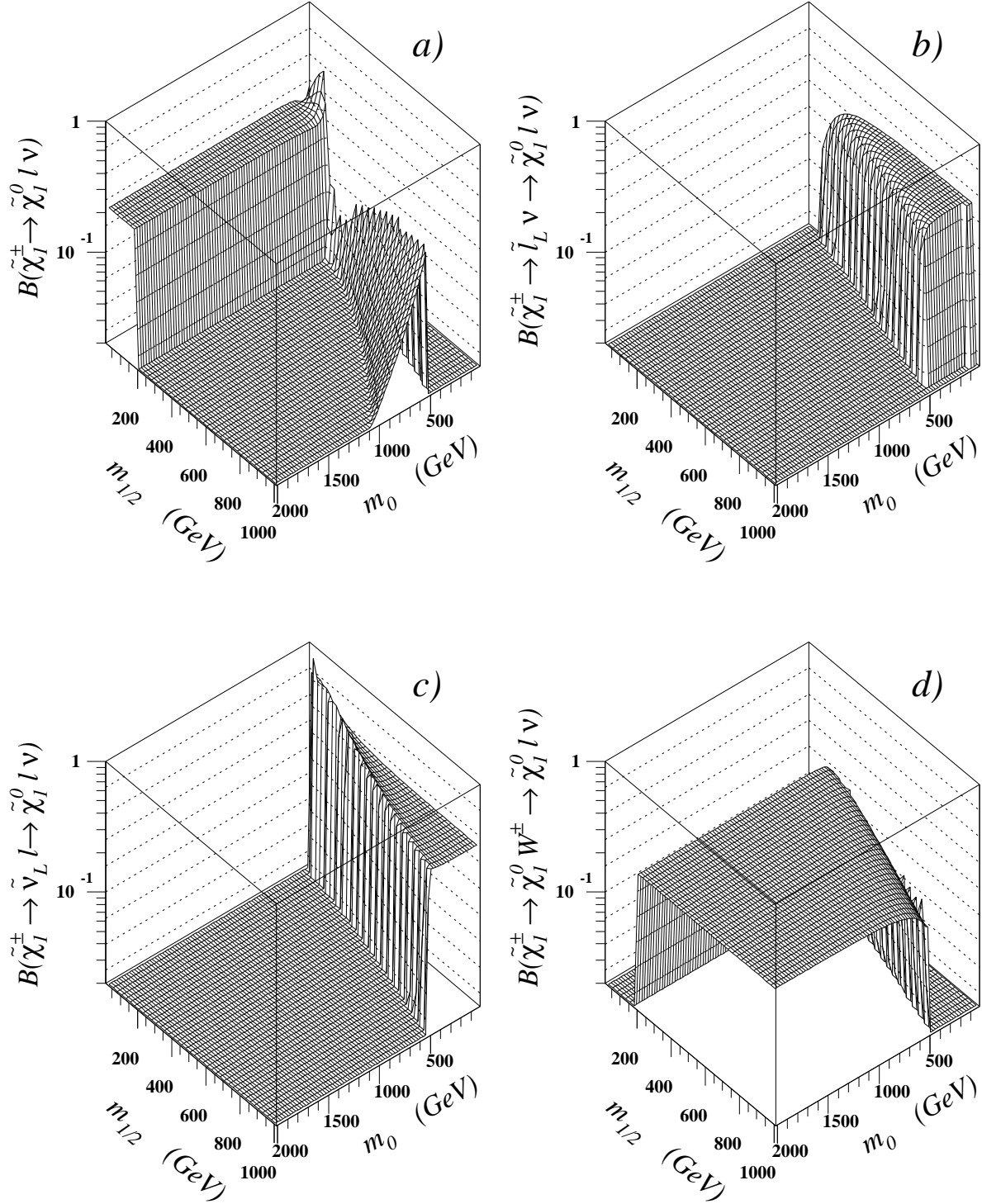


Figure 2.2: Chargino decay branching ratio versus $(m_0, m_{1/2})$: a) $\tilde{\chi}_1^\pm \rightarrow \tilde{\chi}_1^0 l^\pm \nu$, b) $\tilde{\chi}_1^\pm \rightarrow \tilde{l}_L^\pm \nu \rightarrow \tilde{\chi}_1^0 l^\pm \nu$, c) $\tilde{\chi}_1^\pm \rightarrow \tilde{l}_R^\pm \nu \rightarrow \tilde{\chi}_1^0 l^\pm \nu$ and d) $\tilde{\chi}_1^\pm \rightarrow \tilde{\chi}_1^0 W^\pm \rightarrow \tilde{\chi}_1^0 l^\pm \nu$.

mSUGRA parameters: $\tan\beta = 2$, $A_0 = 0$, $\mu < 0$

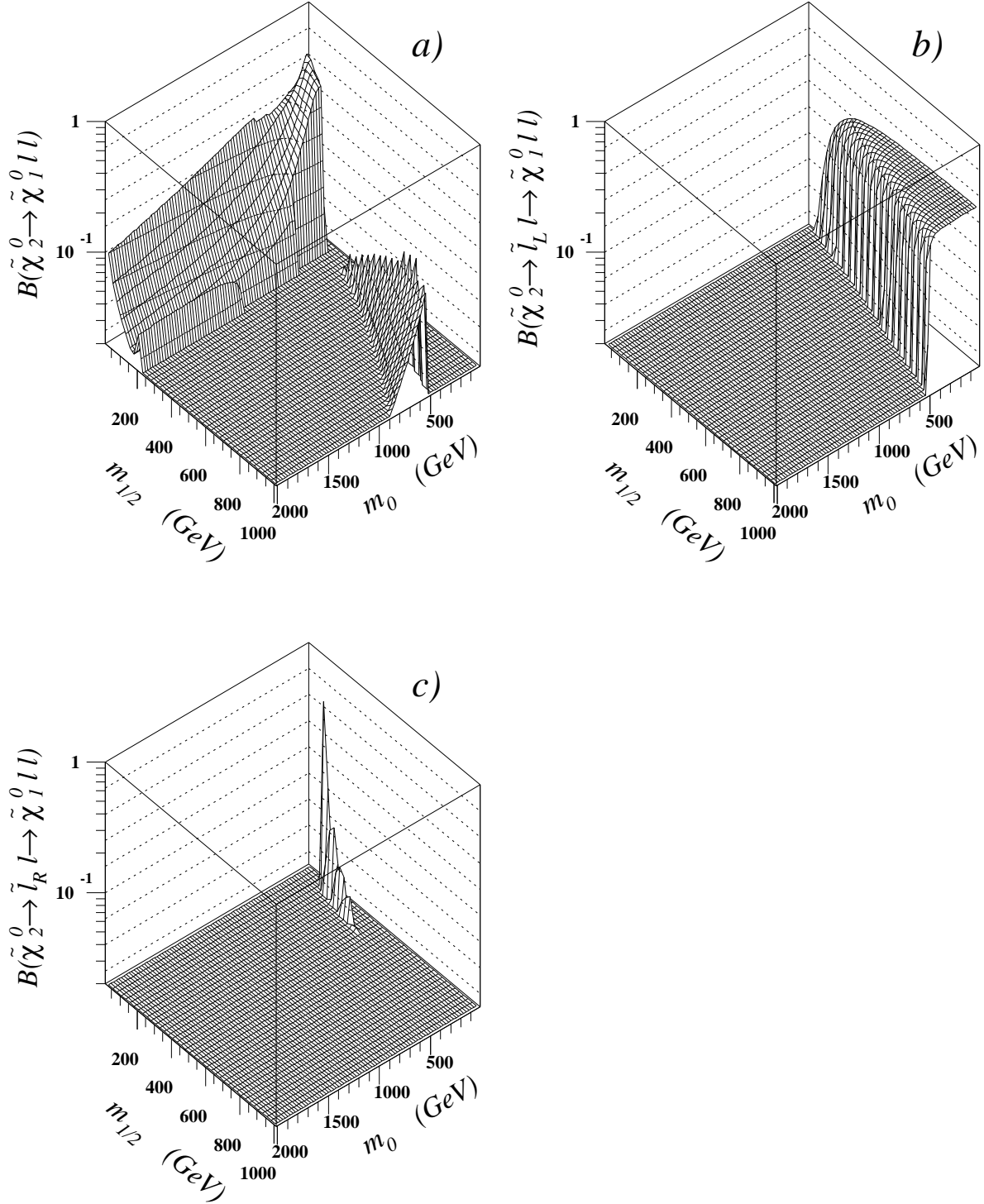


Figure 2.3: Neutralino decay branching ratio versus $(m_0, m_{1/2})$: a) $\tilde{\chi}_2^0 \rightarrow \tilde{\chi}_1^0 l^+ l^-$, b) $\tilde{\chi}_2^0 \rightarrow \tilde{l}_L^\pm l^\mp \rightarrow \tilde{\chi}_1^0 l^+ l^-$ and c) $\tilde{\chi}_2^0 \rightarrow \tilde{l}_R^\pm l^\mp \rightarrow \tilde{\chi}_1^0 l^+ l^-$.

mSUGRA parameters: $\tan\beta = 2$, $A_0 = 0$, $\mu < 0$

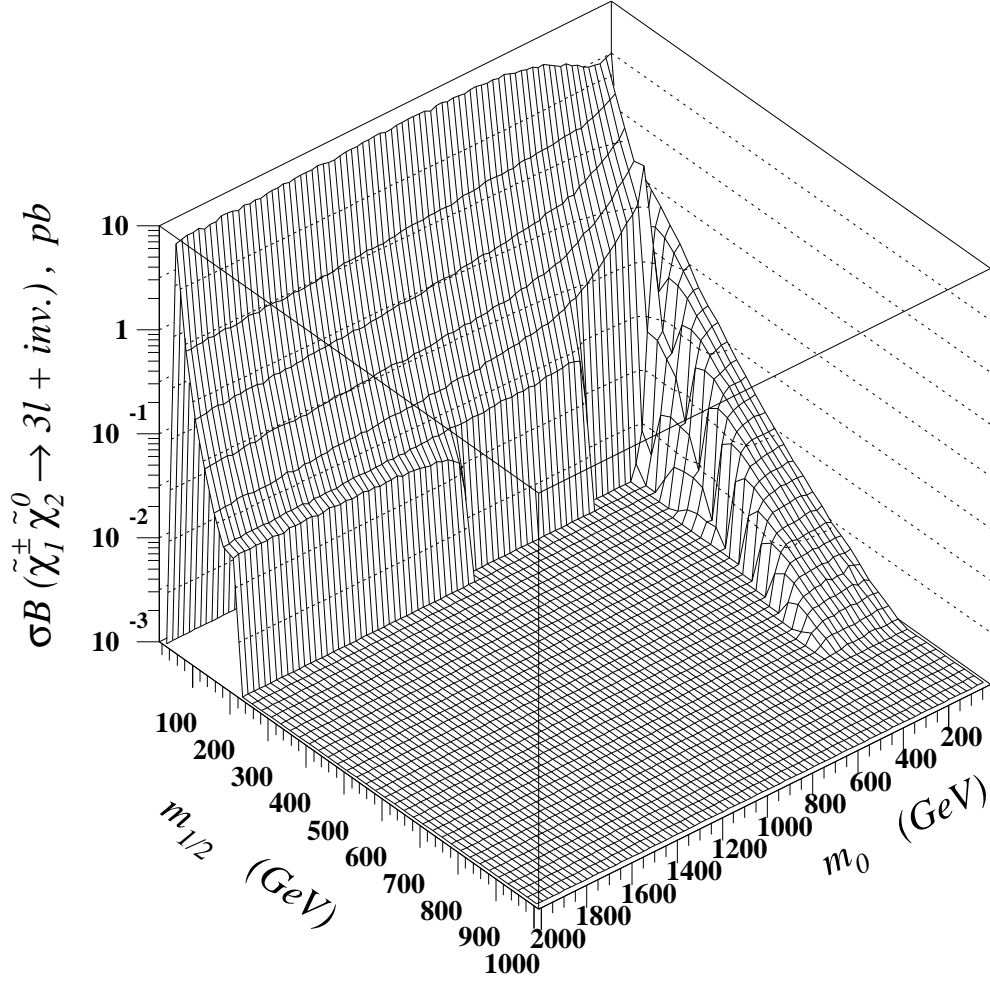


Figure 2.4: Cross-section times branching ratio versus $(m_0, m_{1/2})$ for $\tilde{\chi}_1^\pm \tilde{\chi}_2^0$ direct production followed by leptonic decays.

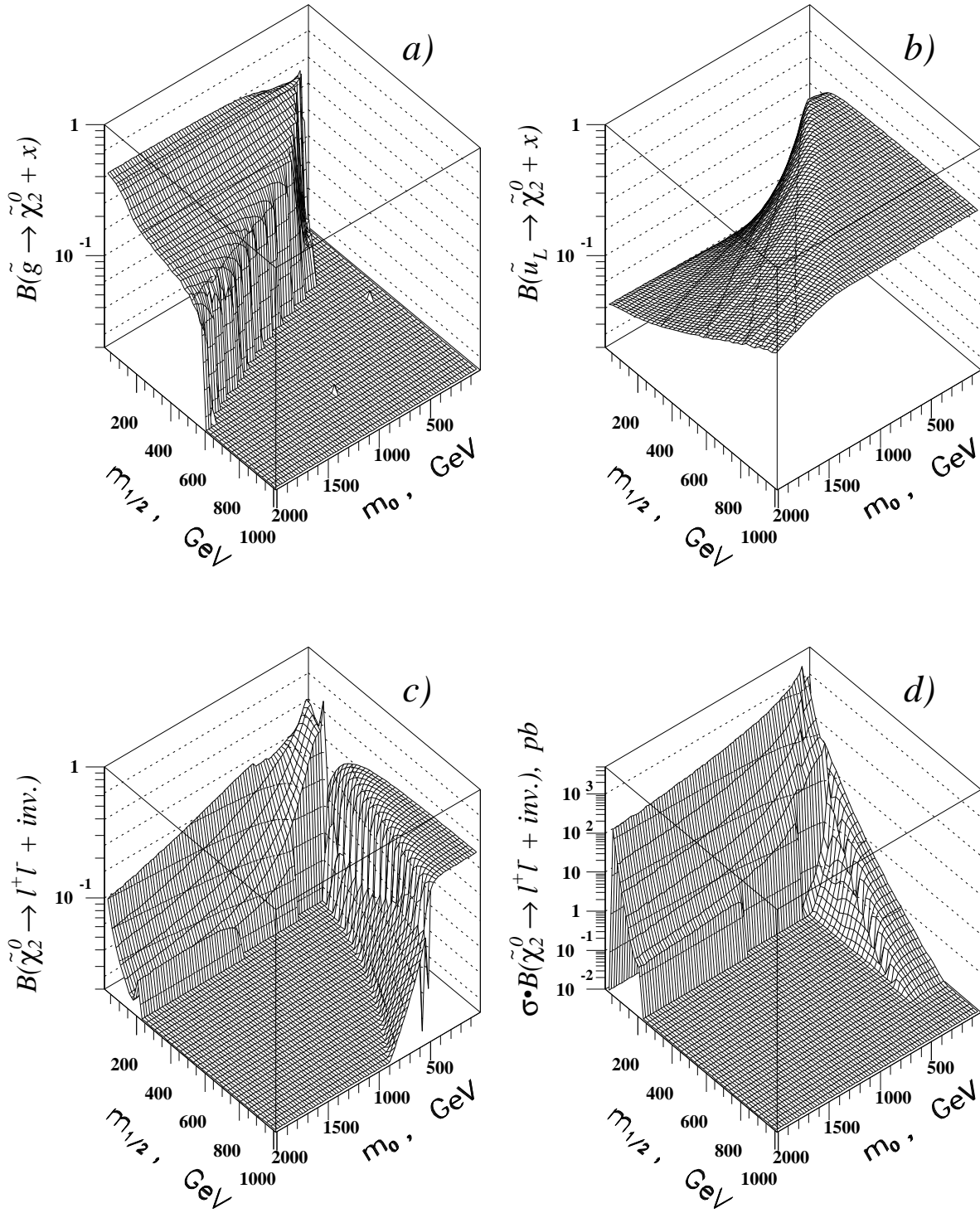


Figure 2.5: $\tilde{\chi}_2^0$ inclusive production and decay: a) branching ratio $B(\tilde{g} \rightarrow \tilde{\chi}_2^0 + x)$, b) $B(\tilde{u}_L \rightarrow \tilde{\chi}_2^0 + x)$, c) $B(\tilde{\chi}_2^0 \rightarrow l^+ l^- + invisible)$ and d) $\tilde{\chi}_2^0$ inclusive production cross-section times branching ratio into $l^+ l^-$.

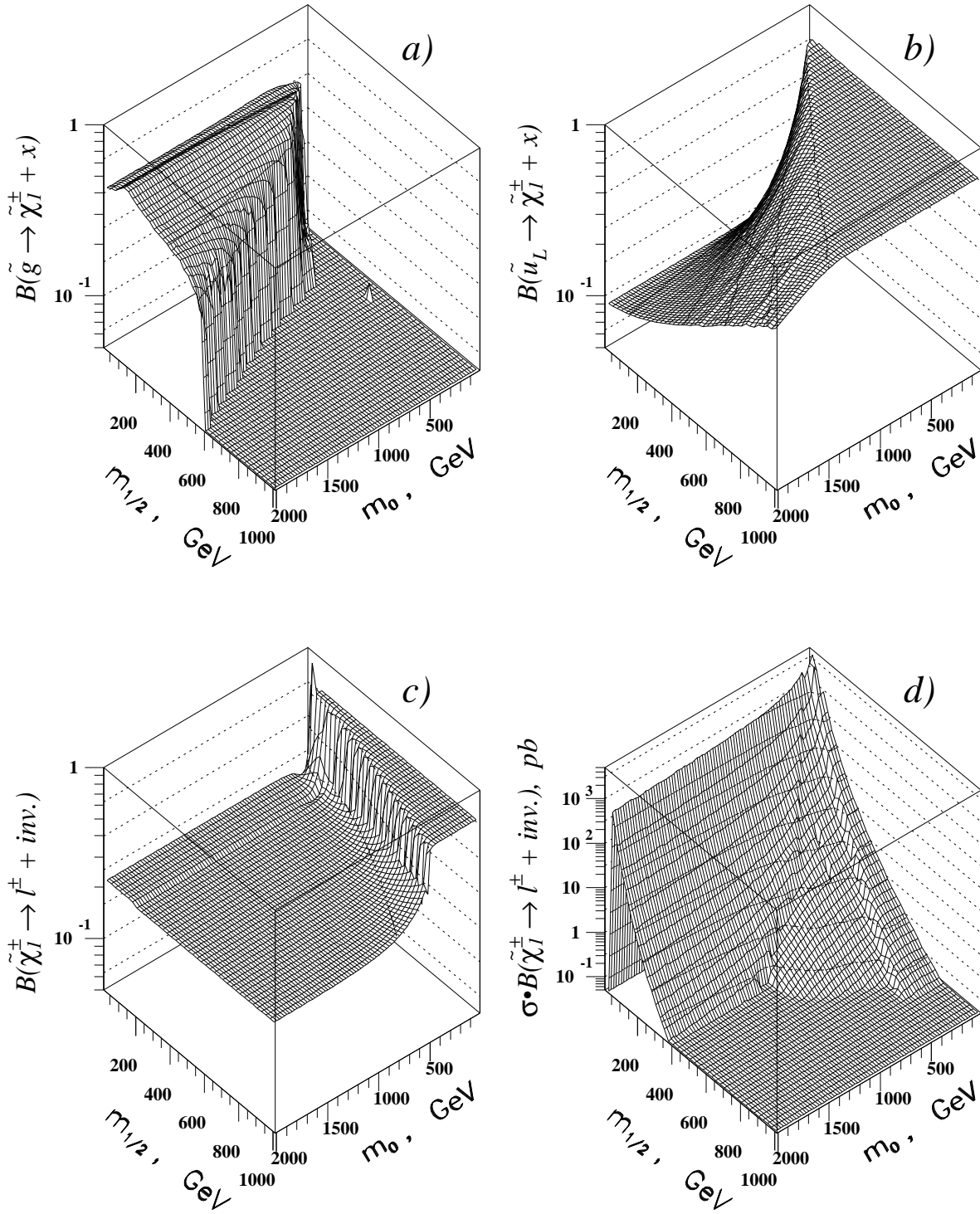


Figure 2.6: $\tilde{\chi}_1^\pm$ inclusive production and decay: a) branching ratio $B(\tilde{g} \rightarrow \tilde{\chi}_1^\pm + x)$, b) $B(\tilde{u}_L \rightarrow \tilde{\chi}_1^\pm + x)$, c) $B(\tilde{\chi}_1^\pm \rightarrow l^\pm + invisible)$ and d) $\tilde{\chi}_1^\pm$ inclusive production cross-section times branching ratio into l^\pm .

$$\text{Br}(\tilde{\chi}_2^0 \rightarrow 11\tilde{\chi}_1^0; 11\tilde{l}_{L,R})$$

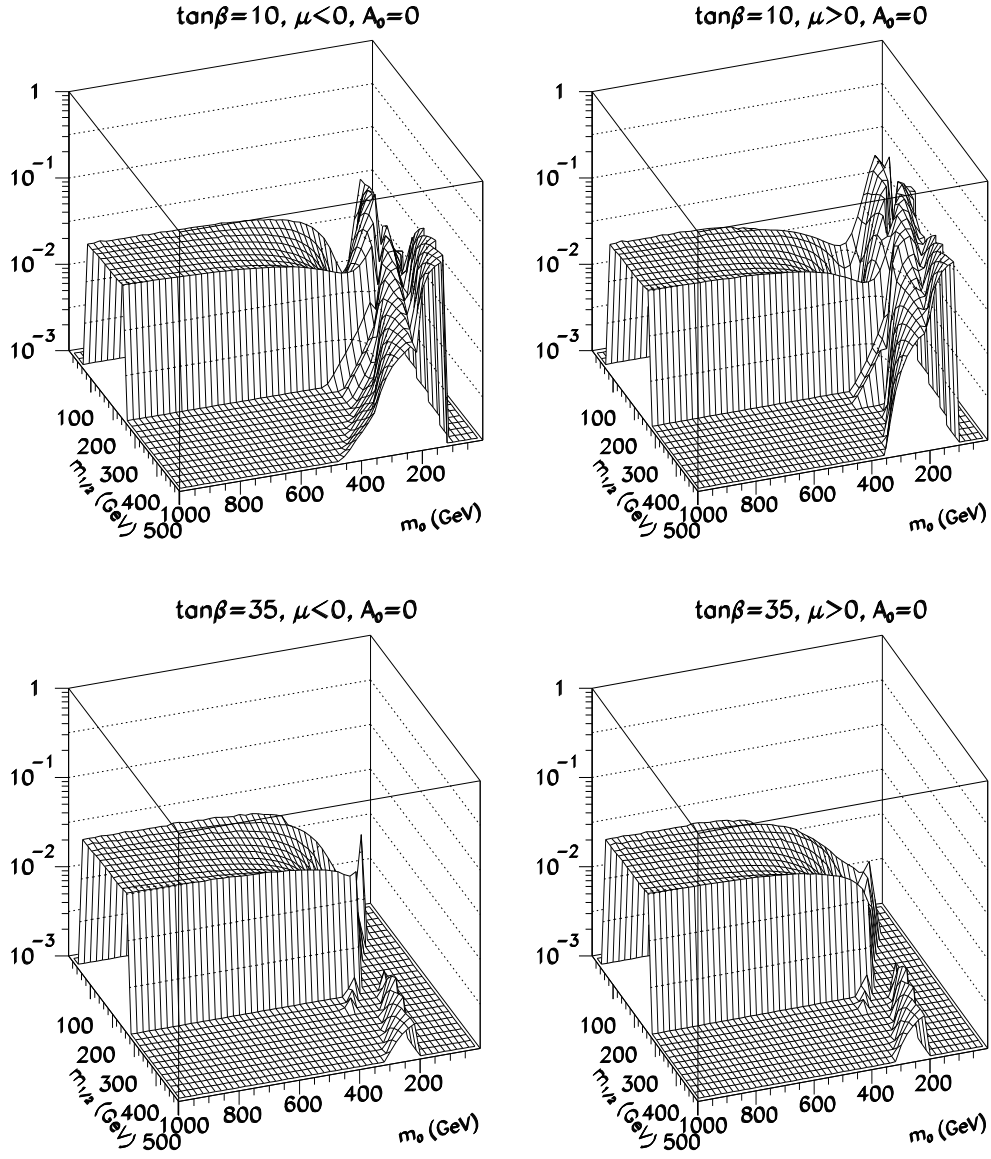


Figure 2.7: The sum of $\tilde{\chi}_2^0 \rightarrow \tilde{\chi}_1^0 l^+ l^-$ and $\tilde{\chi}_2^0 \rightarrow \tilde{l} l \rightarrow \tilde{\chi}_1^0 l^+ l^-$ branching ratios for various values of $\tan\beta = 10$ and 35 for both signs of μ .

Slepton isomass contours:

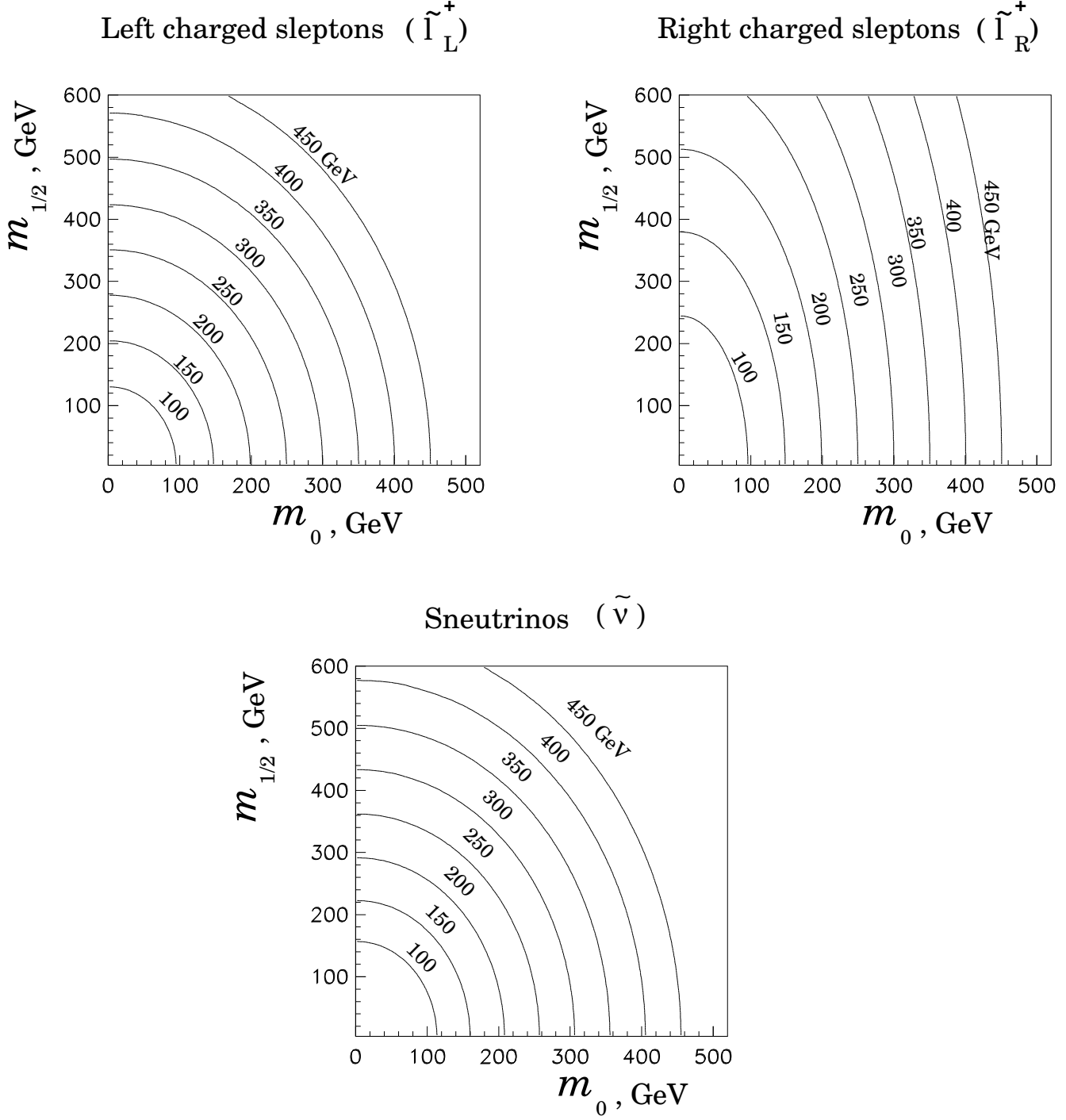


Figure 2.8a: Isomass contours for a) left charged sleptons, b) right charged sleptons and c) sneutrinos in mSUGRA parameter space $(m_0, m_{1/2})$ for $\tan\beta = 2$, $A_0 = 0$, $\mu < 0$.

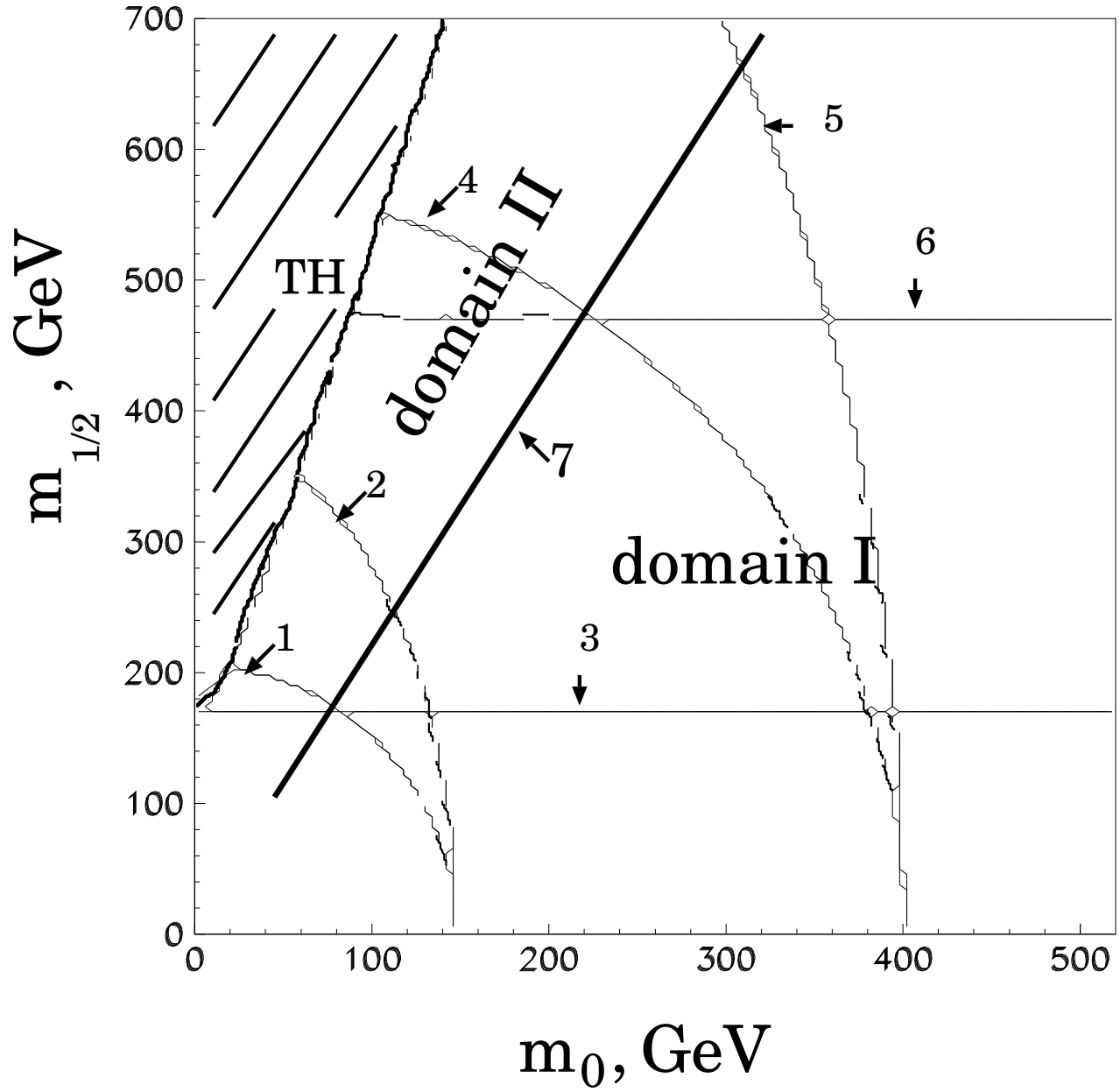


Figure 2.8b: Slepton isomass contours for $m_{\tilde{l}_L} = m_{\tilde{l}_R} = m_{\tilde{\chi}_2^0} = 150$ GeV corresponding to lines 1-3 respectively and $m_{\tilde{l}_L} = m_{\tilde{l}_R} = m_{\tilde{\chi}_2^0} = 400$ GeV, lines 4-6 respectively. Line 7 separates domains I and II of $(m_0, m_{1/2})$ parameter space; in domain II charginos, neutralinos can decay to left sleptons.

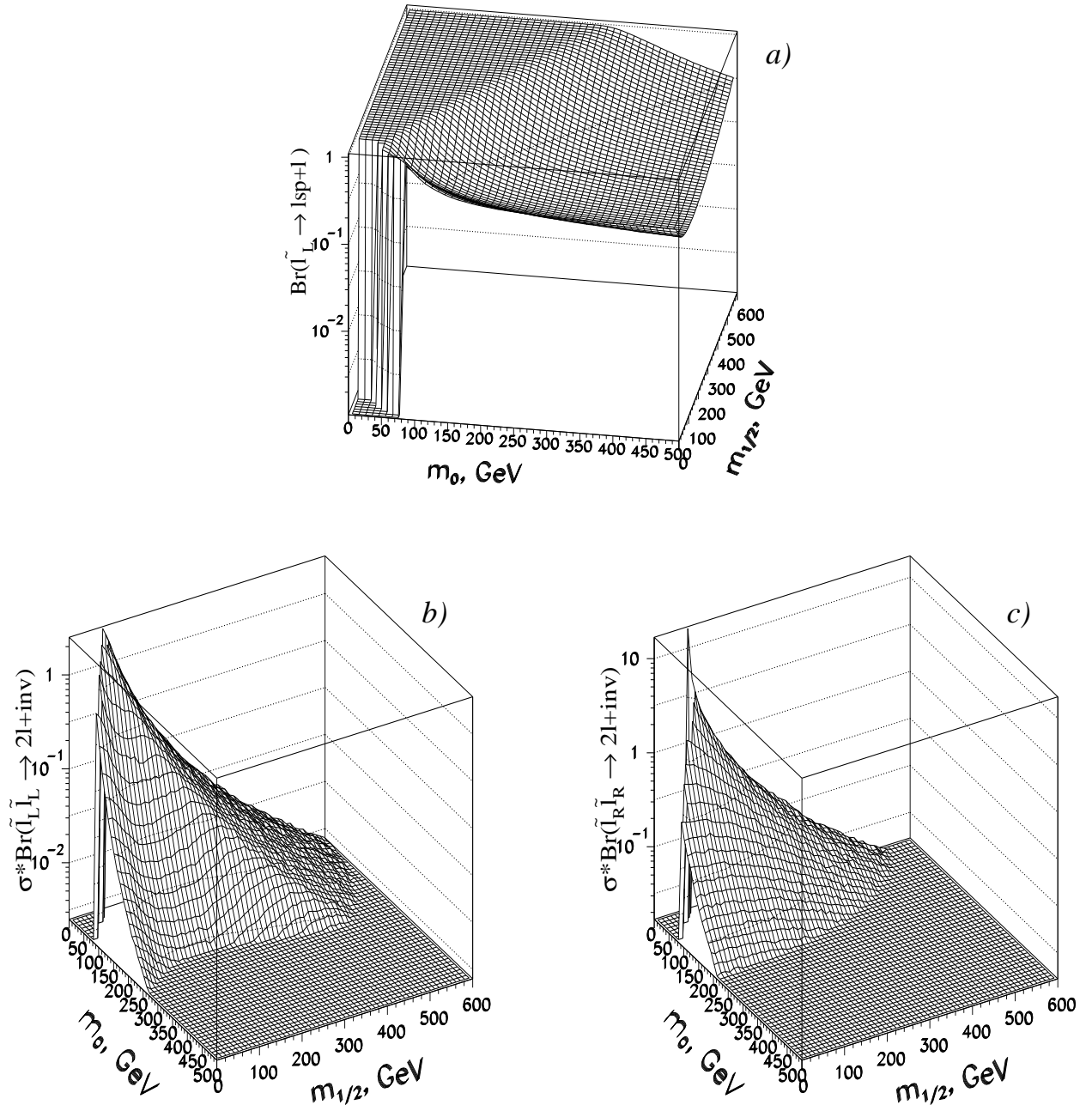


Figure 2.9: a) Branching ratio of $\tilde{l}_L \rightarrow \tilde{\chi}_1^0 + l$; b) cross-section times branching ratio for $2\text{leptons} + E_T^{\text{miss}} + \text{no jets}$ events from direct left slepton pair production; c) cross-section times branching ratio for $2\text{leptons} + E_T^{\text{miss}} + \text{no jets}$ events from direct right slepton pair production.

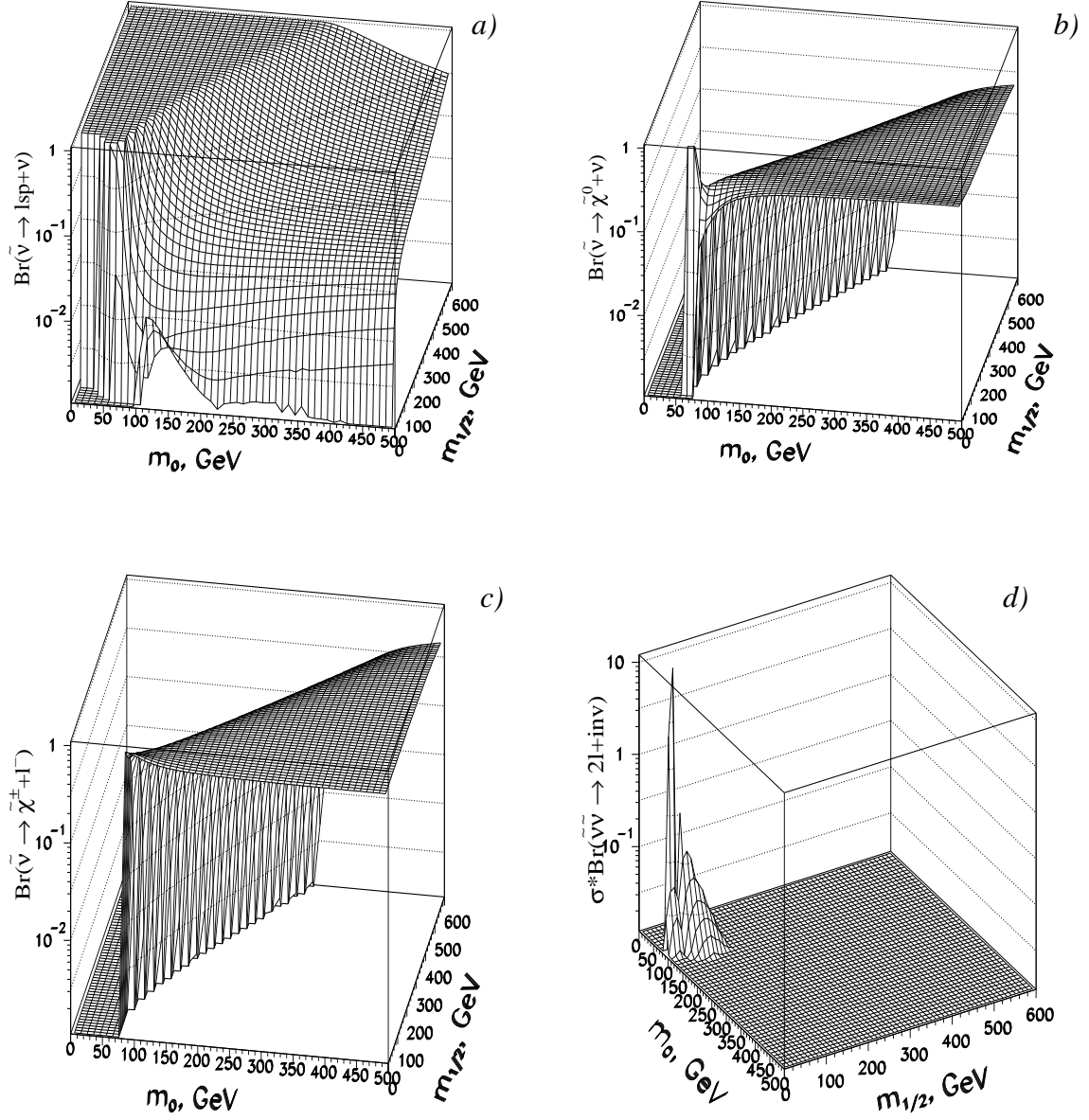


Figure 2.10: Decay branching ratios of sneutrinos: a) $\tilde{\nu} \rightarrow \chi_1^0 + \nu$, b) $\tilde{\nu} \rightarrow \tilde{\chi}_2^0 + \nu$ and c) $\tilde{\nu} \rightarrow \tilde{\chi}_1^\pm + l^\mp$ as a function of $(m_0, m_{1/2})$; d) cross-section times branching ratio for $2\text{leptons} + E_T^{\text{miss}} + \text{no jets}$ events topology from sneutrino pair production.

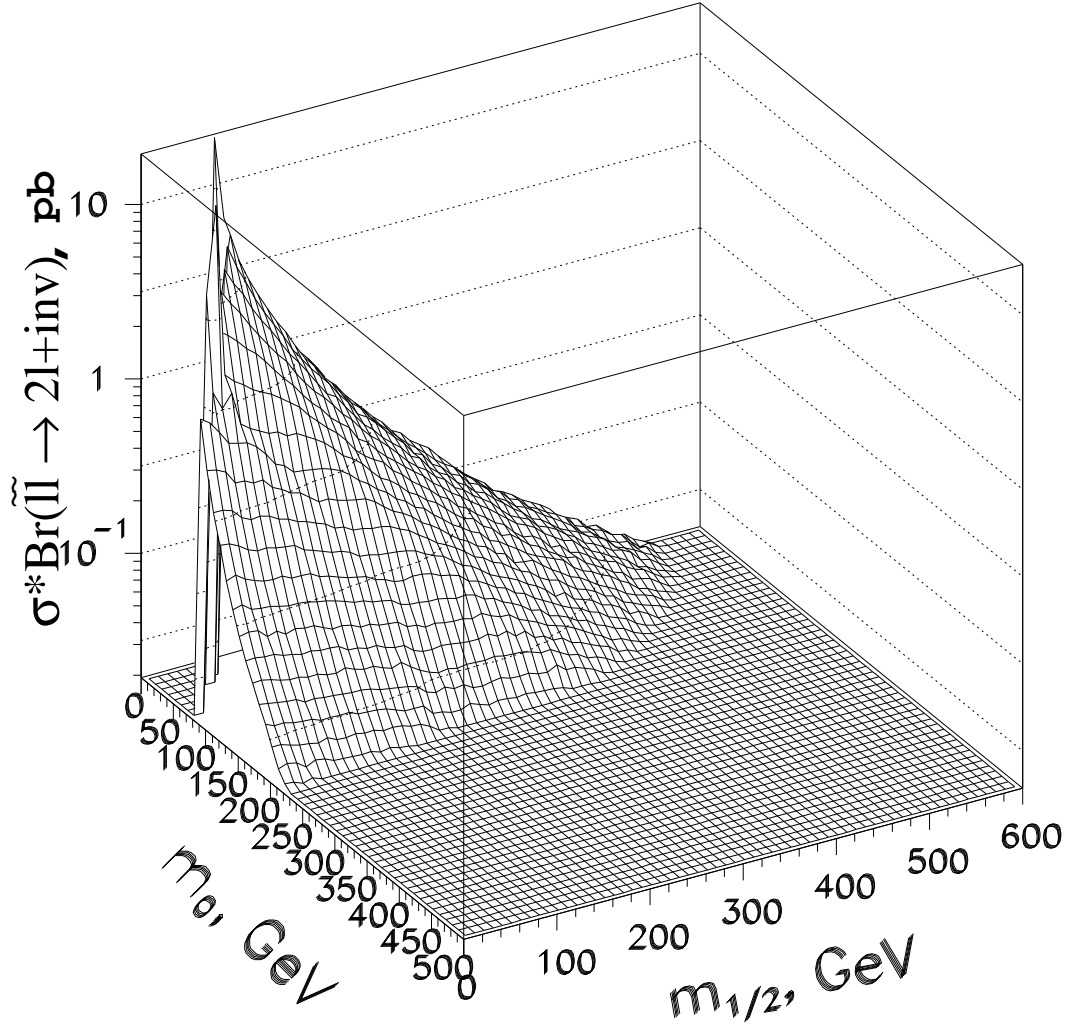


Figure 2.11: Total cross-section times branching ratio for 2 *leptons* + E_T^{miss} events arising from all possible combinations of directly produced slepton pairs, namely $\tilde{l}_L \tilde{l}_L$, $\tilde{l}_R \tilde{l}_R$ and $\tilde{\nu} \tilde{\nu}$.

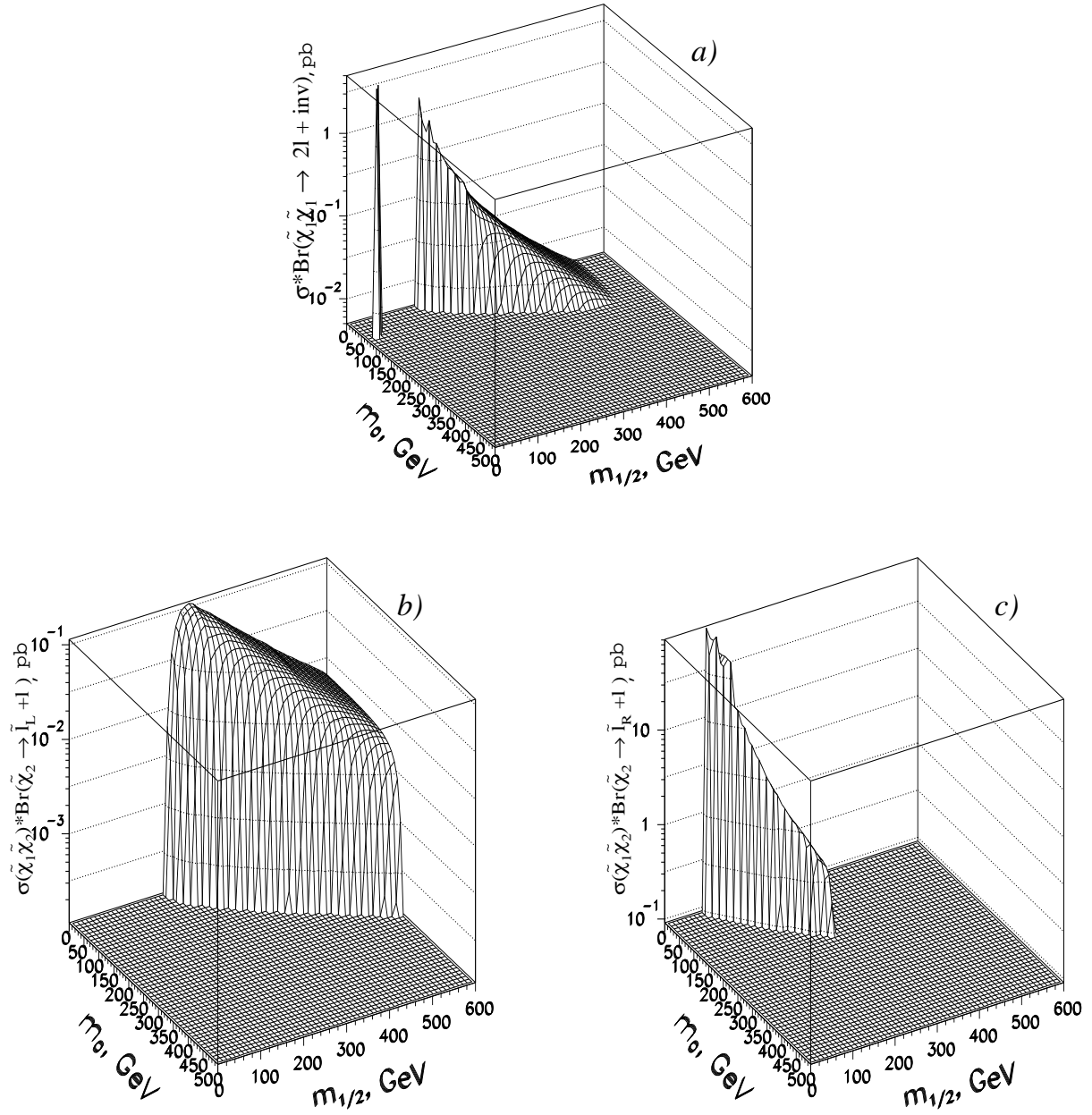


Figure 2.12: Cross-section times branching ratio for a) $\tilde{\chi}_1^\pm \tilde{\chi}_1^\pm$ direct production followed by leptonic decays of at least one of the charginos; b) single sleptons production from directly produced $\tilde{\chi}_1^\pm \tilde{\chi}_2^0$ with $\tilde{\chi}_2^0$ decays to left sleptons $\tilde{\chi}_2^0 \rightarrow \tilde{l}_L l$ (b); c) single sleptons production from directly produced $\tilde{\chi}_1^\pm \tilde{\chi}_2^0$ with $\tilde{\chi}_2^0$ decays to right sleptons $\tilde{\chi}_2^0 \rightarrow \tilde{l}_R l$ (c).

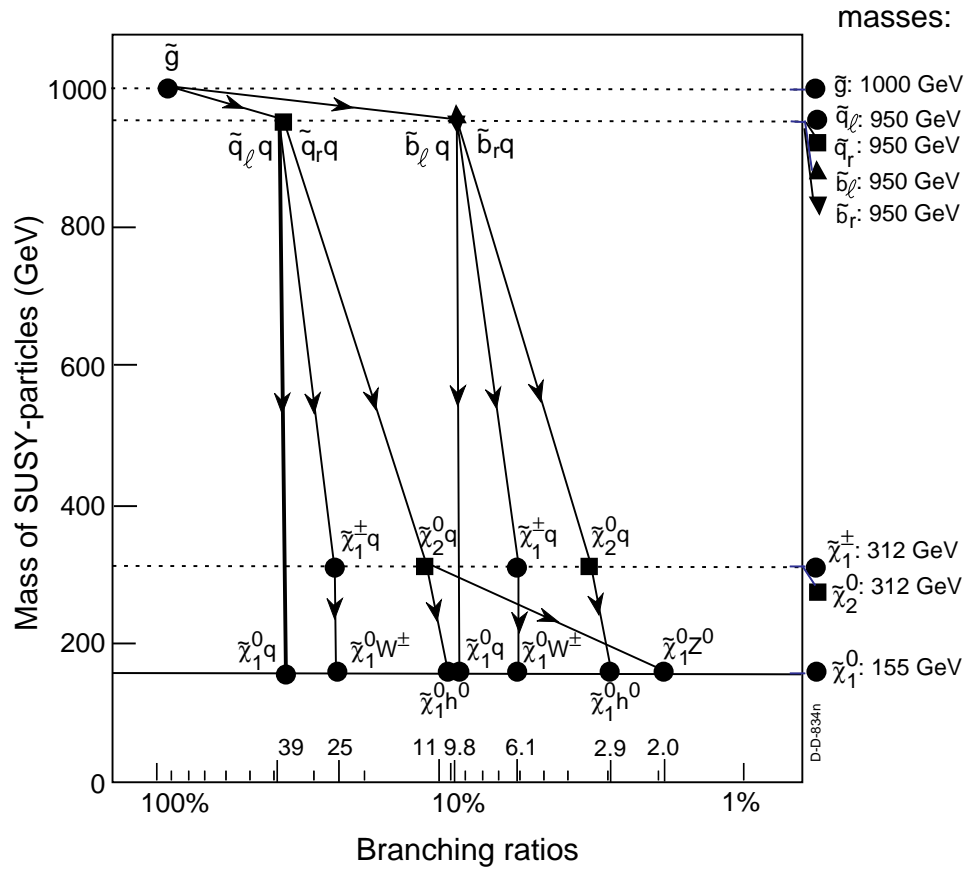


Figure 2.13: Typical decay modes for the massive (1 TeV) gluino illustrating the variety of possible cascade decays.

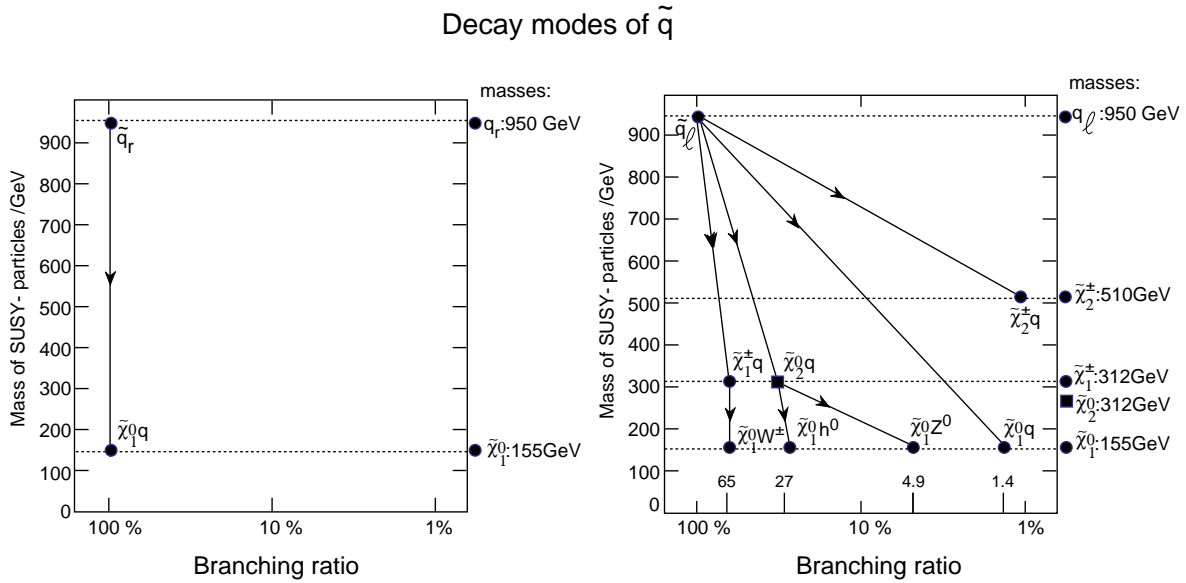


Figure 2.14: Typical decay modes of the massive (0.95 TeV) squark.

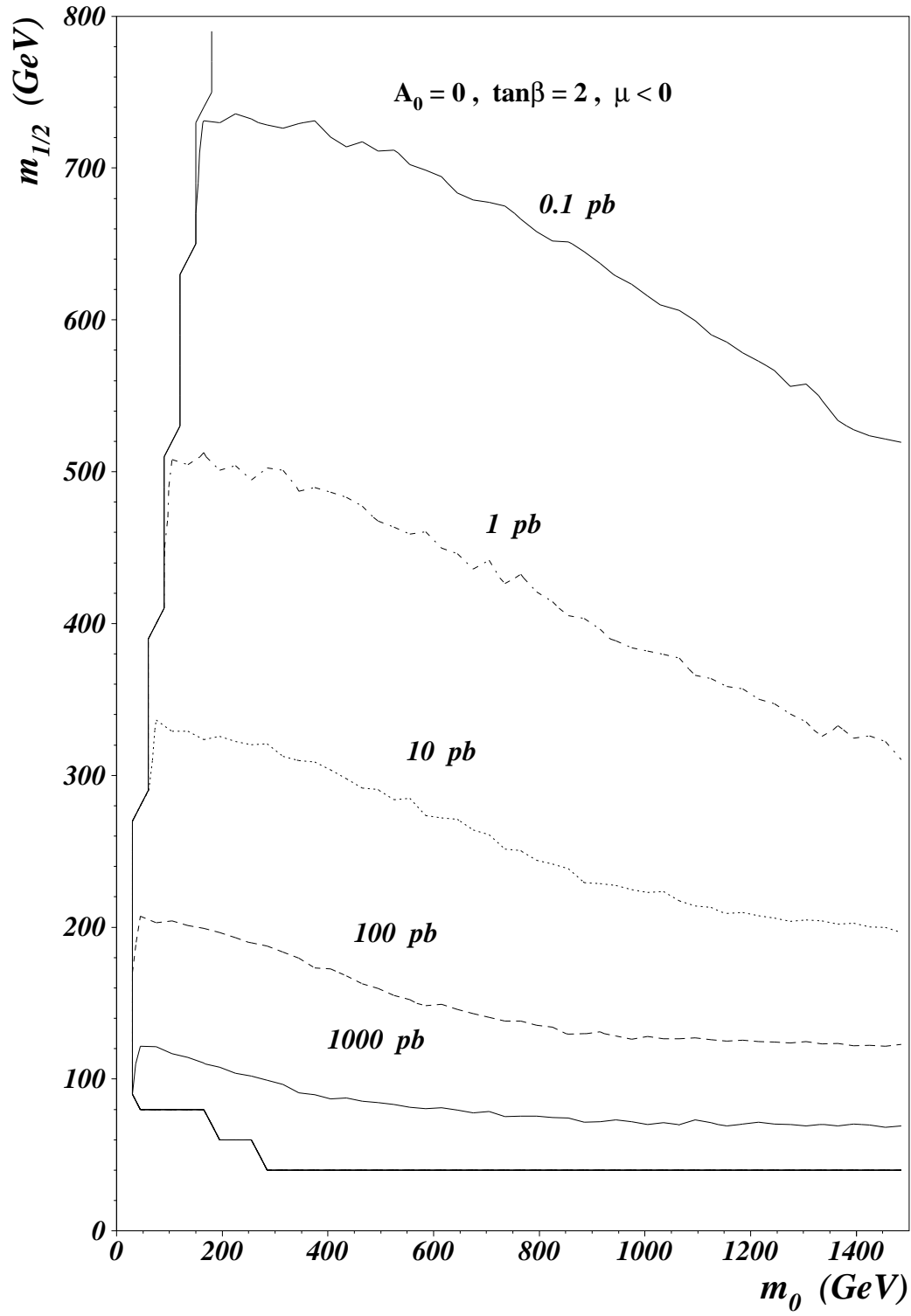


Figure 2.15 Gluino/squark production cross-section versus $(m_0, m_{1/2})$.

$m_{1/2}, \text{ GeV}$

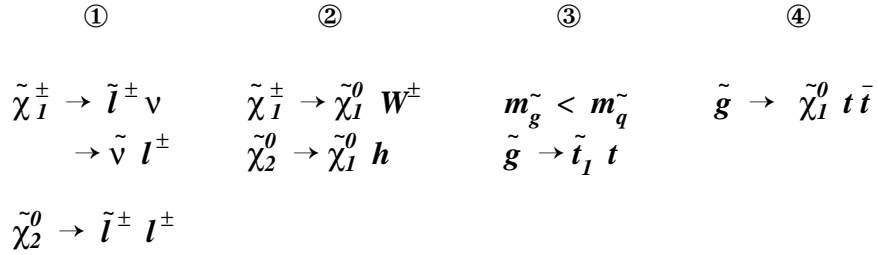
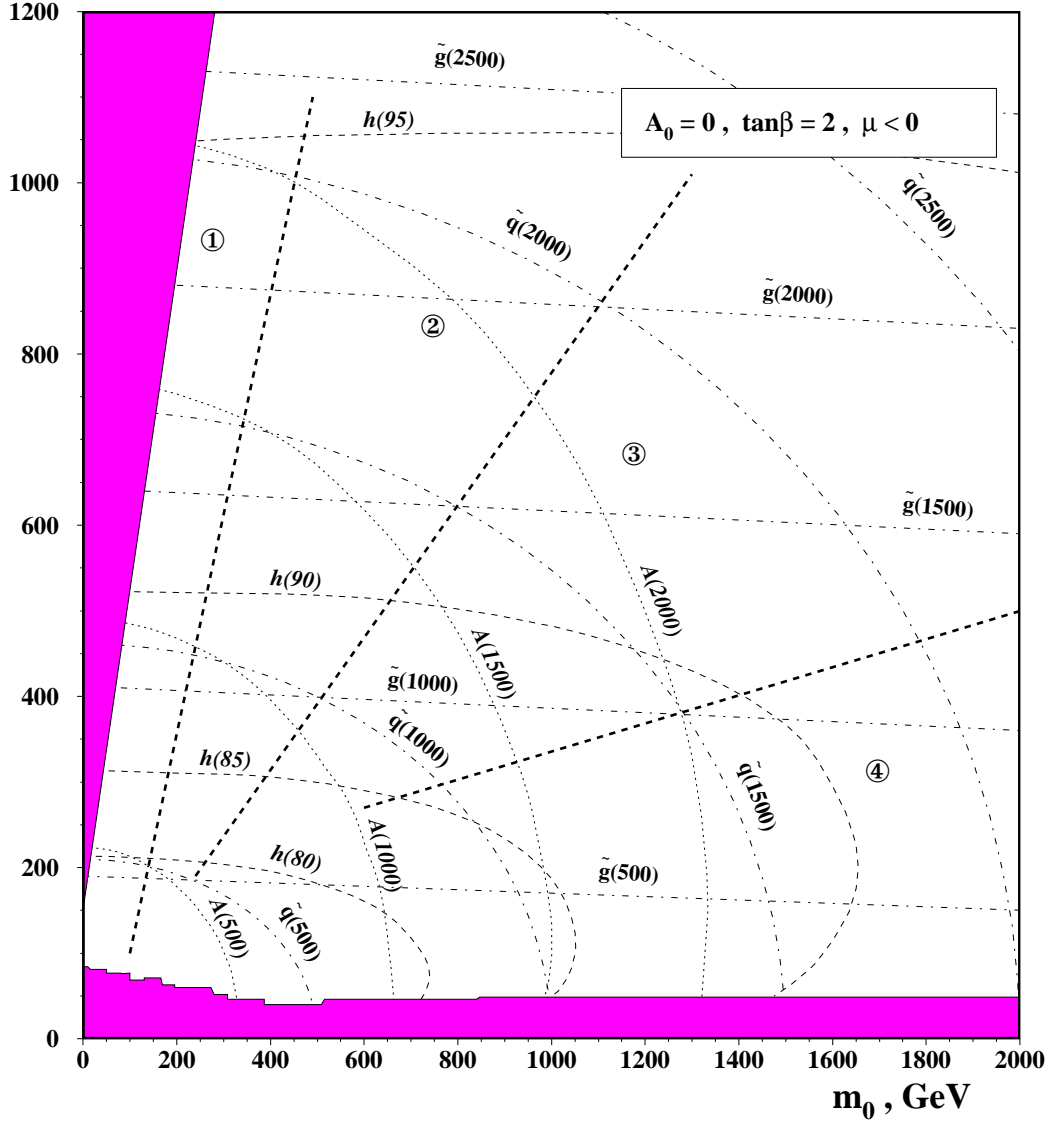


Figure 2.16: Domains of the $(m_0, m_{1/2})$ parameter space with characteristic predominant decay modes. Isomass contours for squarks, gluinos, light and pseudoscalar higgses are also shown. The shaded region near the $m_{1/2}$ axis shows the theoretically forbidden region of parameter space, and a similar region along the m_0 axis corresponds to both, theoretically and experimentally excluded portions of parameter space.

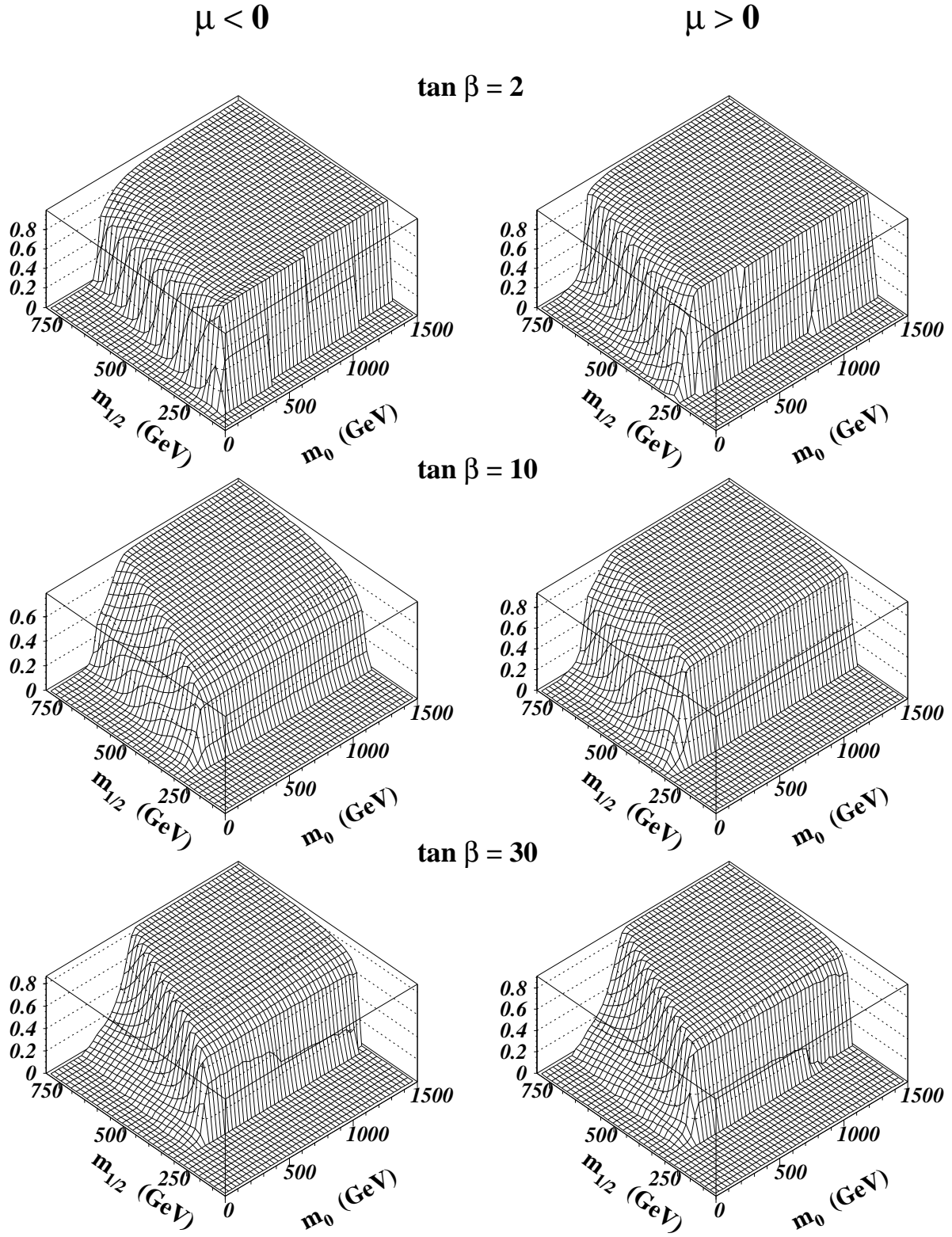


Figure 2.17: $\tilde{\chi}_2^0 \rightarrow \tilde{\chi}_1^0 h$ branching ratio versus $(m_0, m_{1/2})$ for fixed $A_0 = 0$ and different values of $\tan \beta$ and μ .

3 Experimental signatures considered

As described earlier, the highest cross-section for high mass R -parity conserving SUSY at hadron colliders is due to squarks and/or gluinos which decay through a number of steps to quarks, gluons, charginos, neutralinos, sleptons, W , Z , Higgses and ultimately a stable LSP (lightest neutralino in mSUGRA), which is weakly interacting and escapes detection. The final state has missing energy (2 LSP's + neutrinos), a number of jets, and a variable number of leptons, depending on the decay chain. Due to the escaping LSP's, which appear at the end of each sparticle decay chain, the masses of sparticles can not generally be reconstructed explicitly. However, the sparticle production and decay characteristics, discussed in the previous section, lead to a number of specific event topologies, which should allow the discovery of SUSY in general, and specifically the separation of certain SUSY sparticles and processes from SM and other SUSY processes. The LHC must therefore not only be able to discover SUSY, if it is realized at electroweak scale, and if it has not yet been discovered at the Tevatron (which covers a very promising energy/mass range), but the LHC experiments should also be able to disentangle the various SUSY production mechanisms and reconstruct most of the sparticle spectrum, determine or limit the models/scenarios, constrain model parameters, etc. Our present understanding shows that all this is possible at the LHC, but a lot of methodical studies are still required. Usually, one characterizes the general SUSY signal significance by an excess over the expected SM event rates, while for specific SUSY processes the background includes besides SM processes other SUSY reactions contributing to the same final state topology.

The following final states have been investigated in substantial detail in CMS:

1) *leptons + jets + E_T^{miss}* final states with a variable number of leptons and jets and possible requirements on b -jets. These channels provide the maximum mass and parameter reach of SUSY through the production of strongly interacting particles, which in their cascade decays can give rise to many leptons and jets.

2) inclusive 2 *leptons + E_T^{miss} + (jets)* and 3 *leptons + (E_T^{miss})* final states. In these channels SUSY reveals itself through $\tilde{\chi}_2^0$ inclusive production with subsequent decay – directly or via a slepton – into two leptons and $\tilde{\chi}_1^0$. For some regions of parameter space, the two lepton invariant mass with its characteristic shape, a sharp edge at the end point of the spectrum, allows the determination of the sparticle masses, including the slepton mass, and model parameters. These channels could well be the first indication/signature for SUSY production at the LHC.

3) exclusive 2 *leptons + no jets + E_T^{miss}* final state, which is enriched in direct (Drell-Yan) slepton pair production as discussed in section 2.2. The main issue here is to understand and keep under control both the SM background (with many processes to be considered) and internal SUSY backgrounds. This channel could allow discovery and study of slepton production.

4) exclusive 3 *leptons + no jets + E_T^{miss}* final state, which is the signature for direct $\tilde{\chi}_1^\pm \tilde{\chi}_2^0$ production in a Drell-Yan process. It is therefore theoretically most reliable (along with slepton production). For this and the slepton study, to suppress the SM and internal SUSY backgrounds a good response to jets down to $E_T^{jet} \sim 30$ GeV, with a calorimetric coverage up to $|\eta| \sim 4.5$, is required. This exclusive channel could also play a central role in a precise determination of the $\tilde{\chi}_1^0$ – the SUSY dark matter candidate.

For the present study, production of SUSY processes has been simulated using the

ISAJET 7.14 Monte Carlo event generator [17] and the SM backgrounds by PYTHIA 5.7 [19], both with the CTEQ2L structure functions [20]. Before presenting the physics expectations, we discuss the CMS detector optimisation studies done specifically with SUSY searches in mind.

4 Detector issues

4.1 CMS detector optimisation for SUSY studies

The design goals of CMS are to measure muons, electrons and photons with a resolution of $\lesssim 1\%$ over a large momentum range (≤ 100 GeV), to measure jets with a resolution of 10% at $E_T = 100$ GeV and to be highly hermetic, with a missing E_T performance as required for SUSY searches. The central element of CMS is a 13 m long, 6 m diameter solenoid generating a uniform magnetic field of 4 T [21, 22], Fig. 4.1. The magnetic flux is returned through a 1.8 m thick saturated iron yoke instrumented with muon chambers. Muons are precisely measured in the inner tracker and are identified and measured in four muon stations inserted in the return yoke. Precision tracking in the muon stations is carried out with drift tube planes in the barrel and with cathode strip chambers in the endcaps [23]. The goal is to achieve a spatial resolution of ~ 100 μm and an angular accuracy on a local muon track segment of ~ 1 mrad per station. Excellent time resolution is needed to identify the bunch crossing (with a periodicity of 25 nsec). Muon stations therefore also include resistive plate chamber triggering planes with time resolution ~ 2 nsec [23].

The inner tracking system of CMS is designed to reconstruct high- p_T muons, isolated electrons and hadrons over $|\eta| < 2.5$ with a momentum resolution of $\Delta p_T/p_T \simeq 0.15 p_T \oplus 0.5\%$ (p_T in TeV). Silicon and gas microstrip detectors are used to provide the required precision and granularity. In the present design there are about 9×10^6 MSGC detector channels, about 4×10^6 Si microstrip channels and about 8×10^7 Si pixel channels [24]. For high momentum muons the combination of tracker and muon chamber measurements greatly improves the resolution: $\Delta p_T/p_T \simeq 0.06$ for a $p \simeq 1$ TeV muon in $|\eta| < 1.6$ [21].

The calorimeter system of CMS is made of a high resolution lead-tungstate (PbWO_4) crystal electromagnetic calorimeter and a copper-scintillator hadron calorimeter behind it. The primary function of the electromagnetic calorimeter is to precisely measure electrons and photons, and in conjunction with the hadron calorimeter to measure also jets. The arrangement of crystals is shown in Fig. 4.1. In the barrel the crystals are 25 radiation lengths (X_0) deep and the lateral granularity is $\simeq 2 \text{ cm} \times 2 \text{ cm}$ corresponding to $\Delta\eta \times \Delta\phi = 0.014 \times 0.014$. They are read out with Si avalanche photodiodes [25]. The electromagnetic calorimetry extends over $|\eta| < 3$. The total number of crystals is $\sim 1.1 \times 10^5$. With a prototype PbWO_4 calorimeter in a test beam, an energy resolution of $\sigma_E/E \simeq 0.6\%$ has been obtained for electrons of $E = 120$ GeV [26]. Hadron calorimetry with large geometrical coverage for measurement of multi-jet final states and missing transverse energy (E_T^{miss}) is essential in all sparticle searches, as it is the E_T^{miss} which provides evidence for the escaping LSP's (lightest neutralinos). The hadron calorimeter of CMS is made of copper absorber plates interleaved with scintillator tiles read out with embedded wavelength shifting fibers [27]. The readout in the 4 Tesla field is done with hybrid photodetectors [28]. The tiles are organized in towers (Fig. 4.1) giving a lateral

segmentation of $\Delta\eta \times \Delta\phi \simeq 0.09 \times 0.09$. The hadronic resolution obtained in a test beam is $\sigma_E/E \simeq 100\%/\sqrt{E} \oplus 5\%$ for the combined PbWO₄ and hadronic calorimeter system [29]. This central hadron calorimetry extends up to $|\eta| = 3.0$. It is complemented in the forward region $3.0 < |\eta| < 5.0$ by quartz-fiber “very forward calorimeters” (Fig. 4.1) [27, 30]. Their function is to ensure detector hermeticity for good missing transverse energy resolution, and to extend the forward jet detection and jet vetoing capability of CMS which is essential in slepton, chargino, neutralino searches as discussed in the following. Detector hermeticity is particularly important for processes where the physical (real) missing E_T is on the order of few tens of GeV as is the case in $h, H, A \rightarrow \tau\tau, W \rightarrow l\nu, t \rightarrow l\nu b, t \rightarrow H^\pm b \rightarrow \tau\nu b$, etc. and in particular in slepton, chargino and neutralino searches connecting the LEP2/Fermilab and the LHC search ranges.

4.2 HCAL optimisation and tail catcher

A number of steps have been undertaken in the design of CMS to optimise its E_T^{miss} response in view of SUSY searches. These include the inclusion of very forward calorimetry, the addition of a tail catcher behind the coil [31] and optimisation of the crack for the passage of services between the barrel and endcap calorimeters. We now briefly discuss these issues. The central ($|\eta| < 3.0$) calorimetry of CMS is complemented by very forward quartz-fiber calorimeters [30] covering the rapidity range $3 < |\eta| < 5$, Fig. 4.1. Figure 4.2 illustrates the effect of the forward energy flow containment and its effect on missing E_T measurements. It shows the expected instrumental (fake) missing E_T distributions for QCD di-jet events as a function of calorimetric coverage at large rapidities. Calorimetry extending up to $|\eta| \simeq 5$ reduces the fake (instrumental) E_T^{miss} by an order of magnitude in the 20 - 120 GeV range. Furthermore, the missing E_T resolution, $\sigma(E_T^{miss})/\Sigma E_T$ where ΣE_T is the calorimetric transverse energy sum, is also much reduced in the presence of very forward calorimetry, see Fig. 4.3. There is a second requirement on forward calorimetry which turns out to be essential if we hope to eventually extract slepton and chargino/neutralino signals. In the search for direct DY slepton pair production $\tilde{l}\tilde{l} \rightarrow l^+l^- \tilde{\chi}_1^0 \tilde{\chi}_1^0$, or for the associated direct (DY) chargino/neutralino $\tilde{\chi}_1^\pm \tilde{\chi}_2^0 \rightarrow l^\pm \nu \tilde{\chi}_1^0 l^\mp \tilde{\chi}_1^0$ production, leading to final states with two or three isolated leptons, no jets, and missing E_T , it is essential to have the capability to recognise and veto on forward jets. This is needed to suppress the large backgrounds due to $t\bar{t}$, $\tilde{q}\tilde{q}$, $\tilde{g}\tilde{q}$, $\tilde{g}\tilde{g}$ and the associated production modes $\tilde{q}\tilde{\chi}$, $\tilde{g}\tilde{\chi}$ which would otherwise overwhelm the signals. The extension into the forward direction of the central jet vetoing capability provides the needed additional rejection factors to keep these backgrounds under control.

Figure 4.4a shows for the case of direct $\tilde{\chi}_1^\pm \tilde{\chi}_2^0$ production, (discussed in more detail in section 8), the expected rejection factors against the main backgrounds as a function of the rapidity range and detection threshold over which the jets can be recognized. Figure 4.4b shows the rejection factors against internal SUSY and the SM $t\bar{t}$ backgrounds. Here the jet veto is applied after lepton isolation and an E_T^{miss} cut, thus the value of the rejection factor is much reduced. In both cases, the jet coverage needed to obtain sufficient background rejection is $|\eta|$ up to $\simeq 4$ and the loss of signal acceptance due to the jet veto is typically $\sim 10\%$.

The locations of the tail-catcher scintillator layers, two in the barrel region behind the coil and one in the endcap, are shown on the longitudinal cut through the CMS detector in Fig. 4.1. Figure 4.5 shows the depth in interaction lengths λ of calorimetry in CMS,

and the total sampled depth including the tail catcher layers, as a function of rapidity [32]. Whilst the total calorimetric absorber thickness within the coil is somewhat marginal at rapidity $\eta \sim 0$ for full hadronic shower containment, inclusion of tail-catcher layers allows hadron energy measurements with at least 10.5 interaction lengths everywhere.

Figure 4.6 shows the effects on hadron energy measurements of the inclusion of the tail-catcher layers, specifically on the reduction of the low-energy tail in the response to (200 GeV) hadrons [33]. What is shown is the ratio of the (GEANT) simulated response to the incident energy for single pions in the rapidity range 0.33 to 0.86 with no tail catcher, with one, and with two tail catcher layers included in the readout. Mismeasurements of hadronic energies, and in particular the presence of low-energy tails in hadronic (jet) energy measurements is one of the main sources of fake instrumental missing E_T . When due to insufficient shower containment in depth, inclusion of the tail-catcher layers cures this problem to a large extent.

There are two other sources of hadronic mismeasurements and low-energy tails: dead areas and volumes due to detector cracks and matching the hadronic response of ECAL to HCAL.

Special attention has been paid in CMS to the effects on hadronic energy measurements – and thus on missing E_T – of the main crack for services between the barrel and endcap calorimetry at rapidity $\sim 1.2 - 1.5$ (Fig. 4.1). The various configurations which have been studied for this crack are shown in Fig. 4.7 [13]. The aim was to minimize the degradation of the hadronic energy resolution and the level of the low energy tail for hadrons and jets straddling the region of the gap. The optimal choice, from the point of view of hadron response, weight of the cantilevered endcap hadron calorimeter, manoeuvrability of endcaps and margin of freedom to close the detector, is a conical endcap shape with a non-pointing crack at 52 degrees from the beam line labeled TP7 in Fig. 4.7. Figure 4.8 shows the reconstructed energy response (GEANT) to single pions of 100 GeV when incident on and off the crack region, for three crack widths of 11, 18 and 25cm. With the present estimate of the volume of services a gap of 12 cm is needed, plus 2 cm for clearance.

An essential ingredient to obtain optimal E_T^{miss} response of a detector is the linearity of its response as a function of incident hadron (jet) energy. The non-compensating mixed calorimeter of CMS – with a PbWO_4 crystal ECAL compartment followed by a Cu/scintillator sampling HCAL – has significantly different electromagnetic to hadronic (e/h) responses in the two parts, $e/h \sim 1.8$ in the ECAL vs. 1.2 in the HCAL. Linearity is more difficult to achieve in such a mixed calorimeter than in a more homogeneous system. To restore linearity as much as possible, and to compensate for the effects of dead material in the space between the ECAL and HCAL, weighting techniques for responses must be used between ECAL and HCAL, and within HCAL compartments and tail catcher layers. An essential limiting factor is the number of readout channels we can afford for the longitudinal HCAL tower segmentation. The optimal set of weighting factors must be determined on basis of test beam data and detailed simulations of responses to hadrons and jets, taking into account financial limitations. In the present HCAL design [27] a good compromise between expected performance and cost is found by having a very shallow (1 scintillator plane) front HCAL tower readout and second deep ($\simeq 5 \lambda$) HCAL segment readout. The first shallow HCAL segment just behind the ECAL detects hadron interactions in the ECAL – where their energy deposition is underestimated ($e/h \sim 2$) – and compensates by overweighting this layer. Present investigations show that with this

technique the expected non-linearity should not exceed 4% for pions between 20 and 300 GeV [27].

4.3 The role of the tracker in SUSY searches

The inner tracking system of CMS is primarily designed to reconstruct high- p_T muons, isolated electrons and hadrons over $|\eta| < 2.5$ with a momentum resolution of $\Delta p_T/p_T \sim 0.15 p_T \oplus 0.5\%$ (p_T in TeV). Hadrons must be reconstructed down to $\sim 1 - 2$ GeV, as lepton and photon isolation is a very important selection criterion for a number of physics signals, and in particular in the SUSY searches for sleptons, charginos and neutralinos. Another important task of the tracker is to measure track impact parameters allowing the detection and measurement of long-lived particles and the tagging of b -jets. The main problem in tracking is that of pattern recognition. At a luminosity of $10^{34} \text{ cm}^{-2}\text{s}^{-1}$, interesting events will be superimposed on a background of about 500 soft charged tracks within the rapidity range considered, coming from ~ 15 minimum bias events which occur in the same bunch crossing. To solve the pattern recognition problem, detectors with small cell sizes are required. Silicon and gas microstrip detectors provide the required precision and granularity to maintain cell occupancies below 1%, but the number of detector channels is large ($\sim 1.5 \times 10^7$). The design of the CMS tracker is shown in Fig. 4.9.

A track in the barrel part of the tracker, in its present design (summer 1997), first encounters two layers of pixel detectors, then four layers of microstrip Si detectors of 67 and 100 μm pitch followed by seven layers of 200 μm pitch microstrip gas chambers (MSGC; $\sim 50 \mu\text{m}$ precision) [24]. Alternate MSGC and Si microstrip layers are double-sided to allow determination of the z coordinate of a track by a small-angle stereo measurement. The inner cylindrical volume ($r \lesssim 50 \text{ cm}$) with Si detectors will be kept at $\sim -5^\circ \text{ C}$ temperature, whilst the outer (MSGC) part at $\sim 18^\circ \text{ C}$. Figure 4.10 shows the expected track momentum resolutions in the CMS tracker alone. As already mentioned, for high momentum muons the combination of tracker and muon chamber measurements greatly improves the resolution: $\Delta p_T/p_T \simeq 0.06$ for a $p \simeq 1 \text{ TeV}$ muon in $|\eta| < 1.6$ [21]. This requires that the relative alignment of the inner and outer systems be known to within $\sim 100 \mu\text{m}$ [23]. The pixel layers, at radii of 7.7 and 11 cm in the high luminosity pixel detector option, ensure precise impact parameter measurements, with an asymptotic (high momentum) accuracy of $\sigma_{IP} = 23 \mu\text{m}$ in the transverse plane (Fig. 4.10), and of $\simeq 90 \mu\text{m}$ along the z axis [21]. For the initial “low luminosity” ($\lesssim 10^{33} \text{ cm}^{-2}\text{s}^{-1}$) running, the impact parameter performance is improved by having the pixel layers at 4 and 7.7 cm radii.

4.4 Lepton isolation

In the search for direct DY slepton pair production $\tilde{l}\tilde{l} \rightarrow l^+l^- \tilde{\chi}_1^0 \tilde{\chi}_1^0$ or for the associated direct (DY) chargino/neutralino $\tilde{\chi}_1^\pm \tilde{\chi}_2^0 \rightarrow l\nu \tilde{\chi}_1^0 l^+l^- \tilde{\chi}_1^0$ production leading to a final state with two or three isolated leptons, no jets and missing E_T , there are two essential instrumental requirements allowing separation of the signal. The first is lepton isolation, to suppress the copious backgrounds from processes such as $t\bar{t}$, $Zb\bar{b}$, $b\bar{b}$. The rejection factors expected on basis of tracker isolation criteria as a function of the p_T cut on the accompanying tracks are shown in Fig. 4.11 for low and high luminosity running conditions. The second requirement, as discussed previously, is on the detector capability to veto on jets.

4.5 Tagging of b -jets in CMS

As discussed in Section 2.3, an important ingredient for SUSY physics studies is the capability of the detector to tag b -jets. Figures 2.13, 2.14 and 2.15 illustrate the many ways b -jets can serve as final state signatures of \tilde{b} , \tilde{t} , t production in the \tilde{g}/\tilde{q} cascades. Particularly important is the possibility to detect $h \rightarrow b\bar{b}$ in $\tilde{g}/\tilde{q} \rightarrow \tilde{\chi}_2^0 \rightarrow \tilde{\chi}_1^0 h$ decay channel with $S/B \sim 1$ and potentially with much lower integrated luminosity than required to observe $h \rightarrow \gamma\gamma$. Techniques for b -tagging have been studied in detail in CMS. The inner part of the CMS tracker, in particular the two pixel layers, has been optimised in detector positioning and required resolution with b -tagging performance as the main criterion [34]. The expected b -tagging efficiency and sample purity has been studied with several tagging algorithms based on track impact parameter measurements. Figure 4.12 shows, for example, the expected tagging efficiency as a function of jet E_T averaged over the pixel detector acceptance. For b -jets in $t\bar{t}$ events it is $\sim 30\%$, whilst the expected fake rate probability is $\sim 1\%$. The tagging algorithm used for Fig. 4.12 requires ≥ 3 tracks of $p_T \geq 2$ GeV with $\geq 2\sigma$ significance for impact parameter measurements in the transverse plane.

How much the expected tagging efficiency is dependent on the tagging algorithm and what is the possible trade-off between efficiency and sample purity is illustrated by Fig. 4.13 where several tagging algorithms have been exercised. Figure 4.14 shows how the tagging efficiency and purity depends on the radius of the first barrel pixel layer, changing it from 4 cm as possible for the low luminosity running to 7.7 cm as required to sustain the radiation damage at $10^{34} \text{ cm}^{-2} \text{ s}^{-1}$. There would be an important gain in tagging efficiency if the first pixel layer could be always kept at 4 cm radius, at a cost of replacing it (almost) every year. This is particularly important for channels like $h \rightarrow b\bar{b}$ which go with the square of the tagging efficiency. Whilst the tagging efficiency is a simple function of the pixel point resolution and the radial position of the barrel pixel layers, the mistagging probability is dependent on the non-Gaussian part of the measured impact parameter distribution and is more difficult to control as it depends on the overall pattern recognition performance and multiple scattering of the tracker. All the b -tagging efficiencies discussed here rely on impact parameter measurements; further improvements in b -tagging efficiency are possible, including explicit reconstruction of secondary vertices, lepton tags, etc.

4.6 CMSJET – an approximate description of detector response

Understanding of the detector response with an adequate simulation is a very important part of correctly estimating the SUSY discovery potential of the CMS experiment. We have used the CMSJET program, which is a fast, non-GEANT simulation package for the CMS detector [35, 36]. CMSJET provides a satisfactory approximate description of detector components and of the response to hadrons, leptons and gammas. It is a good compromise between performance speed and precision. The following aspects of CMSJET are relevant to this study:

- Charged particles are tracked in a 4 T magnetic field. A reconstruction efficiency of 90% per charged track with $p_T > 1$ GeV and $|\eta| < 2.5$ is assumed.
- The geometrical acceptances for μ and e are $|\eta| < 2.4$ and 2.5, respectively. The lepton momentum is smeared according to parameterizations obtained from full GEANT

simulations. For a 10 GeV lepton the momentum resolution $\Delta p_T/p_T$ is better than 1% over the full η coverage. For a 100 GeV lepton the resolution becomes $\sim 1 \div 5\%$ depending on η . We have assumed a 90% triggering plus reconstruction efficiency per lepton within the geometrical acceptance of the CMS detector. This value is probably pessimistic for muon tracks, but more realistic for electrons.

- The electromagnetic calorimeter of CMS extends up to $|\eta| = 2.61$. There is a pointing crack in the ECAL barrel/endcap transition region between $|\eta| = 1.479 - 1.566$ (6 ECAL crystals) with significantly degraded resolution. The hadronic calorimeter covers $|\eta| < 3$. The Very Forward calorimeter extends from $|\eta| = 3$ to $|\eta| = 5$. The full granularity of the calorimetric system is implemented in CMSJET. The granularity, assumed energy resolutions and electronic noise of calorimeters are listed in Table 4.1. Noise terms have been simulated with Gaussian distributions and zero suppression cuts have been applied.

Table 4.1: CMS calorimeter description

	η region	$\Delta\eta \times \Delta\phi$	$\Delta E/E$	Noise (MeV)
ECAL	$ \eta < 1.479$	0.0145×0.0145	$5\%/\sqrt{E} \oplus 0.5\%$	25, 3σ zero sup.
	$1.566 < \eta < 2.00$	0.0217×0.0218		
	$2.00 < \eta < 2.35$	0.0292×0.0291		
	$2.35 < \eta < 2.61$	0.0433×0.0436		
Crack	$1.479 < \eta < 1.566$	0.0870×6.283	$50\%/\sqrt{E} \oplus 2\%$	–
HCAL	$ \eta < 2.262$	0.087×0.087	η dependent parameterization; $82\%/\sqrt{E} \oplus 6.5\%$ at $\eta=0$	250, 2σ zero sup.
	$2.262 < \eta < 2.61$	0.174×0.175		
	$2.61 < \eta < 3.0$	0.195×0.349		
VF	$3 < \eta < 5$	$0.17 \times 0.17 \div$ 0.175×0.175	$172\%/\sqrt{E} \oplus 9\%$ for hadrons	250, 2σ zero sup.

- e/γ and hadron shower developments are taken into account by parameterization of the lateral and longitudinal profiles of the showers. The starting point of a shower is fluctuated according to an exponential law.

- Jets are reconstructed using a cone algorithm, with a cone radius $R = 0.4 \div 0.9$ and variable transverse energy threshold on jets depending on event kinematics.

- For the high luminosity ($L = 10^{34} \text{ cm}^{-2}\text{s}^{-1}$) study, event pile-up is taken into account by superposition of “hard” pile-up events on top of signal and background. These are represented by PYTHIA QCD jet events with $\hat{p}_T > 5 \text{ GeV}$. The number of superimposed pile-up events has been fluctuated with a Poisson distribution having a mean value of 15.

The CMSJET model of the CMS detector is depicted in Fig. 4.15.

CMS DETECTOR

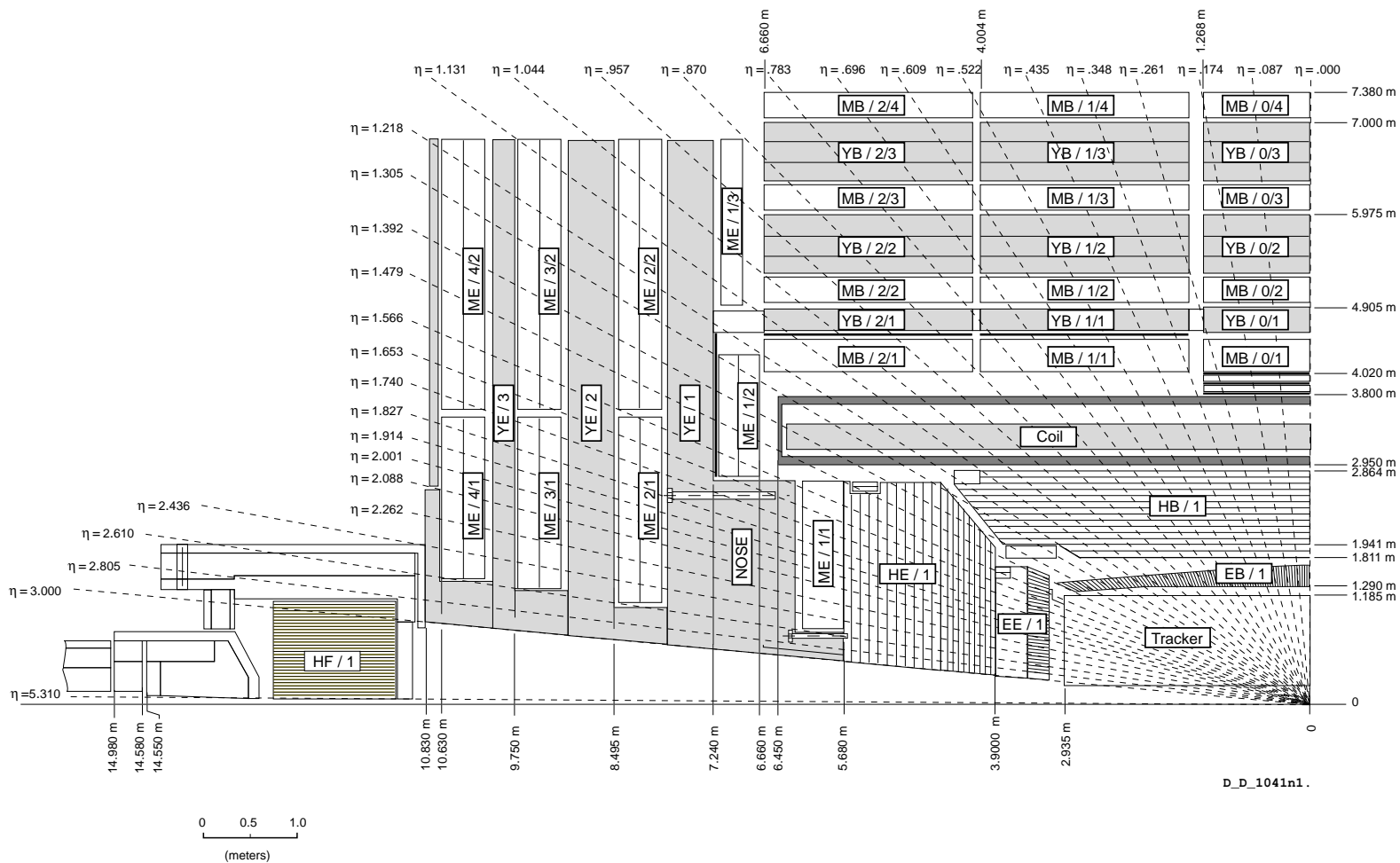


Figure 4.1: Longitudinal cut through the CMS detector. The tower structure of the hadron calorimeter and the arrangement of the electromagnetic calorimeter crystals is indicated, as well as the locations of the tail catcher layers.

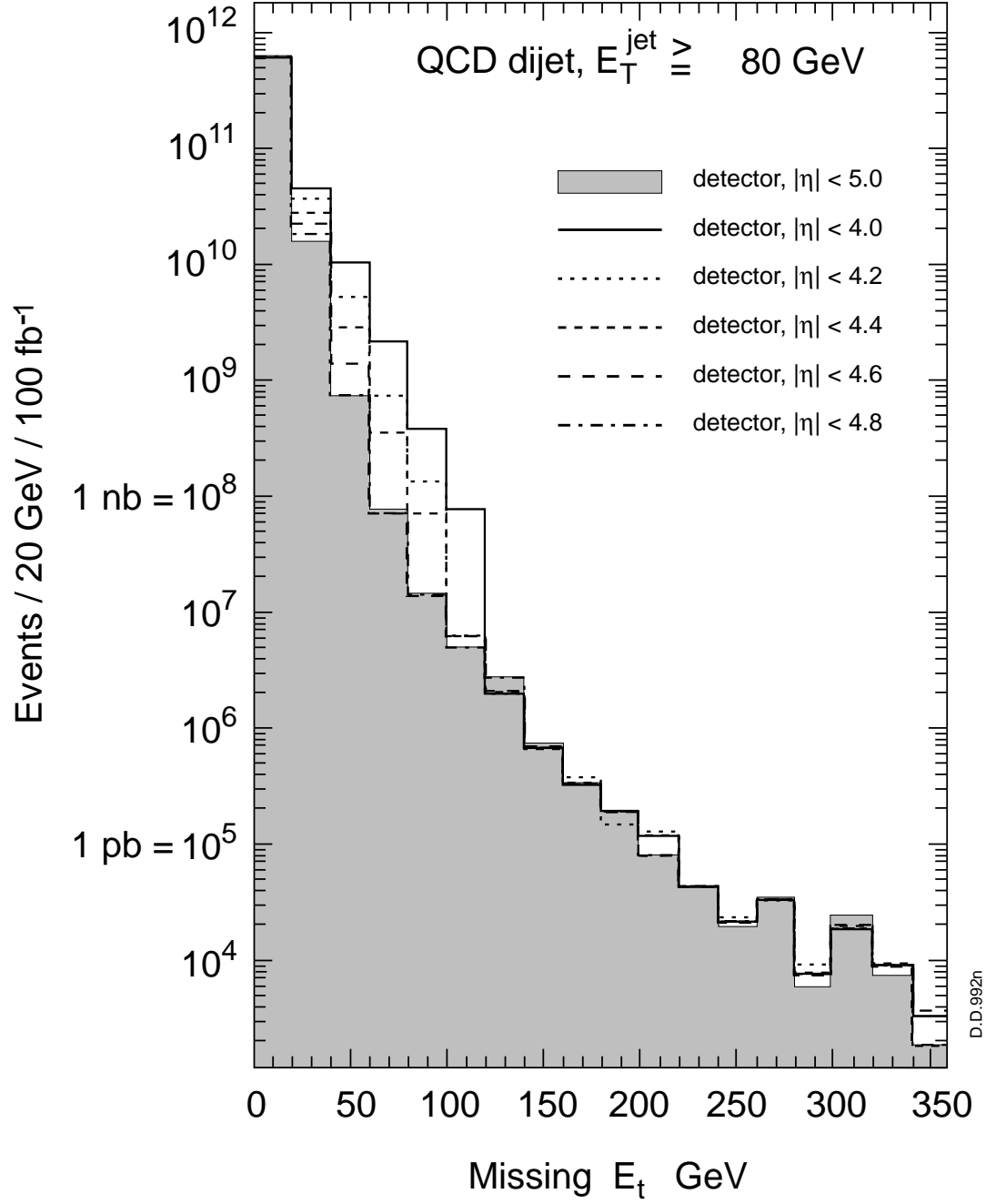


Figure 4.2: Missing E_T distributions for QCD di-jet events as a function of calorimetric coverage at large rapidities.

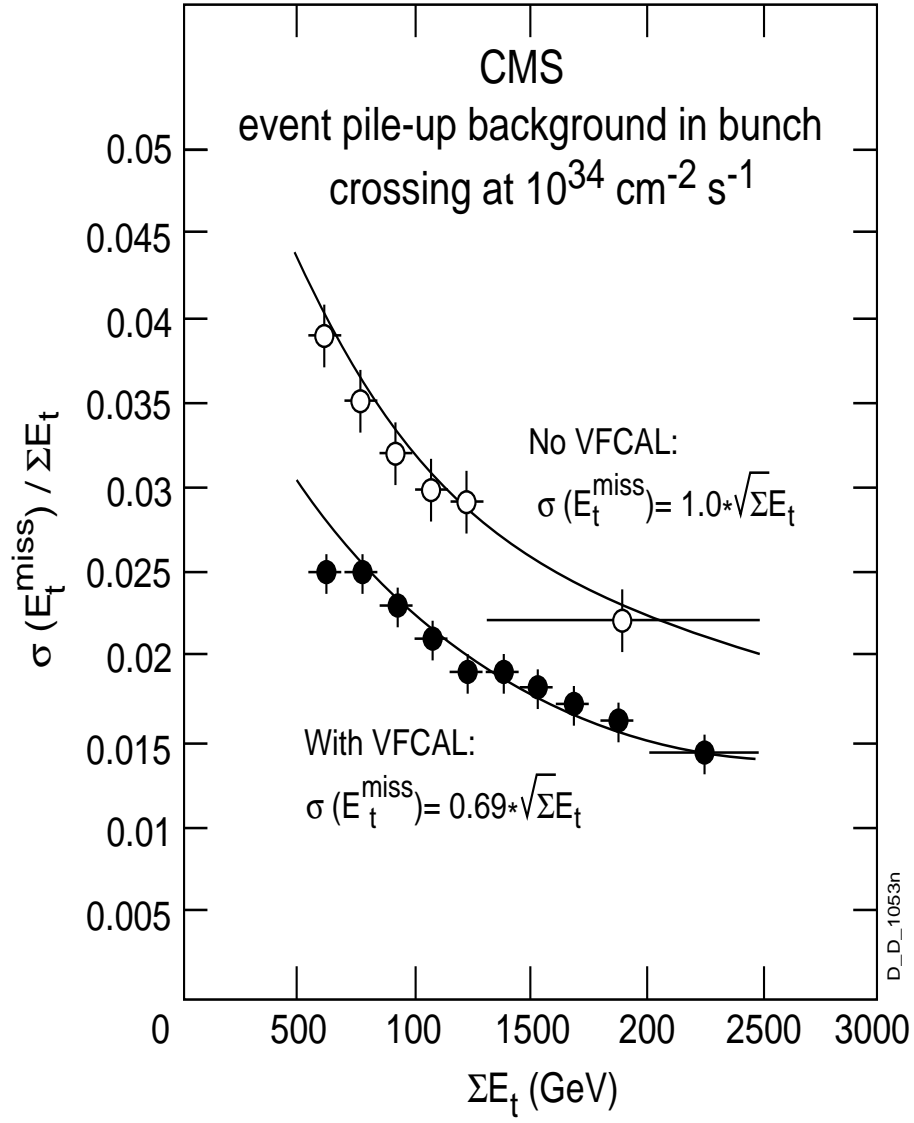


Figure 4.3: Improvement on missing E_T resolution in the presence of very forward calorimetry.

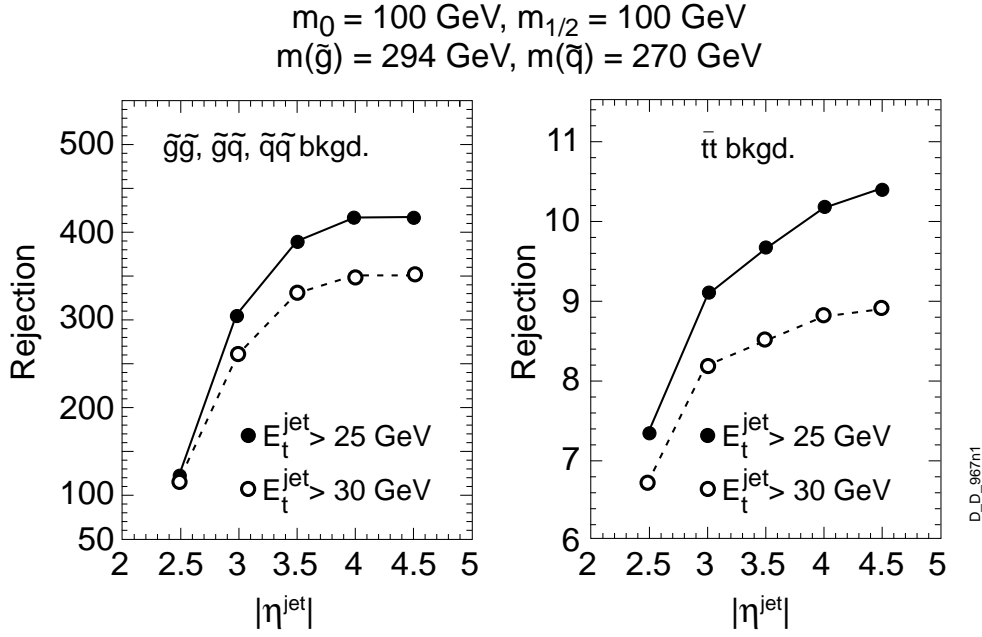


Figure 4.4a: Rejection factors which can be achieved in chargino/neutralino search using a jet veto, as a function of jet acceptance and jet detection threshold.

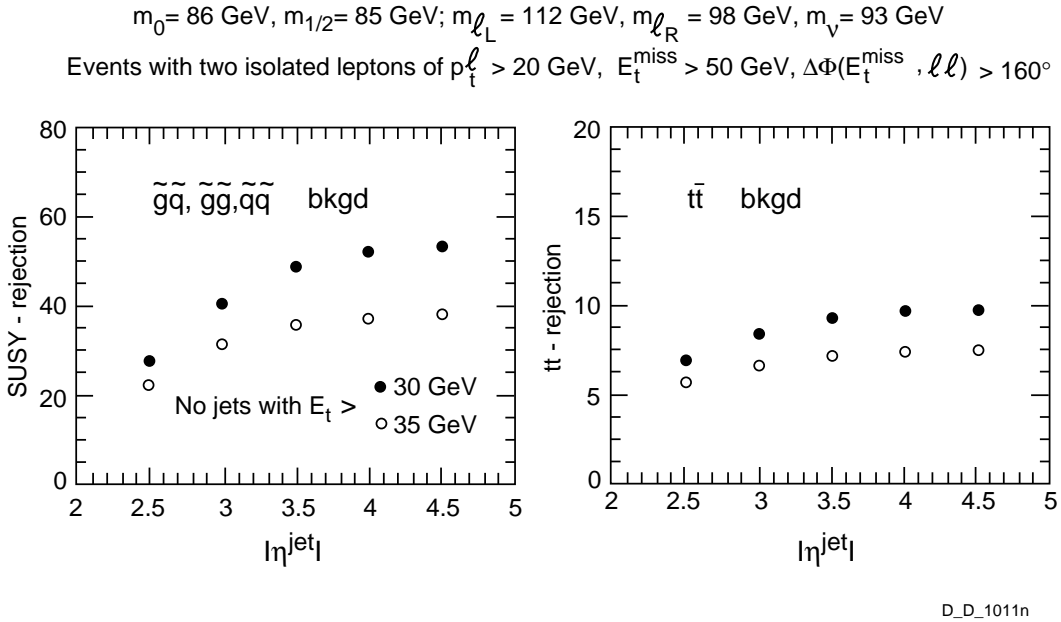


Figure 4.4b: Jet veto rejection factors against squark/gluino and $t\bar{t}$ backgrounds in slepton searches in two-lepton final states.

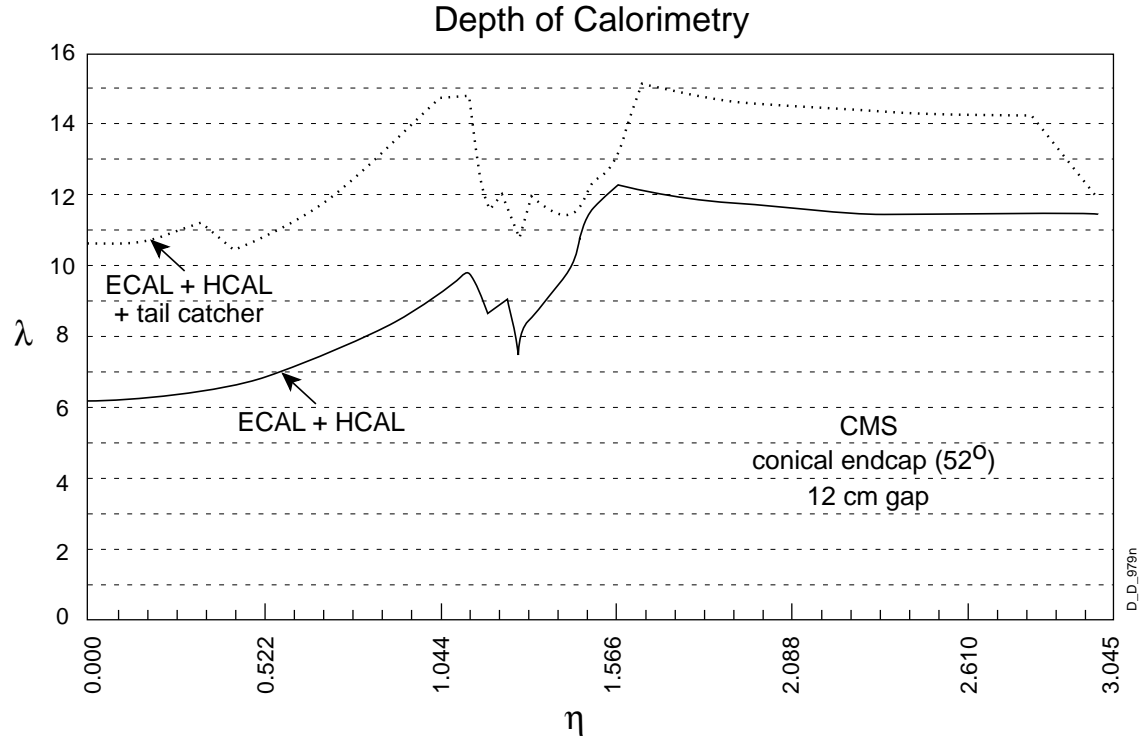


Figure 4.5: Depth of calorimetry and total sampled depth including the tail catcher layers as a function of rapidity in CMS.

Effect of tail catcher layers on reduction of tail in response to pions

$$E_t^{\text{inc}}(\pi^+) = 200 \text{ GeV (GEANT)}$$

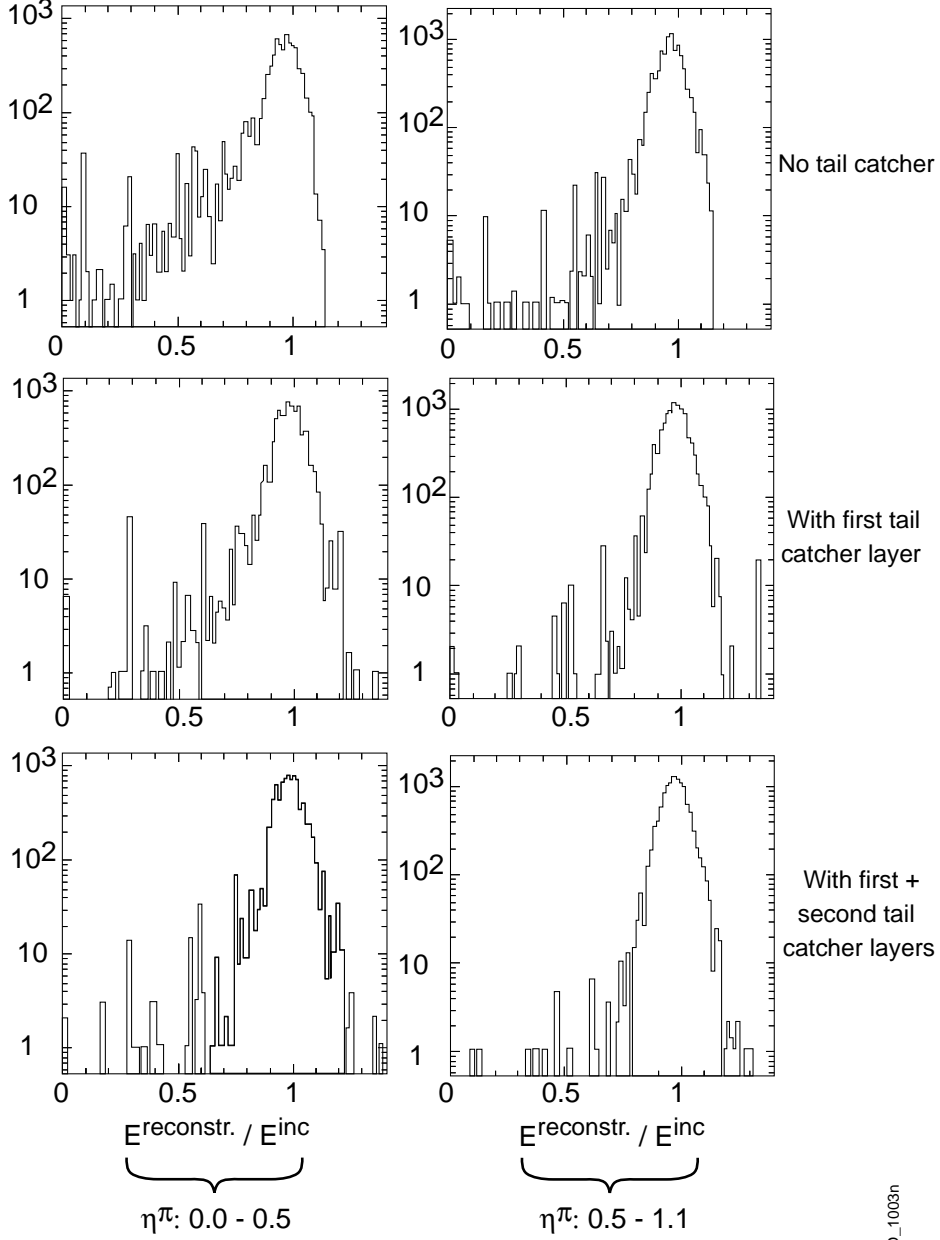


Figure 4.6: Effects on hadron energy measurements of tail catcher layers in the central and next-to-central CMS wheels i.e. in two adjacent rapidity ranges.

HCAL Barrel / endcap designs

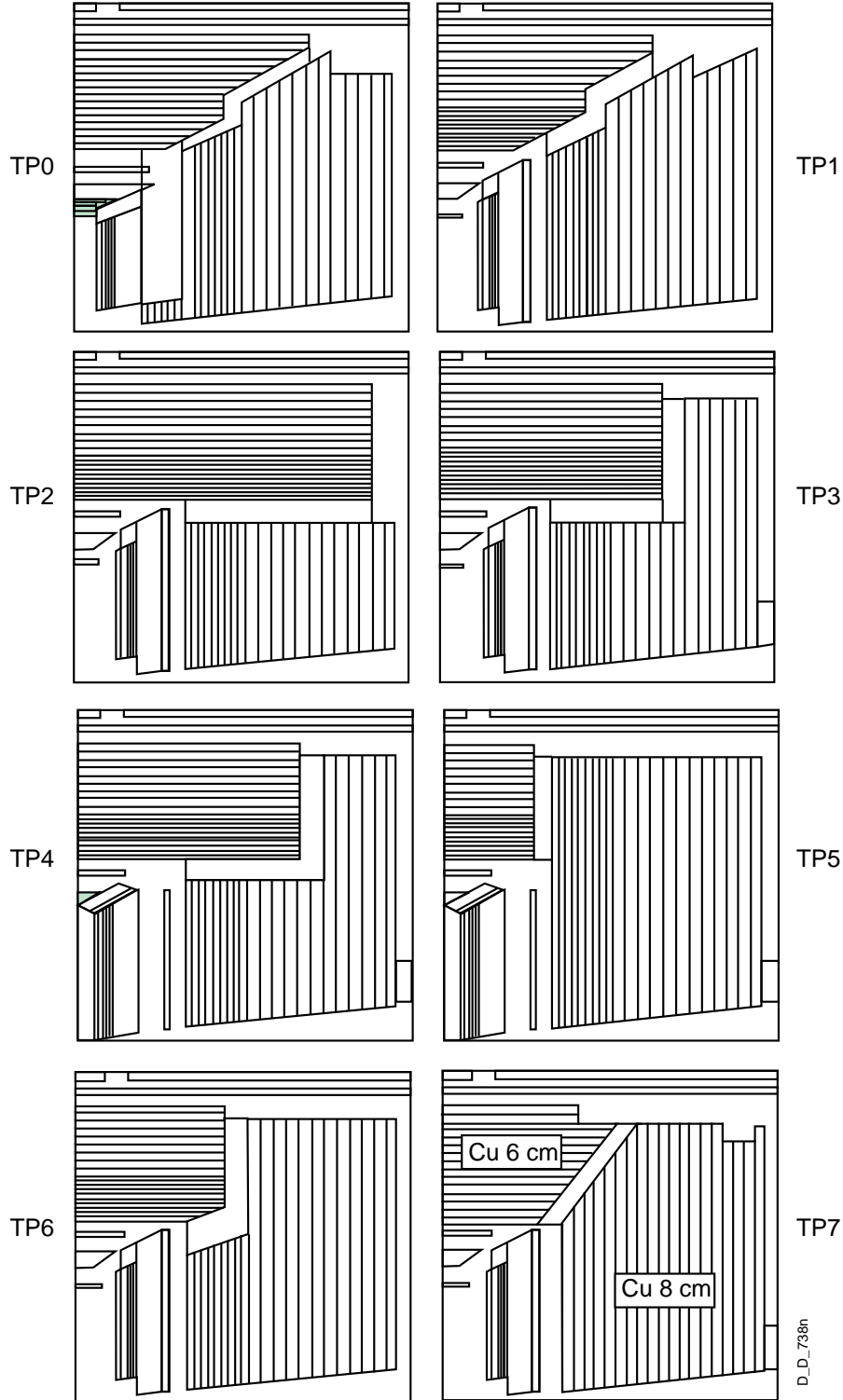


Figure 4.7: Various configurations of the barrel/endcap calorimetry transition region considered.

Effects of crack size on response to pions in "conical endcap" design

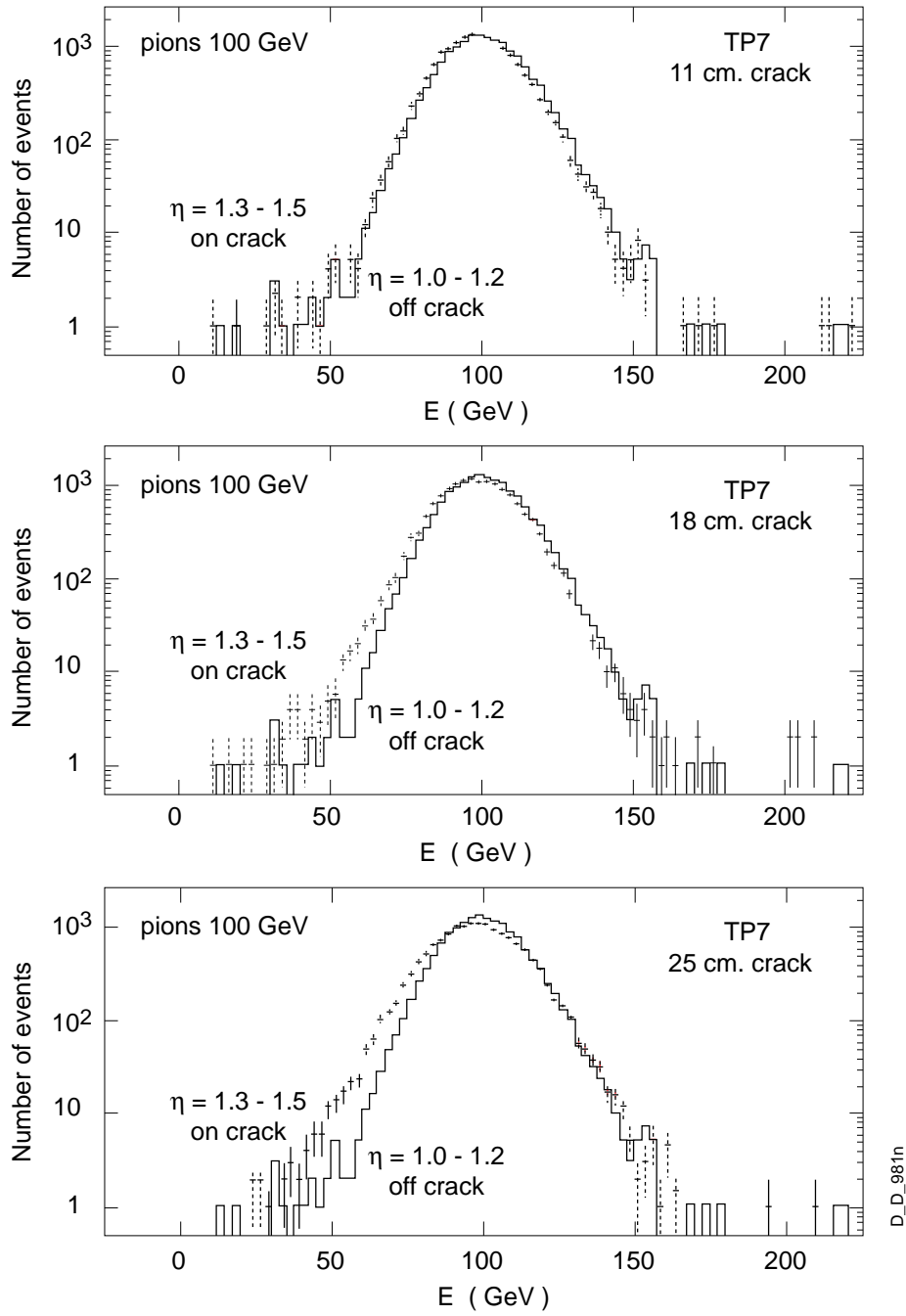


Figure 4.8: Effects on hadron energy measurements of the crack for services between the barrel and the endcap calorimetry for three crack sizes.

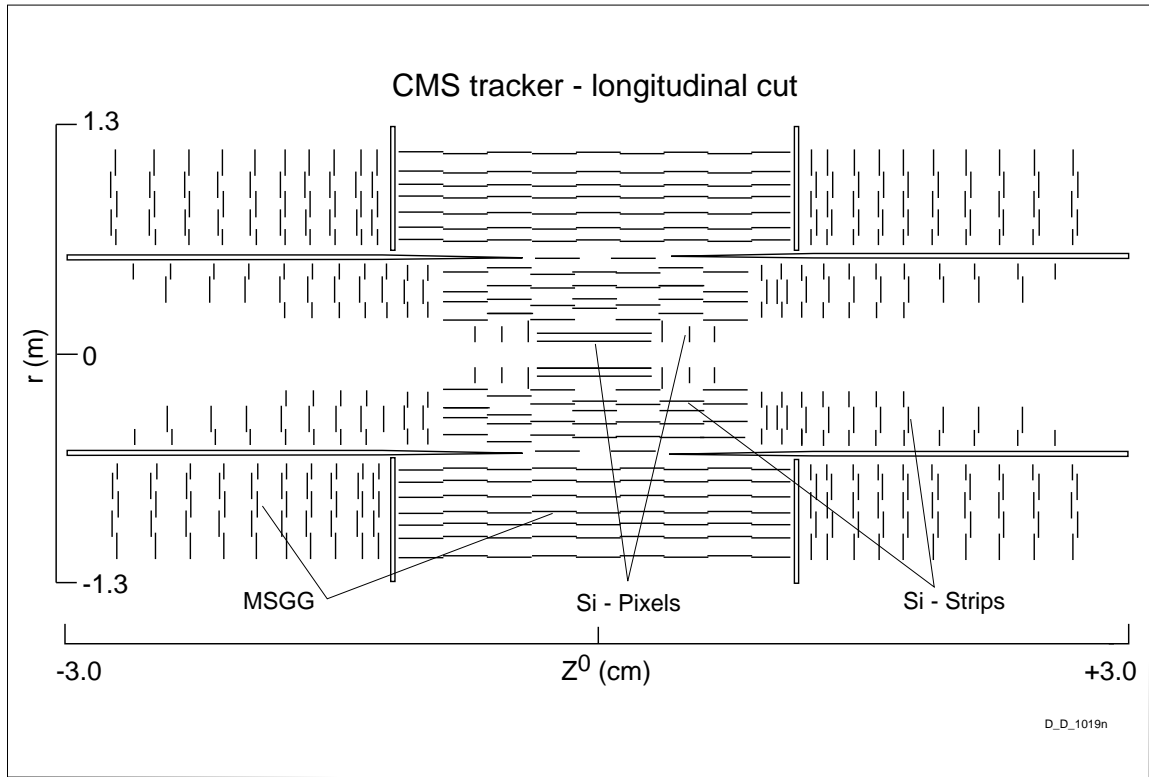
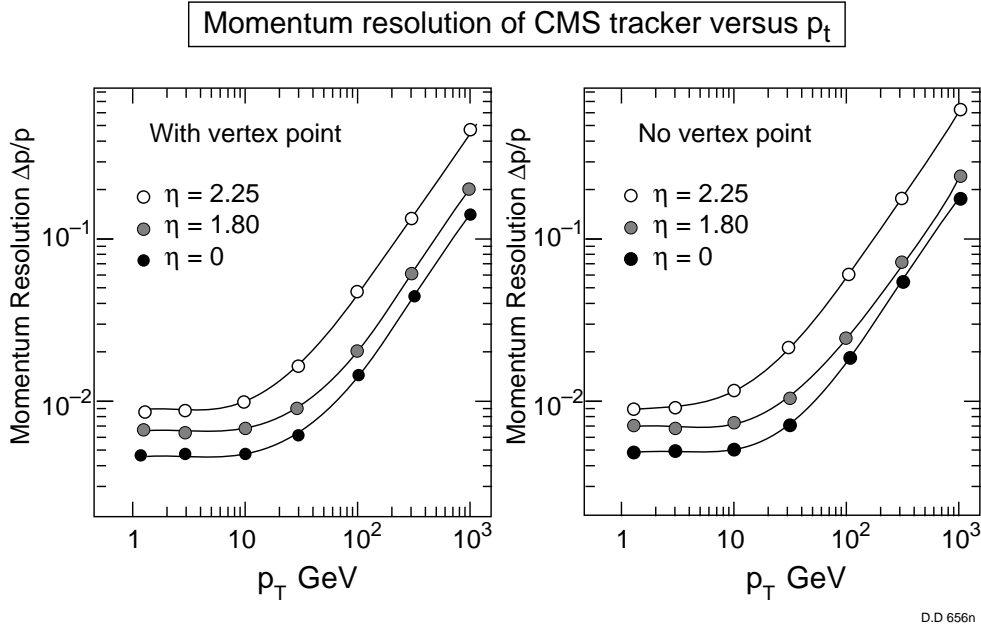


Figure 4.9: Layout of the CMS tracker.



Impact parameter resolution of CMS

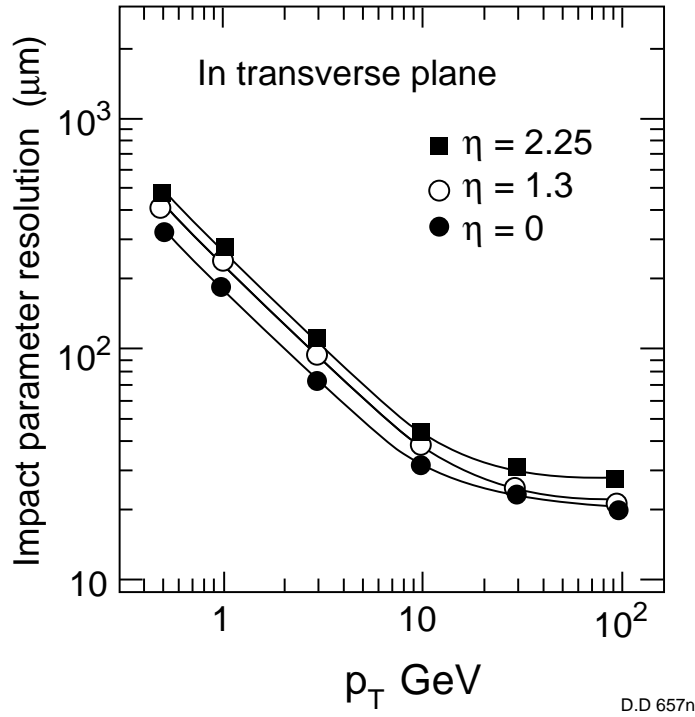


Figure 4.10: Momentum and impact parameter resolutions as a function of p_T at various rapidities.

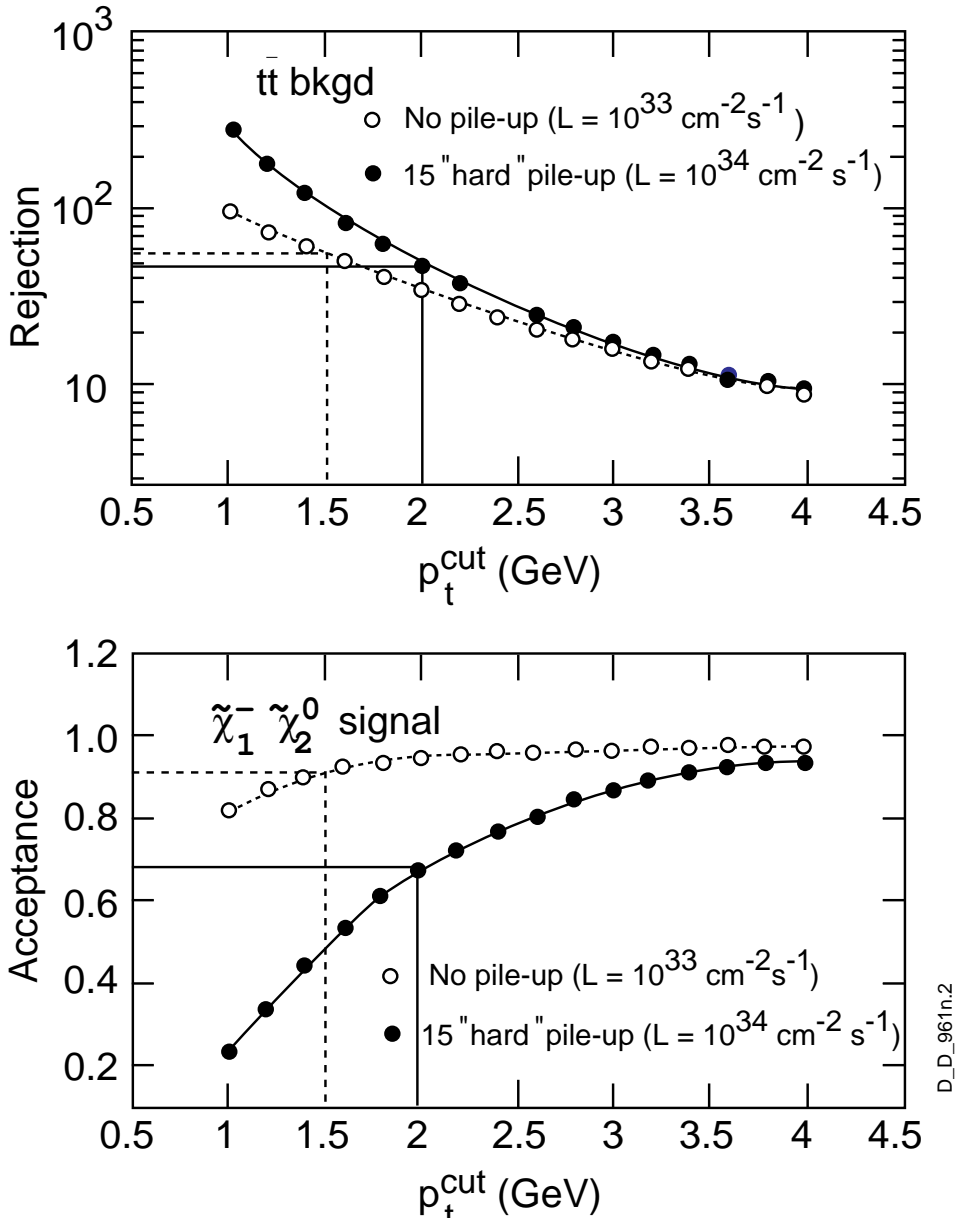


Figure 4.11: The rejection factors against $t\bar{t}$, expected on, the basis of lepton tracker isolation criteria as a function of the p_T cut on the accompanying tracks in a cone of $R = 0.3$.

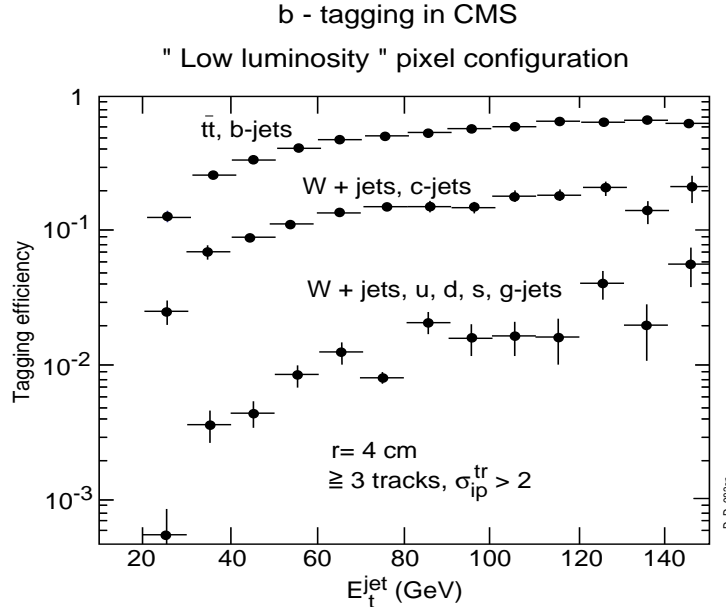


Figure 4.12: Tagging efficiency for b - and c -jets and mistagging probability for light quark and gluon jets. The tagging algorithm requires ≥ 3 tracks of $p_T \geq 2$ GeV with $\geq 2\sigma$ significance for impact parameter measurements in the transverse plane.

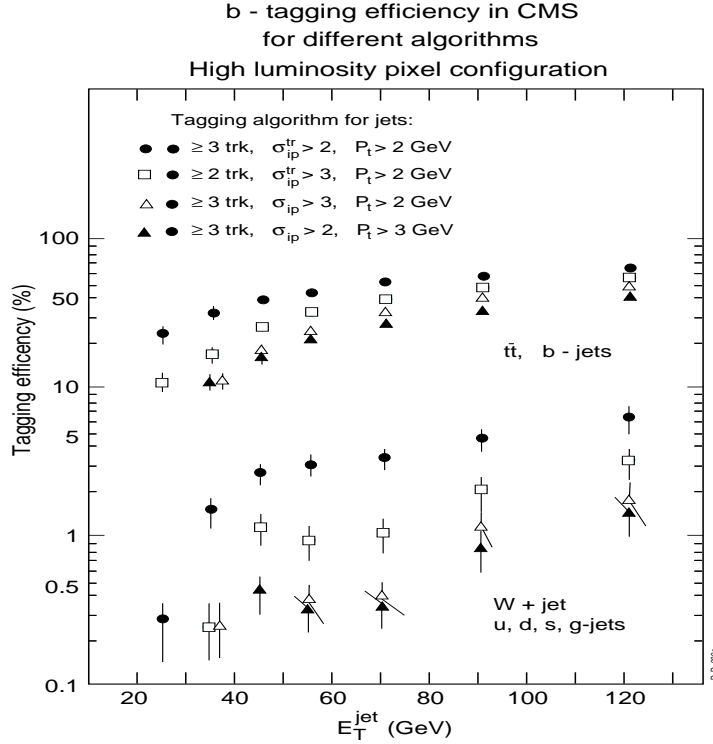


Figure 4.13: Tagging efficiency for b -jets and mistagging probability for light quark and gluon jets for various tagging algorithms.

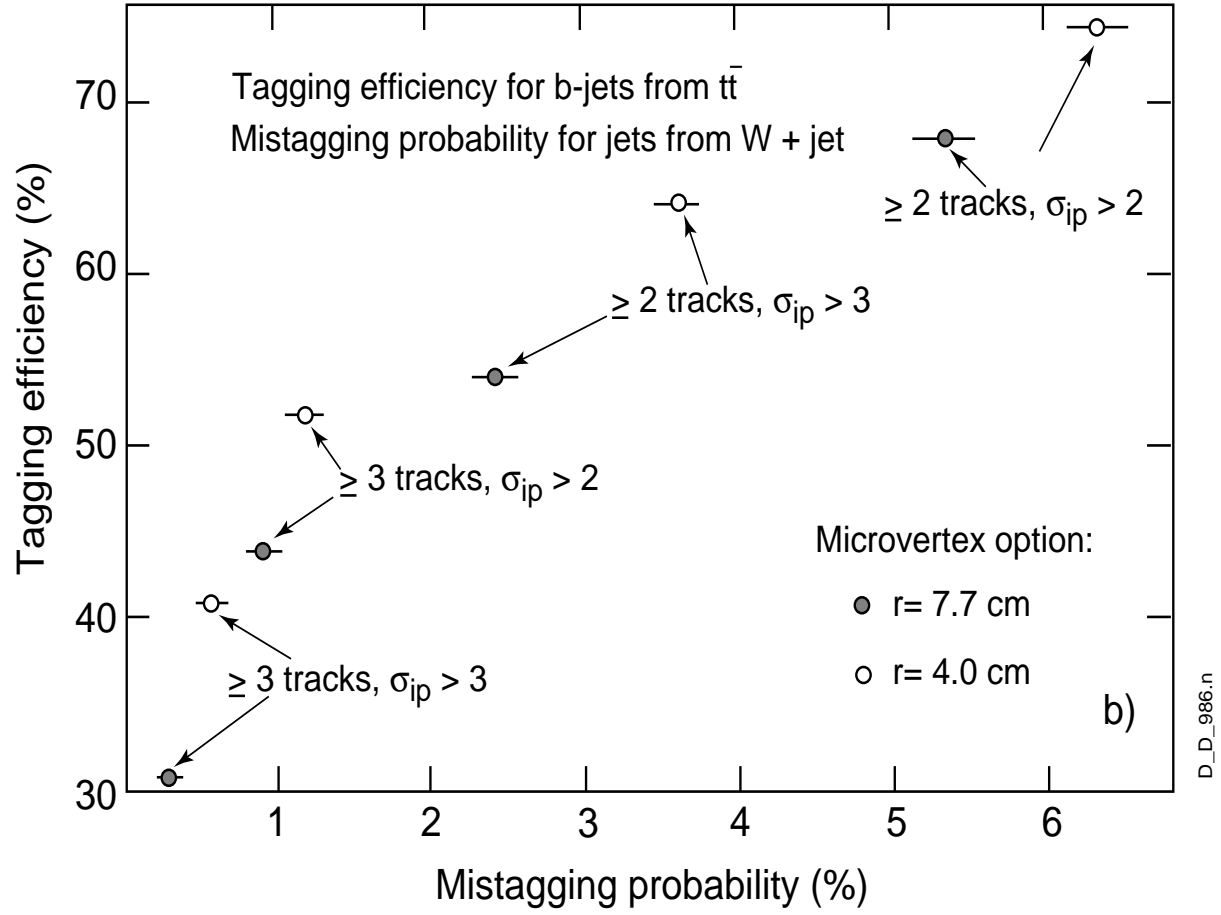


Figure 4.14: Tagging efficiency for b -jets and mistagging probability as a function of the inner barrel pixel layer radius.

CMSJET 3.5 calorimetry model

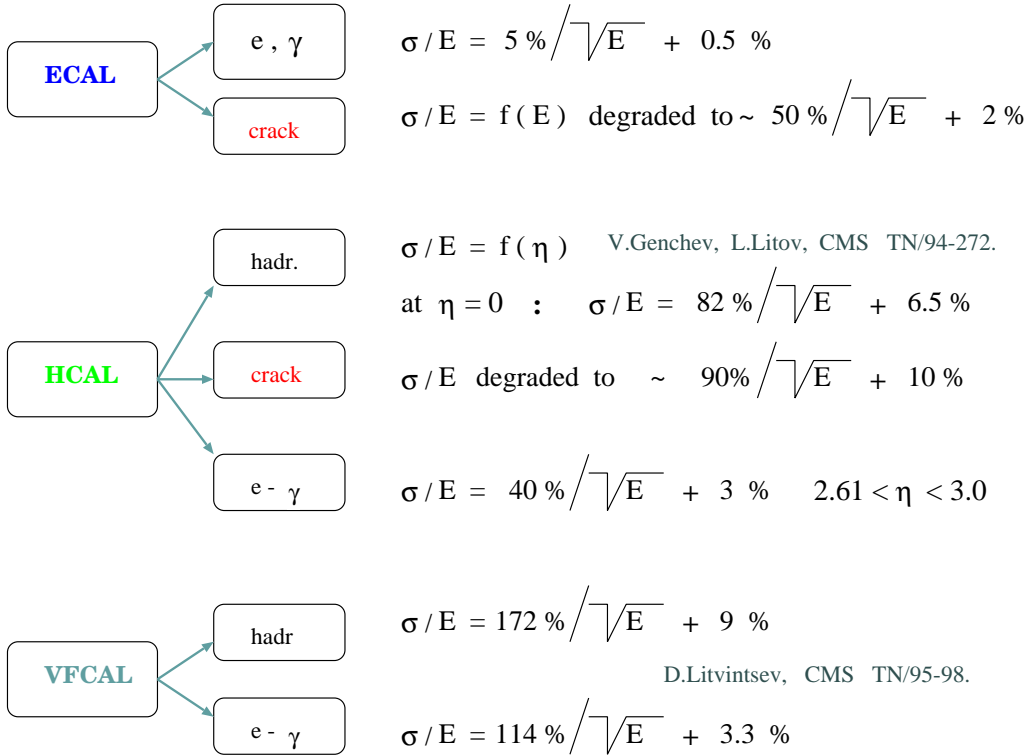
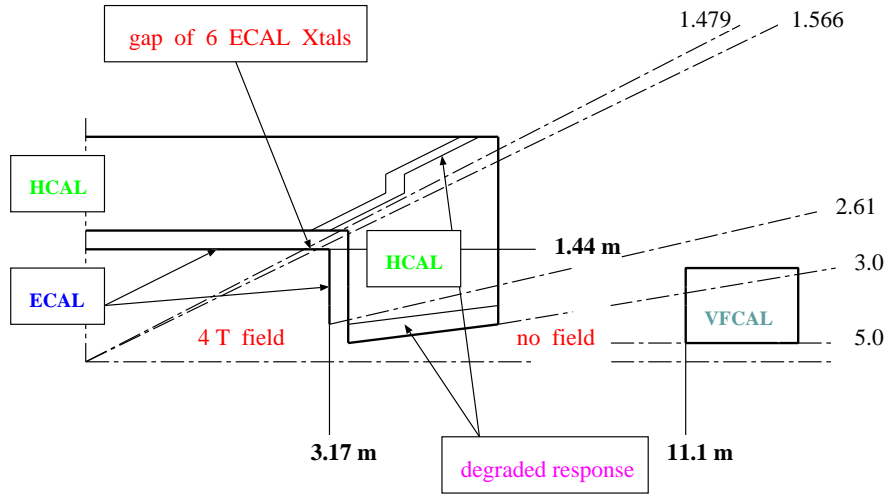


Figure 4.15: The CMS calorimetry model in CMSJET 3.5

5 *Leptons + jets + E_T^{miss} channel – search for gluinos and squarks*

To investigate the maximum reach in parameter space for SUSY via the production of strongly interacting sparticles we study *multilepton + multijet + E_T^{miss}* final states, resulting from the cascade decays of these sparticles [4, 5]. As mentioned previously, a complete mass reconstruction of gluinos and squarks is impossible due to the presence of escaping particles, two LSP's plus possibly neutrinos. So SUSY signal observability is based on an excess of events of a given topology over known (expected) backgrounds. Among the leptonic final states studied, including always at least 2 *jets + E_T^{miss}* in the final state, are one lepton (1*l*), two leptons of the same sign (2*l* SS), two leptons of opposite sign (2*l* OS), and 3,4,5 leptons regardless the sign (3*l*, 4*l*, 5*l*). As discussed in the following, these topologies have been investigated both with and without explicit requirements on muon isolation. The *jets + E_T^{miss}* topology, with no isolated leptons, is not discussed, since it is the most sensitive one to detailed detector simulation, and preliminary studies show that the mass reach is inferior to one of the channels discussed here [2].

In order to establish the limits of the SUSY reach in the $(m_0, m_{1/2})$ parameter space for various integrated luminosities, the signal was generated at more than 100 points. At each point the signal is generated as a mixture of all possible combinations of the strongly interacting sparticle production processes ($\tilde{g}\tilde{g}, \tilde{g}\tilde{q}, \tilde{q}\tilde{q}$) with masses and decay branching ratios corresponding to this point. The set of $m_0, m_{1/2}$ points where the signal samples were generated for $\tan\beta = 2$, $A_0 = 0$, $\mu < 0$ is shown in Fig. 5.1. Figures 5.2a-d give, at four representative points in the parameter space, the main sparticle masses and decay chains with corresponding branching ratios.

The backgrounds considered in this study are: $t\bar{t}$, $W + \text{jets}$, $Z + \text{jets}$, WW , ZZ , ZW , $Zb\bar{b}$ and QCD ($2 \rightarrow 2$ processes including $b\bar{b}$). There could be some double counting between $Z + \text{jets}$ and $Zb\bar{b}$ processes, but in practice this means more conservative background estimates.

No pseudorapidity cuts are applied during background generation to avoid distortion of the event kinematics. All processes were generated in the following \hat{p}_T intervals: 40 - 100, 100 - 200, 200 - 400, 400 - 800, ≥ 800 GeV. This allows the accumulation of significant statistics in the high- p_T range in a more economical way than without subdivision of the generation \hat{p}_T range [4].

The kinematics of signal events is usually harder than for the SM backgrounds, in particular for the interesting regions corresponding to the maximum reach in terms of squark/gluino masses. The cross-sections of the background processes can however be higher by orders of magnitude, and the high- p_T tails of different backgrounds can have a kinematics similar to that of the signal. Figures 5.3-5.5 illustrate kinematical distributions for the signal at three different points in parameter space and compare it to background. More specifically in Fig. 5.3 one can see the comparison between kinematical distributions for the signal point ($m_0 = 200$ GeV, $m_{1/2} = 760$ GeV) and the distributions for the sum of backgrounds in 2*l* SS, 2*l* OS and 3*l* final states. Both signal and background histograms contain only events satisfying first level selection criteria described below. Only the hardest jet and lepton in the event are shown in distributions. The last histogram in each Figure shows the distribution of E_T^{sum} , the scalar sum of all relevant transverse energies for leptons, jets and E_T^{miss} . It reflects the overall transverse energy flow in the

event, the event “hardness”. This variable is also rather insensitive to the transverse energy flow induced by event pile-up since it accounts only for those calorimeter cells which are attached to a jet, and is thus a useful quantity to cut on in the high luminosity regime.

The topology of signal and background events is already rather similar after the first level selection cuts, in terms of angular distributions and circularity, as can be seen in Fig. 5.3a, thus it is not very useful to apply explicit cuts on these variables. The difference between signal and background in the lepton p_T distributions is also not as pronounced as might have been expected, as signal leptons are produced in cascade decays, thus losing “memory” of the hardness of the original process. For extremely high masses of squarks or gluinos in the ~ 2 TeV mass range, the difference in the angular and p_T^l distributions between signal and the total SM background is still significant and helps in obtaining an effective data selection. Ultimately, all the cuts have to be justified from the point of view of the best observability of the signal over expected background.

Since the kinematics of the signal vary significantly with the variation of m_0 and $m_{1/2}$ parameters, Figs. 5.3-5.5, the set of different cuts is applied and optimised independently in each point investigated. These cuts are listed in Table 5.1. The optimisation procedure takes into account the number of jets per event, and parameters of lepton isolation, as discussed in details in the next subsection. The E_T^{miss} cut can be incremented beyond the values listed in Table 5.1, keeping all other cuts untouched, to take advantage of the large values this variable can take when the signal is close to the boundaries of explorable parameter space where masses of squarks and gluino are in the 1-2 TeV range.

We find that requiring more than 2 jets (up to ≥ 4 -5 for 1, 10 fb^{-1} , up to ≥ 6 for 100 fb^{-1}) in the event is useful in many cases, especially in domains 3 and 4 as defined in Fig. 2.16. The exception is domain 1, where requiring ≥ 2 jets (as well as requiring muon isolation for all cases except for 4 and 5 lepton final states) is sufficient to get the best signal observability.

Table 5.1: The various cuts applied to optimise the reach.

CUT	p_T^e (GeV)	p_T^μ (GeV)	$p_T^{jet1,2,3}$ (GeV)	E_T^{miss} (GeV)	E_T^{sum} (GeV)
C1	20	10	40	100	-
C2	20	10	150,80,40	150	500
C3	40,20,20		150,80,40	150	500
C4	40,20,20		200,120,40	200	700
C5	50,30,20		250,150,40	200	1000
C6	80,50,20		300,200,40	250	1200
C7	100,70,20		300,200,40	250	1200

It is also found that some moderate cuts:

- $Circularity > 0.1$
- $\delta\varphi$ (hardest lepton, E_T^{miss}) > 10 -15 deg

are useful to improve signal observability everywhere in $1l$ final states, and in $2l$ OS final states, primarily in the region $m_{1/2} > 600$ GeV for an integrated luminosity $\geq 10 \text{ fb}^{-1}$.

From the chosen multiparametric space of cuts and constraints, we look for those which provide the highest value of $m_{1/2}$ with a 5σ significance excess for signal at each probed m_0 point and for each lepton multiplicity final state investigated [4].

An important issue in this study is the lepton isolation criterion. The term “isolated lepton” means satisfying simultaneously the following two requirements:

- no charged particle with $p_T > 2$ GeV in a cone with defined radius in $\eta - \varphi$ space around the lepton, and
- ΣE_T^{calo} in a cone ring $0.1 < R < 0.3$ around the lepton impact point has to be less than a specified percentage of the lepton transverse energy.

Figure 5.6 shows the acceptance for the signal in two points of parameter space, “**SIGNAL 1**” at $m_0 = 200$ GeV, $m_{1/2} = 700$ GeV chosen in the first characteristic domain in Fig. 2.16; “**SIGNAL 2**” at $m_0 = 1000$ GeV, $m_{1/2} = 600$ GeV in the third domain, and the acceptance for background. The comparison is done for the three final state topologies, namely, two lepton of same sign ($2l$ SS), two leptons of opposite sign ($2l$ OS) and three leptons ($3l$). This is done as a function of the tracker isolation cone size $R = \sqrt{\delta\eta^2 + \delta\varphi^2}$ and for the set of cuts denoted as C2 in Table 5.1. Both electrons and muons are required to be isolated. Each curve corresponds to a specified calorimetric cut: no cut (circles), E_T^{calo} in the cone ring $0.1 < R < 0.3$ not exceeding 10% (squares) and 5% (triangles) of the lepton E_T .

It is rather difficult to deduce from these curves what is in general the most advantageous isolation criterion. Tight isolation is not very useful in case of “**SIGNAL 2**” in $2l$ OS and $3l$ final states, where it leads to a significant loss of signal. At the same time, the background is not suppressed sufficiently, especially in case of $2l$ OS, where it is mainly due to $t\bar{t}$ production giving well isolated leptons through the decay chain $t \rightarrow Wb \rightarrow \nu b$. So, the isolation criterion could also in principle be optimised at every $m_0, m_{1/2}$ point and for each leptonic topology so as to obtain the best signal observability. In practice, since the identification of non-isolated electrons is experimentally difficult, a minimal isolation is always required, e.g. charged particle isolation in a cone of $R = 0.1$ and a requirement of E_T^{calo} in $R = 0.3$ not exceeding 10% of the electron E_T . We find that a still tighter isolation does not further improve the signal observability at all the $m_0, m_{1/2}$ points investigated. As for the muons, we find that a gain of ~ 50 -150 GeV in reach in $m_{1/2}$ is possible if no isolation is applied at all on them. This is valid for all lepton topologies and almost everywhere in the $m_0, m_{1/2}$ plane, except in the first domain in Fig. 2.16. This is due to the copious production of b -quarks in the signal, especially in domains 2-4, giving rise to a significant yield of non-isolated leptons from B -decays. So except when explicitly stated, we do not apply in the following any isolation requirement on muons.

The case of high instantaneous luminosity running requires a separate discussion of lepton isolation due to event pile-up deteriorating lepton (electron) isolation. However, as we use only a loose isolation criterion to begin with, the criterion can easily be changed with only minor loss of efficiency. Furthermore, with a good tracker it should be possible to separate most of the tracks originating from vertices other than the leptonic one. Even in case of confusion with tracks from event pile-up vertices, the probability of the signal lepton to be “moderately” isolated (as we have defined above) in spite of pile-up is still 97 - 98% when averaged over the entire ECAL, as we calculated using PYTHIA pile-up (MSEL = 2) with an average number of pile-up events per bunch-crossing of $\bar{n} = 25$. So

event pile-up at high instantaneous luminosity does not affect significantly the results of our study.

Figures 5.7-5.9 show the final results of our study of squark and gluino observability and mass search in m_0 , $m_{1/2}$ parameter space in the various *multilepton* + *multijet* + E_T^{miss} final states for our standard set of parameters $\tan\beta = 2$, $A_0 = 0$, $\mu < 0$. The results are shown for increasing values of integrated luminosity from 1 to 100 fb^{-1} . All the 5σ boundaries shown are obtained relaxing muon isolation whenever possible, but keeping always the minimal electron isolation criteria needed for unambiguous instrumental electron identification. The maximal squark and gluino mass reach is obtained in 1 lepton final states. With 10^5 pb^{-1} the maximal gluino mass reach varies from ≈ 2.5 to 2.0 TeV, depending on m_0 , whilst the squark mass reach varies between 2.1 - 2.5 TeV. What is important is that already with 10^3 pb^{-1} the $\lesssim 1$ TeV domain can be thoroughly explored, and according to the “no-fine tuning” arguments this mass domain is the most plausible one.

In Fig. 5.8 one can see that the cosmologically interesting region [37] is entirely contained within the domain explorable already with 10 fb^{-1} in all topologies considered. The Figure shows the relic neutralino dark matter density contours corresponding to Ωh^2 values of 0.25, 0.5 and 1, where Ω is the neutralino density relative to the critical density of the Universe and h is the Hubble constant scaling factor ($h \sim 0.7$). The preferred mixed dark matter scenario corresponds to values of Ωh^2 between 0.15 and 0.4.

Figure 5.10 illustrates the gain in mass reach which can be obtained when non-isolated muons are taken into account in the analysis. Figure 5.11 shows the expected signal-to-background ratio at the 5σ boundaries in each topology. It is always bigger than 1, thus we may expect that the maximum reach will not be very sensitive to a possible underestimation of the background cross-sections. To estimate the influence of systematic uncertainties on the background cross-sections on the \tilde{g} , \tilde{q} observability contours, we increased all the background cross-sections by a factor of 2, and the W/Z + jets background by a factor of 5. Figure 5.12 shows how the 5σ significance contours are modified under these conditions for an integrated luminosity of 10 fb^{-1} . The loss of reach is small in all cases.

We also checked the sensitivity of our results to changes in some of our basic parameters. The change of the sign of μ , keeping $\tan\beta = 2$, $A_0 = 0$, affects primarily charginos and neutralinos. It changes their masses, decay modes and branching ratios, and these alter the final state kinematic and topology. In the squark sector, a positive sign of μ decreases the \tilde{t}_1 mass by $\approx 30 - 50 \text{ GeV}$ compared to the $\mu < 0$ case. Consequently, final state leptons coming from stops and top quarks will be slightly “softer”, thus requiring lower threshold cuts and causing modified background levels compared to the $\mu < 0$ case. Figure 5.13 gives the maximum expected reach of the CMS detector for squark and gluino searches in different multilepton final states for 10^4 pb^{-1} with $\mu > 0$ [5]. The reach is again greatest in the single lepton channel, and extends up to gluino and squark masses of $\sim 2 \text{ TeV}$. Relaxation of the muon isolation requirements increases the reach by $\approx 50 \text{ GeV}$ in the single lepton case, and by $\approx 200 \text{ GeV}$ in the trilepton case. The $4l$ channel with 10^4 pb^{-1} has an interesting explorable domain only if muons are not isolated [38]. Figure 5.14 gives the same results for $L_{int} = 10^5 \text{ pb}^{-1}$ [5]. With this luminosity and with full muon isolation (not shown), the $4l$ maximal reach region in fact becomes “a band of observability” approximately between $m_{1/2} \approx 200 \text{ GeV}$ and $m_{1/2} \approx 350 \text{ GeV}$ [38]. The lower boundary is mainly caused by a decrease of the branching ratio for $\tilde{g} \rightarrow \tilde{\chi}_1^0 t\bar{t}$. For

$m_0 < 200$ GeV the region of observability extends up to $m_{1/2} \approx 650$ GeV, as here there is a high yield of leptons from chargino and neutralino decays.

The main conclusions of this particular study are the following: within the mSUGRA model, the SUSY signal due to production of \tilde{q} and \tilde{g} would be detectable as an excess of events over SM expectations up to masses $m_{\tilde{q}} \sim m_{\tilde{g}} \sim 1$ TeV with only 10^3 pb^{-1} . The ultimate reach, for 10^5 pb^{-1} , would extend up to $m_{\tilde{q}} \sim 2500$ GeV for small m_0 ($\lesssim 400$ GeV) and up to ~ 2000 GeV for any reasonable value of m_0 ($\lesssim 2000$ GeV); squark masses can be probed for values in excess of 2000 GeV. This means that the entire plausible domain of EW-SUSY parameter space (for $\tan\beta = 2$) can be probed with these *lepton(s) + jets* + E_T^{miss} final states. Furthermore, the S/B ratios are > 1 everywhere in parameter space (with the appropriate cuts) thus allowing a study of the kinematics of \tilde{q} , \tilde{g} production and obtaining information on their masses [39]. The cosmologically interesting region $\Omega h^2 \leq 1$ can be entirely probed with an integrated luminosity not in excess of $\sim 10^3 \text{ pb}^{-1}$, thus with a very large safety margin.

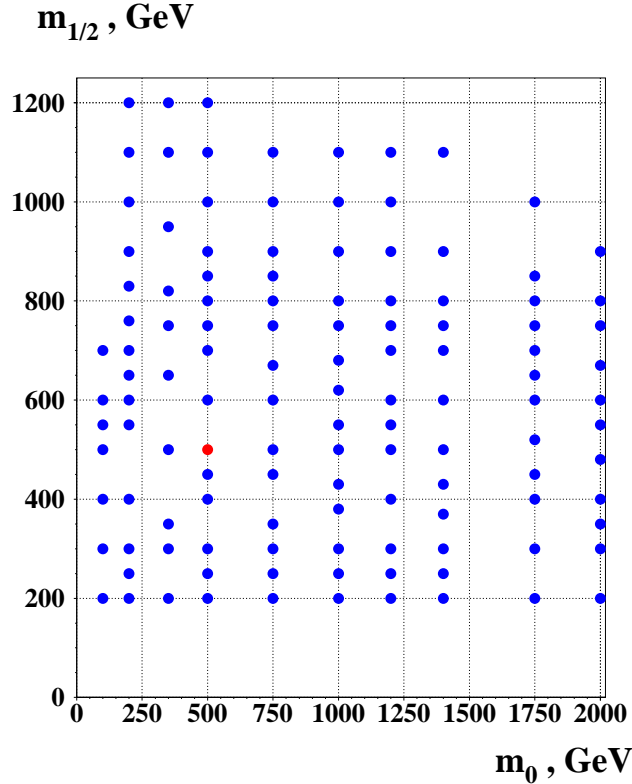


Figure 5.1: The set of generated data points in the $(m_0, m_{1/2})$ mSUGRA plane for $\tan\beta = 2$, $A_0 = 0$, $\mu < 0$.

● $m_0 = 500 \text{ GeV}, \quad m_{1/2} = 500 \text{ GeV}$

$$\begin{array}{ll}
m_{\tilde{g}} = 1765 \text{ GeV} & m_{\tilde{q}} < m_{\tilde{g}} \quad m_{\tilde{t}_1} = 1208 \text{ GeV} \\
m_{\tilde{\chi}_1^0} = 333 \text{ GeV} & \\
m_{\tilde{\chi}_1^\pm} = 647 \text{ GeV} & m_{\tilde{e}_L} = 566 \text{ GeV} \\
\tilde{g} \longrightarrow \tilde{q}\bar{q} \quad (\tilde{t}_1\bar{t} \sim 24\%, \tilde{t}_2\bar{t} \sim 10\%, \tilde{b}_L\bar{b} \sim 11\%)
\end{array}$$

$$\begin{array}{l}
 \tilde{q}_L \rightarrow \begin{cases} \tilde{\chi}_1^+ q \sim 2/3 \\ \quad \downarrow \\ \quad \tilde{l}^+ \tilde{\nu} \\ \quad \tilde{\nu} l^+ \\ \tilde{\chi}_2^0 q \sim 1/3 \\ \quad \downarrow \\ \quad \tilde{l}^+ \tilde{l}^- \\ \tilde{\chi}_1^0 l^+ l^- \sim 32\% \end{cases} \\
 \tilde{t}_1 \rightarrow \begin{cases} \tilde{\chi}_1^0 t \sim 92\% \\ \quad \downarrow \\ \quad W^+ b \\ \quad \quad \downarrow \\ \quad \quad l^+ \nu \sim 20\% \end{cases} \\
 \tilde{b}_L \rightarrow \begin{cases} \tilde{\chi}_1^- t \sim 59\% \\ \tilde{\chi}_2^0 b \sim 31\% \\ \tilde{t}_1 W^- \sim 8\% \end{cases} \\
 \tilde{q}_R \rightarrow \tilde{\chi}_1^0 q \sim 100\%
 \end{array}$$

$$\begin{array}{lll} m_{\tilde{g}} = 1221 \text{ GeV} & m_{\tilde{q}} \lesssim m_{\tilde{g}} & m_{\tilde{t}_1} = 856 \text{ GeV} \\ m_{\tilde{\chi}_1^0} = 217 \text{ GeV} & & \\ m_{\tilde{\chi}_1^\pm} = 427 \text{ GeV} & m_{\tilde{e}} = 611 \text{ GeV} & m_h = 101 \text{ GeV} \end{array}$$

$$\begin{array}{l}
 \tilde{g} \longrightarrow q\bar{q} \quad (\tilde{l}_L \sim 50\%, \quad \tilde{b}_L \sim 18\%) \\
 \\
 \tilde{q}_L \left\{ \begin{array}{ll} \xrightarrow{\tilde{\chi}_1^\pm} q & \sim 2/3 \\ \xrightarrow{\tilde{\chi}_2^0} W^\pm & \sim 100\% \\ \xrightarrow{\tilde{\chi}_2^\pm} q & \sim 1/3 \end{array} \right. \\
 \\
 \begin{array}{rcl} & \downarrow & \\ & \tilde{\chi}_1^0 & h \sim 93\% \\ & & \downarrow b\bar{b} \sim 87\% \\ & \tilde{\chi}_1^\pm Z & \sim 3\% \end{array} \\
 \\
 \tilde{l}_L \longrightarrow \tilde{\chi}_1^0 l \sim 91\% \\
 \quad \quad \quad \downarrow W^\pm b \\
 \quad \quad \quad \quad \quad l^\pm \nu \sim 20\% \\
 \\
 \tilde{q}_R \longrightarrow \tilde{\chi}_1^0 q \sim 100\%
 \end{array}$$

- $m_0 = 1000 \text{ GeV}$, $m_{1/2} = 620 \text{ GeV}$

$$\begin{array}{lll} m_{\tilde{g}} = 1519 \text{ GeV} & m_{\tilde{q}} \geq m_{\tilde{g}} & m_{\tilde{t}_1} = 1087 \text{ GeV} \\ m_{\tilde{\chi}_1^0} = 271 \text{ GeV} & & \\ m_{\tilde{\chi}_1^\pm} = 530 \text{ GeV} & m_{\tilde{e}_L} = 1088 \text{ GeV} & \end{array}$$

$$\begin{array}{l}
 \bar{g} \longrightarrow \bar{t}_1 \bar{t} \sim 89\%, \longrightarrow \bar{X}_1^+ t \bar{t} \sim 98\%, \\
 \bar{b}_1 b \sim 9\% \\
 \quad \downarrow \\
 \quad \bar{X}_1^- t \sim 2/3 \\
 \quad \bar{X}_2^0 b \sim 1/3 \\
 \\
 \bar{q}_L \left\{ \begin{array}{l} \longrightarrow \bar{X}_1^+ q \sim 2/3 \\ \quad \downarrow \longrightarrow \bar{X}_1^+ W^+ \sim 100\% \\ \longrightarrow \bar{X}_2^0 q \sim 1/3 \\ \quad \downarrow \longrightarrow \bar{X}_1^+ h \sim 98\% \\ \quad \quad \downarrow \longrightarrow W^+ J^+ \nu \sim 8\% \\ \quad \quad \quad \longrightarrow W^+ q q \sim 24\% \end{array} \right. \\
 \\
 \bar{q}_R \left\{ \begin{array}{l} \longrightarrow \bar{X}_1^0 q \\ \longrightarrow \bar{g} \bar{q} \end{array} \right.
 \end{array}$$

● $m_0 = 2000 \text{ GeV}, m_{1/2} = 480 \text{ GeV}$

$$\begin{array}{lll} m_{\tilde{g}} = 1261 \text{ GeV} & m_{\tilde{q}} \sim 2 m_{\tilde{g}} & m_{\tilde{t}_1} = 1106 \text{ GeV} \\ m_{\tilde{\chi}_1^0} = 211 \text{ GeV} & & \\ m_{\tilde{\chi}_1^\pm} = 415 \text{ GeV} & m_{\tilde{e}_L} = 2027 \text{ GeV} & \end{array}$$

$$\begin{array}{l}
 \tilde{g} \longrightarrow \left\{ \begin{array}{l} \tilde{\chi}_1^0 \text{ t } \bar{t} \sim 72 \% , \\ \tilde{\chi}_1^\pm \text{ q } \bar{q} \sim 20 \% , \\ \tilde{\chi}_2^0 \text{ q } \bar{q} \sim 8 \% , \end{array} \right. \\
 \quad \longmapsto \left\{ \begin{array}{l} \tilde{\chi}_1^\pm \text{ W}^\mp \sim 100 \% \\ \tilde{\chi}_1^0 \text{ h} \sim 100 \% \end{array} \right. \\
 \quad \quad \quad \longmapsto \left\{ \begin{array}{l} \text{W}^\pm \text{ l }^\mp \nu \sim 8 \% \\ \text{W}^\pm \text{ q } \bar{q} \sim 24 \% \\ \text{W}^\pm \tau^\mp \nu \sim 4 \% \end{array} \right. \\
 \\
 \tilde{q}_L \longrightarrow \left\{ \begin{array}{l} \tilde{g} \text{ q} \sim 75 \% \\ \tilde{\chi}_1^\pm \text{ q} \sim 16 \% \\ \tilde{\chi}_2^0 \text{ q} \sim 8 \% \end{array} \right| \begin{array}{l} 63 \% \\ 24 \% \\ 8 \% \end{array} \left(\tilde{\chi}_1^\pm \text{ t} \right) \longrightarrow \tilde{t}_L \\
 \\
 \tilde{t}_I \longrightarrow \tilde{\chi}_1^0 \text{ t} \sim 100 \% \\
 \\
 \tilde{q}_R \longrightarrow \tilde{g} \text{ q} \sim 94 - 98 \%
 \end{array}$$

Figure 5.2: Some typical points in parameter space.

$m_0 = 200 \text{ GeV}$, $m_{1/2} = 760 \text{ GeV}$
21 OS case, both leptons are isolated

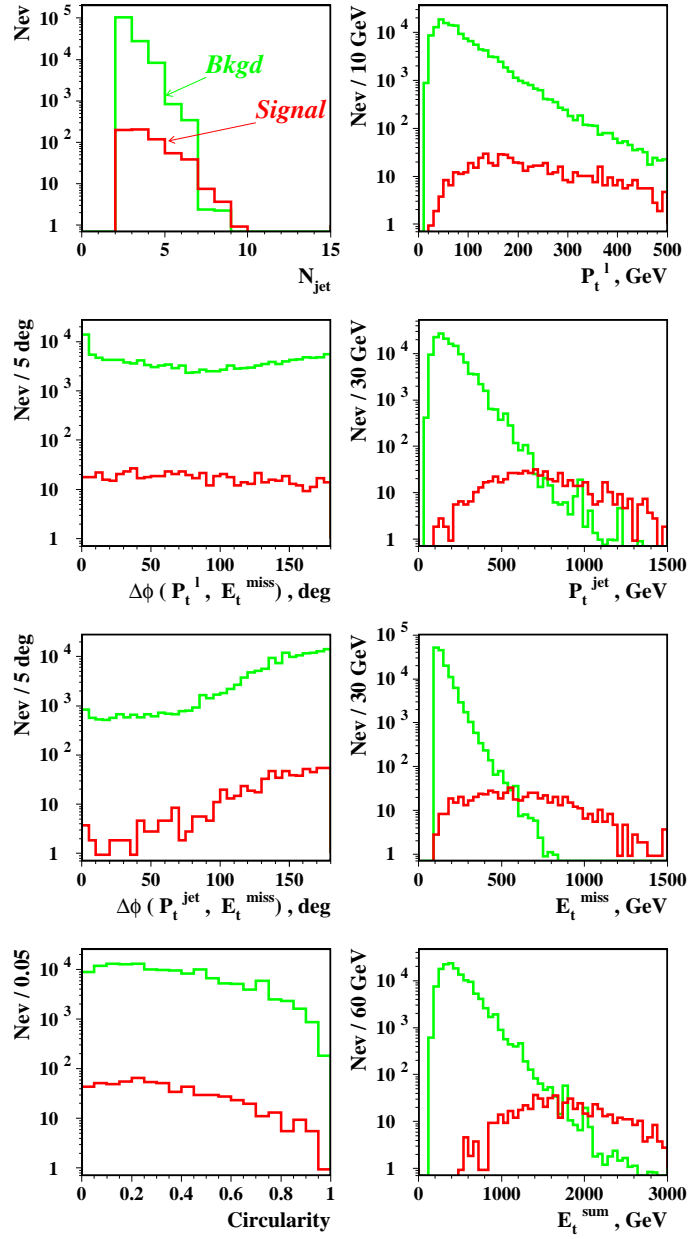


Figure 5.3a: Comparison of the signal and background kinematics at one point in mSUGRA parameter space, after requiring two leptons of opposite sign (plus jet and E_T^{miss}).

2 1 SS case, both leptons are isolated

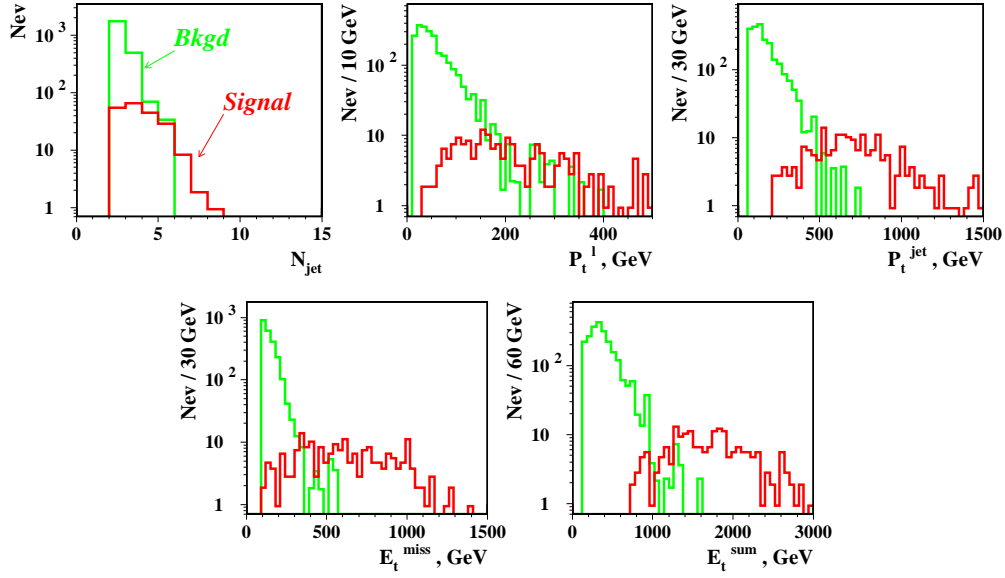


Figure 5.3b: Comparison of the signal and background kinematics in the same point as in in Fig. 5.3a, but for 2 l SS final state topology.

3 1 case, all leptons are isolated

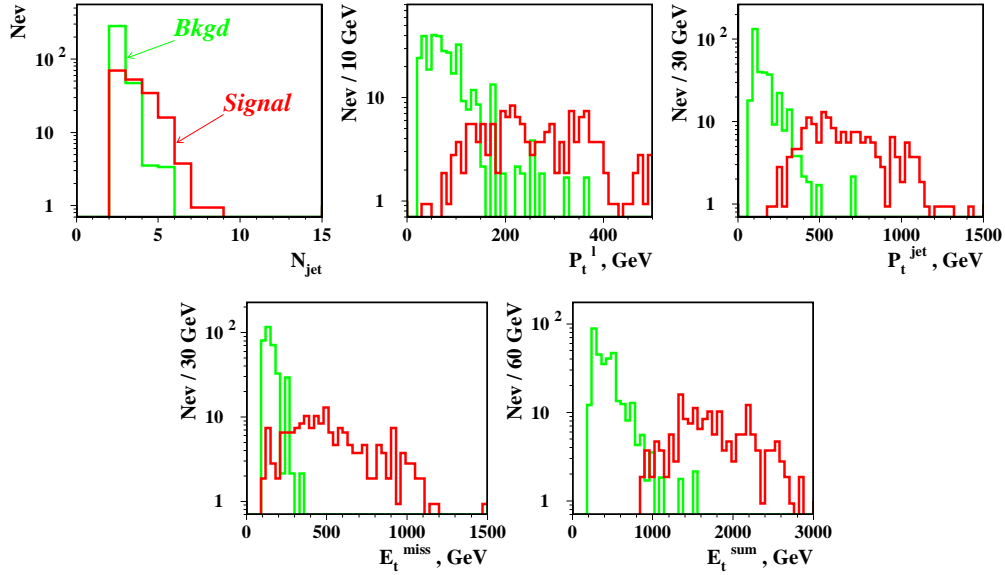


Figure 5.3c: Comparison of the signal and background kinematics in the same point as in in Fig. 5.3a, but for 3 l final state topology.

$m_0 = 500 \text{ GeV}$, $m_{1/2} = 500 \text{ GeV}$
21 SS case, both leptons are isolated

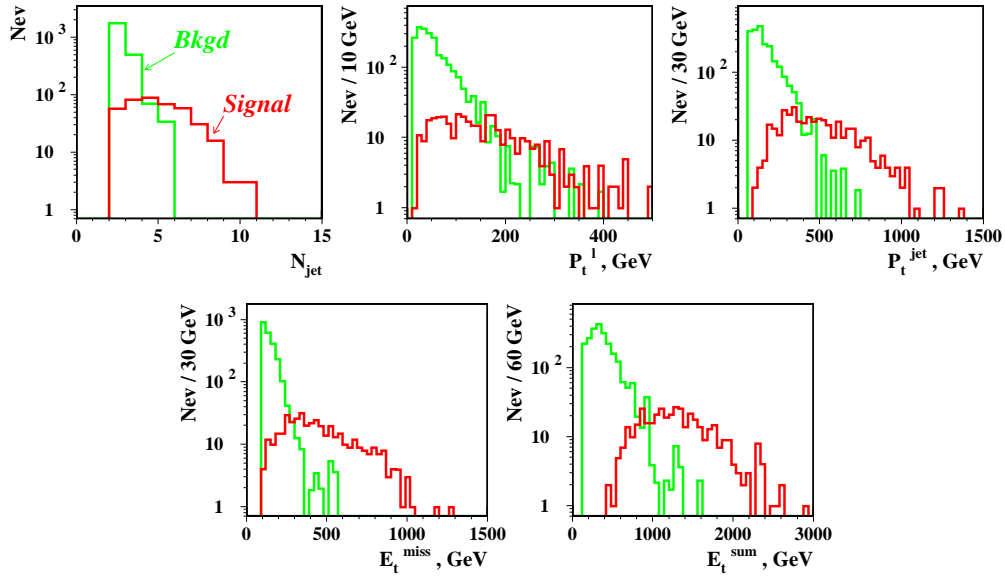


Figure 5.4: Comparison of the signal and background kinematics for a second point in parameter space.

$m_0 = 2000 \text{ GeV}$, $m_{1/2} = 400 \text{ GeV}$
21 SS case, both leptons are isolated

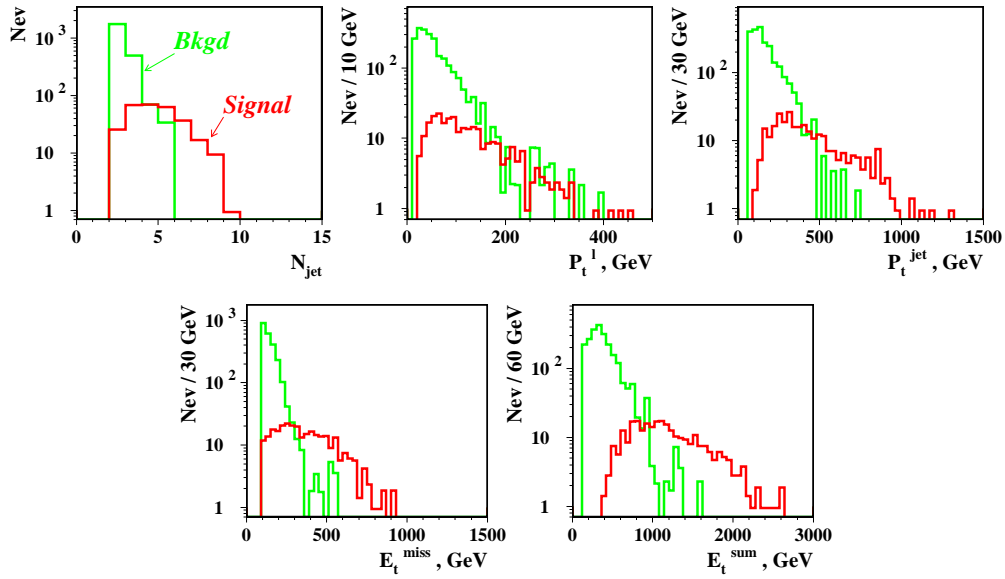


Figure 5.5: Comparison of the signal and background kinematics for a third point in parameter space.

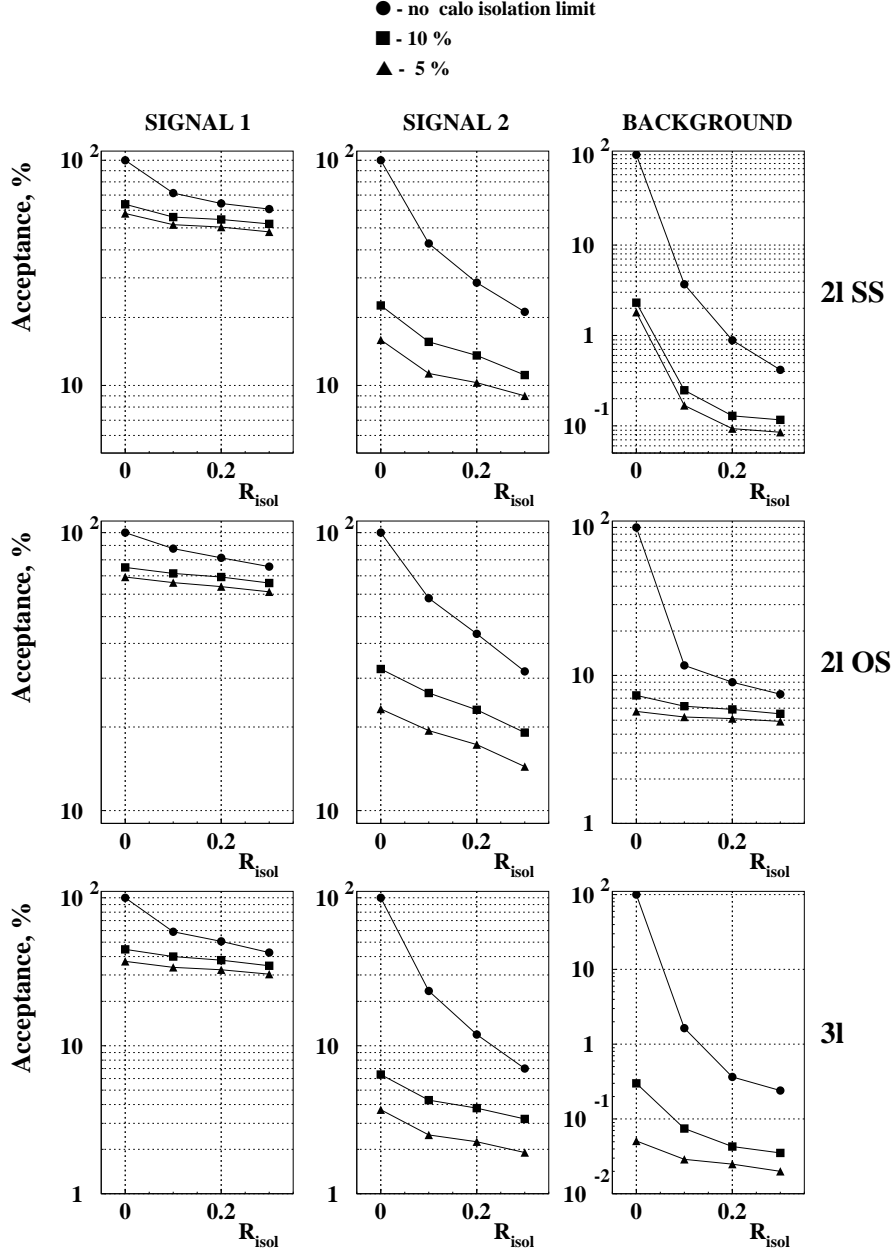


Figure 5.6: Effect of the lepton isolation criterion on signal and background, at two different points in parameter space: “**SIGNAL 1**” is $m_0 = 200$ GeV, $m_{1/2} = 700$ GeV, “**SIGNAL 2**” is $m_0 = 1000$ GeV, $m_{1/2} = 600$ GeV, as a function of R_{isol} , the tracker isolation cone size $R_{isol} = \sqrt{\delta\eta^2 + \delta\varphi^2}$. The results are shown for three choices of calorimetric isolation parameter (sum of calorimeter energy deposit in a cone ring $0.1 < R < 0.3$ around the lepton impact point) and for three event topologies.

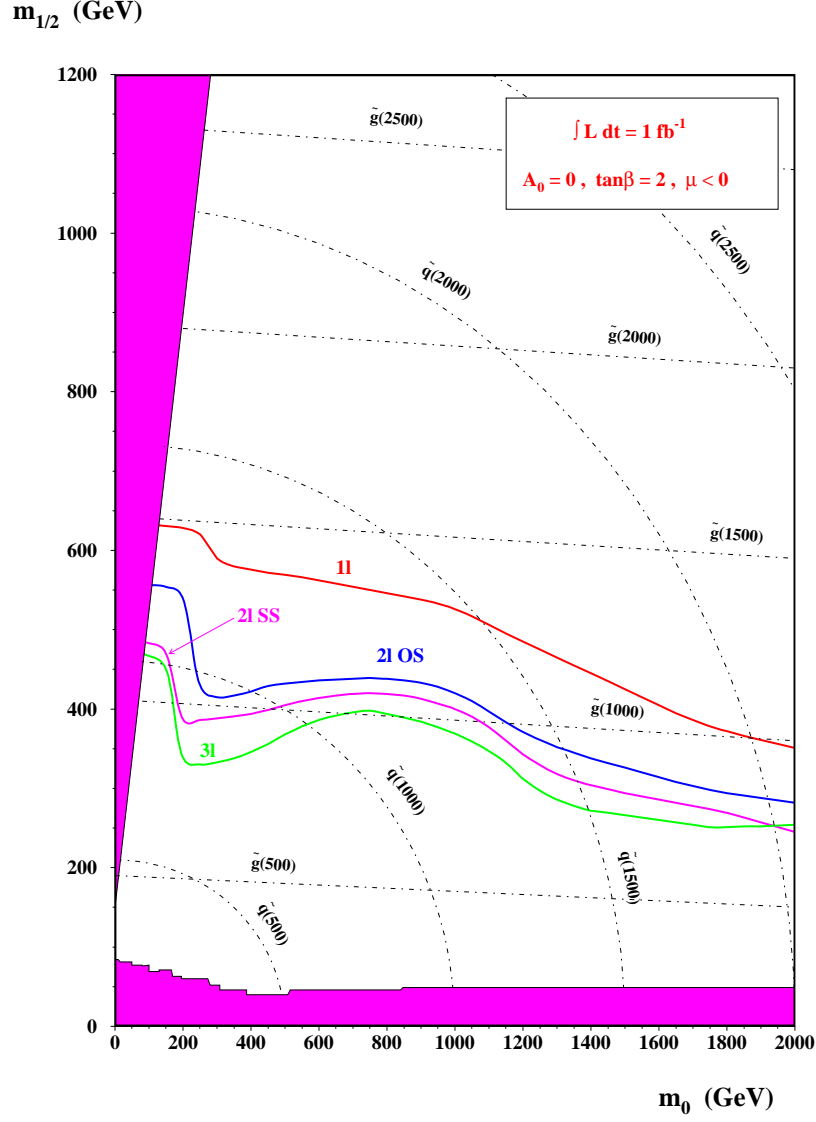


Figure 5.7: 5σ gluino/squark contours in various lepton multiplicity final states for 1 fb^{-1} and our standard set of model parameter values $\tan\beta = 2$, $A_0 = 0$, $\mu < 0$. Squark and gluino isomass curves shown by dash-dotted lines.

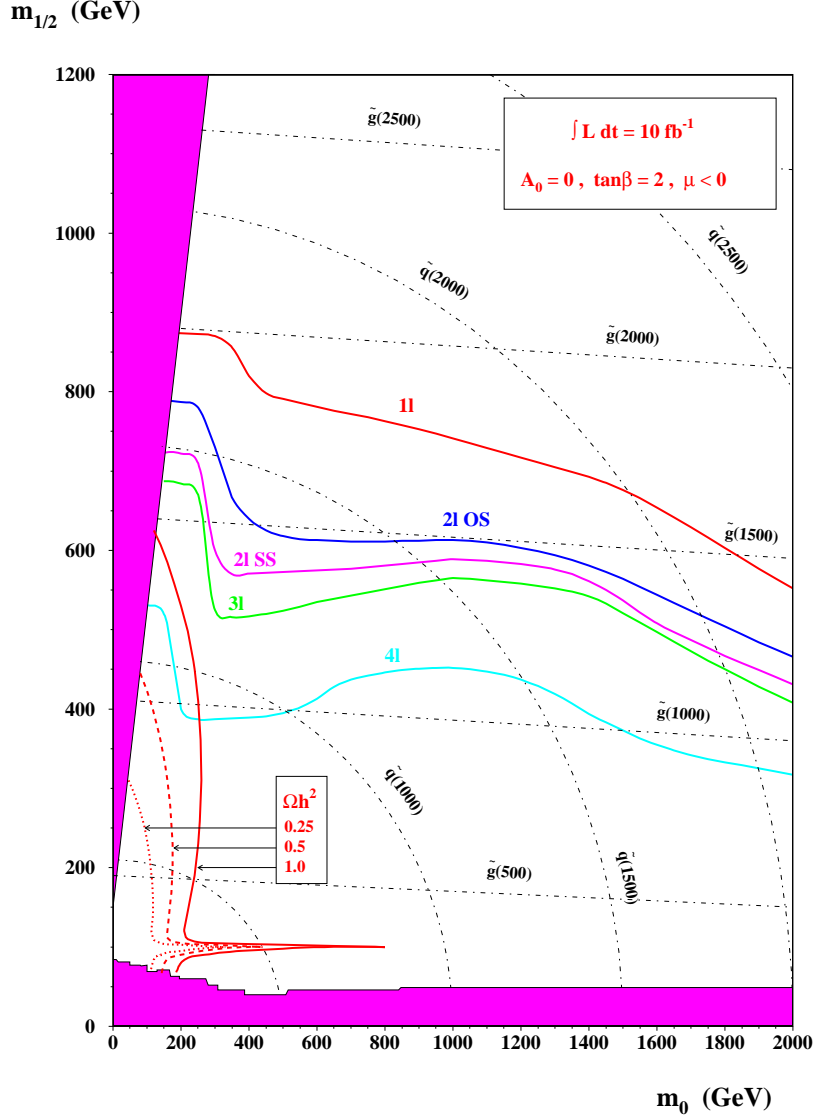


Figure 5.8: 5σ contours as in Fig. 5.7, but for 10 fb^{-1} . The relic neutralino dark matter density contours of $\Omega h^2 = 0.25, 0.5$ and 1.0 are also shown. The region of Ωh^2 between 0.15 and 0.4 is preferred by mixed dark matter models [37]; the $\Omega h^2 = 1$ contour is the upper limit.

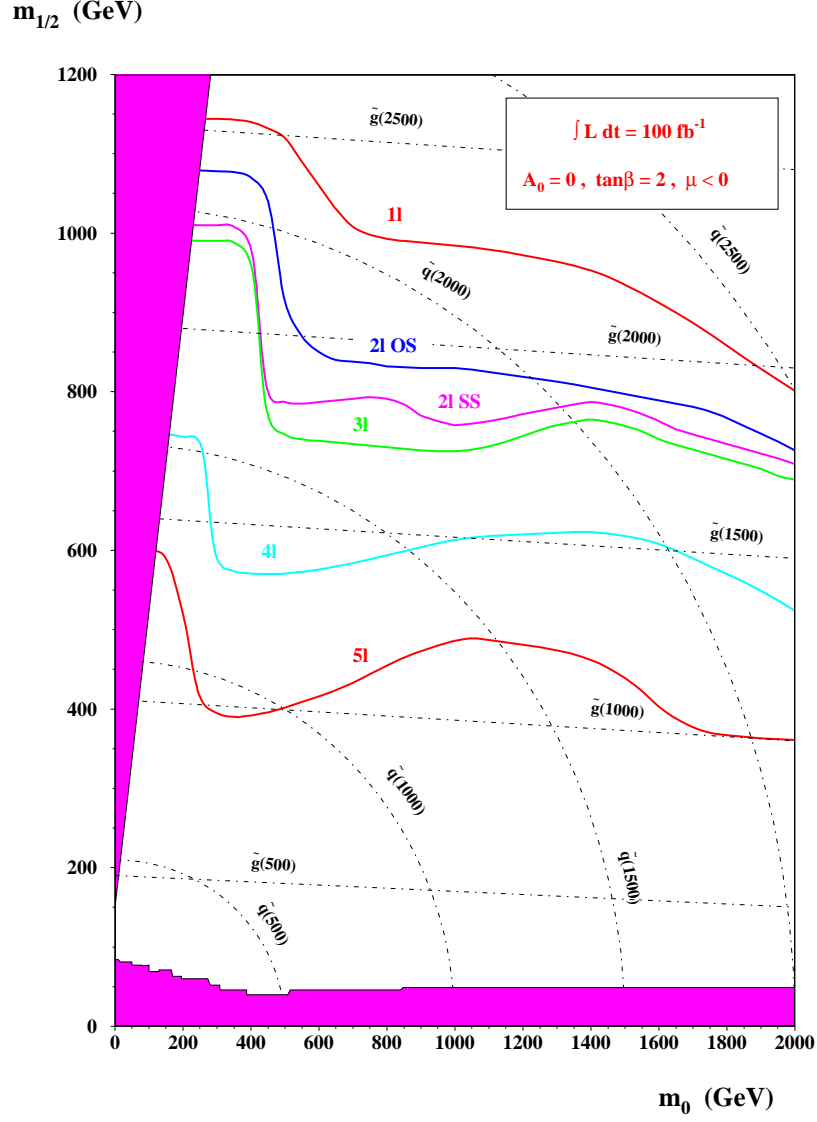


Figure 5.9: Ultimate squark and gluino mass reach, in terms of a $\geq 5\sigma$ observation contour for 100 fb^{-1} , in various lepton multiplicity final states .

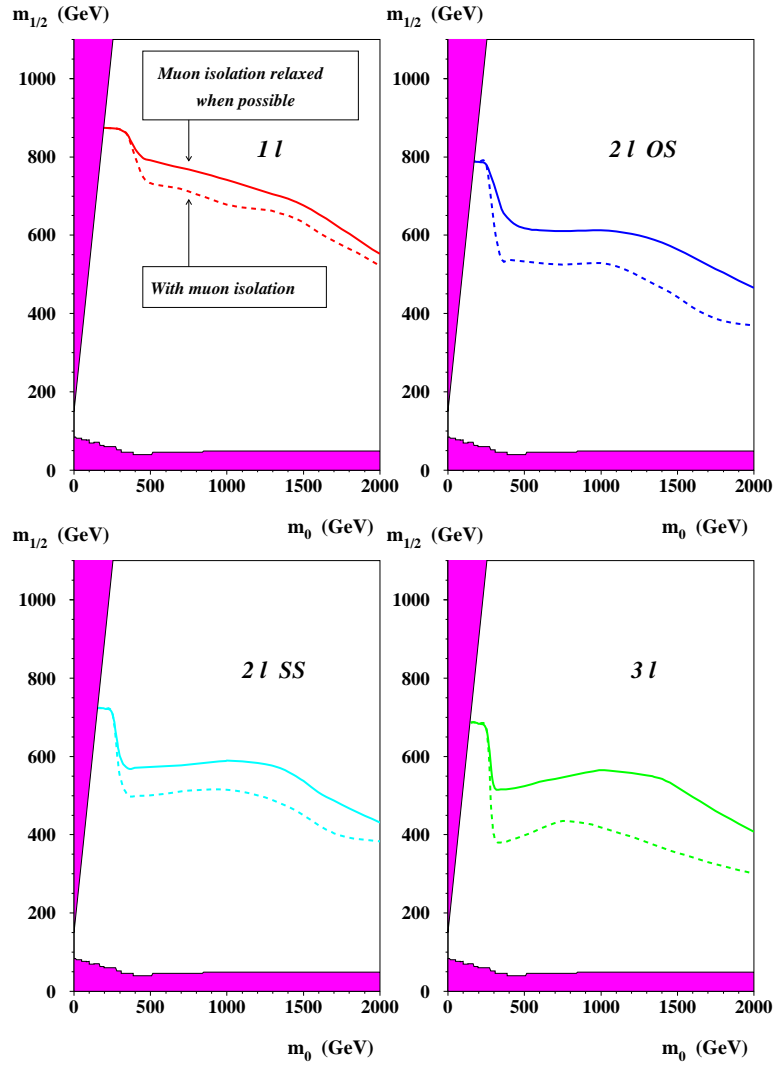


Figure 5.10: Influence of muon isolation on the 5σ contours in various topologies for 10 fb^{-1} .

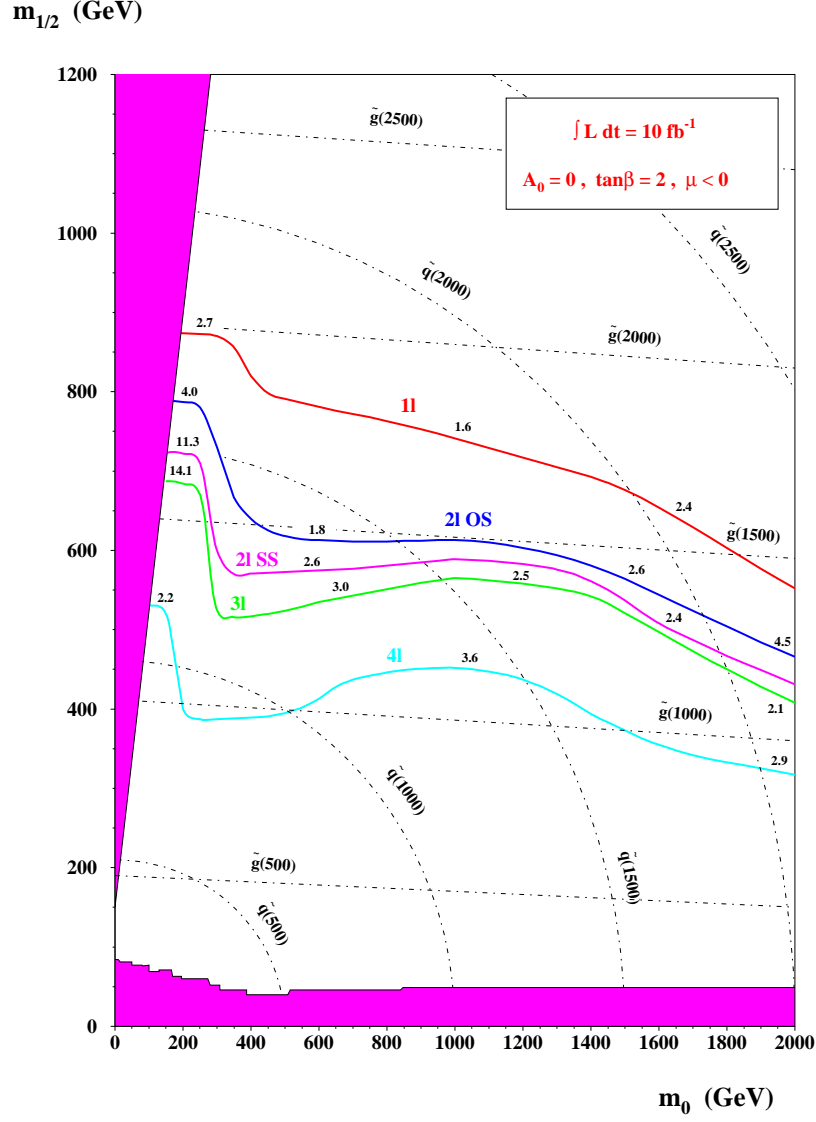


Figure 5.11: Signal to SM background ratio on the 5σ reach boundaries in various lepton multiplicity final state topologies, for 10 fb^{-1} .

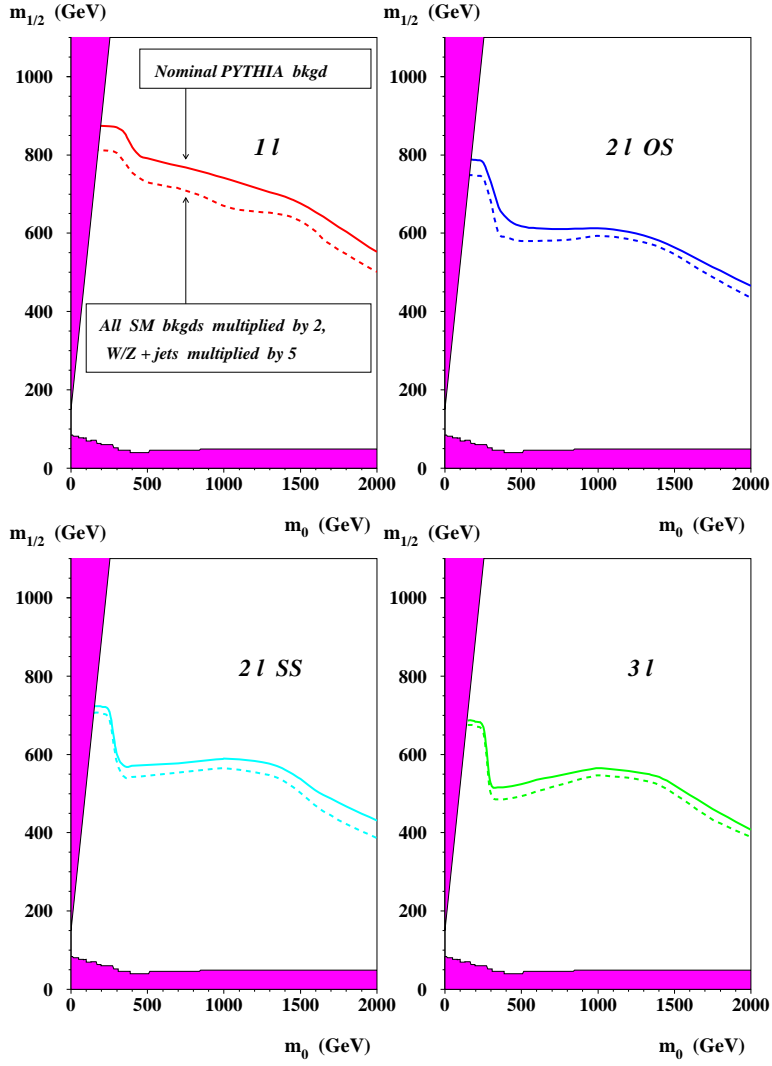


Figure 5.12: Sensitivity in the systematic uncertainties in background cross section on the 5σ contours in various lepton multiplicity final state topologies, for 10 fb^{-1} .

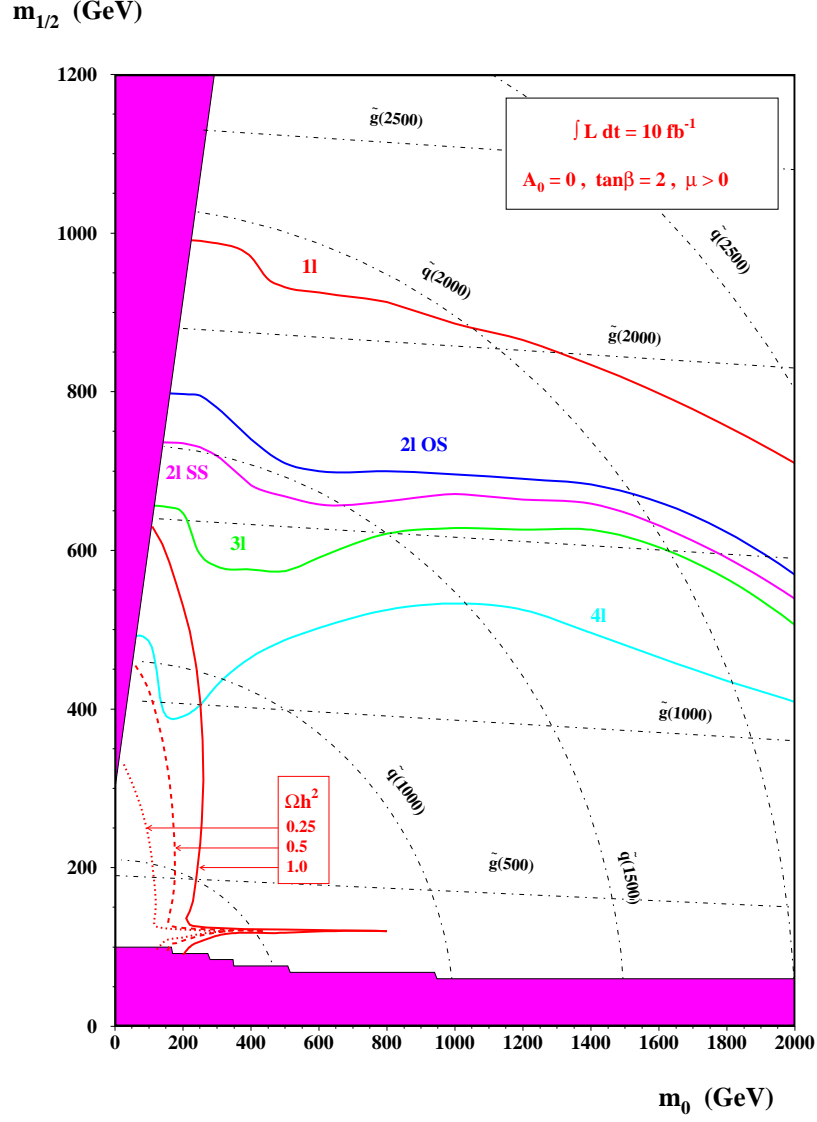


Figure 5.13: Maximal squark/gluino reach for $\mu > 0$ for 10 fb^{-1} in different final state topologies. The relic neutralino dark matter density contours of $\Omega h^2 = 0.25, 0.5$ and 1.0 are also shown for this set of model parameters.

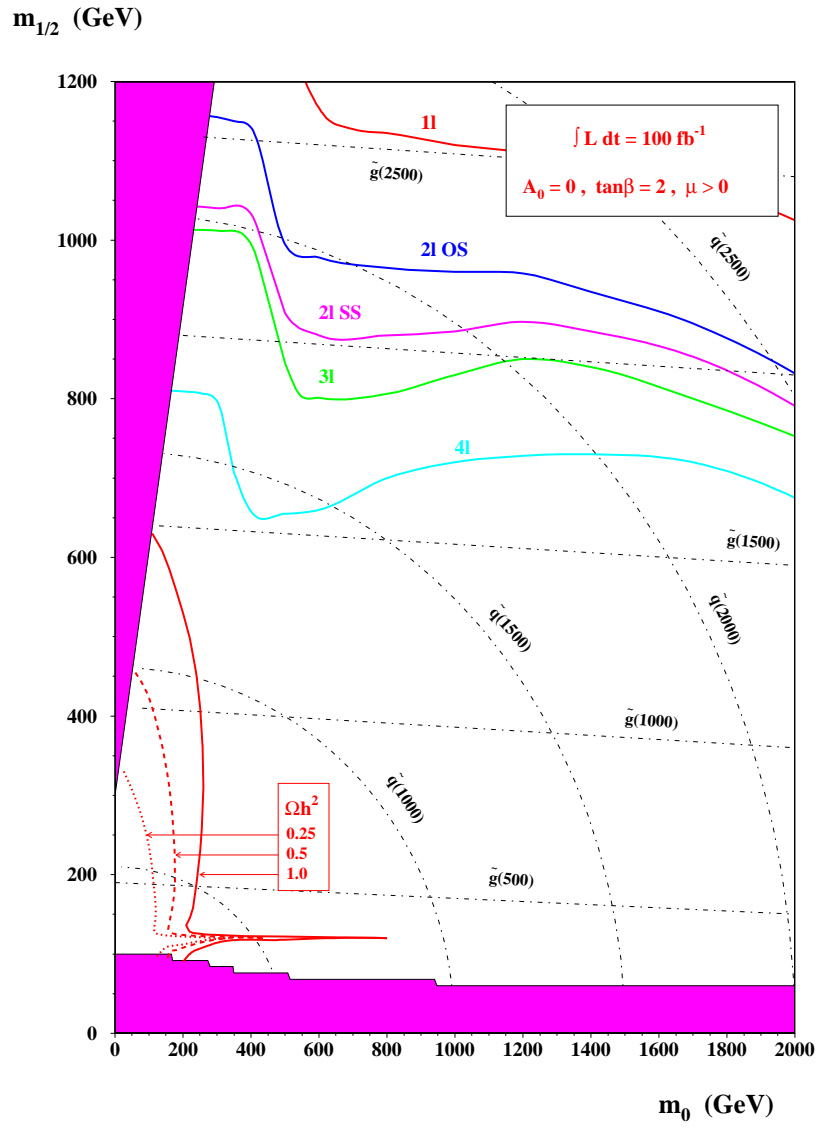


Figure 5.14: Same as in Fig. 5.13, but for 100 fb^{-1} .

6 Search for next-to-lightest neutralino

Leptonic decays of the second-lightest neutralino, $\tilde{\chi}_2^0$ have a useful kinematical feature: the dilepton invariant mass spectrum has a sharp edge near the kinematical upper limit with $M_{l^+l^-}^{max} = M_{\tilde{\chi}_2^0} - M_{\tilde{\chi}_1^0}$ in the case of direct three-body decays $\tilde{\chi}_2^0 \rightarrow l^+l^- \tilde{\chi}_1^0$ and $M_{l^+l^-}^{max} = \sqrt{(M_{\tilde{\chi}_2^0}^2 - M_l^2)(M_l^2 - M_{\tilde{\chi}_1^0}^2)}/M_l$ in the case of two-body cascade decays $\tilde{\chi}_2^0 \rightarrow l^\pm \tilde{l}_{L,R}^\mp \rightarrow l^+l^- \tilde{\chi}_1^0$. This feature was first discussed in Ref. [40] for $\tilde{\chi}_1^\pm \tilde{\chi}_2^0$ direct (EW) production. On the other hand, at LHC, the $\tilde{\chi}_2^0$ is abundantly produced from gluinos and squarks over whole $(m_0, m_{1/2})$ plane, see e.g. Figs. 2.5a-b, and this source of $\tilde{\chi}_2^0$ is much more prolific than direct EW production. Therefore, we propose to perform an inclusive search for $\tilde{\chi}_2^0$ and to use the specific shape of the dilepton mass spectrum as evidence for SUSY [41, 9]. For the SM background suppression, besides *two same-flavor opposite-sign leptons*, one can ask for an additional signature characterizing SUSY. This can be: missing energy taken away by escaping LSPs, or additional jets coming from gluinos and squarks cascade decays, or an extra high- p_T lepton from charginos, neutralinos, sleptons, vector bosons, or b -quarks copiously produced in SUSY. Depending on the sparticle masses and predominant decay modes one of these extra requirements can turn out to be more advantageous than the others, or to be complementary. In the following we discuss the inclusive $2 \text{ leptons} + E_T^{miss} + (jets)$ and $3 \text{ leptons} + (E_T^{miss})$ channels and determine the region of $(m_0, m_{1/2})$ parameter space where the dilepton invariant mass edge is visible in these final states.

6.1 Inclusive $2 \text{ leptons} + E_T^{miss} + (jets)$ channel

The most straightforward signature for selecting the $\tilde{\chi}_2^0$ decays is provided by the topology with two same-flavor opposite-sign leptons accompanied by large missing transverse energy and usually accompanied by a high multiplicity of jets. Here we concentrate on the $2 \text{ leptons} + E_T^{miss} + (jets)$ channel, where the final state leptons are electrons and muons [7, 42].

The largest SM background is due to $t\bar{t}$ production, with both W 's decaying into leptons, or one of the leptons coming from a W decay and the other from the b -decay of the same t -quark. We also considered other SM backgrounds: $W + jets$, WW , WZ , Wtb , $b\bar{b}$ and $\tau\tau$ -pair production, with decays into electrons and muons. Chargino pair production $\tilde{\chi}_1^\pm \tilde{\chi}_1^\mp$ is the largest SUSY background but gives a small contribution compared to the signal.

To observe an edge in the $M_{l^+l^-}$ distributions with the statistics provided by an integrated luminosity $L_{int} = 10^3 \text{ pb}^{-1}$ in a significant part of the $(m_0, m_{1/2})$ parameter plane, it is enough to require two hard isolated leptons ($p_T^{l_{1,2}} > 15 \text{ GeV}$) accompanied by large missing energy, $E_T^{miss} > 100 \text{ GeV}$. Our criterion for observing an edge in the $M_{l^+l^-}$ distribution contains two requirements: $(N_{EV} - N_B)/\sqrt{N_{EV}} \geq 5$ and $(N_{EV} - N_B)/N_B \geq 1.3$, where N_{EV} is the number of events with $M_{l^+l^-} \leq M_{l^+l^-}^{max}$, and N_B is number of the expected background events. Fig. 6.1a shows the invariant mass spectra of the two leptons at various $(m_0, m_{1/2})$ points for $\tan\beta = 2$, $\mu < 0$. The observability of the ‘‘edge’’ varies from 77σ and signal to background ratio 31 at point (200,160) to 27σ and a signal to background ratio 2.3 at point (60,230). The appearance of the edges in the distributions is sufficiently pronounced already with $L_{int} = 10^3 \text{ pb}^{-1}$ in a significant part of $(m_0, m_{1/2})$

parameter plane. The edge position can be measured with a precision of ~ 0.5 GeV.

With increasing m_0 and $m_{1/2}$ the cross-sections are decreasing and therefore higher luminosity and harder cuts are needed. To achieve maximum reach in $m_{1/2}$ with $L_{int} = 10^4 pb^{-1}$ for points where $\tilde{\chi}_2^0$ has two-body decays via \tilde{l}_L ($m_0 \lesssim 0.45 \cdot m_{1/2}$), a cut up to $E_T^{miss} > 300$ GeV is necessary to sufficiently suppress the background. For points with large m_0 , in the region where $\tilde{\chi}_2^0$ has three-body decay ($m_0 \gtrsim 0.5 \cdot m_{1/2}$, $m_{1/2} \lesssim 200$ GeV) the transverse momentum p_T of the leptons and E_T^{miss} are not very large, but there are more hard jets due to gluino and squark decays. Thus for these points we keep the same cuts for leptons and missing energy as before ($p_T^{l_{1,2}} > 15$ GeV, $E_T^{miss} > 100$ GeV) and require in addition a jet multiplicity $N_{jet} \geq 3$, with energy $E_T^{jet} > 100$ GeV, in the rapidity range $|\eta_{jet}| < 3.5$. To optimise the edge visibility we also apply an azimuthal angle cut, $\Delta\phi(l^+l^-) < 120^\circ$. This jet multiplicity requirement is also helpful for the first domain, where $\tilde{\chi}_2^0$ decays to leptons through \tilde{l}_L ($m_0 \lesssim 0.45 \cdot m_{1/2}$), Right sleptons are too light to provide large lepton p_T and E_T^{miss} , and to use cuts on p_T^l and E_T^{miss} alone is not very advantageous. With $L_{int} = 10^5 pb^{-1}$, to suppress the background at larger accessible m_0 , $m_{1/2}$ values, we have to require at least 2 or 3 jets, depending on the m_0 , $m_{1/2}$ region to be explored. Fig. 6.1b shows invariant dilepton mass distributions at some ($m_0, m_{1/2}$) points close to maximum reach with $L_{int} = 10^4 pb^{-1}$ and $L_{int} = 10^5 pb^{-1}$ respectively.

Figure 6.2 shows the inclusive dilepton spectrum for larger values of $\tan\beta = 10$ and 35. Despite decreasing branching ratios as visible in Fig. 2.7, the dilepton (e^+e^- , $\mu^+\mu^-$) edge is visible for low $m_{1/2}$ values already with $10^3 pb^{-1}$ [42].

The regions of the ($m_0, m_{1/2}$) parameter plane where an edge in the M_{l+l^-} spectra for $\tan\beta = 2$, $\mu < 0$ can be observed at different luminosities are shown in Fig. 6.3. In Fig. 6.4 we show separately the three domains where an edge due to $\tilde{\chi}_2^0 \rightarrow l\tilde{\chi}_1^0$, $\tilde{l}_R l$ and $\tilde{l}_L l$ decays can be observed at $L_{int} = 10^3 pb^{-1}$. One can notice a small overlapping region, where we expect to observe two edges, due to $\tilde{\chi}_2^0 \rightarrow l^+l^-\tilde{\chi}_1^0$ and to $\tilde{\chi}_2^0 \rightarrow \tilde{l}_R^\pm l^\mp \rightarrow l^+l^-\tilde{\chi}_1^0$ decays (*case 1*). With increasing luminosity and correspondingly higher statistics, this overlapping region increases, see Figs. 6.5 and 6.6. These plots show the same as Fig. 6.4, but for $L_{int} = 10^4 pb^{-1}$ and $L_{int} = 10^5 pb^{-1}$, respectively.

6.2 Inclusive 3 leptons channel

In this channel an extra high- p_T lepton is required to suppress the SM backgrounds [41, 9]. This can be either an isolated lepton, e.g. from the $\tilde{\chi}_1^\pm$ decay which has a similar behavior to $\tilde{\chi}_2^0$ (Fig. 2.6), or a non-isolated lepton from the abundant production of high transverse momentum b -jets in SUSY events. Thus in the inclusive 3 *lepton* channel we require:

- two opposite-sign, same-flavor leptons (μ or e) with $p_T > 10$ GeV;
- a third “tagging” lepton with $p_T > 15$ GeV;
- lepton isolation: if there is no track with $p_T > 2$ (1.5) GeV within $\Delta R = \sqrt{\Delta\eta^2 + \Delta\phi^2} < 0.3$ about the lepton direction, it is considered as isolated.

The lepton p_T thresholds can be varied depending on the region of ($m_0, m_{1/2}$) studied and in some cases leptons are not required to be isolated. In the selected 3 *lepton* events we reconstruct the invariant mass M_{l+l^-} of a lepton pair with the same flavor and opposite sign. When several l^+l^- combinations per event are possible, the one with minimal separation ΔR_{l+l^-} is chosen. Any significant deviation from the expected SM l^+l^- invariant mass spectrum then provides evidence for SUSY.

We stress that no other requirements, such as missing transverse energy, jet activity,

etc., are imposed in the inclusive 3 *leptons* channel. The price for this simplicity is a decrease of signal acceptance due to the requirement on the third lepton, and somewhat higher p_T of leptons needed to sufficiently suppress the SM backgrounds. Thus there is complementarity between this search which relies on lepton (e, μ) measurements and the tracker for lepton isolation and momentum measurement, and the search, in inclusive 2 *leptons* + E_T^{miss} channel which relies on lepton detection and overall calorimetry, HCAL in particular, for E_T^{miss} measurement.

The main SM sources of three leptons considered are production of WZ, $t\bar{t}$, ZZ and $Zb\bar{b}$. The expected SM background to 3 *leptons* final states at an integrated luminosity of $L_{int} = 10^4 \text{ pb}^{-1}$ is shown in Fig. 6.7. Near the Z mass the main contribution comes from the WZ production, while $t\bar{t}$ production dominates at lower invariant masses.

Dilepton spectra for the mSUGRA “Point 4” (see Table 1.1), superimposed on the SM background, are shown in Fig. 6.8. The number of events corresponds to an integrated luminosity of $L_{int} = 20 \text{ pb}^{-1}$, i.e. just a few hours of initial LHC running. The p_T threshold on all three leptons is 15 GeV. In Fig. 6.8a no isolation requirement is applied, whereas in Fig. 6.8b the two leptons entering the dilepton mass distribution are isolated. The contribution from the SM background is negligible in the latter case. In both cases the specific shape of the l^+l^- distribution, with its sharp edge, reveals $\tilde{\chi}_2^0$ production. At this mSUGRA point the $\tilde{\chi}_2^0$ has a three-body decay mode with a branching ratio $B(\tilde{\chi}_2^0 \rightarrow l^+l^- + \tilde{\chi}_1^0) = 0.32$ ($l = e, \mu$) and the masses are $M_{\tilde{\chi}_2^0} = 97 \text{ GeV}$, $M_{\tilde{\chi}_1^0} = 45 \text{ GeV}$. The sharp edge is situated at the expected value of $M_{l^+l^-}^{max} = 52 \text{ GeV}$.

Figure 6.9 shows the $M_{l^+l^-}$ distribution for mSUGRA “Point 1” (see Table 1.1) with an integrated luminosity of $L_{int} = 10^4 \text{ pb}^{-1}$. The p_T thresholds for leptons are 15, 15, 30 GeV and all three leptons are isolated. At this mSUGRA point the $\tilde{\chi}_2^0$ possesses a two-body decay mode with the branching ratio $B(\tilde{\chi}_2^0 \rightarrow \tilde{l}_R + l) = 0.24$. The sparticle masses are $M_{\tilde{\chi}_2^0} = 231 \text{ GeV}$, $M_{\tilde{\chi}_1^0} = 122 \text{ GeV}$, $M_{\tilde{l}_R} = 157 \text{ GeV}$. The “edge” of the distribution is situated near 108 GeV, as expected. We define a signal significance as $S = N_S / \sqrt{N_S + N_B}$, where N_S and N_B are the numbers of signal and background events, respectively, in a mass window below the edge. In this particular case signal and background events are calculated in a mass window of $100 \text{ GeV} < M_{l^+l^-} < 110 \text{ GeV}$, $N_S = 140$ and $N_B = 39$, resulting in signal significance of $S = 10.5$. N_B consists of 18, 8, 11 and 2 events coming from WZ, $t\bar{t}$, ZZ and $Zb\bar{b}$ production, respectively.

An example for the mSUGRA “Point 5” is shown in Fig. 6.10. The cuts are the same as in the previous case. At this point $\tilde{\chi}_2^0$ has three-body decay modes with $B(\tilde{\chi}_2^0 \rightarrow l^+l^- + \tilde{\chi}_1^0) = 0.06$ and the masses are $M_{\tilde{\chi}_2^0} = 124 \text{ GeV}$, $M_{\tilde{\chi}_1^0} = 73 \text{ GeV}$. The observed value of $M_{l^+l^-}^{max}$ is close to the expected value of 51 GeV. In a mass window of $20 \text{ GeV} < M_{l^+l^-} < 52 \text{ GeV}$ the numbers of signal and background events are $N_S = 588$ and $N_B = 402$ giving a signal significance of $S = 19$. N_B consists of 113, 139, 65 and 85 events coming from WZ, $t\bar{t}$, ZZ and $Zb\bar{b}$ production, respectively.

By the same procedure the mSUGRA parameter space $(m_0, m_{1/2})$ was scanned for fixed $\tan\beta = 2$, $A_0 = 0$ and $\mu < 0$ [9]. Figures 6.11a-c show the $M_{l^+l^-}$ distributions for three different mSUGRA points with the optimal thresholds on lepton p_T and isolation requirement in inclusive 3 *lepton* events. Generally, with increasing $m_{1/2}$ the observation of the edge becomes more difficult due to the rapidly decreasing gluino and squark production cross-sections. Nonetheless, this spectacular structure in the dilepton mass spectrum reflecting $\tilde{\chi}_2^0$ decays, may be among the first ways through which presence of SUSY may reveal itself. It may appear with very modest statistics, in a non-sophisticated analysis

and with only modest demands on detector performance. The precision for “edge” measurement in most of the region, where it is detectable is expected to be $\lesssim 0.5$ GeV. Note, that the Z peak seen in Figs. 6.8-6.11 serves as an overall calibration signal; it allows to control the mass scale as well as the production cross-section.

Asking for a statistical significance $S > 7$ with at least 40 signal events calculated in a mass interval > 10 GeV below the edge the domain explorable with an integrated luminosity of $L_{int} = 10^4 \text{ pb}^{-1}$ is shown in Fig. 6.12. It entirely covers the cosmologically preferred region $0.15 < \Omega h^2 < 0.4$ [37]; here Ω is the ratio of the relic particle density to critical density, h is the Hubble constant scaling factor and bounds are obtained assuming $\tilde{\chi}_1^0$ is the cold dark matter particle in the mixed dark matter scenario for the Universe, varying h over the allowed range $0.5 < h < 0.8$.

For some regions of mSUGRA parameter space $M_{l+l^-}^{max}$ is close to, or even hidden by the Z signal. At these points the accuracy of an edge measurement is ~ 10 GeV. Applying a cut on missing transverse energy (and/or jets) suppresses the contribution from the SM Z production, improving signal visibility.

6.3 Inclusive 3 leptons + E_T^{miss} channel

With increasing $m_{1/2}$, gluino and squark masses increase and the missing transverse energy becomes larger. Requiring $E_T^{miss} > 200$ (300) GeV rejects most of the SM background leaving a big fraction of signal events. Figures 6.11d-e show the dilepton spectra for various mSUGRA points in the 3 lepton + E_T^{miss} final states. In the region of high $m_{1/2}$, dileptons are mainly produced in the cascade decays of $\tilde{\chi}_2^0$. The third, “tagging” lepton predominantly comes from $\tilde{\chi}_1^\pm$ which also has cascade leptonic decays. Thus in this region of parameter space a large fraction of 3 lepton + E_T^{miss} events are in fact inclusively produced $\tilde{\chi}_1^\pm \tilde{\chi}_2^0$ pairs. Therefore all three leptons are required to be isolated. The lepton p_T thresholds are chosen to be quite asymmetric: 50, 25, 10 GeV, to account for the cascade nature of the $\tilde{\chi}_2^0$ and $\tilde{\chi}_1^\pm$ decays. The region of mSUGRA parameter space, where the $\tilde{\chi}_2^0$ is observable from the dilepton mass distribution shape in the 3 lepton + E_T^{miss} events at $L_{int} = 10^5 \text{ pb}^{-1}$ luminosity is shown in Fig. 6.12 [9]. The reach extends up to $m_{1/2} \sim 900$ GeV and a detectable edge is seen as long as $\sigma \cdot B \gtrsim 10^{-2} \text{ pb}$ (see Fig. 2.5).

We conclude that

- Observation of an edge in the dilepton invariant mass spectrum reflects the production of $\tilde{\chi}_2^0$ and hence establishes the existence of SUSY; this observation in some cases is possible with very small statistics and could be the first evidence for SUSY at LHC.
- With no great demand on detector performance a large portion of mSUGRA parameter space including the cosmologically preferred domain can be explored with an integrated luminosity as low as $L_{int} = 10^4 \text{ pb}^{-1}$.

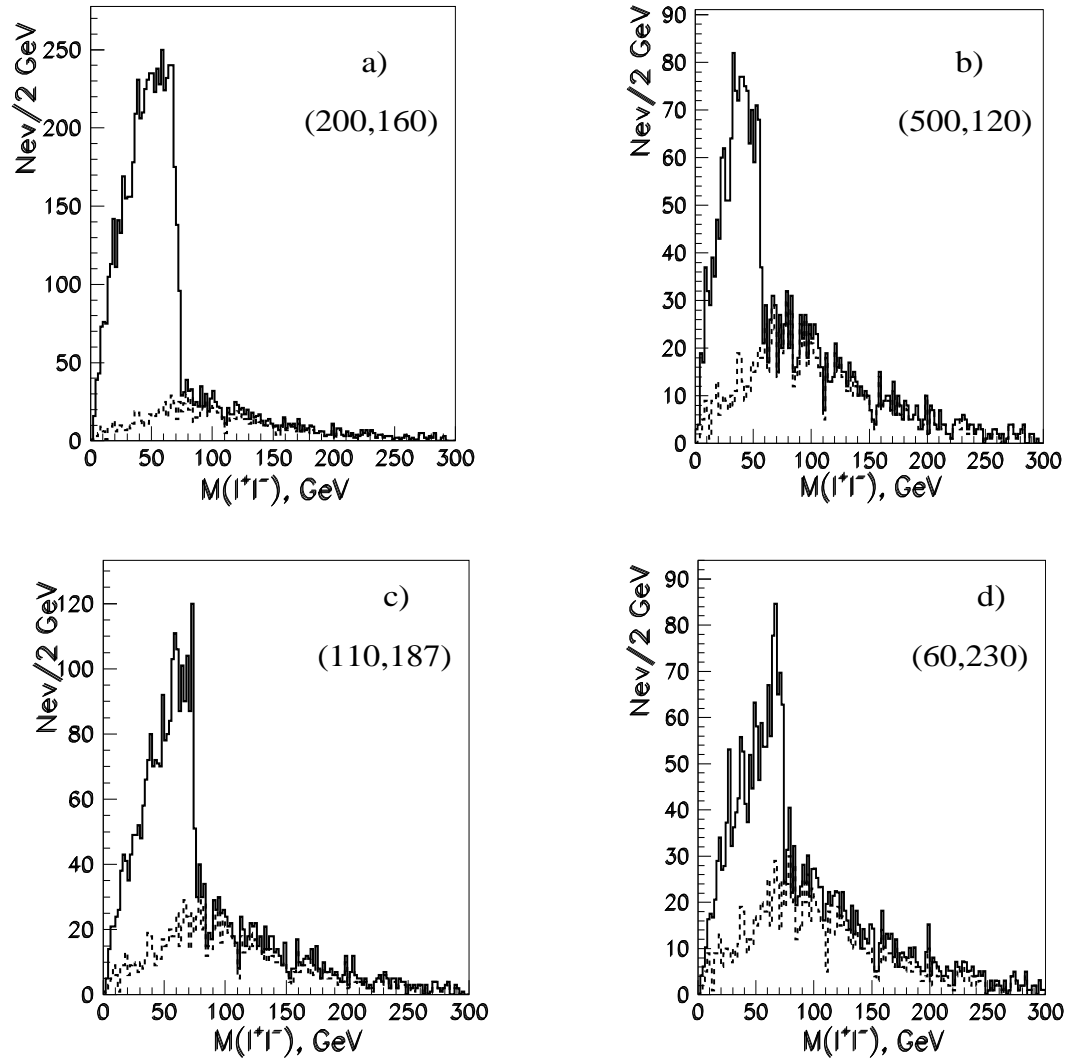


Figure 6.1a: Invariant mass distribution of two same-flavor, opposite-sign leptons at various $(m_0, m_{1/2})$ points for $\tan\beta = 2$, $\mu < 0$ with $L_{int} = 10^3 \text{ pb}^{-1}$. SM background is also shown (dashed line).

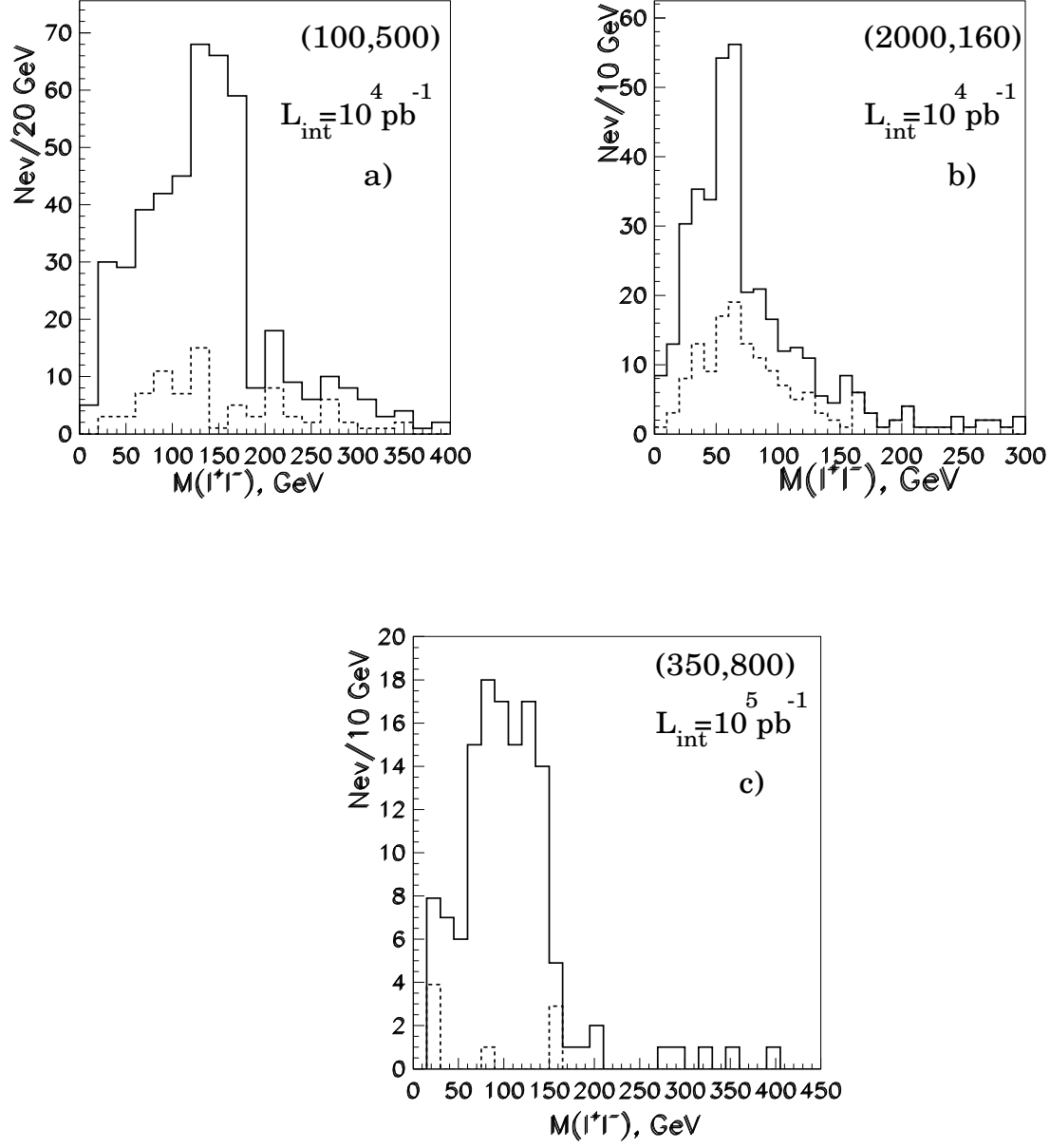


Figure 6.1b: Invariant mass distribution of two same-flavor, opposite-sign leptons at $(m_0, m_{1/2})$ points close to the experimental reach at corresponding luminosities $L_{int} = 10^4 \text{ pb}^{-1}$ and 10^5 pb^{-1} for $\tan\beta = 2$, $\mu < 0$. SM background is also shown (dashed line).

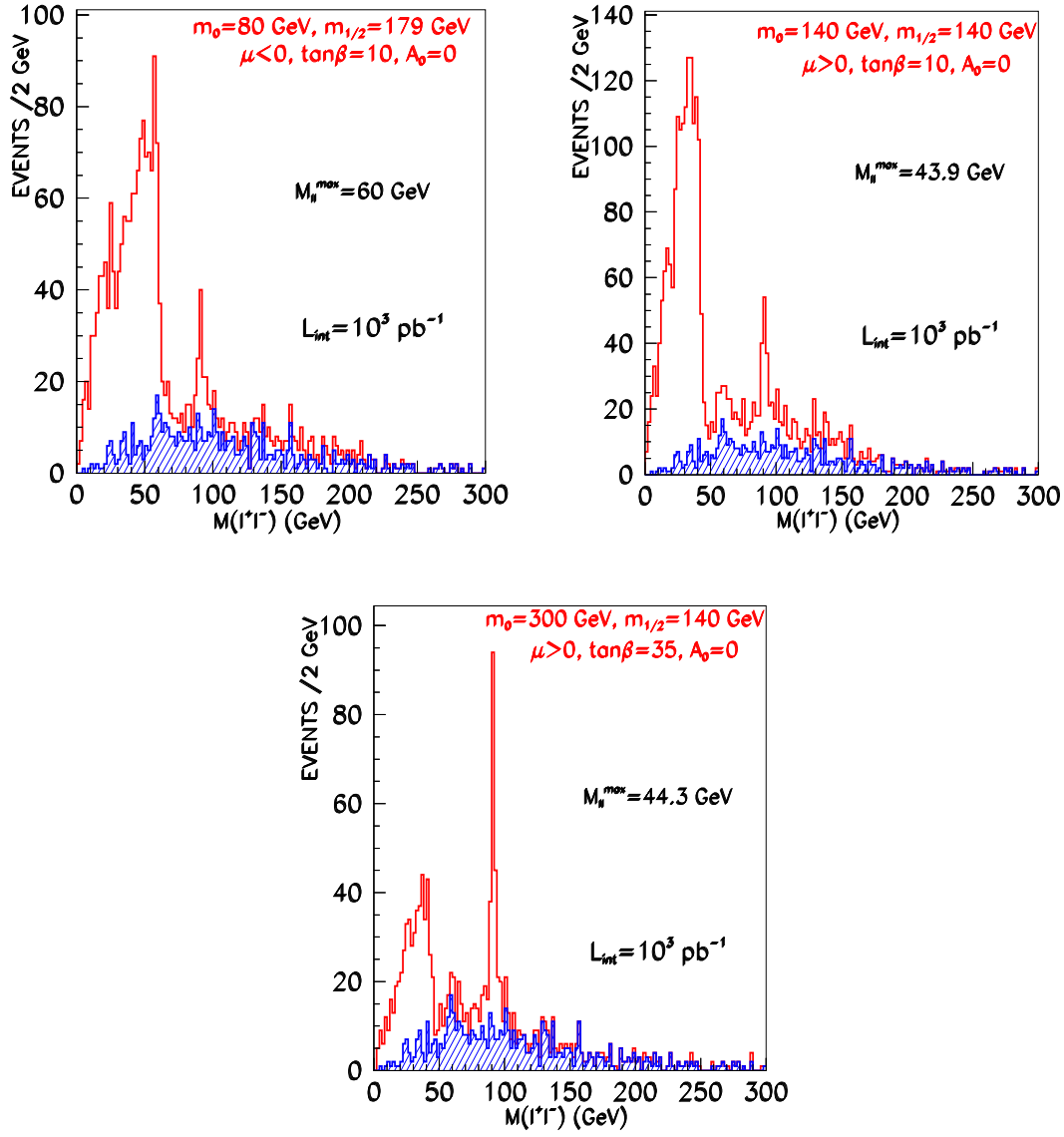


Figure 6.2: Invariant mass distribution of two same-flavor, opposite-sign leptons at various $m_0, m_{1/2}, \tan\beta$ and μ points for $L_{int} = 10^3 \text{ pb}^{-1}$. SM background is also shown.

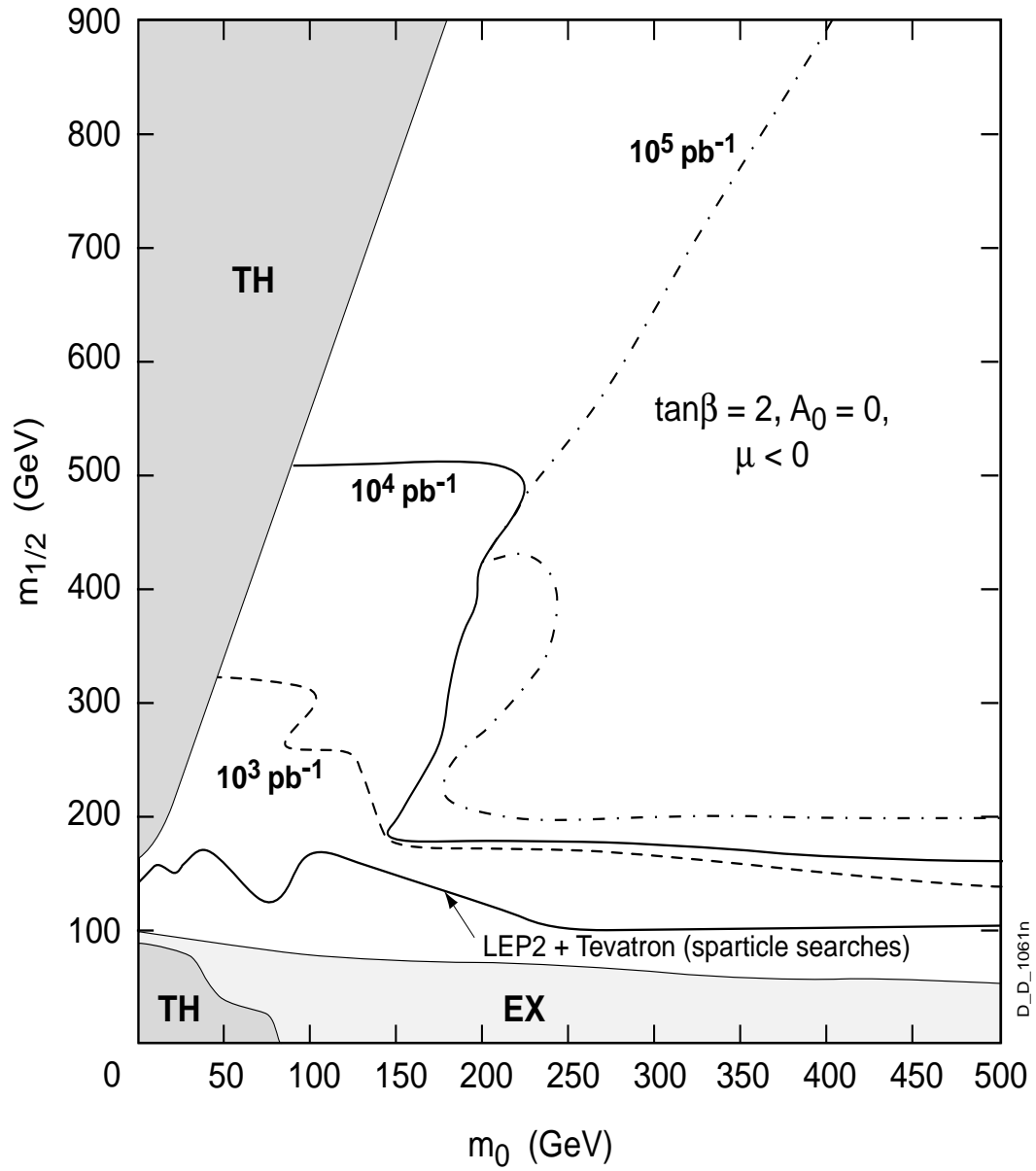


Figure 6.3: Observability of edges in invariant dilepton mass distribution with luminosities 10^3 pb^{-1} (dashed line), 10^4 pb^{-1} (solid line) and 10^5 pb^{-1} (dashed-dotted line). Also shown are the explorable domain in sparticle searches at LEP2 (300 pb^{-1}) and the Tevatron (1 fb^{-1}), theoretically and experimentally excluded regions.

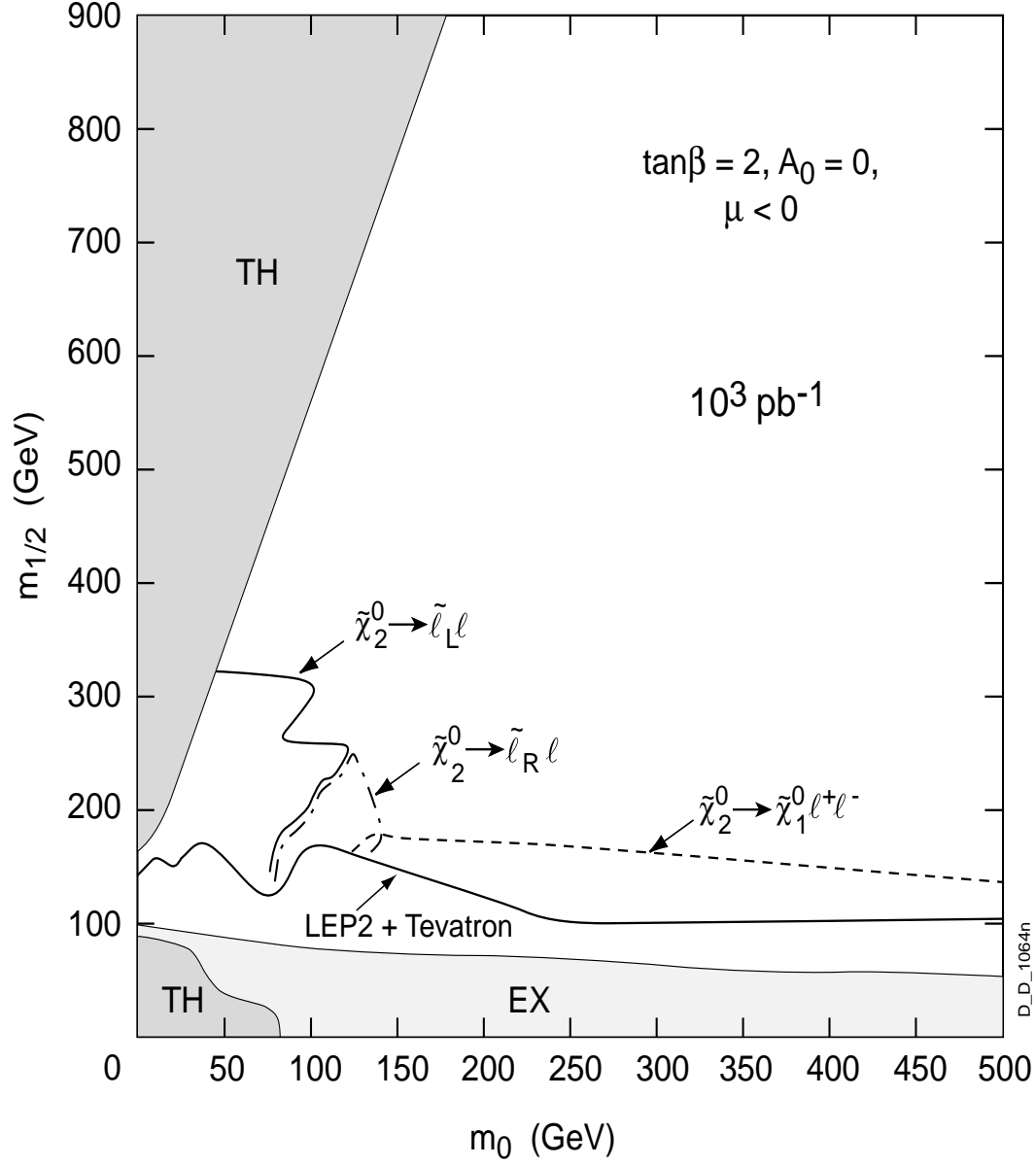


Figure 6.4: Domains where the observed edge in the M_{l+l^-} distribution is due to the decays $\tilde{\chi}_2^0 \rightarrow \tilde{l}_L^\pm l^\mp \rightarrow \tilde{\chi}_1^0 l^+ l^-$ (solid line), $\tilde{\chi}_2^0 \rightarrow \tilde{l}_R^\pm l^\mp \rightarrow \tilde{\chi}_1^0 l^+ l^-$ (dashed-dotted line), $\tilde{\chi}_2^0 \rightarrow \tilde{\chi}_1^0 l^+ l^-$ (dashed line), $L_{int} = 10^3 \text{ pb}^{-1}$.

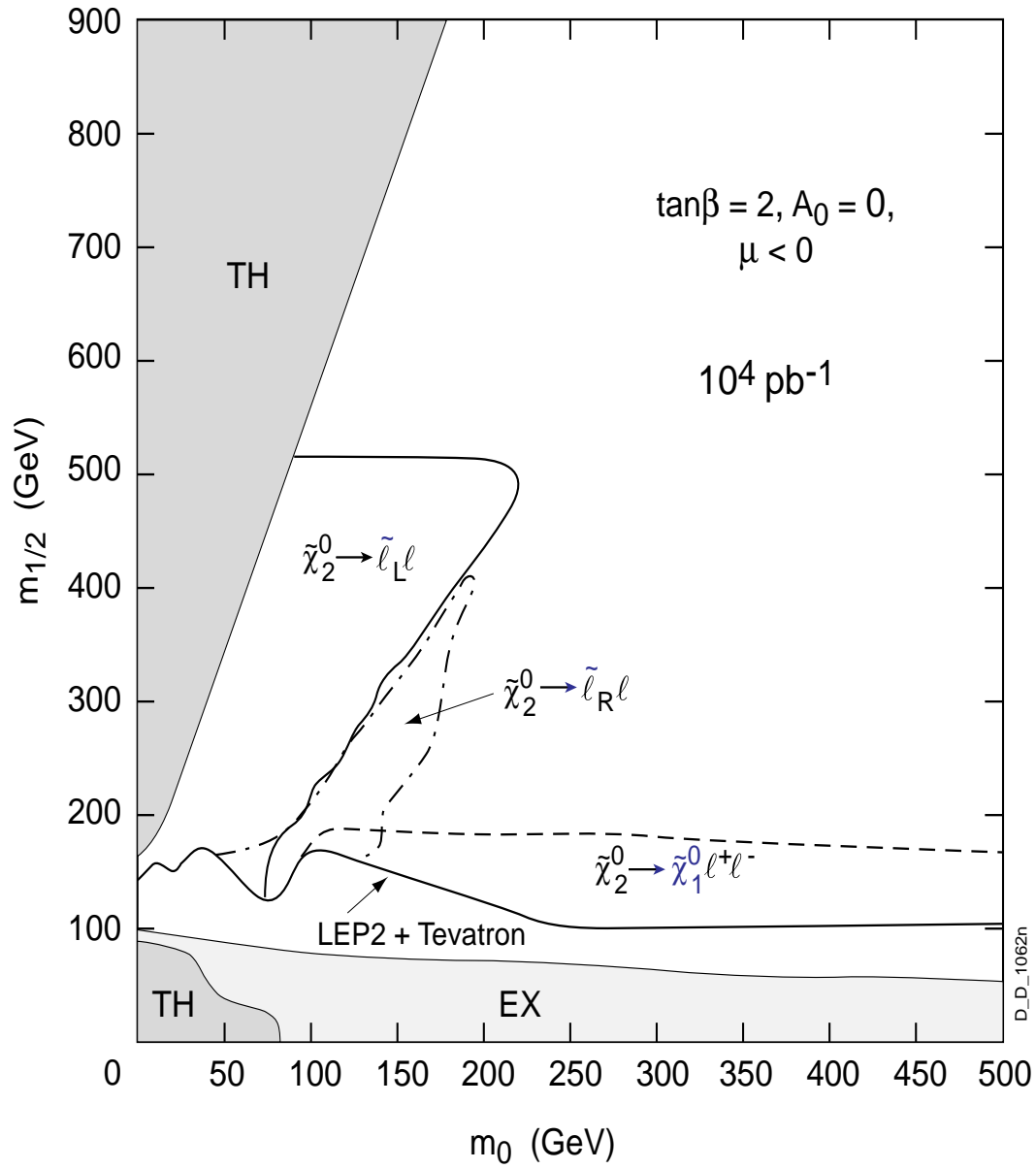


Figure 6.5: Domains where the observed edge in the M_{l+l^-} distribution is due to the decays $\tilde{\chi}_2^0 \rightarrow \tilde{l}_L^\pm l^\mp \rightarrow \tilde{\chi}_1^0 l^+ l^-$ (solid line), $\tilde{\chi}_2^0 \rightarrow \tilde{l}_R^\pm l^\mp \rightarrow \tilde{\chi}_1^0 l^+ l^-$ (dashed-dotted line), $\tilde{\chi}_2^0 \rightarrow \tilde{\chi}_1^0 l^+ l^-$ (dashed line), $L_{int} = 10^4 \text{ pb}^{-1}$.

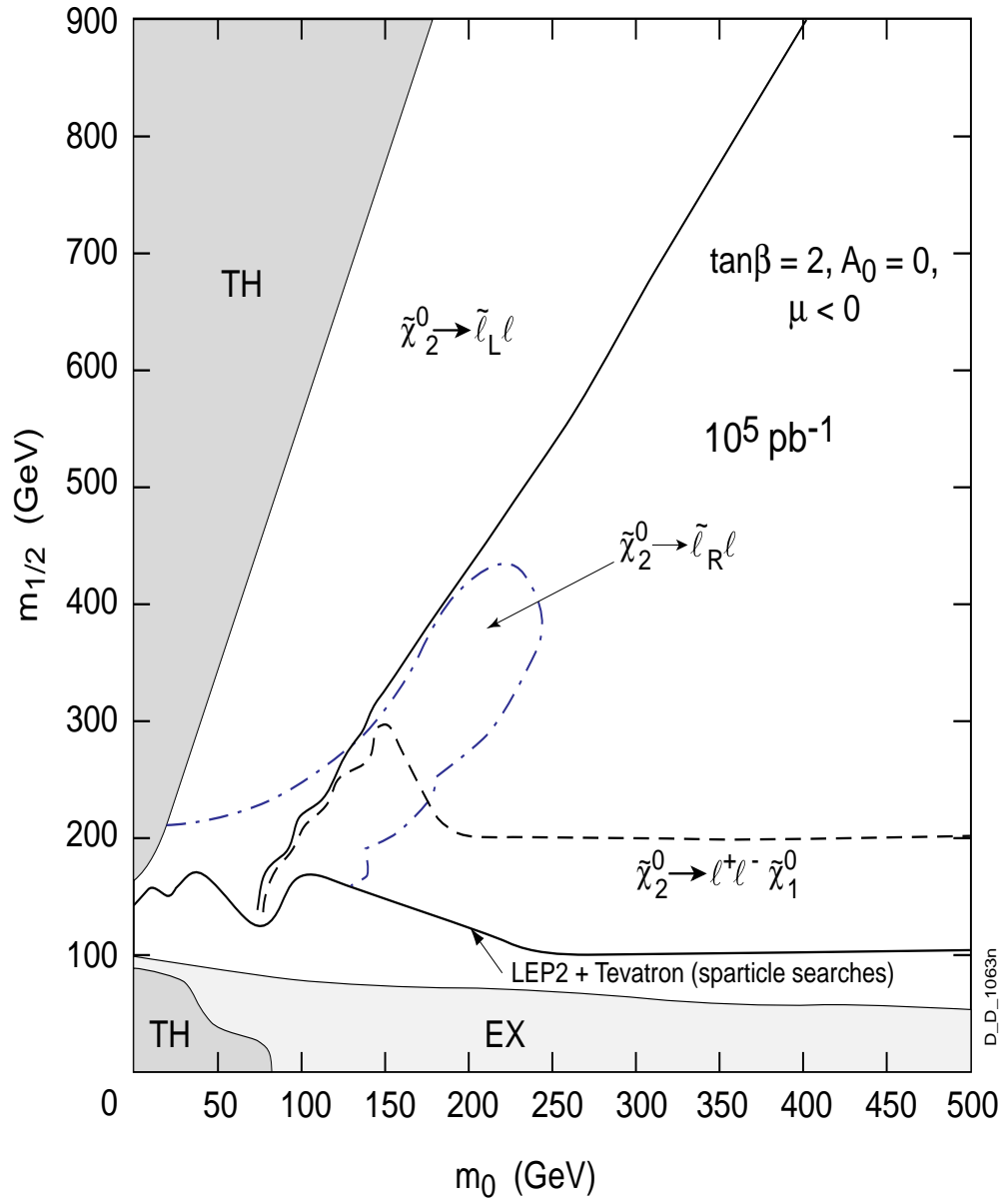


Figure 6.6: Domains where the observed edge in the M_{l+l^-} distribution is due to the decays $\tilde{\chi}_2^0 \rightarrow \tilde{l}_L^\pm l^\mp \rightarrow \tilde{\chi}_1^0 l^+ l^-$ (solid line), $\tilde{\chi}_2^0 \rightarrow \tilde{l}_R^\pm l^\mp \rightarrow \tilde{\chi}_1^0 l^+ l^-$ (dashed-dotted line), $\tilde{\chi}_2^0 \rightarrow \tilde{\chi}_1^0 l^+ l^-$ (dashed line), $L_{int} = 10^5 \text{ pb}^{-1}$.

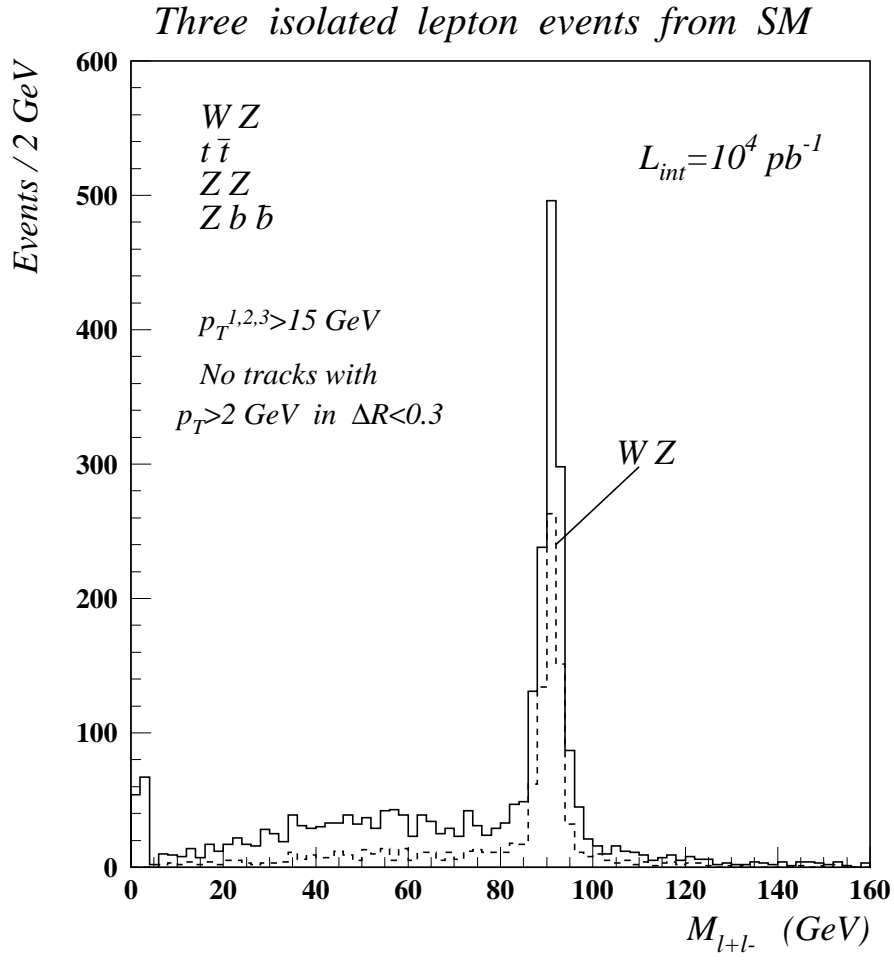


Figure 6.7: Expected Standard Model background in inclusive 3 *lepton* final state.

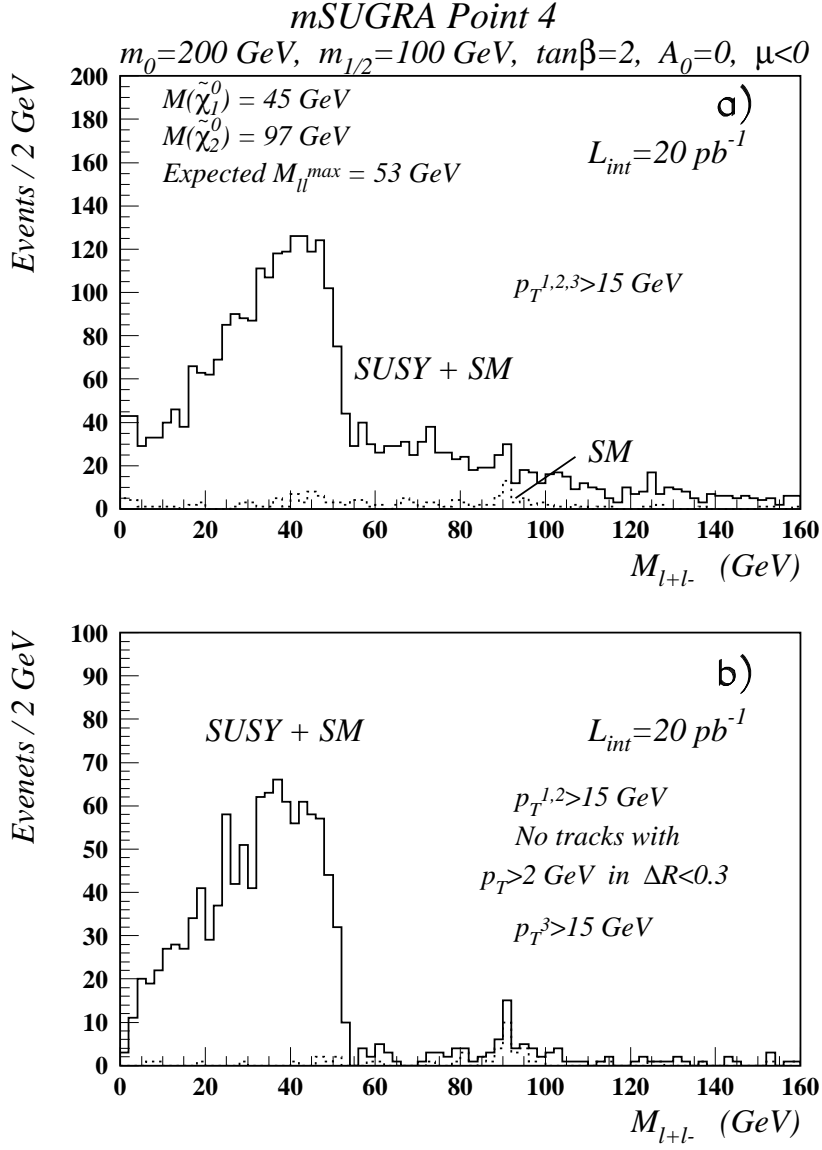


Figure 6.8: Expected l^+l^- mass spectrum for mSUGRA Point 4: $m_0 = 200 \text{ GeV}$, $m_{1/2} = 100 \text{ GeV}$, $\tan\beta=2$, $A_0 = 0$ and $\mu < 0$. a) Leptons with $p_T > 15 \text{ GeV}$ in $|\eta| < 2.4$ are considered; b) as in previous case, but two leptons which enter invariant mass spectrum are required to be isolated. The dotted histogram corresponds to the SM background.

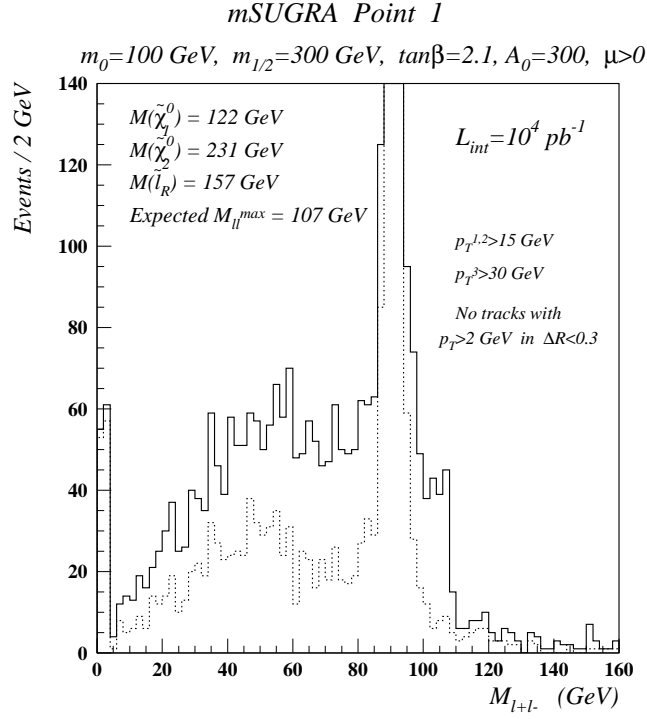


Figure 6.9: Expected l^+l^- mass spectrum for mSUGRA Point 1: $m_0 = 100 \text{ GeV}$, $m_{1/2} = 300 \text{ GeV}$, $\tan\beta=2.1$, $A_0 = 300 \text{ GeV}$ and $\mu > 0$. The dotted histogram corresponds to the SM background.

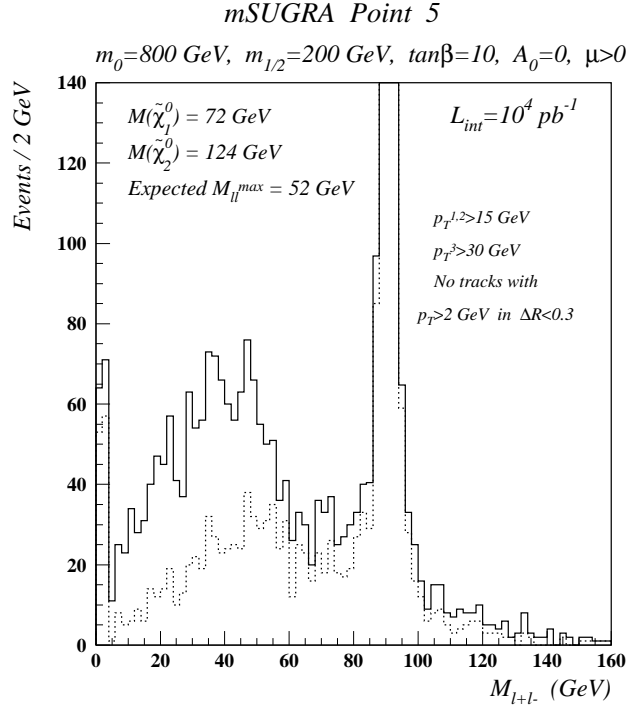


Figure 6.10: Expected l^+l^- mass spectrum for mSUGRA Point 5: $m_0 = 800 \text{ GeV}$, $m_{1/2} = 200 \text{ GeV}$, $\tan\beta=10$, $A_0 = 0$ and $\mu > 0$. The dotted histogram corresponds to the SM background.

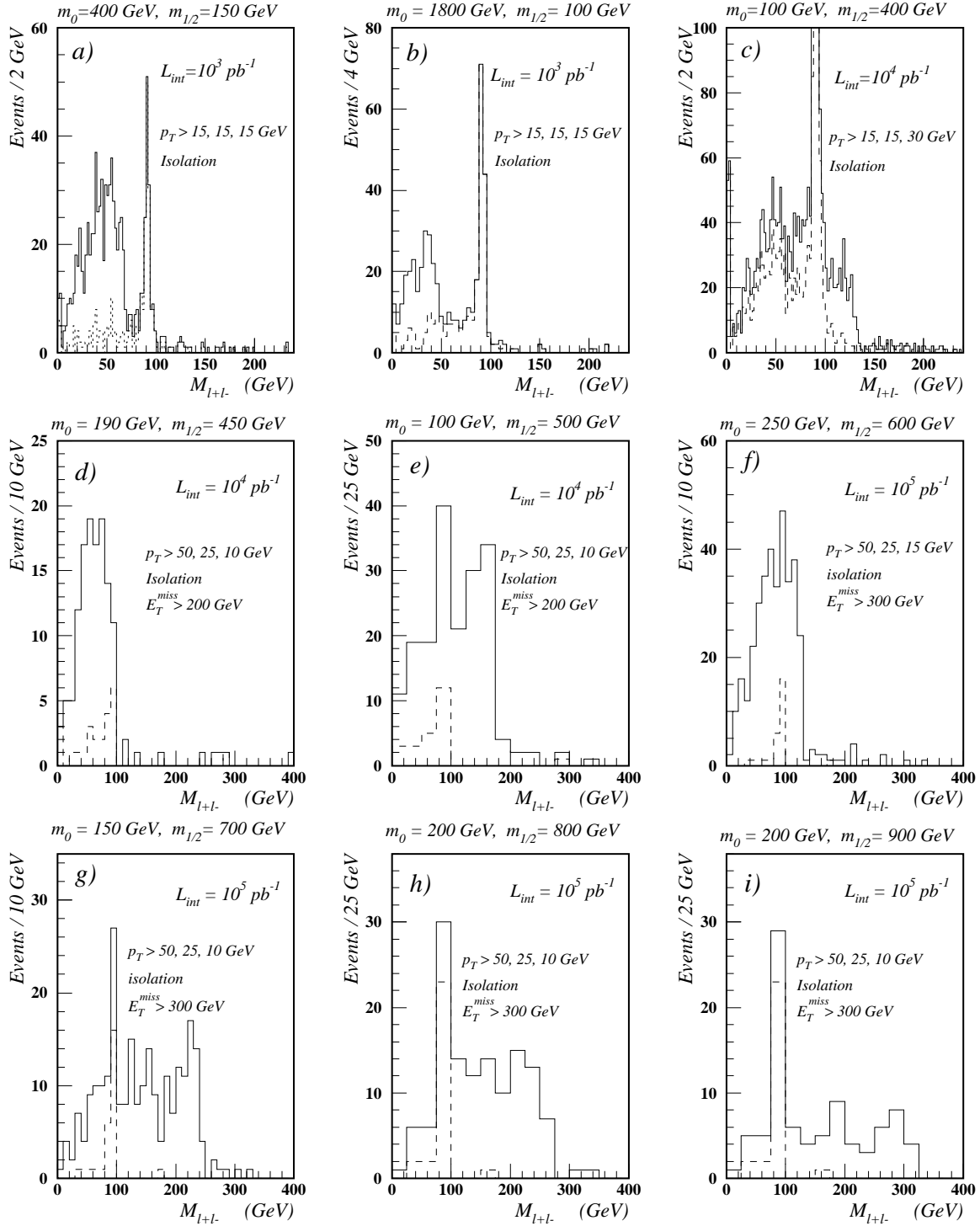


Figure 6.11: Dilepton mass spectrum for mSUGRA Point from different $(m_0, m_{1/2})$ regions in inclusive 3 leptons and $3\text{ leptons} + E_T^{\text{miss}}$ channels. Contribution from SM background is shown with dashed histogram. The other mSUGRA parameters are: $\tan\beta=2$, $A_0 = 0$ and $\mu < 0$.

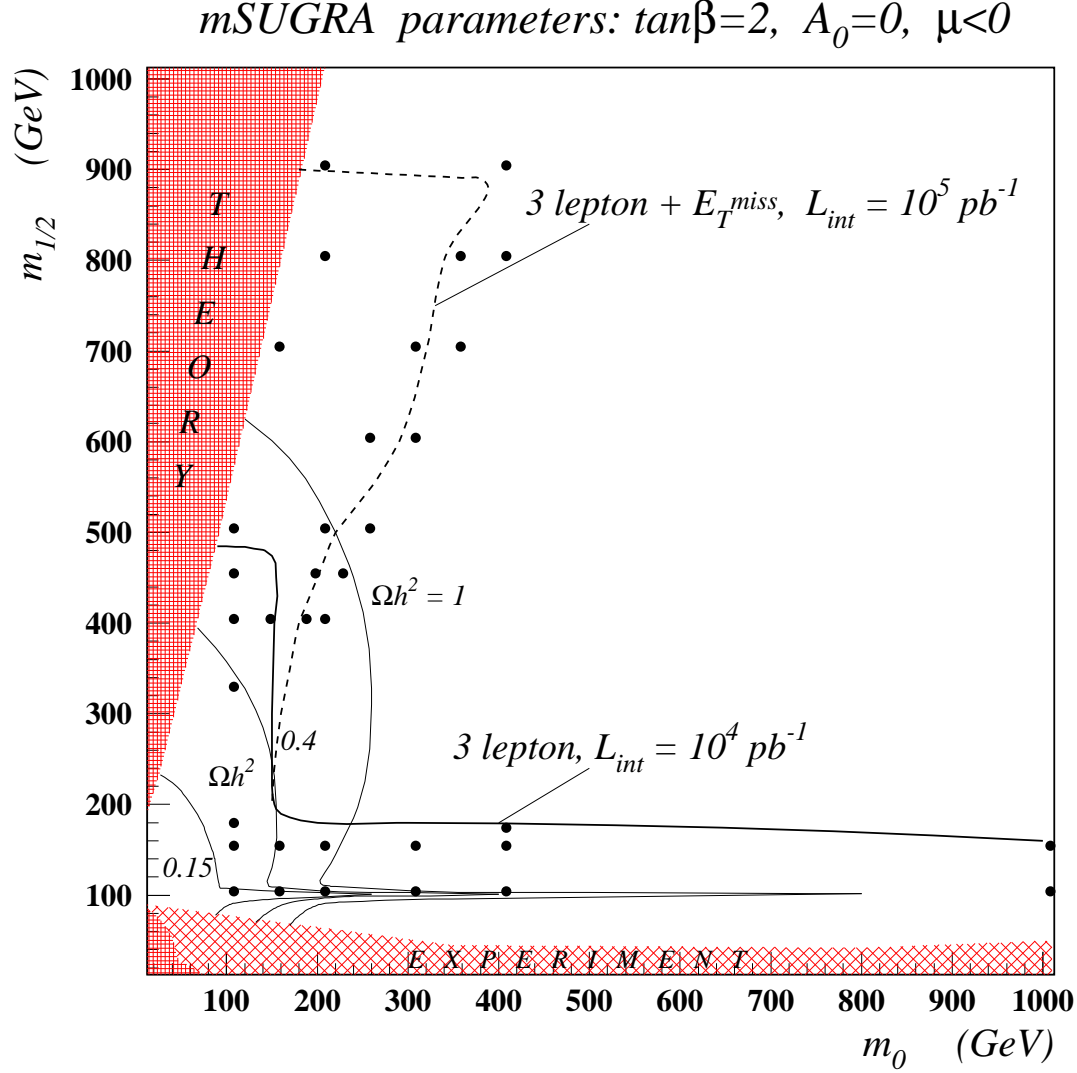


Figure 6.12: Explorable region of mSUGRA in inclusive 3 *leptons* and 3 *leptons* + E_T^{miss} channels at $L_{int} = 10^4 \text{ pb}^{-1}$ and $L_{int} = 10^5 \text{ pb}^{-1}$, respectively. Shaded regions are excluded by theory ($m_0 \lesssim 80 \text{ GeV}$) and experiment ($m_{1/2} \lesssim 90 \text{ GeV}$). The cosmologically preferable region $0.15 < \Omega h^2 < 0.4$ is also given. Simulated mSUGRA Points are shown as well.

7 Exclusive 2 leptons + no jets + E_T^{miss} channel – search for sleptons

The previous two sections described inclusive searches suitable for the discovery of SUSY. We now focus on more exclusive final states where individual SUSY particles may be targeted.

The slepton production and decay features described in section 2.2 give rise to several interesting experimental signatures. In this study we concentrate on the possibilities to detect a slepton signal in the simplest event topology *two leptons + E_T^{miss} + no jets* taking into account all possible SUSY and SM contributions to this topology [6]. The observability of the slepton signal is evaluated summing all flavors and all production mechanisms which contribute to the *two same-flavor opposite-sign leptons + E_T^{miss} + no jets* final state. Evidence for a *slepton signal* will be judged from an excess over full *SUSY and SM backgrounds*, but presence of a *SUSY signal* will be estimated from an excess over only the expected *SM backgrounds*.

The main expected Standard Model background is $t\bar{t}$ production, with both W 's decaying to leptons, or one of the leptons coming from a W decay and the other from the b -decay of the same t -quark. The other SM backgrounds considered are $Wt\bar{b}$, WW , WZ , $b\bar{b}$ and $\tau\tau$ -pair production, with decays to electrons and muons. The assumed cross-sections are: $\sigma_{t\bar{t}}=660$ pb ($M_t = 175$ GeV), $\sigma_{Wt\bar{b}}=160$ pb, $\sigma_{WW}=70$ pb, $\sigma_{WZ}=26$ pb, $\sigma_{\tau\tau}=7.5$ pb, $\sigma_{b\bar{b}}=5000$ pb ($p_T^b \geq 100$ GeV). No forcing of decay modes is implemented.

As internal SUSY backgrounds we consider processes $\tilde{q}\tilde{q}$, $\tilde{g}\tilde{q}$, $\tilde{g}\tilde{g}$ which, through cascade decays with jets outside the acceptance, below the detection threshold, or lost in cracks, can also lead to *two leptons + E_T^{miss} + no jets* final states. The $\tilde{\chi}_1^\pm \tilde{\chi}_2^0$ process for example leads mainly to three-lepton final states. However, it can also contribute to two-lepton final states if one of the leptons is outside the acceptance or is misidentified, or if only the $\tilde{\chi}_2^0$ decays to leptons, and jets from the $\tilde{\chi}_1^\pm$ decay are not reconstructed.

We perform a mapping of the mSUGRA parameter space to determine the optimal set of signal selection cuts in the various regions of $(m_0, m_{1/2})$ plane, taking into account event kinematical properties, and evaluate the observability of the signal. An important issue is to find out if there is a gap in slepton detectability, especially in the low mass range at the junction between the observability domains at LEP2, Tevatron and the LHC. The mSUGRA-parameter space points $(m_0, m_{1/2})$ probed are shown in Fig. 7.1. This figure also shows the masses $m_{\tilde{l}_L}$ and $m_{\tilde{\chi}_1^0}$ at each point, the theoretically and experimentally excluded regions and the explorable domains in sparticle searches at LEP2 (300 pb⁻¹) and the Tevatron (1 fb⁻¹).

Taking into account the signal and background event topologies the following kinematical variables are found useful for slepton signal extraction:

i) for leptons:

- p_T^l -cut on leptons and lepton isolation (*Isol*), which is defined here as the calorimetric energy flow around the lepton in a cone of $\Delta R < 0.5$ divided by the lepton energy;
- effective mass of two same-flavor opposite-sign leptons, to suppress WZ and potential ZZ backgrounds by rejecting events in a $m_Z \pm \delta M_Z$ band;
- $\Delta\phi_{l+l-}$, the relative azimuthal angle between two same-flavor opposite-sign leptons;

- ii) for E_T^{miss} :
 - E_T^{miss} -cut,
 - $\Delta\phi(E_T^{miss}, l^+l^-)$, the relative azimuthal angle between E_T^{miss} and vector sum of the transverse momenta of the two leptons.
- iii) for jets:
 - “jet veto”-cut: no jet with E_T^{jet} lower than certain threshold, in some rapidity interval, typically $|\eta_{jet}| < 4.5$.

The data selection cuts based on these variables are separately optimised in various parts of the explored parameter space [6]. For illustration we show some typical distributions. Figure 7.2 shows the E_T^{miss} distributions for signal and various SUSY backgrounds at two $(m_0, m_{1/2})$ points, one with low and one with high slepton masses. The hardest spectra in both figures correspond to $\tilde{q}\tilde{q}$ production and the softest ones to chargino-neutralino production. This figure also shows the main SM backgrounds. For low slepton mass there is no big difference in shape between signal and SM-background spectra, thus it is not very advantageous to apply a hard E_T^{miss} cut.

Figure 7.3 shows the $\Delta\phi(E_T^{miss}, l^+l^-)$ distribution at the point from the low slepton mass region, $m_0 = 86$ GeV, $m_{1/2} = 85$ GeV, after $p_T^{l_{1,2}}$, cuts on lepton isolation and E_T^{miss} . The internal SUSY and SM backgrounds are still much larger in magnitude than the signal. Keeping only events with large relative azimuthal angles significantly improves the signal to background ratio.

Figure 7.4 illustrates the expected rejection factors which can be obtained by a “central” jet veto for two E_T^{jet} thresholds as a function of jet acceptance at point $m_0 = 86$ GeV, $m_{1/2} = 85$ GeV. Signal acceptance decreases slightly with increasing $|\eta_{jet}|$ of the jet veto region, whilst for sufficient rejection of SUSY and SM backgrounds ($t\bar{t}$) it is important to have calorimetric coverage up to $|\eta| = 3.5 - 4.0$. The rejection power against \tilde{g}, \tilde{q} and $t\bar{t}$ improves by a factor of 1.5-1.8 with increasing coverage from $|\eta| < 2.5$ to $|\eta| < 3.5$. To achieve significant background rejection reliable jet detection down to $E_T \approx 30$ GeV is also essential.

Figure 7.5 shows the $\Delta\phi_{l+l-}$ distribution for the main SM and SUSY backgrounds and events with direct slepton production at the same point $m_0 = 86$ GeV, $m_{1/2} = 85$ GeV. For the signal, small $\Delta\phi_{l+l-}$ events come from $\tilde{\nu}_l\tilde{\bar{\nu}}_l$ production whilst events with large $\Delta\phi_{l+l-}$ are due to charged slepton production. The main contribution to the slepton signal from $\tilde{\chi}_1^\pm\tilde{\chi}_2^0$ production in the two-lepton final state comes from decays of $\tilde{\chi}_2^0$, thus the distribution of these events also peaks at low relative azimuthal angles. All processes which go through $\tilde{\chi}_2^0$ decays to leptons, including \tilde{g}, \tilde{q} contributions have almost the same shape $\Delta\phi$ -distribution. In some parts of parameter space it may be more advantageous to keep only events with large $\Delta\phi_{l+l-}$, which rejects most of the internal SUSY backgrounds. However, this cut also eliminates direct $\tilde{\nu}$ production events and the indirect contribution from $\tilde{\chi}_2^0$ decays. Only $\tilde{\chi}_1^\pm\tilde{\chi}_1^\pm$ events with leptons coming from different parent charginos survive as a significant SUSY background.

To extract the slepton signal at points from domain I in Fig. 2.8b ($m_0 \gtrsim 0.5m_{1/2}$) with $m_{\tilde{L}} \sim 100$ GeV, just beyond of the LEP2 and Tevatron sparticle reaches, where the SM backgrounds are dominant, the selection **Set 0** is appropriate at low luminosity. The **Set 0'** is better adapted for the points from domain II ($m_0 \lesssim 0.5m_{1/2}$), see Table 7.1.

The expected number of signal and background events in this particular difficult region, after all cuts, is shown in Table 7.2. We also give the signal to background ratio and

Table 7.1. Low mass slepton selection criteria

	Set 0	Set 0'
$Isol <$	0.1	0.1
$p_T^{l_{1,2}} > (\text{GeV})$	20	20
$E_T^{miss} > (\text{GeV})$	50	50
$\Delta\phi(E_T^{miss}, l^+l^-) > (^0)$	160	160
No jets in $ \eta_{jet} < 4.5$ with $E_T^{jet} > (\text{GeV})$	30	30
No $M_{ll} \in M_Z \pm \delta m$ (GeV)	91 ± 5	91 ± 5
$\Delta\phi_{l+l-} > (^0)$	130	no cut

significance for slepton production and the same quantities for overall SUSY production.

It is clear that in this domain of parameter space, the slepton ($m_{\tilde{l}} \sim 100$ GeV) contribution to the finale state topology is only a modest one. The slepton signal can be detected from an excess of events over background expectations, but not from any particular kinematical feature. The S/B is about 0.3. Of the SM backgrounds, WW is the largest and essentially irreducible, $t\bar{t}$ and $Wt\bar{b}$ are comparable and at the same level as the signal after hard jet veto cuts. The main SUSY background is due to $\tilde{\chi}_1^\pm \tilde{\chi}_1^\mp$. For the point $m_0 = 85$ GeV, $m_{1/2} = 86$ GeV, from domain I, the total number of signal events N_S^{Sl-tot} is just due to direct slepton production, i.e. there are no indirect slepton contributions, but there are additional SUSY contributions to this topology.

For points with $m_0 \lesssim 0.5m_{1/2}$ (domain II), no $\Delta\phi_{l+l-}$ cut is applied so as to take advantage of all SUSY processes contributing to slepton production. N_S^{Sl-tot} in this case has contributions from both direct and indirect slepton production. The contribution from indirect slepton production is comparable to the direct one and helps to reach a 5σ significance level needed for slepton signal visibility. In this region the only backgrounds are SM contributions. The irreducible WW is still the dominant, and $Wt\bar{b}$ increases significantly.

To achieve the highest mass reach with $10^4 pb^{-1}$ a somewhat harder set of cuts is appropriate, (**Set 1** in Tab. 7.3). The reach in parameter space with $10^4 pb^{-1}$ is shown in Fig. 7.6; it corresponds to left-slepton masses up to $\simeq 160 - 180$ GeV, i.e. well above the LEP2 reach ($m_{\tilde{l}} \lesssim 95$ GeV). In the region $m_0 \lesssim 0.5m_{1/2}$ (domain II) the total slepton signal coincides with the overall SUSY signal, but for points from region $m_0 \gtrsim 0.5m_{1/2}$ (domain I) the additional SUSY processes contribute to the overall SUSY signal, but not to the slepton signal.

With $10^5 pb^{-1}$, a significantly higher slepton mass range becomes accessible. The average lepton transverse momentum and missing energy increasing with $m_{\tilde{l}}$ become significantly harder than for the main backgrounds. Harder kinematical cuts are therefore preferable. Slepton production becomes the main and ultimately the dominant contribution to this topology. We use four main different sets of cuts (Table 7.3) optimised for different regions of $(m_0, m_{1/2})$ parameters space. These sets are chosen taking into account the mass relations, production mechanisms and decay patterns discussed in section 2.2.

“**Set 2**” is used to explore the $m_{\tilde{l}_L} \sim 200$ GeV domain. The $t\bar{t}$, $Wt\bar{b}$ backgrounds are

Table 7.2: Expected number of direct (N_S^{Sl-dir}) and indirect ($N_S^{Sl-indir}$) slepton signal events, and SM (N_B^{SM}) and SUSY background (N_B^{SUSY}) events, after cuts, at 10^4 pb^{-1} .

The signal to background ratio N_S^{Sl-tot}/N_B^{tot} and significance of slepton signal $N_S^{Sl-tot}/\sqrt{N_S^{Sl-tot} + N_B^{tot}}$ are also given; the same for overall SUSY signal N_S^{SUSY}/N_B^{SM} , $N_S^{SUSY}/\sqrt{N_S^{SUSY} + N_B^{SM}}$.

$(m_0, m_{1/2}) \rightarrow$	(86,85)	(4,146)	(20,160)	(20,190)
	Set 0	Set 0'	Set 0'	Set 0'
$\tilde{l}\tilde{l}$	323	315	319	214
$\tilde{\chi}_1^\pm \tilde{\chi}_2^0$	14	45	48	40
$\tilde{\chi}_1^\pm \tilde{\chi}_1^\mp$	46	253	217	168
$\tilde{g}\tilde{q}$	13	8	—	—
$\tilde{q}\tilde{q}$	35	6	—	—
$\tilde{g}\tilde{g}$	0	2	—	—
WW	454	1212	1212	1212
Wtb	163	577	577	577
t \bar{t}	345	574	574	574
WZ	15	43	43	43
$\tau\tau$	15	15	15	15
N_S^{Sl-dir}	323	315	319	214
$N_S^{Sl-indir}$	—	314	265	208
N_S^{SUSY}	431	629	584	422
N_B^{SUSY}	108	—	—	—
N_B^{SM}	992	2421	2421	2421
N_S^{Sl}/N_B^{tot}	0.3	0.26	0.24	0.17
$N_S^{Sl-tot}/\sqrt{N_S^{Sl-tot} + N_B^{tot}}$	8.6	11.4	10.7	7.9
N_S^{SUSY}/N_B^{SM}	0.4	0.26	0.24	0.17
$N_S^{SUSY}/\sqrt{N_S^{SUSY} + N_B^{SM}}$	11.4	11.4	10.7	7.9

suppressed with hard cuts on p_T of the leptons, E_T^{miss} and the “jet veto”. This last cut eliminates entirely the backgrounds from strongly interacting sparticles. We keep events with small relative azimuthal angle between the leptons $\Delta\phi_{l+l-}$ mainly to improve the rejection of SM backgrounds, and to eliminate $\tilde{\chi}_1^\pm \tilde{\chi}_1^\mp$ production when it is necessary. The slepton S/B ratio is about 1.

“**Set 3**” is used for $m_{\tilde{l}_L} \sim 300 \text{ GeV}$ at points with $m_0 \lesssim 0.5m_{1/2}$, whilst for points with $m_0 \lesssim 0.5m_{1/2}$ “**Set 4**” is more appropriate, as the cross-sections are smaller. Furthermore, there is no source of indirect slepton production. “**Set 4**” is also used to explore the slepton mass range $300 \text{ GeV} \lesssim m_{\tilde{l}_L} \lesssim 350 \text{ GeV}$. “**Set 4'**” is used for masses $350 \text{ GeV} \lesssim m_{\tilde{l}_L} \lesssim 440 \text{ GeV}$, and “**Set 4''**” for $m_{\tilde{l}_L} \gtrsim 440 \text{ GeV}$. Details of the signal and background contribution at each simulated point can be found in [6].

Figure 7.6 summarizes the results of this study. At each point investigated the expected slepton signal significance, $n\sigma$, and the signal to background ratio (in parentheses) is given,

Table 7.3. High mass slepton selection criteria

	Set 1	Set 2	Set 3	Set 4	Set 4'	Set 4''
$Isol <$	0.1	0.1	0.1	0.1	0.1	0.03
$p_T^{l_{1,2}} > (\text{GeV})$	20	50	50	60	60	60
$E_T^{miss} > (\text{GeV})$	100	100	120	150	150	150
$\Delta\phi(E_T^{miss}, l^+l^-) > (^0)$	150	150	150	150	150	150
No jets in $ \eta_{jet} < 4.5$ with $E_T^{jet} > (\text{GeV})$	30	30	30	45	45	45
No $M_{ll} \in M_Z \pm \delta m$ (GeV)	91 ± 5	91 ± 5	91 ± 5	91 ± 5	91 ± 5	91 ± 5
$\Delta\phi_{l+l-} < (^0)$	130	130	130	130	140	130

for an integrated luminosity of 10^5 pb^{-1} . The 5σ reach is shown as well. Recall that the selection procedure has been optimised in terms of signal significance $N_S/\sqrt{N_S + N_B}$ to investigate the maximum slepton mass reach, and not in terms of sample purity (i.e. S/B ratio). The reason is that if SUSY were found at Fermilab where \tilde{g}/\tilde{q} masses up to $\lesssim 400 - 450 \text{ GeV}$ can be probed, sleptons can be probed at the Tevatron and LEP2 only up to a mass of $m_{\tilde{l}} \lesssim 100 \text{ GeV}$, thus the main task of LHC would be to explore slepton spectroscopy, with masses up to $m_{\tilde{q}/\tilde{g}} \lesssim 400 \text{ GeV}$. Figure 7.7 shows the same information as Fig. 7.6, but in terms of left slepton and lightest neutralino LSP masses. The domain that can be explored extends up to $m_{\tilde{L}} \sim 340 \text{ GeV}$ for all allowed $m_{LSP} (< 200 \text{ GeV})$, and up to $m_{\tilde{L}} \sim 340 - 440 \text{ GeV}$ only if $m_{LSP} \gtrsim (0.45 - 0.6) \cdot m_{\tilde{L}}$ for a given $m_{\tilde{L}}$. The mass reach for right sleptons is up to 340 GeV . As the main SM background is WW production, to study the stability of our results we assumed a 50% uncertainty in the WW cross-section. Figure 7.8 shows how much the 5σ reach boundary would be modified if the WW cross-section were twice as large as predicted by PYTHIA.

A very interesting aspect of slepton searches at LHC from the cosmological point of view is that, in this topologically simplest channel, the explorable domain for 10^5 pb^{-1} almost coincides with the regions of parameter space where the LSP would be cosmologically relevant (Figs. 7.6 and 7.7). The boundaries for the domains we can probe in slepton searches and the neutralino dark matter Ωh^2 density contours have shapes similar to slepton isomass curves as both are largely determined by slepton masses. In particular, neutralino annihilation is governed by slepton exchange with $\sigma_{ann} \sim 1/m_{\tilde{l}}^4$. Too large a slepton mass would induce too small an annihilation cross-section and thus too large a relic density which would overclose the Universe. The Ωh^2 range preferred by mixed dark matter scenarios is for $0.15 \lesssim \Omega h^2 \lesssim 0.4$ (with the Hubble scaling constant $0.5 \lesssim h^2 \lesssim 0.8$) which corresponds to a slepton mass range $100 \text{ GeV} \lesssim m_{\tilde{l}} \lesssim 250 \text{ GeV}$, (see [11], [37].)

We conclude that to search for direct production of sleptons the most appropriate channel is $2 \text{ leptons} + E_T^{miss}$ and no jets. In regions of low $m_0, m_{1/2}$, just beyond the sparticle reaches at LEP2 and the Tevatron, the slepton signal can be detected, but the search will be difficult as \tilde{l} is not the dominant contribution to this final state. In significant parts of the explorable $(m_0, m_{1/2})$ space, however, direct slepton pair production is the main contribution to this final state, with non-negligible contributions from indirect production too, mostly through $\tilde{\chi}_1^\pm, \tilde{\chi}_2^0$. The inclusion of this indirect slepton production improves the mass reach. With 10^4 pb^{-1} luminosity, CMS is sensitive up to $m_{\tilde{L}} \lesssim 160$

GeV. With 10^5 pb^{-1} luminosity the reach extends up to $m_{\tilde{l}_L} \sim 340 \text{ GeV}$ for all allowed $m_{LSP} (< 200 \text{ GeV})$, and up to $m_{\tilde{l}_L} \sim 340\text{--}440 \text{ GeV}$ if $m_{LSP} \sim (0.45\text{--}0.6) \cdot m_{\tilde{l}_L}$ for a given $m_{\tilde{l}_L}$. Throughout the domain where the slepton signal should be detectable, it is always contaminated by backgrounds. The dominant background is always WW production. In the $m_{\tilde{l}_L} \sim 100 \text{ GeV}$ domain the WW background exceeds the number of signal events, whilst for $m_{\tilde{l}_L} \gtrsim 200 \text{ GeV}$ the number of background events is comparable or smaller than the expected number of signal events. The “jet veto” cut effectively eliminates the \tilde{g}, \tilde{q} backgrounds, but also the potentially important indirect slepton production from \tilde{g} and \tilde{q} . This issue requires a separate study.

In the region $m_0 \lesssim 0.45 \cdot m_{1/2}$ sleptons decay directly into the LSP and sneutrinos thus decay invisibly, $\tilde{\nu} \rightarrow \tilde{\chi}_1^0 \nu$. In this portion of parameter space only charged sleptons can be detected. As right sleptons are also significantly lighter than left ones they are mostly eliminated by the hard selection cuts needed to suppress the backgrounds, so mainly left sleptons are present in the final event sample. Left sleptons will thus be detectable in the entire region where a slepton signal is seen, whilst right sleptons will be detectable mainly in domain $m_0 \gtrsim 0.45 \cdot m_{1/2}$. Sneutrinos will contribute to this final state only in a very limited area with $m_{1/2} \lesssim 160 \text{ GeV}$ and $m_0 \lesssim 150 \text{ GeV}$.

The search for sleptons is important and significant, as LEP2 and the Tevatron can only explore the slepton mass range up to $m_{\tilde{l}_L} \simeq 100 \text{ GeV}$. The domain of $(m_0, m_{1/2})$ parameter space explorable through this simplest experimental channel, with two *same-flavor, opposite-sign leptons + E_T^{miss} + no jets*, covers almost the entire domain of parameter space where SUSY is plausible in general terms (minimal fine-tuning) and covers all of the parameter space where SUSY would be of cosmological significance (at least for $\tan\beta = 2, A_0 = 0, \mu < 0$), with $> 10^4 \text{ pb}^{-1}$ of integrated luminosity.

Slepton mapping of parameter space

mSUGRA-MSSM ; $\tan \beta = 2$, $A_0 = 0$, $\mu < 0$

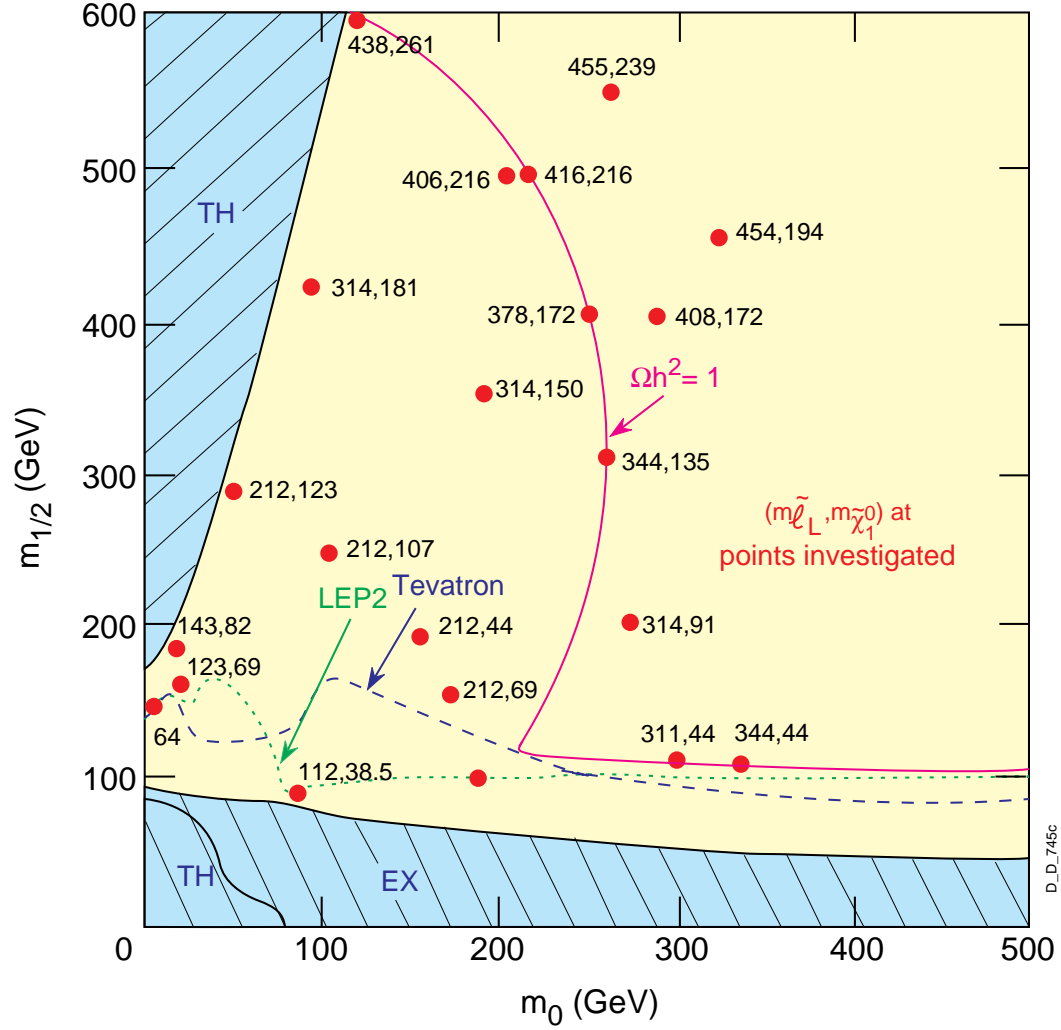


Figure 7.1: Points in mSUGRA parameter space where slepton production has been studied. The numbers at each point give corresponding values of $m_{\tilde{L}}$ and $m_{\tilde{\chi}_1^0}$. The shaded areas represent excluded regions on the bases of LEP and Tevatron data. The dashed lines represent the expected reach with sparticle searches of LEP2 and Tevatron with 1 fb^{-1} . The $\Omega h^2 = 1$ absolute upper limit contour for neutralino dark matter is also shown.

E_T^{miss} distributions at points:

$$m_0 = 86 \text{ GeV}, \quad m_{1/2} = 85 \text{ GeV:}$$

$$m_{\tilde{l}_L} = 112 \text{ GeV}, \quad m_{\tilde{l}_R} = 98 \text{ GeV},$$

$$m_{\tilde{\nu}} = 93 \text{ GeV}$$

$$m_0 = 97 \text{ GeV}, \quad m_{1/2} = 420 \text{ GeV:}$$

$$m_{\tilde{l}_L} = 314 \text{ GeV}, \quad m_{\tilde{l}_R} = 192 \text{ GeV},$$

$$m_{\tilde{\nu}} = 308 \text{ GeV}$$

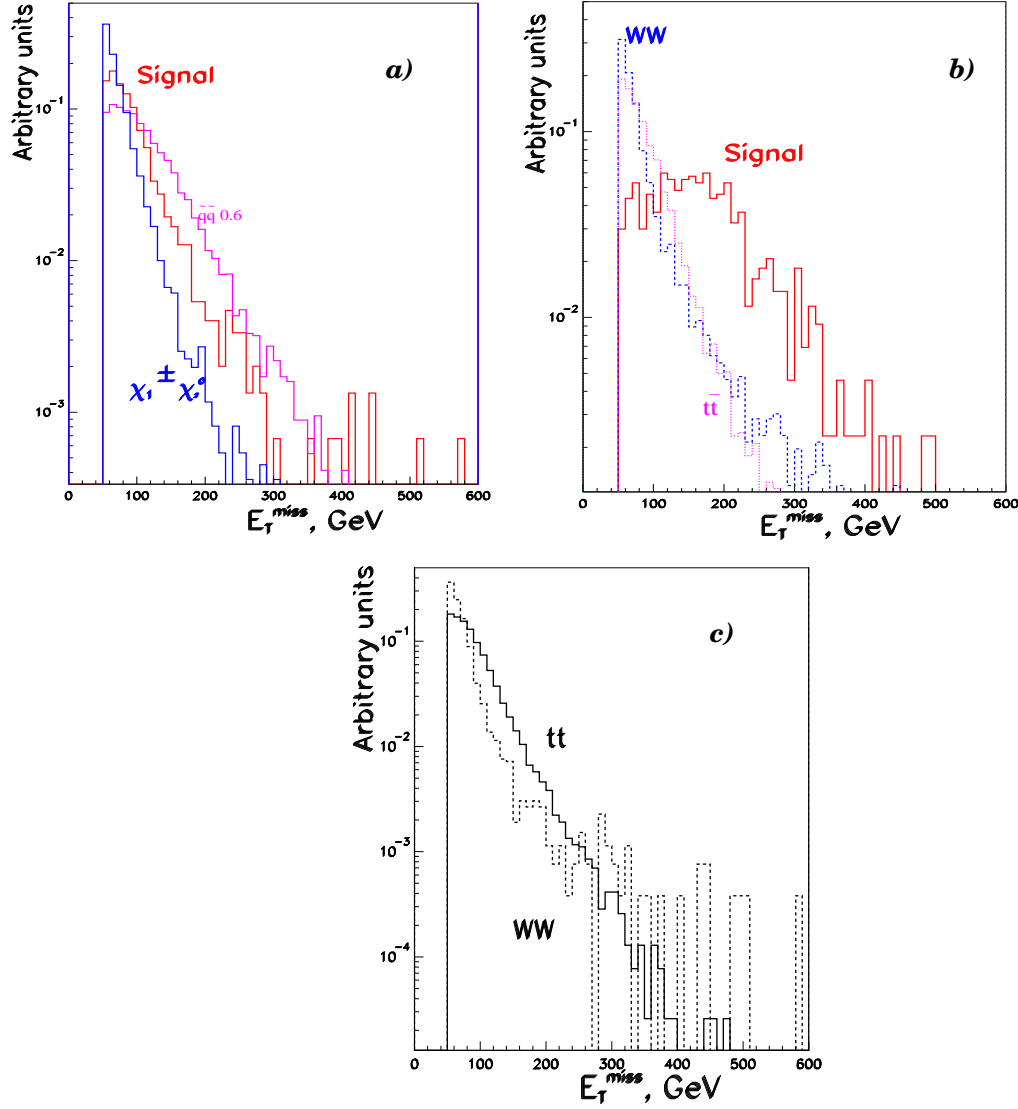


Figure 7.2: E_T^{miss} distribution for slepton signal (DY production), SUSY backgrounds ($\tilde{g}, \tilde{q}, \tilde{\chi}_1^\pm \tilde{\chi}_2^0$) at two parameter space points: a) $m_0 = 86 \text{ GeV}, m_{1/2} = 85 \text{ GeV}$, b) $m_0 = 97 \text{ GeV}, m_{1/2} = 420 \text{ GeV}$ and c) the main SM backgrounds (WW, $t\bar{t}$).

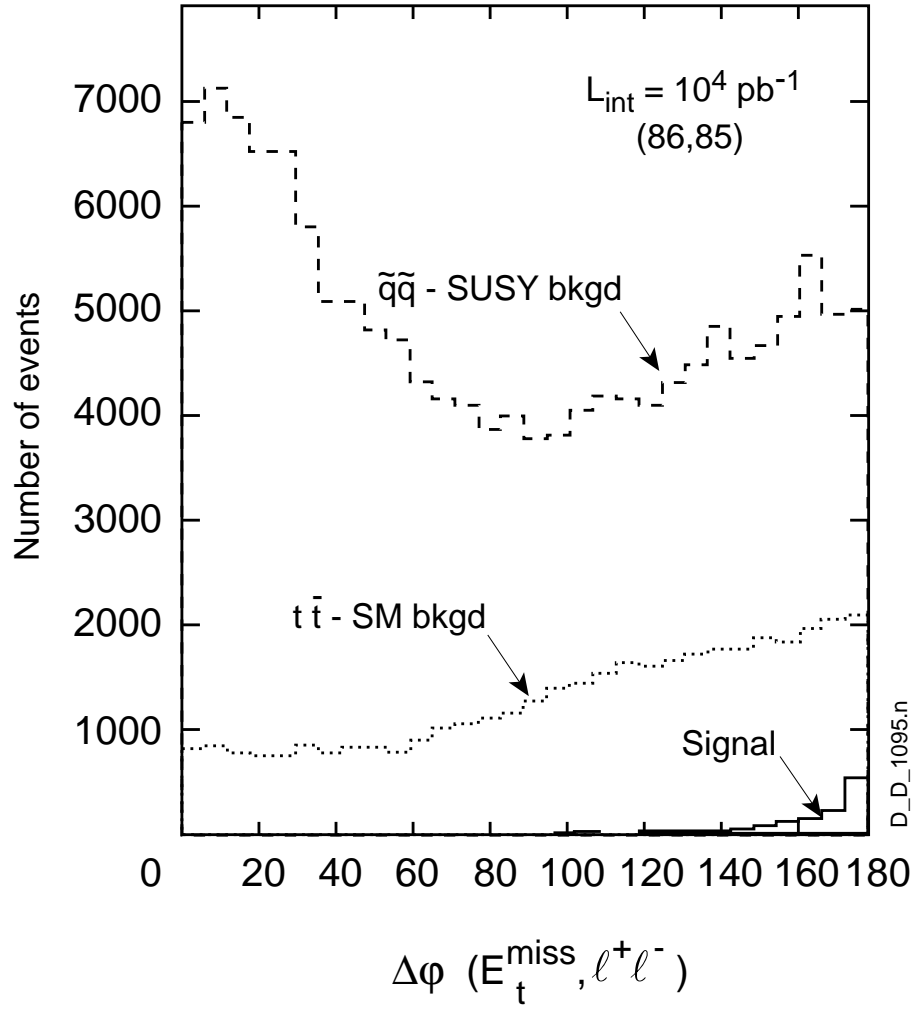


Figure 7.3: Relative azimuthal angle between E_T^{miss} and the resulting dilepton momentum for the slepton signal and main SM and SUSY backgrounds in $2\text{leptons} + E_T^{\text{miss}} + \text{nojets}$ final states.

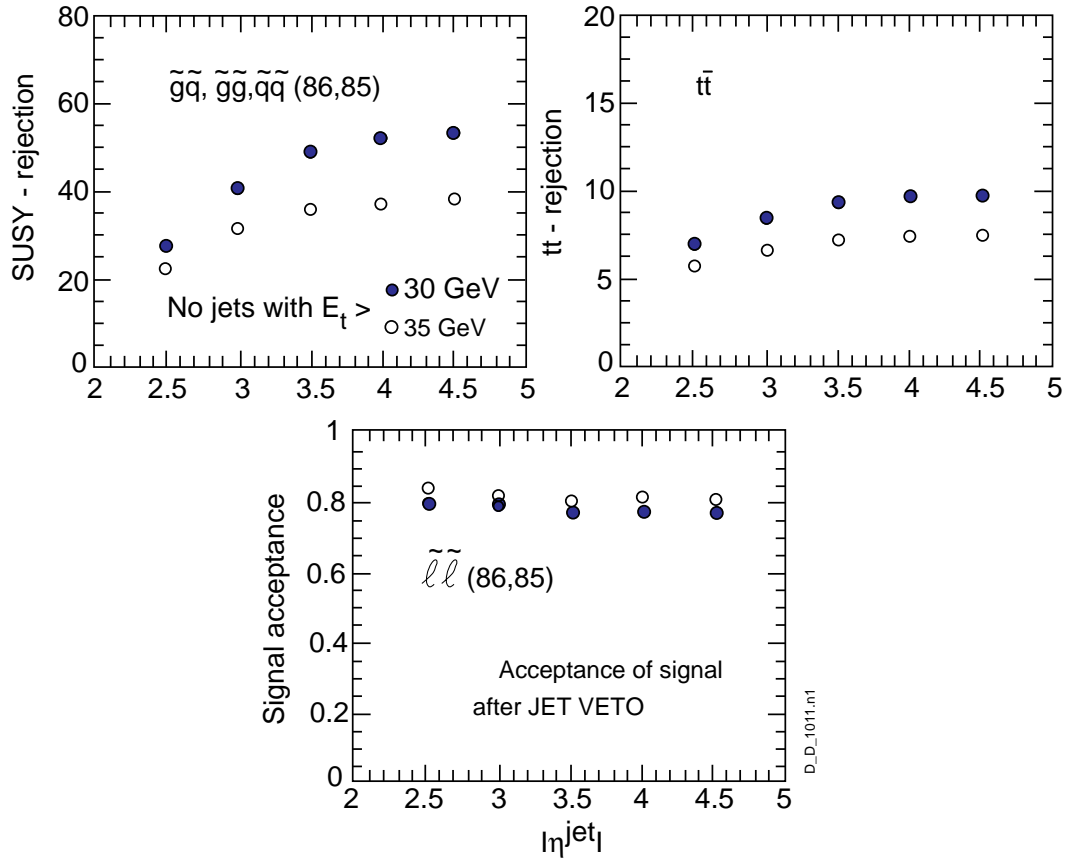


Figure 7.4: Rejection factors a) for internal SUSY backgrounds, b) for SM backgrounds by central “jet veto”, and c) slepton signal acceptance, as a function of jet rapidity acceptance $|\eta_{jet}|$ and for two jet detection thresholds.

Relative azimuthal angle between the two leptons

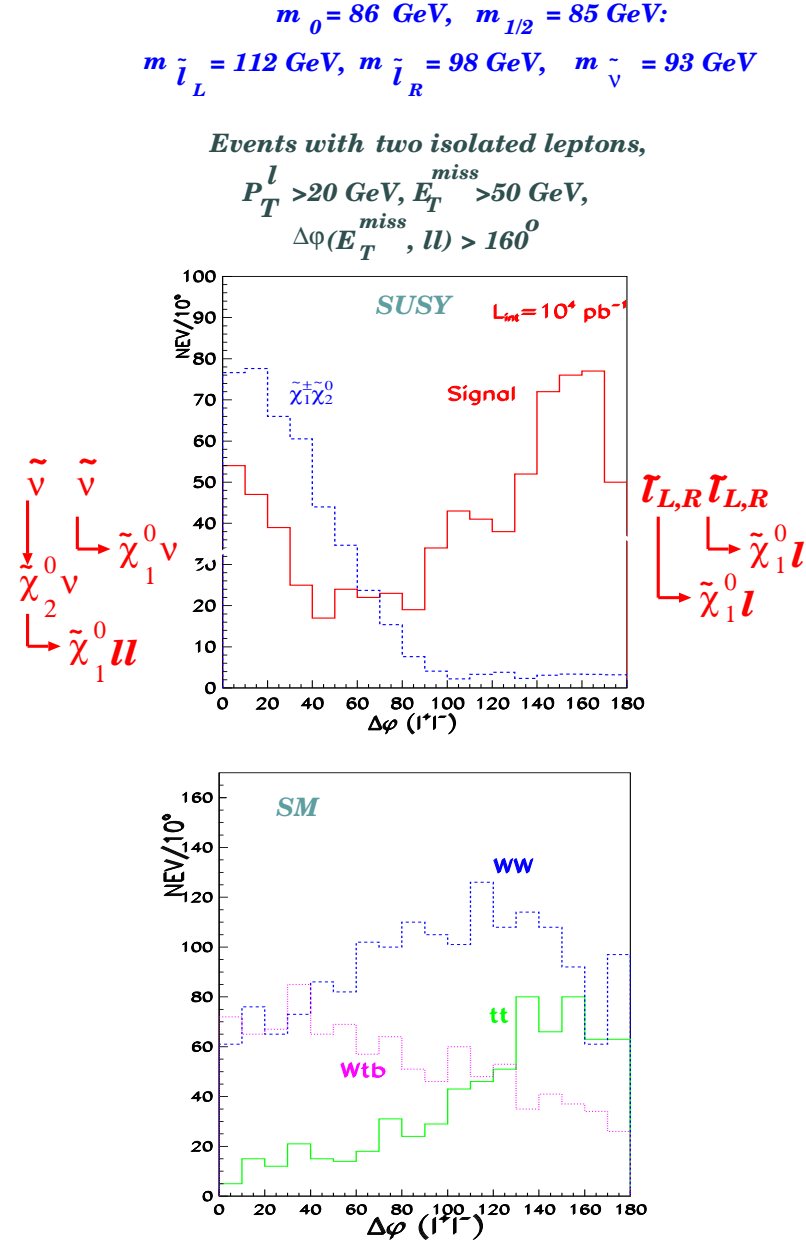


Figure 7.5: Relative azimuthal angle between two same-flavor opposite-sign leptons at one point on parameter space, a) for the various contributions to the SUSY slepton signal and for a SUSY background ($\tilde{\chi}_1^\pm \tilde{\chi}_2^0$), and b) for the main SM backgrounds, in $2leptons + E_T^{\text{miss}}$ + no jets final states.

Slepton mapping of parameter space

m SUGRA-MSSM ; $\tan \beta = 2$, $A_0 = 0$, $\mu < 0$

Significance of expected excess of events in 2 lepton
final state over SM + SUSY bkgd with 10^5 pb^{-1}

5 σ contour, $\sigma = S / \sqrt{S+B}$

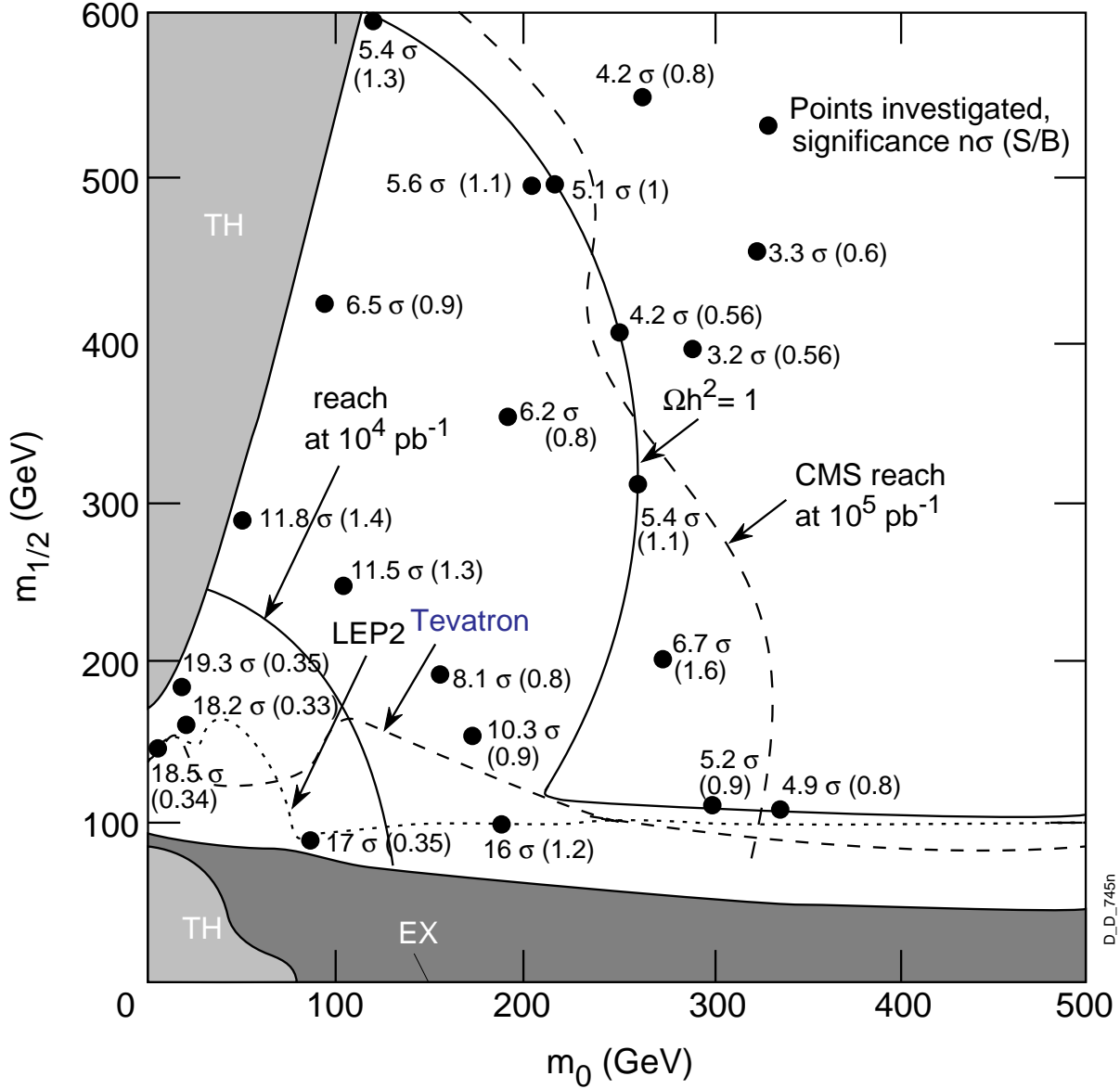


Figure 7.6: Expected reach in parameter space for slepton searches in the $2\text{leptons} + E_T^{\text{miss}} + \text{no jets}$ final states with 10^4 pb^{-1} and 10^5 pb^{-1} in CMS. The reach is given as a 5 σ contour. At each point investigated the slepton signal significance is indicated as $n\sigma$, and the S/B ratio is given in parenthesis, where B is the full SM + SUSY background to the slepton signal. The cosmological absolute upper bound ($\Omega_{\tilde{\chi}_1^0} = 1$, $h = 1$) density contour for neutralino dark matter $\Omega h^2 = 1$ is indicated.

Explorable range of $\tilde{\ell}, \tilde{\chi}_1^0$ masses in slepton searches in CMS

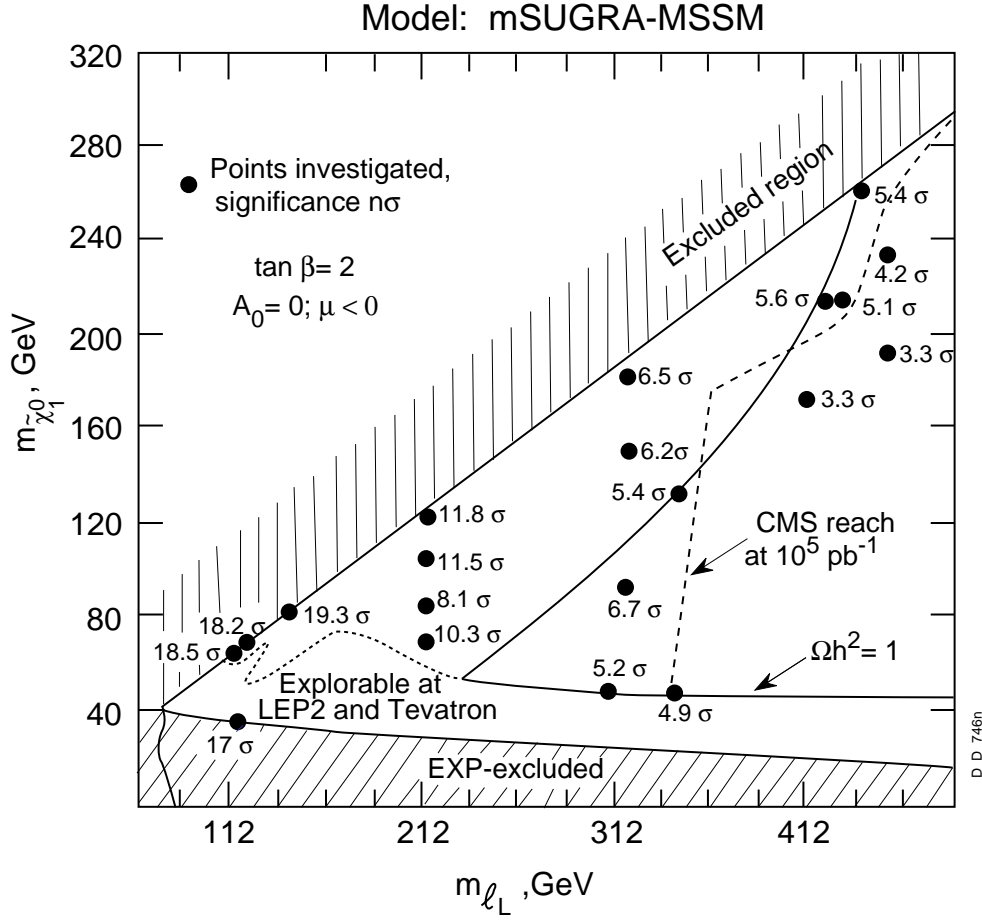


Figure 7.7: Same mapping as in Fig. 7.6, but in terms of masses of the left slepton and the LSP.

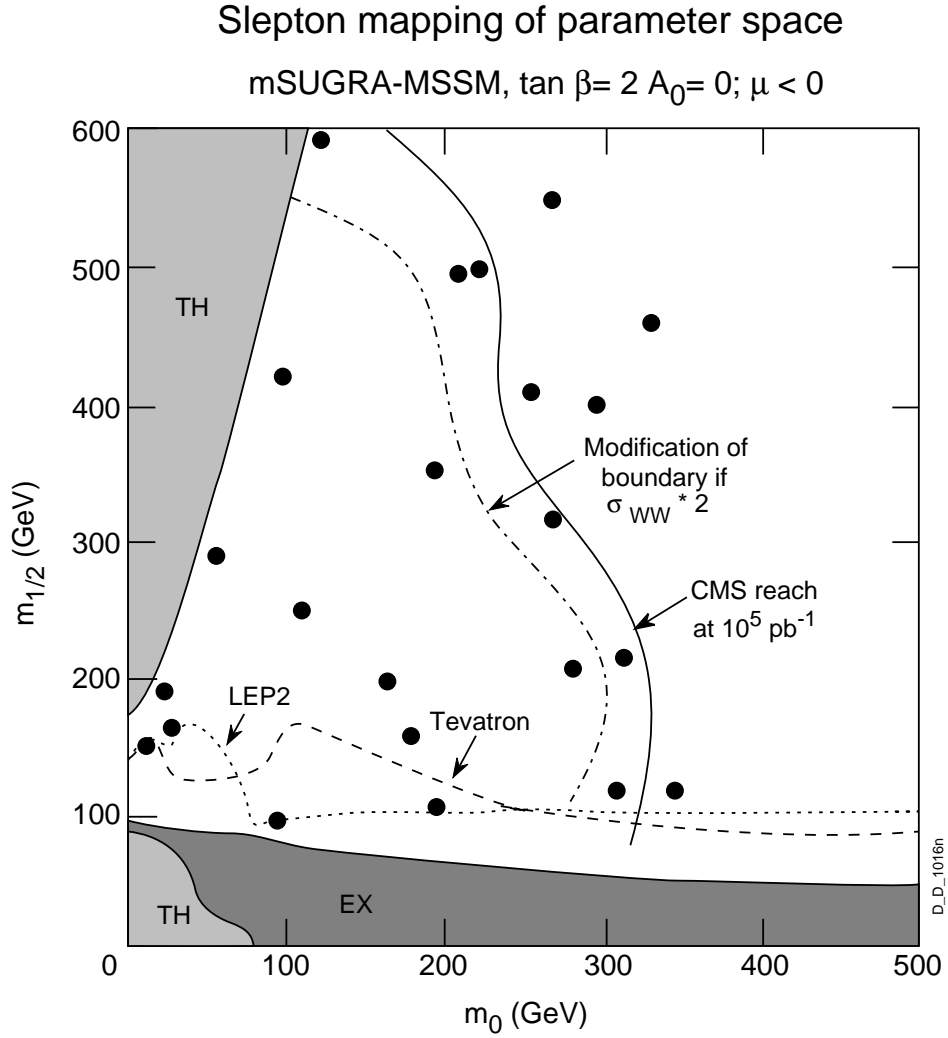


Figure 7.8: Modification of the 5σ reach in slepton searches if the production cross-section for the main SM background of WW pair production is increased by a factor of 2.

8 Exclusive 3 leptons + no jets + E_T^{miss} channel – search for chargino/neutralino pair production

Direct production of $\tilde{\chi}_1^\pm \tilde{\chi}_2^0$ followed by leptonic decays of both sparticles (see section 2.1) gives three high- p_T isolated leptons accompanied by missing energy. These events are free from jet activity except for those coming from initial-state QCD radiation. Therefore we search for $\tilde{\chi}_1^\pm \tilde{\chi}_2^0$ pair production in 3 leptons + no jets + E_T^{miss} final states [8].

We have considered the following SM processes contributing to the background: WZ, ZZ, $t\bar{t}$, Wtb , $Zb\bar{b}$, $b\bar{b}$ with the cross-sections $\sigma_{WZ} = 26$ pb, $\sigma_{ZZ} = 15$ pb, $\sigma_{t\bar{t}} = 670$ pb for a top mass of 170 GeV, $\sigma_{Wtb} = 160$ pb, $\sigma_{Zb\bar{b}} = 600$ pb, $\sigma_{b\bar{b}} = 500$ μ b. Three leptons in the final state are obtained by folding the appropriate leptonic decay modes. We have forced $Z \rightarrow l^+ l^-$, $W^\pm \rightarrow l^\pm \nu$ and $b \rightarrow cl\nu$ decays, where $l = \mu, e, \tau$. In case of $t\bar{t}$ and Wtb only one W has been forced. These SM backgrounds, except ZZ production, can be suppressed by requiring that all three leptons be isolated, and vetoing central jets. ZZ events contain four isolated leptons and asking for exactly three isolated leptons in the event leaves only a small fraction of the ZZ continuum, when one of the leptons escapes detector acceptance. The WZ, ZZ and $Zb\bar{b}$ backgrounds can be suppressed by removing events with a dilepton invariant mass close to the Z mass. At each investigated point in the $(m_0, m_{1/2})$ plane we have studied all SUSY production processes which can lead ultimately to three leptons in the final state. These are the strong interaction production of $\tilde{g}\tilde{g}$, $\tilde{g}\tilde{q}$, $\tilde{q}\tilde{q}$ pairs; associated production of $\tilde{g}\tilde{\chi}$, $\tilde{q}\tilde{\chi}$ pairs; chargino-neutralino $\tilde{\chi}\tilde{\chi}$ pair production, and slepton pair production, $\tilde{l}\tilde{l}$, $\tilde{l}\tilde{\nu}$, $\tilde{\nu}\tilde{\nu}$. The SUSY event sample with three high- p_T isolated leptons is dominated by strong production; but, of course, the jet veto requirement is very efficient in reducing \tilde{g} and \tilde{q} events which in their cascade decays produce many central high- E_T jets. It has to be pointed out that SUSY events other than the directly produced $\tilde{\chi}_1^\pm \tilde{\chi}_2^0$ and which survive all selection criteria, may still contain some $\tilde{\chi}_1^\pm \tilde{\chi}_2^0$'s produced in cascade decays of heavier sparticles. These events can be considered as an “indirect” $\tilde{\chi}_1^\pm \tilde{\chi}_2^0$ signal, a situation similar to the one encountered in discussing slepton searches.

In Fig. 8.1 we show the fully simulated SUSY points in the $(m_0, m_{1/2})$ plane, as representatives of various regions according to the predominant or characteristic decay modes. In order to illustrate event kinematics we choose three points from different $(m_0, m_{1/2})$ regions among those shown in Fig. 8.1:

- S1 $(m_0, m_{1/2}) = (100 \text{ GeV}, 100 \text{ GeV})$ with
 $M(\tilde{\chi}_1^\pm) \simeq M(\tilde{\chi}_2^0) = 98 \text{ GeV}$, $M(\tilde{\chi}_1^0) = 45 \text{ GeV}$,
 $M(\tilde{g}) = 294 \text{ GeV}$, $M(\tilde{q}) = 270 \text{ GeV}$
- S2 $(m_0, m_{1/2}) = (2000 \text{ GeV}, 175 \text{ GeV})$ with
 $M(\tilde{\chi}_1^\pm) \simeq M(\tilde{\chi}_2^0) = 154 \text{ GeV}$, $M(\tilde{\chi}_1^0) = 76 \text{ GeV}$,
 $M(\tilde{g}) = 551 \text{ GeV}$, $M(\tilde{q}) = 2032 \text{ GeV}$
- S3 $(m_0, m_{1/2}) = (100 \text{ GeV}, 400 \text{ GeV})$ with
 $M(\tilde{\chi}_1^\pm) \simeq M(\tilde{\chi}_2^0) = 341 \text{ GeV}$, $M(\tilde{\chi}_1^0) = 172 \text{ GeV}$,
 $M(\tilde{g}) = 983 \text{ GeV}$, $M(\tilde{q}) = 861 \text{ GeV}$

Figure 8.2 shows the $d\sigma/dp_T^l$ distribution in the three-lepton event sample with $p_T^l > 15$ GeV. Distributions are shown for signal and SM background. At this stage the dominant SM backgrounds are $t\bar{t}$ and $Zb\bar{b}$. For high $m_{1/2}$, e.g. point S3, the lepton p_T cut can be set at 20 GeV. The loss in signal acceptance is $\sim 12\%$ compared to a 15 GeV cut, whilst

$t\bar{t}$ and $Zb\bar{b}$ are reduced by an additional factor of ~ 2 .

To suppress background events with leptons originating from semileptonic decays of b -quarks, we apply tracker isolation, requiring all three leptons to be isolated. If there is no charged track with p_T greater than a certain threshold p_T^{cut} in a cone of $R = \sqrt{\Delta\eta^2 + \Delta\phi^2} = 0.3$ about the lepton direction, it is considered as isolated. Figure 8.3 a shows the lepton isolation rejection factor against $t\bar{t}$ background versus the p_T^{cut} on charged tracks. The two curves correspond to two different instantaneous luminosity regimes, $L = 10^{33} \text{ cm}^{-2}\text{s}^{-1}$ and $L = 10^{34} \text{ cm}^{-2}\text{s}^{-1}$. In the latter case we have superimposed 15 “hard” pile-up events. Figure 8.3 b shows signal acceptance versus p_T^{cut} . We choose $p_T^{cut} = 1.5 \text{ GeV}$ and 2 GeV for low and high luminosity running, respectively. The corresponding rejection factors against $t\bar{t}$ are about 60 and 50, whereas signal acceptance decreases from about 90% to 70%. The next requirement is the central jet veto, which allows us reject the internal SUSY background coming from \tilde{g} and \tilde{q} cascade decays overwhelming $\tilde{\chi}_1^\pm \tilde{\chi}_2^0$ direct production. This cut also reduces some SM backgrounds. In Fig. 8.4 we show jet multiplicity and jet E_T distributions for signal, SUSY $\tilde{g}\tilde{g}$, $\tilde{g}\tilde{q}$, $\tilde{q}\tilde{q}$ background events at point S1, and for the $t\bar{t}$ background. Since at this $(m_0, m_{1/2})$ point the gluino is heavier than the squark, it decays to a squark-quark pair. Therefore gluino events are richer in jets compared to squark events. Figure 8.5 shows jet veto rejection factors against $\tilde{g}\tilde{g}$, $\tilde{g}\tilde{q}$, $\tilde{q}\tilde{q}$ and $t\bar{t}$ backgrounds and the signal acceptance as a function of jet pseudorapidity, $|\eta^{jet}|$, for two jet detection thresholds: $E_T^{jet} > 25 \text{ GeV}$ and $E_T^{jet} > 30 \text{ GeV}$. As the jet veto region is decreased down to $|\eta^{jet}| \simeq 3.5$, the rejections/acceptance are not too sensitive to jet rapidity coverage, but below this value of $|\eta^{jet}|$, rejection factors decrease rapidly, degrading significantly the separation of direct $\tilde{\chi}_1^\pm \tilde{\chi}_2^0$ production from internal SUSY and SM backgrounds. The reconstruction of jets at $|\eta^{jet}| \sim 3.5$ implies calorimetric coverage up to $|\eta| \sim 4.3$ at least, as the jets are collected in a cone of $\Delta R = 0.8$. With increasing m_0 and/or $m_{1/2}$ squarks and/or gluinos become heavier. Thus jets are harder and SUSY events are easier to suppress by a jet veto with relaxed requirement on $|\eta^{jet}|$ and E_T^{jet} . Furthermore, for the signal events the QCD radiation becomes harder ($\tilde{\chi}_1^\pm$, $\tilde{\chi}_2^0$ are more massive) and the low production cross-section requires the highest LHC luminosity, with an event pile-up contaminated environment. For this region, the jet veto threshold can be set with E_T^{jet} as high as 50 GeV and is justified by the need to suppress the SM (mainly $t\bar{t}$) background.

Despite the fact that missing energy is always present in SUSY signals (at least in R -parity conserving models), for some regions of mSUGRA parameter space, it is advantageous not to apply any specific cut on it. Figure 8.6 shows the distribution of E_T^{miss} in events with three isolated high- p_T leptons and no jets for the signal and the two main SM backgrounds: $t\bar{t}$ and WZ . For point S1 the shape of the distribution is very similar to that of the background and therefore no cut on E_T^{miss} is applied. For point S3 requiring $E_T^{miss} > 80 \text{ GeV}$ significantly reduces $t\bar{t}$ and WZ backgrounds whilst keeping more than 75% of signal events [8].

For WZ background suppression, which after all the previous requirements remains the dominant SM background, an M_Z cut is necessary. In the signal events, the shape of the (same-flavor opposite-sign) dilepton invariant mass M_{l+l-} distribution is determined by the $\tilde{\chi}_2^0$ decay kinematics and has a very sharp edge. Figure 8.7 shows the M_{l+l-} distribution for the signal at three parameter space points S1, S2, S3 and for WZ events. In events having all leptons of the same flavor, the combinatorial background obscures the sharp mass edge in the signal events. A rejection factor of ~ 17 for WZ is obtained by

Table 8.1: Selection criteria

Set 1 appropriate for $m_{1/2} \lesssim 140$ GeV	p_T cut	$3l$ with $p_T^l > 15$ GeV in $ \eta^l < 2.4(2.5)$
	Isolation	No track with $p_T > 1.5$ GeV in $R = 0.3$
	Jet veto	No jet with $E_T^{jet} > 25$ GeV in $ \eta^{jet} < 3.5$
	Z -mass cut	$M_{l+l-} < 81$ GeV
Set 2 appropriate for $140 \text{ GeV} \lesssim m_{1/2} \lesssim 180$ GeV	p_T cut	$3l$ with $p_T^l > 15$ GeV in $ \eta^l < 2.4(2.5)$
	Isolation	No track with $p_T > 1.5$ GeV in $R = 0.3$
	Jet veto	No jet with $E_T^{jet} > 30$ GeV in $ \eta^{jet} < 3$
	Z -mass cut	$M_{l+l-} < 81$ GeV
Set 3 appropriate for $180 \text{ GeV} \lesssim m_{1/2} \lesssim 300$ GeV	p_T cut	$3l$ with $p_T^l > 15$ GeV in $ \eta^l < 2.4(2.5)$
	Isolation	No track with $p_T > 2$ GeV in $R = 0.3$
	Jet veto	No jet with $E_T^{jet} > 40$ GeV in $ \eta^{jet} < 3$
	missing E_T	$E_T^{miss} > 50$ GeV
	Z -mass cut	$M_Z \pm 10$ GeV
Set 4 appropriate for $m_{1/2} \gtrsim 300$ GeV	p_T cut	$3l$ with $p_T^l > 20$ GeV in $ \eta^l < 2.4(2.5)$
	Isolation	No track with $p_T > 2$ GeV in $R = 0.3$
	Jet veto	No jet with $E_T^{jet} > 50$ GeV in $ \eta^{jet} < 3$
	missing E_T	$E_T^{miss} > 80$ GeV
	Z -mass cut	$M_Z \pm 10$ GeV

removing events with $M_{l+l-} > M_Z - 10$ GeV, whilst the small loss of signal events, $\lesssim 10\%$ for point S1, comes from events when all three leptons have the same flavor. However, for higher values of $m_{1/2}$, e.g. point S3, the endpoint of the M_{l+l-} distribution is above the Z peak; in this case we cut only events falling within the Z mass window: $M_Z - 10 \text{ GeV} < M_{l+l-} < M_Z + 10 \text{ GeV}$.

On the basis of the above considerations we adopt four sets of selection criteria, appropriate for different $(m_0, m_{1/2})$ regions, given in Table 8.1.

The $m_{1/2}$ boundaries are approximate and, for optimal cuts, they depend also on m_0 .

Except for Set 4, which we apply for rather massive $\tilde{\chi}_1^\pm \tilde{\chi}_2^0$, the p_T cuts on leptons are the same, i.e. $p_T^l > 15$ GeV. Set 1 and Set 2 are appropriate for the regions where the signal is accessible already at low luminosity. In the regions where we apply the cuts of Set 3 or Set 4 a high luminosity is required, as they correspond to smallest cross-sections; the luminosity determines the isolation requirement. With increasing $m_{1/2}$ the jet veto is relaxed, varying the E_T^{jet} threshold from 25 to 50 GeV. A cut on E_T^{miss} is applied only for Set 3 and Set 4; and finally, the M_Z cut is looser for higher $m_{1/2}$.

Table 8.2 gives the SM background cross-sections for these selection criteria after each cut. The two main SM backgrounds surviving these cuts are WZ and $t\bar{t}$. With Set 1 and Set 2 the dominant background is WZ and with Set 3 and Set 4 it is $t\bar{t}$.

Details on each simulated point can be found in [8]. The signal significance is defined as the number of signal events divided by the square root of all events (SUSY + SM) passing our selection criteria. With this definition we give: i) evidence for existence of Supersymmetry in $3l + no\ jets + E_T^{miss}$ channel; ii) overall evidence for $\tilde{\chi}_1^\pm \tilde{\chi}_2^0$ production and iii) evidence for direct production of $\tilde{\chi}_1^\pm \tilde{\chi}_2^0$. The ratio of direct $\tilde{\chi}_1^\pm \tilde{\chi}_2^0$ events over other

Table 8.2: SM background cross-sections (in fb) at each step of applied cuts.

Set of cuts	Cuts	WZ	ZZ	$t\bar{t}$	Wtb	Zbb	bb
Set 1	p_T^l	111	21.7	2544	139.1	731	9300
	Isolation	102	19.7	39.8	4.09	28.8	< 0.30
	Jet veto	73.8	11.6	4.12	1.71	14.6	< 0.15
	M_Z	4.19	0.89	2.18	0.86	0.76	< 0.15
Set 2	p_T^l	111	21.7	2544	139.1	731	9300
	Isolation	102	19.7	39.8	4.09	28.8	< 0.30
	Jet veto	76.1	12.7	4.84	1.90	16.1	< 0.15
	M_Z	4.49	0.99	2.48	1.05	0.91	< 0.15
Set 3	p_T^l	111	21.7	2544	139.1	731	9300
	Isolation	75.4	14.7	46.3	4.82	32.9	< 0.45
	Jet veto	51.3	8.69	4.77	1.91	15.7	< 0.40
	E_T^{miss}	22.0	2.61	3.01	0.48	1.42	< 0.01
	M_Z	1.93	0.35	2.63	0.40	0.06	< 0.01
Set 4	p_T^l	88.4	16.6	1330	65.2	378	2800
	Isolation	60.5	11.4	19.0	1.33	10.3	< 0.04
	Jet veto	46.4	7.92	3.25	0.53	4.78	< 0.04
	E_T^{miss}	5.77	0.68	0.73	0.05	0.30	< 0.001
	M_Z	0.45	0.09	0.60	< 0.05	< 0.04	< 0.001

events surviving the cuts, $N_{\tilde{\chi}_1^\pm \tilde{\chi}_2^0}^{dir} / (N_{ALL} - N_{\tilde{\chi}_1^\pm \tilde{\chi}_2^0}^{dir})$, is also given. All investigated points are analyzed in a similar manner and 5σ significance contours are obtained in the $(m_0, m_{1/2})$ plane, as shown in Fig. 8.8.

In the regions of small m_0 and $m_{1/2}$ ($\lesssim 200$ GeV and $\lesssim 150$ GeV, respectively) indirectly produced $\tilde{\chi}_1^\pm \tilde{\chi}_2^0$ events contribute significantly in the $3l + no\ jets + E_T^{miss}$ channel. However, this contribution is expected to be less than $\sim 15\%$ of the overall $\tilde{\chi}_1^\pm \tilde{\chi}_2^0$ production. Therefore, we can give 5σ significance contours for direct $\tilde{\chi}_1^\pm \tilde{\chi}_2^0$ production.

From Fig. 8.8 one can see that at a low integrated luminosity of $L_{int} = 10^4$ pb $^{-1}$ the direct production of $\tilde{\chi}_1^\pm \tilde{\chi}_2^0$ can be distinguished from background up to $m_{1/2} \lesssim 150$ GeV for all m_0 . A further increase of luminosity up to $L_{int} = 10^5$ pb $^{-1}$ extends the explorable region only by about $10 \div 20$ GeV for $m_0 \gtrsim 120$ GeV. However, for $m_0 \lesssim 120$ GeV the gain in parameter space is much larger – up to $m_{1/2} \lesssim 420$ GeV, reflecting the more advantageous behavior of the production cross-section times branching ratio shown in Fig. 2.4.

It should be pointed out that the internal SUSY backgrounds are particularly dangerous for small m_0 , $m_{1/2}$, in the region $m_0 \lesssim 200$ GeV, $m_{1/2} \lesssim 150$ GeV, generating a background higher or comparable to the SM contribution because of the high production cross-sections of the relatively light gluinos and squarks. Softness of these gluino/squark events makes it difficult to suppress them below the SM level, even with a very strict jet veto requirement (selection criteria Set 1). For some regions of the $(m_0, m_{1/2})$ parameter plane, chargino/neutralino and slepton pair productions are comparable to gluino/squark contributions. As m_0 and $m_{1/2}$ increase, more massive gluinos and squarks result in

harder jets, and decreased cross-sections, and hence the SUSY background becomes negligible. At the 5σ boundary with an integrated luminosity of 10^5 pb^{-1} , background events dominantly consist of SM processes. At this boundary the signal to background ratio is expected to be $\gtrsim 0.20$ with about 150 signal events ($L_{int} = 10^5 \text{ pb}^{-1}$) for $m_0 \gtrsim 120 \text{ GeV}$. In this region the dominant SM background is WZ production which cannot be suppressed by a stronger jet veto or lepton isolation requirements. For $m_0 \lesssim 120 \text{ GeV}$ the signal to background ratio is $\gtrsim 0.60$ with about 70 signal events. Here the dominant SM background is $t\bar{t}$ production. The lower number of signal events needed to attain a 5σ significance and the higher signal to background ratio in this region is the result of the harder event kinematics of $\tilde{\chi}_1^\pm \tilde{\chi}_2^0$, allowing for more stringent selection criteria (Set 4). As a consequence the SM contamination is smaller [8].

At small m_0 , the $\tilde{\chi}_1^\pm \tilde{\chi}_2^0$ reach in parameter space is very luminosity-dependent. This region of small m_0 is of particular importance, since it is the preferred one from the cosmological point of view, where $\tilde{\chi}_1^0$ is the candidate for the cold dark matter in the Universe. With the present lifetime of the Universe ($\gtrsim 10^{10}$ years) and the estimate of the relic neutralino abundance at freeze-out time as a function of $(m_0, m_{1/2})$, one can determine regions of parameter space where $\Omega h^2 < 1$; here Ω is the ratio of the relic neutralino density to the critical density which closes the Universe and h is the Hubble constant scaling factor, $0.5 \lesssim h \lesssim 0.8$. In Fig. 8.8, the $\Omega h^2 = 0.15$ and $\Omega h^2 = 0.4$ contours mark the most probable region of the parameter space, corresponding to a mixed dark matter scenario with 60% of neutralino dark matter. One can see that $\tilde{\chi}_1^\pm \tilde{\chi}_2^0$ direct production covers a significant part of this preferred region of parameter space.

We can conclude, that:

- by measuring the excess of events in the $3l + no \text{ jets} + E_T^{miss}$ channel over SM and internal SUSY backgrounds, $\tilde{\chi}_1^\pm \tilde{\chi}_2^0$ direct production can be investigated in mSUGRA parameter space up to $m_{1/2} \lesssim 170 \text{ GeV}$ (150 GeV) for all m_0 at a luminosity $L_{int} = 10^5 \text{ pb}^{-1}$ (10^4 pb^{-1});
- with a high integrated luminosity of $L_{int} = 10^5 \text{ pb}^{-1}$ and for $m_0 \lesssim 120 \text{ GeV}$, the discovery region for direct production of $\tilde{\chi}_1^\pm \tilde{\chi}_2^0$ extends up to $m_{1/2} \lesssim 420 \text{ GeV}$.

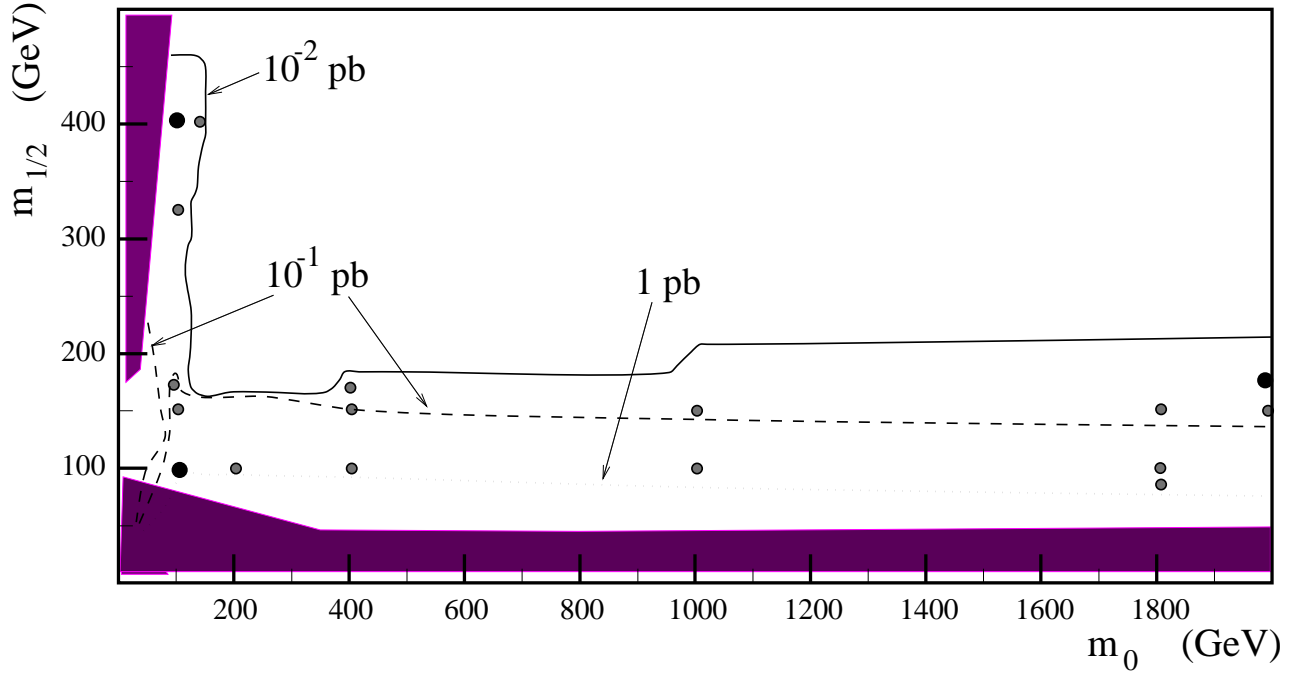


Figure 8.1: Simulated SUSY points for chargino/neutralino pair production. Sigma times branching ratio contours are also shown. Shaded regions are excluded by theory ($m_0 \lesssim 80$ GeV) and experiment ($m_{1/2} \lesssim 90$ GeV).

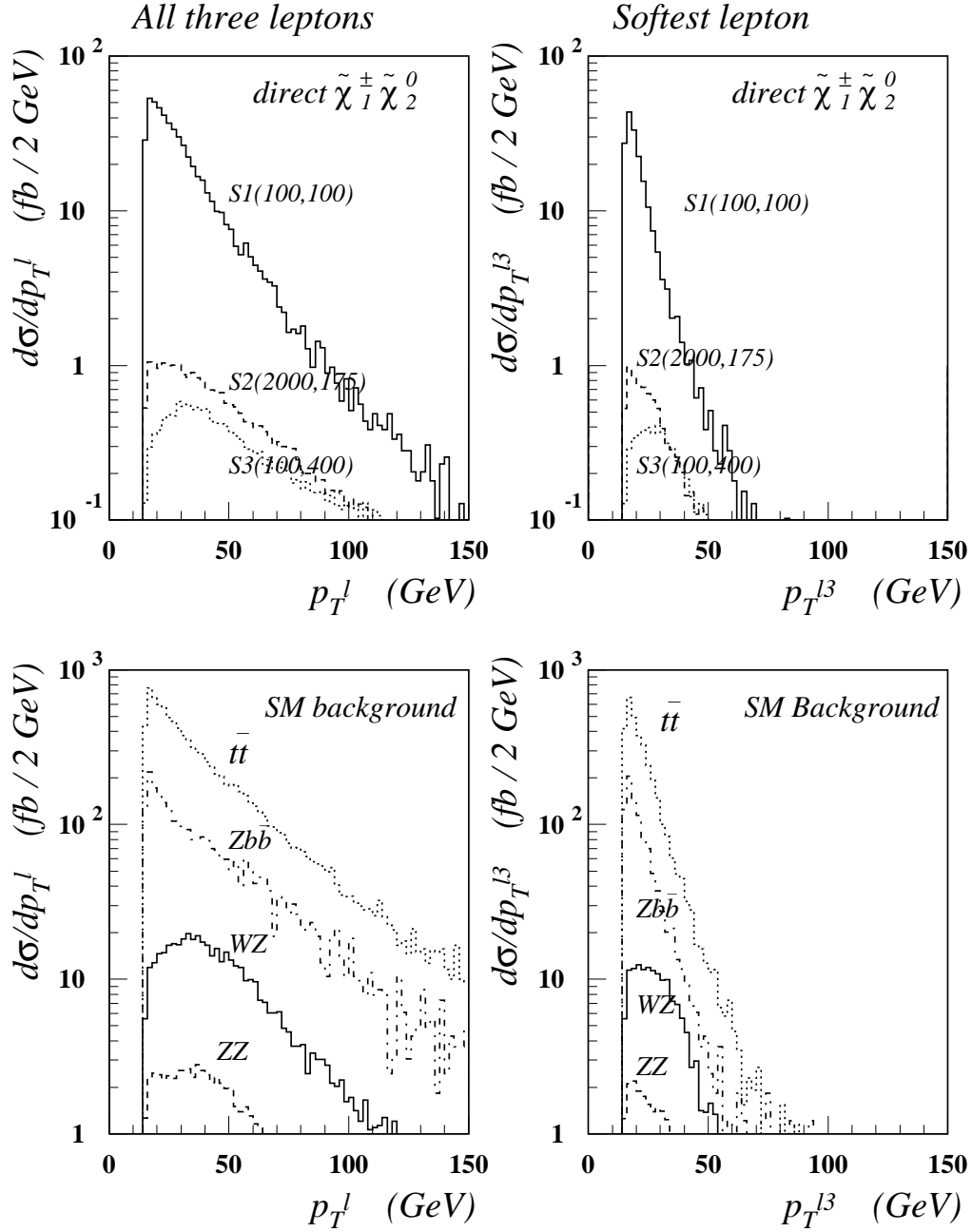


Figure 8.2: $d\sigma/dp_T^l$ distributions for signal and SM background. Left plots show distributions for all three leptons and the right ones for softest lepton in the event.

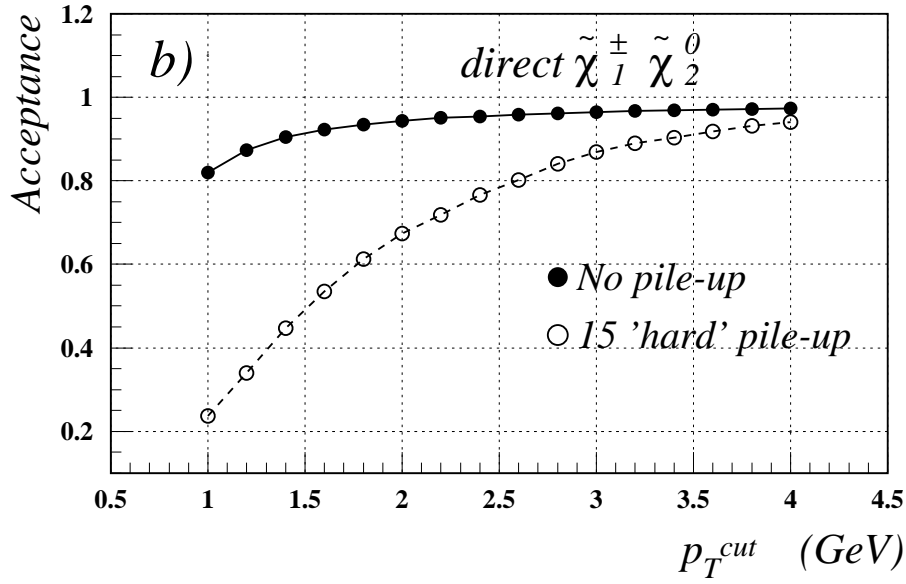
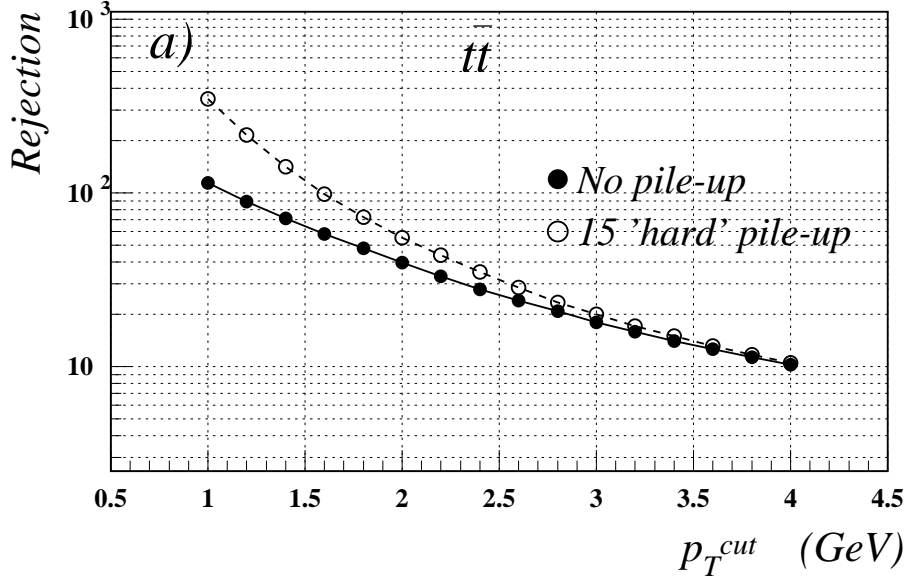


Figure 8.3: Tracker isolation: a) $t\bar{t}$ background rejection versus p_T^{cut} on charged track, b) signal acceptance versus p_T^{cut} on charged track. Events are selected with three leptons of $p_T > 15$ GeV and all of them are required to be isolated. Full and open circles correspond to low, $L = 10^{33} \text{ cm}^{-2} \text{ s}^{-1}$, and high, $L = 10^{34} \text{ cm}^{-2} \text{ s}^{-1}$, luminosity regimes, respectively.

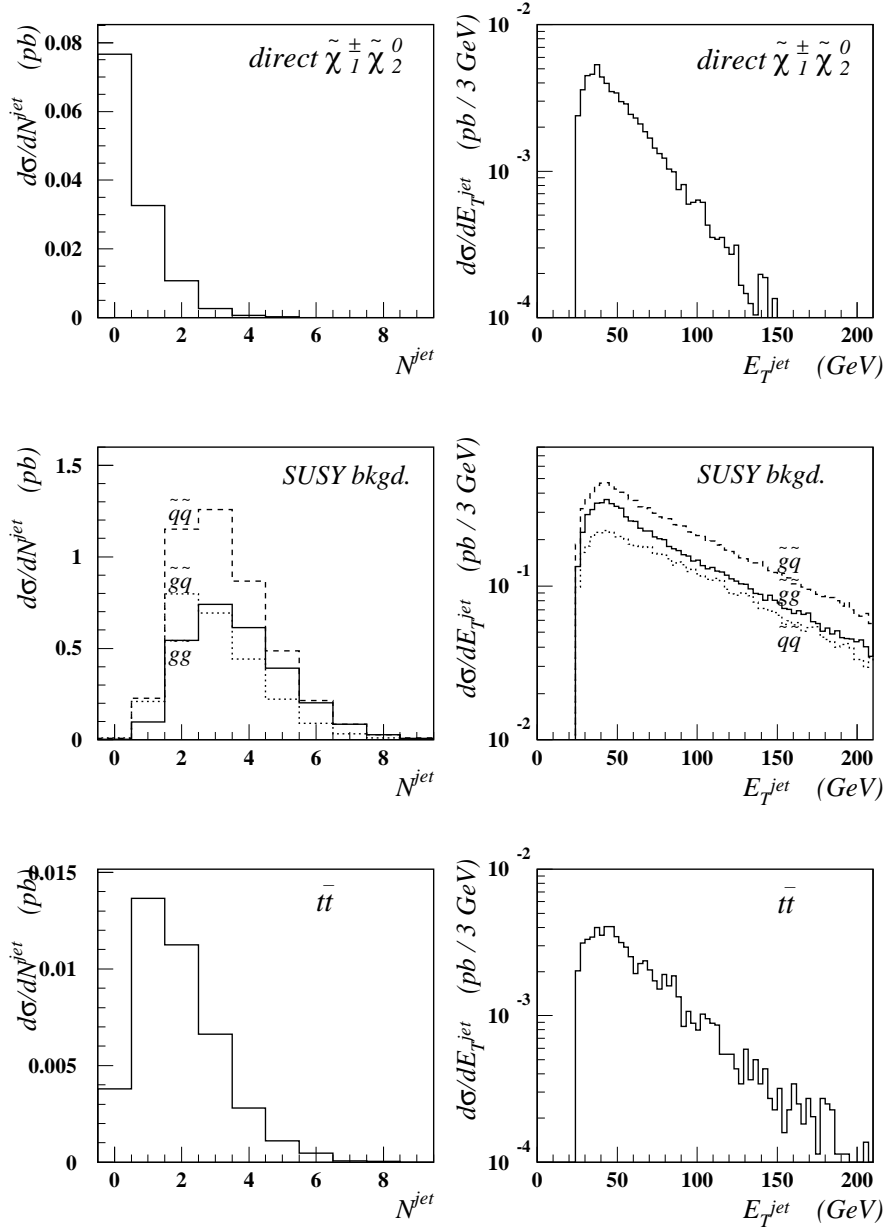


Figure 8.4: Jet multiplicity and transverse energy distributions for the signal and internal SUSY background at mSUGRA point S1(100 GeV, 100 GeV) and the $t\bar{t}$ background. Events are selected with three isolated leptons of $p_T > 15$ GeV.

$$m_0 = 100 \text{ GeV}, m_{1/2} = 100 \text{ GeV}$$

$$m(\tilde{g}) = 294 \text{ GeV}, m(\tilde{q}) = 270 \text{ GeV}$$

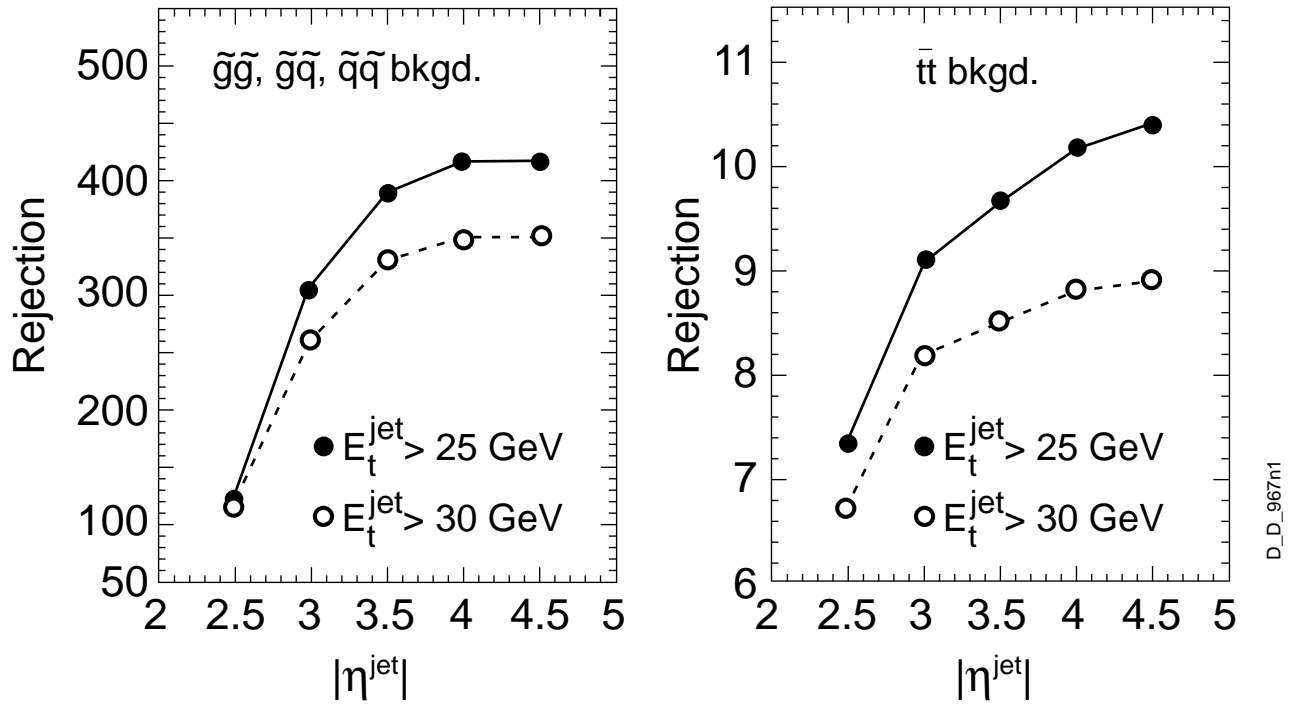


Figure 8.5: Jet veto rejection/acceptance versus $|\eta^{\text{jet}}|$ in $\tilde{\chi}_1^\pm \tilde{\chi}_2^0$ searches. Full circles correspond to $E_T^{\text{jet}} > 25 \text{ GeV}$ and the open ones to $E_T^{\text{jet}} > 30 \text{ GeV}$.

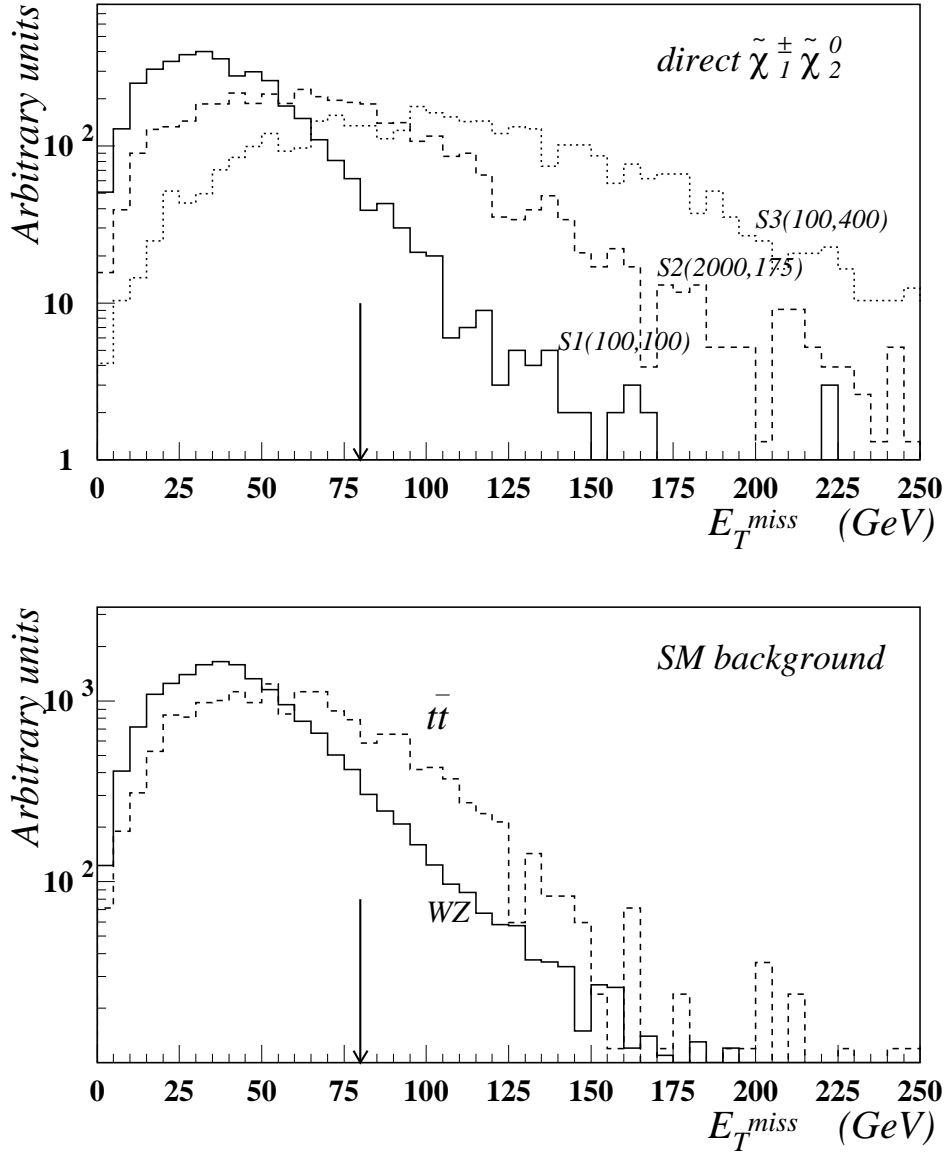


Figure 8.6: Missing transverse energy distributions in signal and background events with three isolated leptons of $p_T > 15$ GeV and no jets.

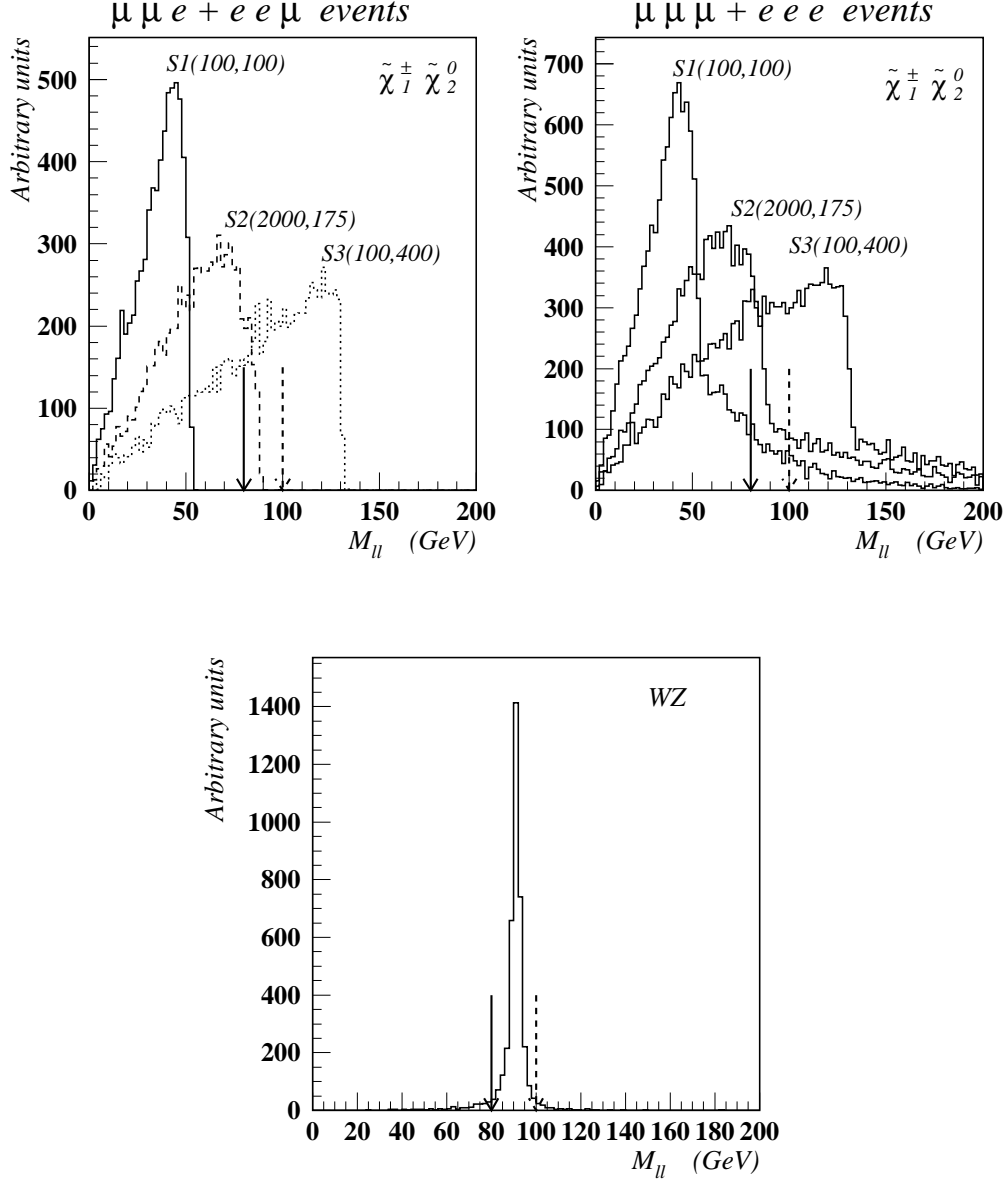


Figure 8.7: Dilepton invariant mass distributions in signal and WZ background events with three isolated leptons of $p_T > 15$ GeV and no jets.

Direct Chargino - Neutralino Production 5σ significance contours at different luminosities

$$\sigma = N_{\tilde{\chi}_1^\pm \tilde{\chi}_2^0} / \sqrt{N_{\text{all}}}$$

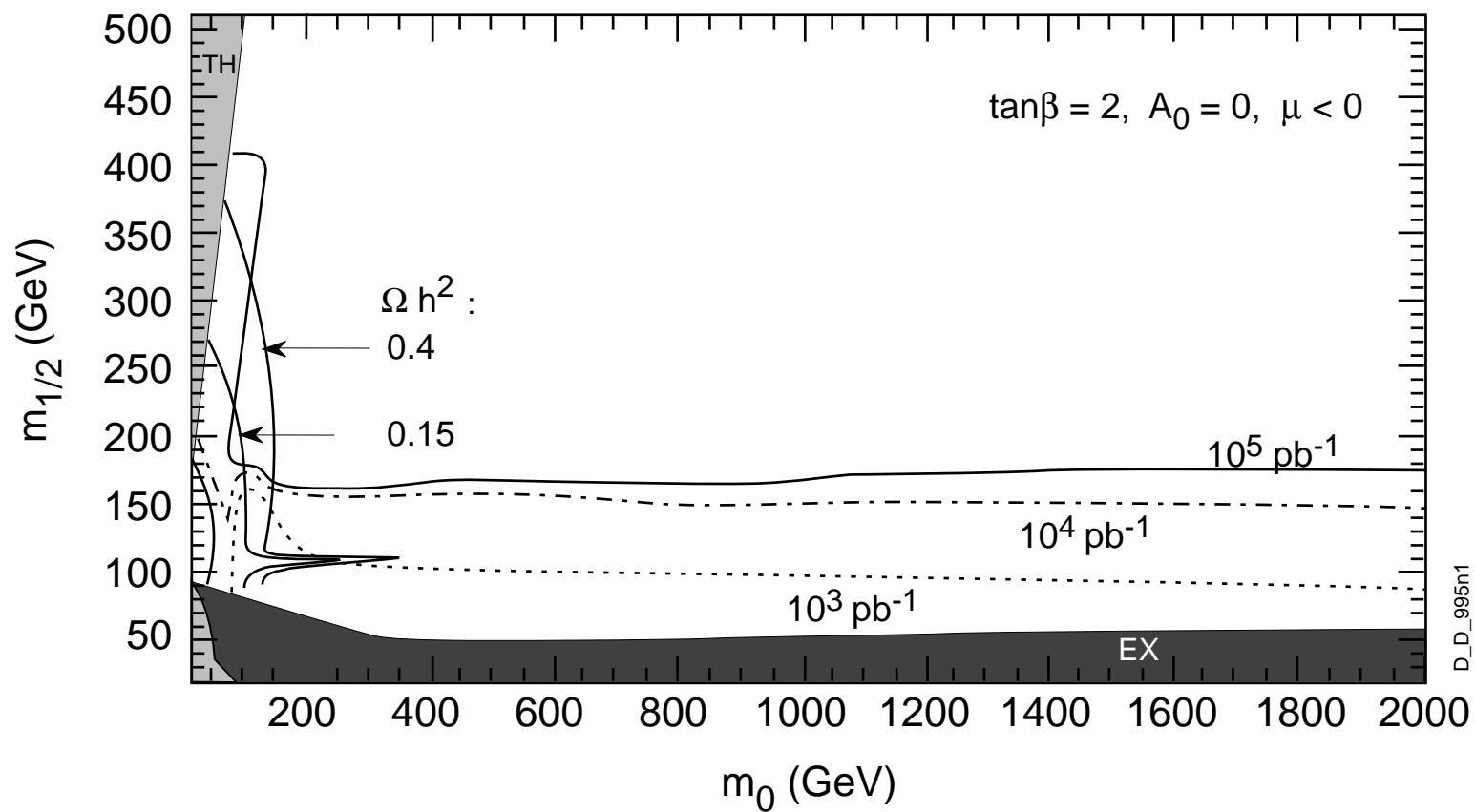


Figure 8.8: 5σ significance contours at different luminosities.

9 Possibility of observing $h \rightarrow b\bar{b}$ in squark and gluino decays

The usual way to search for the lightest CP-even Higgs (h) of the MSSM is through its direct production by gluon fusion or in association with W , $b\bar{b}$ or $t\bar{t}$ and its decay into $\gamma\gamma$, $ZZ^* \rightarrow 4l$, $\mu\mu$ or $b\bar{b}$ [14, 21, 43]. All these production mechanisms are Electroweak. Each of these channels has some limitations, such as high $\tan\beta$ for the $\mu\mu$ mode, or high mass, $m_h \gtrsim 130$ GeV and large stop mixing for the $ZZ^* \rightarrow 4l$ mode, for example. The most general way is to search for inclusive $h \rightarrow \gamma\gamma$, which, with $L_{int} = 10^5 \text{ pb}^{-1}$, would allow us to explore a domain approximately given by $m_A \gtrsim 250$ GeV and $\tan\beta \gtrsim 3$ [14]. With the $h \rightarrow \gamma\gamma$ mode we expect a signal on top of a large irreducible $\gamma\gamma$ background with a signal to background ratio of $\lesssim 1/20$. The instrumental requirements on the ECAL are very demanding, a $\gamma\gamma$ effective mass resolution better than $\simeq 1$ GeV at $m_h \simeq 100$ GeV [43]. In the associated production modes Wh and $t\bar{t}h$ with $h \rightarrow \gamma\gamma$, the S/B ratio is of order 1 and calorimeter performance is less demanding: but these channels require $\geq 10^5 \text{ pb}^{-1}$ [44]. Evaluations of ways to exploit the $h \rightarrow b\bar{b}$ decay mode in the Wh or $t\bar{t}h$ final states leave little hope – no way to get a really significant signal has been found up to now [45].

It is well known that the MSSM h can be abundantly produced in the decays of charginos and neutralinos (primarily $\tilde{\chi}_2^0$). In turn, the $\tilde{\chi}_2^0$ is a typical decay product of squarks and gluinos (see Figs. 2.5a,b) which are also produced abundantly. The idea is thus to use strongly produced \tilde{q}/\tilde{g} and to look for the dominant decay mode $h \rightarrow b\bar{b}$, if $\tilde{\chi}_i^0 \rightarrow \tilde{\chi}_j^0 h$ is kinematically allowed, and require E_T^{miss} and jet multiplicity to suppress the background [12, 46].

In this study we fix only one of the mSUGRA parameters, $A_0 = 0$, and vary the other four: m_0 , $m_{1/2}$, $\tan\beta$, $sign(\mu)$. The most pronounced variation of physics quantities (masses, branching ratios, cross-section) is with m_0 and $m_{1/2}$, thus the investigation is done in the m_0 , $m_{1/2}$ parameter plane for several representative values of $\tan\beta$ and $sign(\mu)$. When $M_{\tilde{\chi}_2^0} - M_{\tilde{\chi}_1^0} > m_h$ the main source of Higgs is the decay $\tilde{\chi}_2^0 \rightarrow \tilde{\chi}_1^0 h$. This decay has a significant ($\simeq 20\text{-}90\%$) branching ratio in a large portion of the parameter space, see Fig. 2.17. In regions of $m_{1/2} \lesssim 200\text{-}300$ GeV (depending on $\tan\beta$) the three body decays $\tilde{\chi}_2^0 \rightarrow \tilde{\chi}_1^0 q\bar{q}$, $\tilde{\chi}_2^0 \rightarrow \tilde{\chi}_1^0 l^+l^-$ take over because the $\tilde{\chi}_2^0 \rightarrow \tilde{\chi}_1^0 h$ decays are not kinematically allowed. The boundary at $m_0 \sim 200\text{-}300$ GeV, on the other hand, corresponds to the opening of two-body cascade modes, e.g. $\tilde{\chi}_2^0 \rightarrow \tilde{l}_{L,R}^\pm l^\mp \rightarrow \tilde{\chi}_1^0 l^+l^-$. Figure 2.17 also shows that the $\tan\beta = 2$, $\mu < 0$ case looks the most promising one, whereas the $\tan\beta = 10, 30$, $\mu < 0$ seem the least favorable among the possibilities considered, the $\tilde{\chi}_2^0 \rightarrow \tilde{\chi}_1^0 h$ branching ratio being the smallest on average in these latter cases. Depending on $\tan\beta$, there is potentially a gap between the upper limit explored up to now or foreseeable at LEP2 and Tevatron at $m_{1/2} \simeq 100$ GeV ($m_h \lesssim 100$ GeV) and the lower limit at $m_{1/2} \simeq 200\text{-}250$ GeV where $\tilde{\chi}_2^0 \rightarrow \tilde{\chi}_1^0 h$ opens up. This comes about because within mSUGRA there are simple mass relations: $M_{\tilde{\chi}_2^0} \simeq 2M_{\tilde{\chi}_1^0} \simeq m_{1/2}$, and the LSP mass is typically $\gtrsim 100$ GeV in the regions where $\tilde{\chi}_2^0 \rightarrow \tilde{\chi}_1^0 h$ is allowed. The range of the h mass varies from $\simeq 80$ to $\simeq 120$ GeV and the exact upper limit is determined by the order to which the radiative corrections have been calculated.

With increasing m_0 (at fixed $m_{1/2}$) squarks become more massive than gluino at some point (see, e.g. Fig. 2.16) and thus gluino decays into squarks are not allowed anymore,

decreasing significantly the yield of $\tilde{\chi}_2^0$ from squark decays. Furthermore, the $B(\tilde{q} \rightarrow \tilde{\chi}_2^0 q)$ also decreases with increasing m_0 because the decay $\tilde{q} \rightarrow \tilde{g}q$ plays an increasingly important role. These factors, with the variation of the total production cross-section (shown in Fig. 2.15) and the variation of the kinematics of the decay chains, require that for a quantitative evaluation of the regions where $h \rightarrow b\bar{b}$ could be observed one needs to investigate the parameter space point by point and optimise cuts accordingly [12].

We considered the following SM background processes: QCD $2 \rightarrow 2$ (including $b\bar{b}$), $t\bar{t}$ and Wtb . The \hat{p}_T range of all these processes is subdivided into several intervals to facilitate accumulation of statistics in the high- \hat{p}_T region: 100-200 GeV (except for QCD), 200-400 GeV, 400-800 GeV and > 800 GeV. The accumulated statistics for all channels correspond to 100 fb^{-1} , except for the QCD jet (instrumental mismeasurement) background where the statistics correspond to $0.2 - 50 \text{ fb}^{-1}$ depending on the \hat{p}_T interval. It is very time consuming to produce a representative sample of QCD jets in the low- p_T range, since the cross section is huge and we need extreme kinematical fluctuations and non-Gaussian tail instrumental contributions for this type of background to be within the signal selection cuts. On the other hand, our simulation of instrumentally induced missing transverse energy is not yet fully reliable as it strongly depends on the still evolving estimates of dead areas, volumes due to services, non-Gaussian calorimeter response, etc. So we cannot go confidently below $\simeq 100$ GeV with the cut on E_T^{miss} , where the QCD jet background becomes the dominant contribution.

Initial requirements for all the SM and SUSY samples are the following:

- at least 4 jets with $E_T^{jet} > 20 \text{ GeV}$ in $|\eta^{jet}| < 4.5$,
- $E_T^{miss} > 100 \text{ GeV}$,
- *Circularity* > 0.1 .

No specific requirements are put on leptons. If there are isolated muons or electrons with $p_T^{\mu,e} > 10 \text{ GeV}$ within the acceptance they are also recorded. The term “isolated lepton” here means satisfying simultaneously the following two requirements:

- no charged particle with $p_T > 2 \text{ GeV}$ in a cone $R = 0.3$ around the direction of the lepton,
- ΣE_T^{calo} in the annular region $0.1 < R < 0.3$ around the lepton impact point has to be less than 10% of the lepton transverse energy.

At a later stage we investigate whether selection or vetoing on isolated leptons can be used to help suppress the SM or internal SUSY backgrounds.

In this study we used an evaluation of the b -tagging performance of CMS from impact parameter measurement in the tracker [34]. An example is shown in Fig. 4.11. The b -tagging efficiency and mistagging probability for jets is evaluated as a function of E_T and jet pseudorapidity. It is obtained from a parameterized Gaussian impact parameter resolution, dependent on the pixel point resolution, radial position of the pixel layers and the effects of multiple scattering on intervening materials, with the addition of a non-Gaussian impact parameter measurement tail based on CDF data. Although there are some specific assumptions made concerning the tails of the impact parameter distributions extending beyond the parameterized Gaussian parts in [34], the presently on-going study

of the expected impact parameter resolution, with full pattern recognition and track finding in CMS [47] is in a very good agreement with the results used as an input in the present study.

The b -jet tagging efficiency is parameterized as a function of E_T^{jet} in 3 intervals of η : 0 - 1, 1 - 1.75 and 1.75 - 2.4. A typical b -tagging efficiency at $\eta \simeq 0$ for $E_T^{jet} = 40$ GeV is $\simeq 30\%$, reaching a maximal efficiency of $\simeq 60\%$ for high- E_T jets. Charm-jets have a typical tagging efficiency of about 10%, and for light quarks and gluons the b -tagging (mistagging) efficiency reaches a maximum of about 3% for high- E_T jets. At the analysis stage the jets produced by the event generator are “ b -tagged” according to the tagging efficiency for b -jets and mistagging probability for quark and gluon jets. If not specially mentioned otherwise, $h \rightarrow b\bar{b}$ decay jets are tagged only in the barrel $|\eta| < 1.75$ interval and in all di-jet mass distributions we take only one pair of b -jets per event, those closest to each other in $\eta - \varphi$ space. No attention is paid to jet “charge” or “leading charge”. More details can be found in [12].

As an example let us consider a representative mSUGRA point $m_0 = m_{1/2} = 500$ GeV, $\tan\beta = 2$, $\mu < 0$. Here the masses of relevant sparticles are: $m_{\tilde{g}} = 1224$ GeV, $m_{\tilde{u}_L} = 1170$ GeV, $m_{\tilde{\chi}_2^0} = 427$ GeV, $m_{\tilde{\chi}_1^0} = 217$ GeV, $m_h = 89.7$ GeV. In Fig. 9.1 we compare kinematical distributions for this point with the SM background for $L_{int} = 100 \text{ fb}^{-1}$. The E_T^{miss} distributions show the most pronounced difference between signal and background, this then being the most important variable for the background suppression. A significant difference exists also in the jet multiplicity distributions. A specific optimisation of cuts on E_T^{miss} , E_T^{jet} , etc., is however performed in various regions of mSUGRA parameter space.

Figure 9.2 shows the b - b (jet-jet) mass distribution for the sum of the SUSY and SM events assuming an ideal b -tagging performance, i.e. 100% b -tagging efficiency with 0% mistagging probability for jets. The cuts are $E_T^{miss} > 400$ GeV and $E_T^{jet} > 40$ GeV. The SM background shown in Fig. 9.2 separately as a shaded histogram is small compared to the internal SUSY background. The $b\bar{b}$ mass distribution is fitted with a sum of a Gaussian and a quadratic polynomial. The width of the signal peak is determined entirely by the jet-jet effective mass resolution of the detector (the intrinsic h width varies from 3.2 to 4.3 MeV over the entire mSUGRA parameter space). The position of the peak is shifted to lower mass since energy losses in jets (finite cone size, neutrinos generated in hadronic showers, etc.) are not corrected for. The three distributions in the lower half in Fig. 9.2 are for events in the M_{bb} mass window 70 - 100 GeV to illustrate the kinematics of the $h \rightarrow b\bar{b}$ decay. The average b -jet transverse energy is ~ 110 GeV, and the b -jets are very central as they result from the decay of massive (~ 1200 GeV) squarks and gluinos which are centrally produced. Clearly, b -tagging beyond $|\eta^{jet}| \simeq 1.5$ is not very helpful in this search.

If one now applies the nominal b -tagging performance expectations described previously, we obtain the $b\bar{b}$ mass distribution given in Fig. 9.3a. Under these nominal conditions and with 100 fb^{-1} the expected signal significance calculated as S/\sqrt{B} within a $\pm 1\sigma$ interval around the peak value is 18.3. The background is dominated by the internal SUSY background which is largely irreducible, originating mainly from additional real b -jets in the event, rather than from mistagged jets. An improvement could possibly be obtained by taking into account “jet charge” and thus enriching the sample in $b\bar{b}$ pairs as compared to $b\bar{b} + b b/\bar{b}\bar{b}$. This however requires track reconstruction and charge determination for fast tracks in jets, a task still under study in CMS [47].

Figures 9.3-9.5 illustrate the expected sensitivity of the $h \rightarrow b\bar{b}$ signal to various

instrumental factors [12]. In Fig. 9.3b all bb -combinations per event are included in the distribution (instead of just the one with the closest distance in $\eta - \varphi$ space) and the signal significance is now worse by $\simeq 12\%$. Figures 9.3c and 9.3d show the effect of increasing, or decreasing, the b -tagging efficiency by 15% in absolute value, whilst keeping mistagging at the nominal level. The dependence on the b -tagging efficiency is very pronounced, the signal significance varying by respectively $\pm 25\%$. This is not surprising as the b -tagging efficiency enters quadratically in the number of signal events. Figures 9.4a and 9.4b illustrate the effect of the η acceptance of the silicon pixel detector. As can be expected on the basis of Fig. 9.2, increased acceptance beyond $|\eta^{jet}| \simeq 1.5$ does not bring a significant improvement as the signal b -jets are very central. With tagging acceptance increasing from $|\eta^{jet}| = 1.0$ to 1.75 and 2.4, signal significance improves from 17.2 to 18.3 and 18.8, respectively. Figures 9.4c and 9.4d illustrate the dependence on tagging purity, where one keeps the nominal b -tagging efficiency unchanged, but varies the mistagging probability for all non- b -jets. Increasing the mistagging probability by a factor of 3 degrades signal significance by $\simeq 25\%$.

Since the observed width of the $h \rightarrow b\bar{b}$ peak is entirely determined by the calorimetric jet-jet effective mass resolution, one can expect dependence of the signal observability on the energy resolution. This is illustrated in Fig. 9.5. The upper plot is for the nominal HCAL performance, corresponding to $\sigma_E/E = 82\%/\sqrt{E} \oplus 6.5\%$ at $\eta = 0$ and the lower plot corresponds to the HCAL energy resolution degraded to $120\%/\sqrt{E} \oplus 10\%$. The resolution of the Gaussian fit to the Higgs peak is 7.6 GeV in the first case and 11 GeV in the second. The difference in S/B between Figs. 9.5a and 9.5b is significant, but not dramatic. This is due to the fact that the $h \rightarrow b\bar{b}$ pair has a significant boost, $p_T^{b\bar{b}} \sim 200$ GeV (Fig. 9.2) and the jet-jet opening angle, whose measurement precision is determined by calorimeter granularity plays an important role in the effective mass resolution. The mass resolution also contains irreducible contributions from final state gluon radiation, jet cone size and fragmentation effects.

Figure 9.6 illustrates the $h \rightarrow b\bar{b}$ signal observability as a function of m_h over the allowed range of ~ 80 to 120 GeV. For this we select the points all at the same $m_0 = m_{1/2} = 500$ GeV, but different values of $\tan\beta$ and μ , with nominal b -tagging performance and $L_{int} = 100 \text{ fb}^{-1}$. One can clearly see that the signal becomes broader with increasing Higgs mass since the jet $E_T > 40$ GeV cut-off does not play such a role as for a low-mass.

It is worth mentioning, that a significant part of the mSUGRA parameter space can be explored already at a very low luminosities. For example, Fig. 9.7 shows the expected Higgs signal with $L_{int} = 3 \text{ fb}^{-1}$ for a few points. All the distributions in this Figure are obtained with the cuts: $E_T^{miss} > 200$ GeV and $E_T^{jet} > 40$ GeV. For comparison, searches in the $h \rightarrow \gamma\gamma$ channel at the corresponding mSUGRA points would require ~ 10 times higher integrated luminosity [12].

Let us turn to the main problem, how general is the possibility to observe this $h \rightarrow b\bar{b}$ signal in \tilde{q}, \tilde{g} decays. Figure 9.8 shows the domain of parameter space where the $h \rightarrow b\bar{b}$ signal is visible with $S/\sqrt{B} > 5$ for the case $\tan\beta = 2$, $A_0 = 0$, $\mu < 0$ with nominal b -tagging performance of CMS, for 10 and 100 fb^{-1} integrated luminosities. The isomass curves for the CP-even (h) and CP-odd (A) Higgses are also shown in Fig. 9.8 by the dash-dotted lines. The bold broken line denotes the region where $B(\tilde{\chi}_2^0 \rightarrow \tilde{\chi}_1^0 h) = 50\%$. The shaded regions along the axes denote the present theoretically (TH) or experimentally (EX) excluded regions of parameter space not yet including LEP 96/97 results. The LEP2 and Tevatron (with 1 fb^{-1}) sparticle reaches are also shown by solid lines. With $L_{int} \leq 1$

fb^{-1} the threshold of visibility of $h \rightarrow b\bar{b}$ at lowest $m_{1/2} = 170\text{-}180$ GeV corresponds to $m_{\tilde{g},\tilde{q}} \geq 400\text{-}450$ GeV, i.e. it begins just where the Tevatron searches will stop with $\sim 5 \text{ fb}^{-1}$. With 100 fb^{-1} the reach extends up to $m_h \simeq 90$ GeV, $m_A \lesssim 1500$ GeV. Figures 9.9 and 9.10 show the domains of h signal visibility for $\tan\beta = 10$, $\mu < 0$ and $\tan\beta = 30$, $\mu > 0$, respectively. In both cases there seems to be a significant observability gap between the upper reach of LEP2 or the Tevatron and the LHC/CMS low m_h reach using this method to look for h . This has to be studied in more detail in the future.

We conclude that the search for the $h \rightarrow b\bar{b}$ decay, when the lightest Higgs is produced in the cascade decays of the strongly interacting sparticles, seems to be a promising channel. The large rejection factor needed to suppress backgrounds and achieve a S/B of ~ 1 is here provided by the E_T^{miss} cut. Nothing similar can be obtained in the search for the SM Higgs in $H \rightarrow b\bar{b}$ nor for MSSM $h \rightarrow b\bar{b}$ in inclusive h , Wh and $t\bar{t}h$ final states. mass in the $\simeq 450$ to 700 GeV range for this search to be possible. The study carried out here in the mSUGRA framework shows that there is a significant domain of parameter space, just beyond the \tilde{g}/\tilde{q} mass reach of the Tevatron ($\sim 400\text{-}450$ GeV), where observation of the $h \rightarrow b\bar{b}$ decay would be possible with an integrated luminosity of only $1\text{-}3 \text{ fb}^{-1}$. This parameter space domain can be significantly extended with 100 fb^{-1} , where \tilde{g} , \tilde{q} with masses in 1.5 TeV range are probed. The h mass range from $\simeq 80$ GeV up to $\simeq 125$ GeV can be covered.

Our investigations show that for the observation of the $h \rightarrow b\bar{b}$ signal a calorimetric energy resolution of $\simeq 100\%/\sqrt{E} \oplus 10\%$ is adequate, but it should not be significantly worse than this. The signal visibility depends most critically on the b -tagging efficiency and to a lesser extent on the mistagging probability; the acceptance of the b -tagging pixel devices is not a real issue, provided the coverage is no smaller than $|\eta| \simeq 1.5$. A significant improvement in b -tagging efficiency could be obtained with a third pixel layer, or by having pixel layer at a radius of 4 cm even for high luminosity running, to be replaced every (few) year(s). The mistagging probability depends on the non-Gaussian part of the impact parameter measurement distribution, and thus on the overall pattern recognition performance in the region close to the beam, e.g. on the balance between Si and MSGC layers in the tracker. Optimisation of this aspect might then involve increasing the number of Si layers from 4 to 5 , possibly 6 , reducing correspondingly the MSGC layers and deserves a dedicated study.

If this method is to become a viable alternative to the $h \rightarrow \gamma\gamma$ search, it is important to evaluate how general are the results of the present study, i.e. what happens outside the mSUGRA scheme where masses are not so constrained, for example in the MSSM. Presumably what is found here in the framework of mSUGRA-MSSM is valid as soon as the $\tilde{g}/\tilde{q} \rightarrow \tilde{\chi}_2^0 \rightarrow \tilde{\chi}_1^0 h$, or even more generally, the $\tilde{g}/\tilde{q} \rightarrow \tilde{\chi}_i^0 \rightarrow \tilde{\chi}_j^0 h$ chains are kinematically allowed and the $\tilde{\chi}_i^0 \tilde{\chi}_j^0 h$ couplings non-vanishing. A particular point of interest in this respect is the gap at the lower \tilde{q}/\tilde{g} masses, between the domains where SUSY can be explored at the Tevatron with $5\text{-}6 \text{ fb}^{-1}$, the LEP2 reach in terms of m_h and the lower mass reach of this channel, if it exists in mSUGRA, can it be overcome in the MSSM where mass relations are less rigid?

$$\begin{aligned}
M(\tilde{g}) &= 1224 \text{ GeV} & M(\tilde{u}_L) &= 1170 \text{ GeV} & M(\tilde{t}_1) &= 852 \text{ GeV} \\
M(\tilde{\chi}_2^0) &= 427 \text{ GeV} & M(\tilde{\chi}_1^0) &= 217 \text{ GeV} & M(h) &= 89.7 \text{ GeV}
\end{aligned}$$

$$\begin{aligned}
&E_T^{\text{miss}} > 200 \text{ GeV} \\
&\geq 4 \text{ jets}, p_T^{\text{jet}} > 40 \text{ GeV}, |\eta^{\text{jet}}| < 4.5 \\
&\text{circularity} > 0.1
\end{aligned}$$

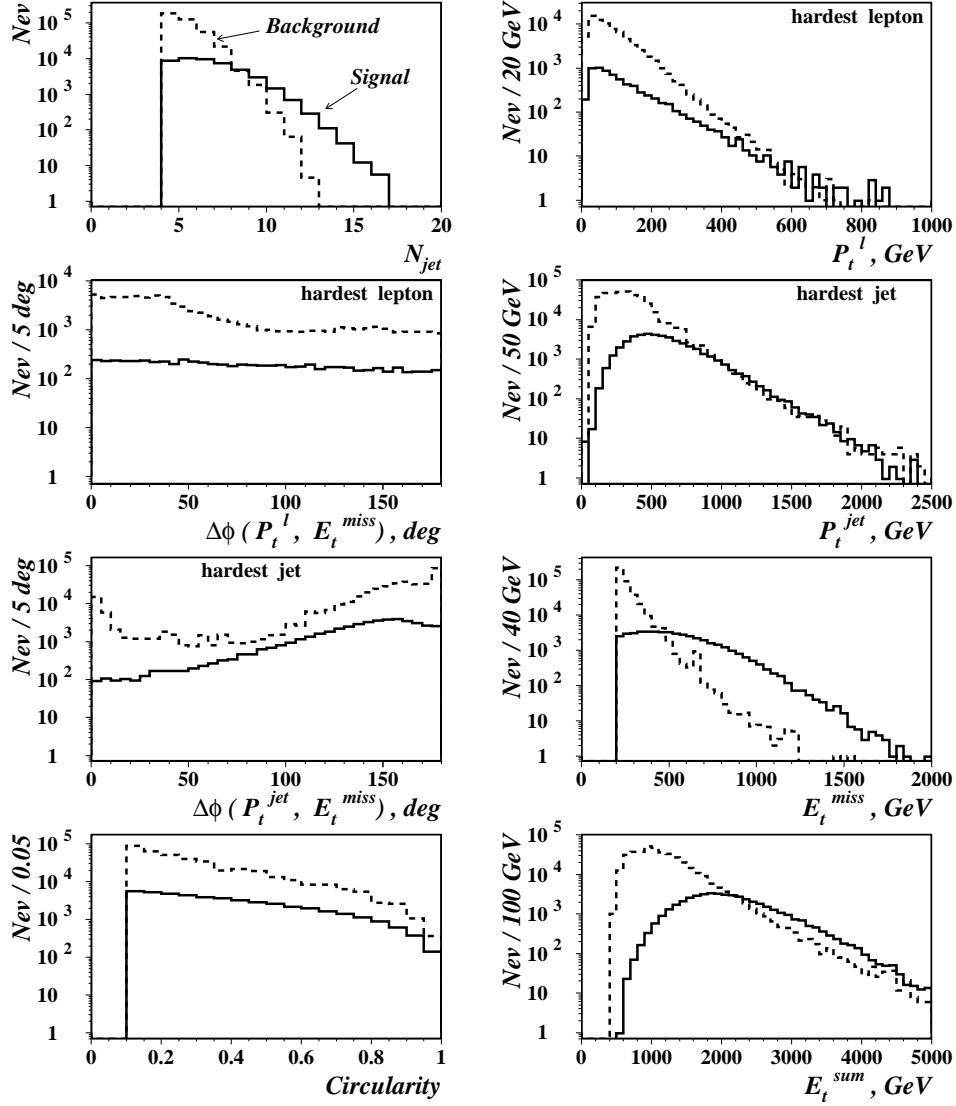
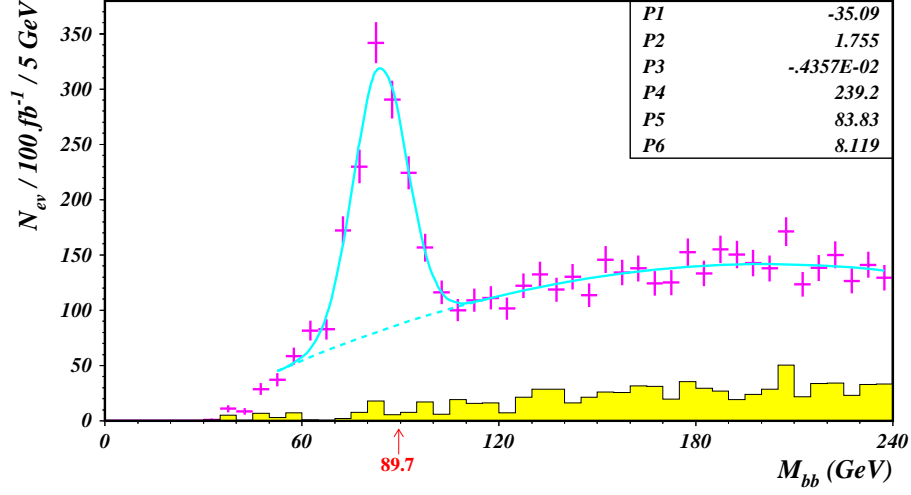


Figure 9.1: Comparison of mSUGRA signal at $m_0 = m_{1/2} = 500 \text{ GeV}$, $\tan\beta=2$, $\mu < 0$. and SM background distributions.



for $70 \text{ GeV} < M_{bb} < 100 \text{ GeV}$:

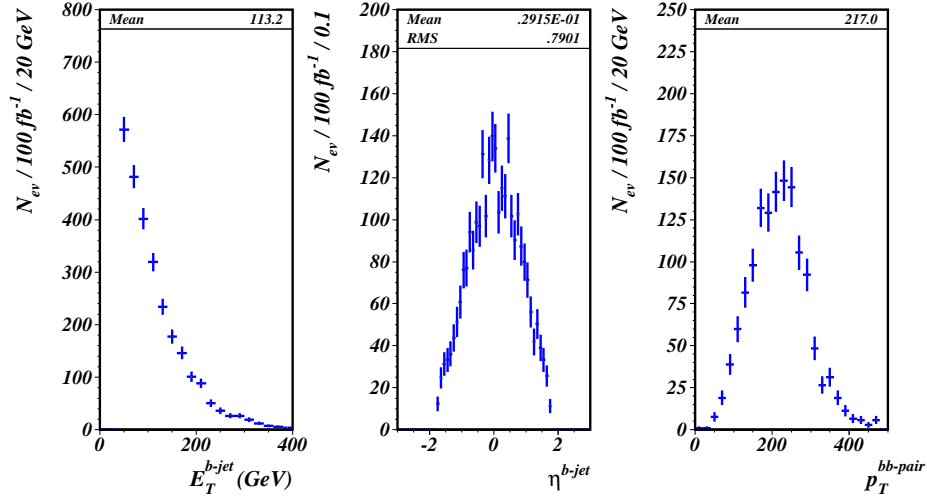


Figure 9.2: b -jet related distributions for the same point as in Fig. 9.1 in case of ideal tagging performance. The three distributions in the lower part are for events in the M_{bb} mass window 70 - 100 GeV.

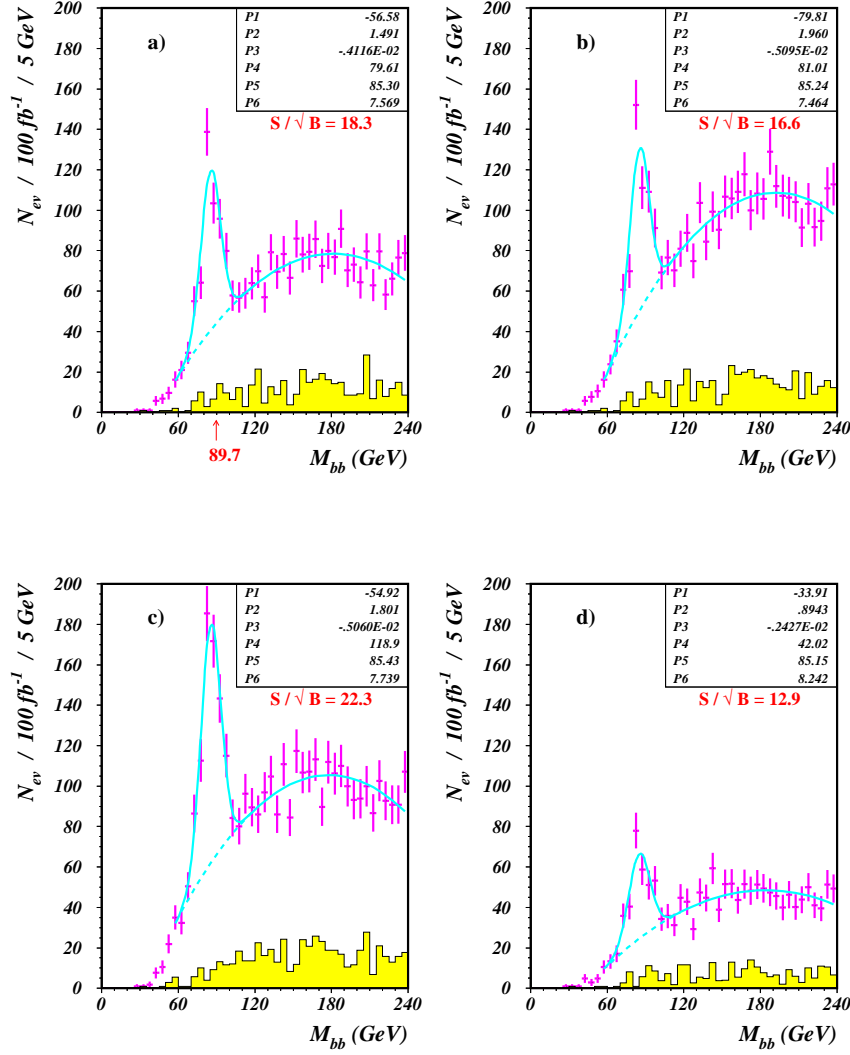


Figure 9.3: Influence of the various instrumental factors on signal observability in the same parameter space point as in Fig. 9.2 with 100 fb⁻¹: a) with “nominal” b -tagging performance and data selection, b) all bb -combinations per event are included in histogram, c) b -tagging efficiency increased by 15% and d) b -tagging efficiency decreased by 15%. The nominal mistagging probability is assumed in all cases.

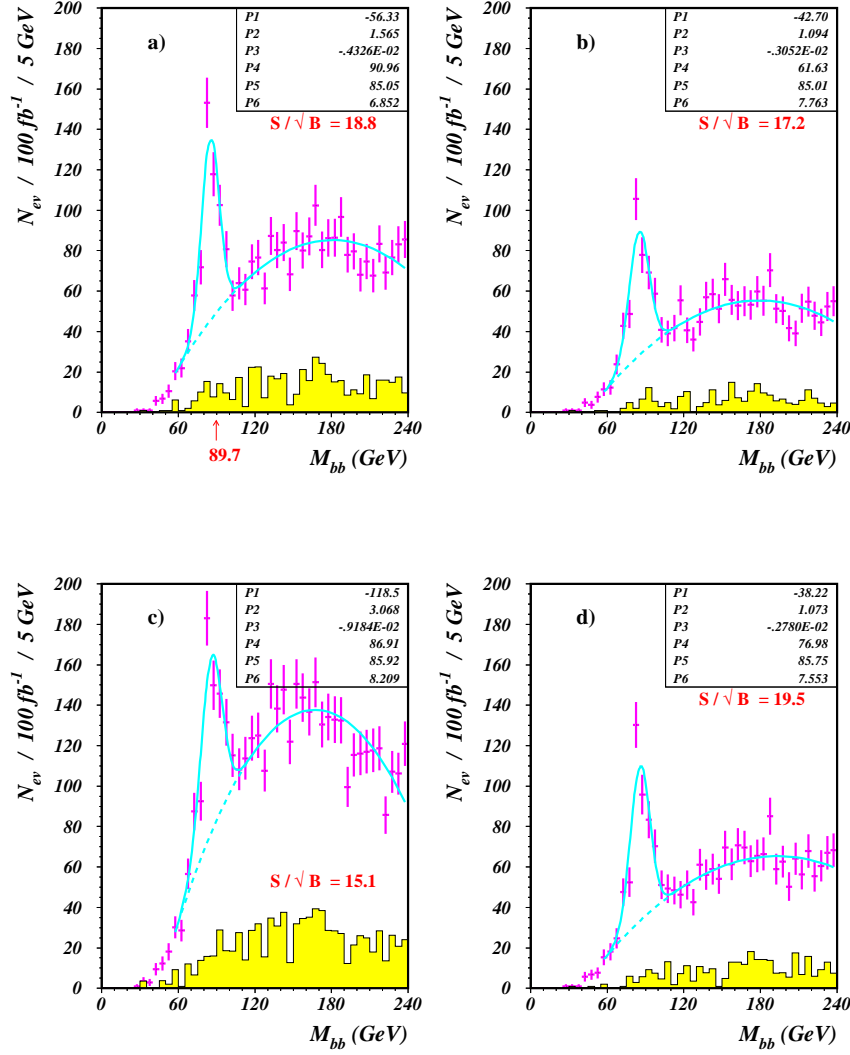


Figure 9.4: Influence of various instrumental factors on $h \rightarrow b\bar{b}$ signal visibility in the same parameter space point as in Fig. 9.2: a) tagging acceptance increased compared to “nominal” from $|\eta| < 1.75$ up to $|\eta| < 2.4$, b) tagging acceptance decreased to $|\eta| < 1.0$, c) mistagging probability increased by a factor of 3 and d) mistagging probability decreased by a factor of 2 relative to nominal expectations.

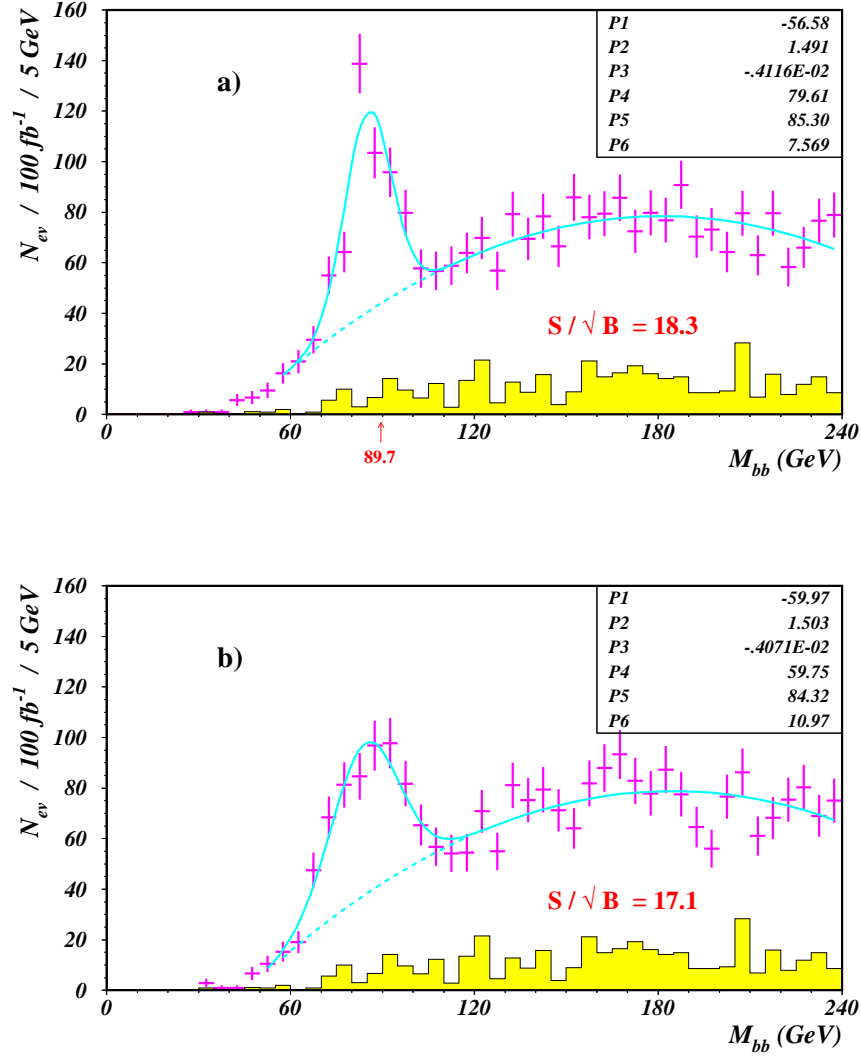


Figure 9.5: Effect of the assumed single hadron energy resolution on the signal visibility: a) the nominal HCAL performance, $\sigma_E/E = 82\%/\sqrt{E} \oplus 6.5\%$ at $\eta \sim 0$; b) the HCAL energy resolution deteriorated to $120\%/\sqrt{E} \oplus 10\%$. mSUGRA point as in Figs. 9.2-9.4.

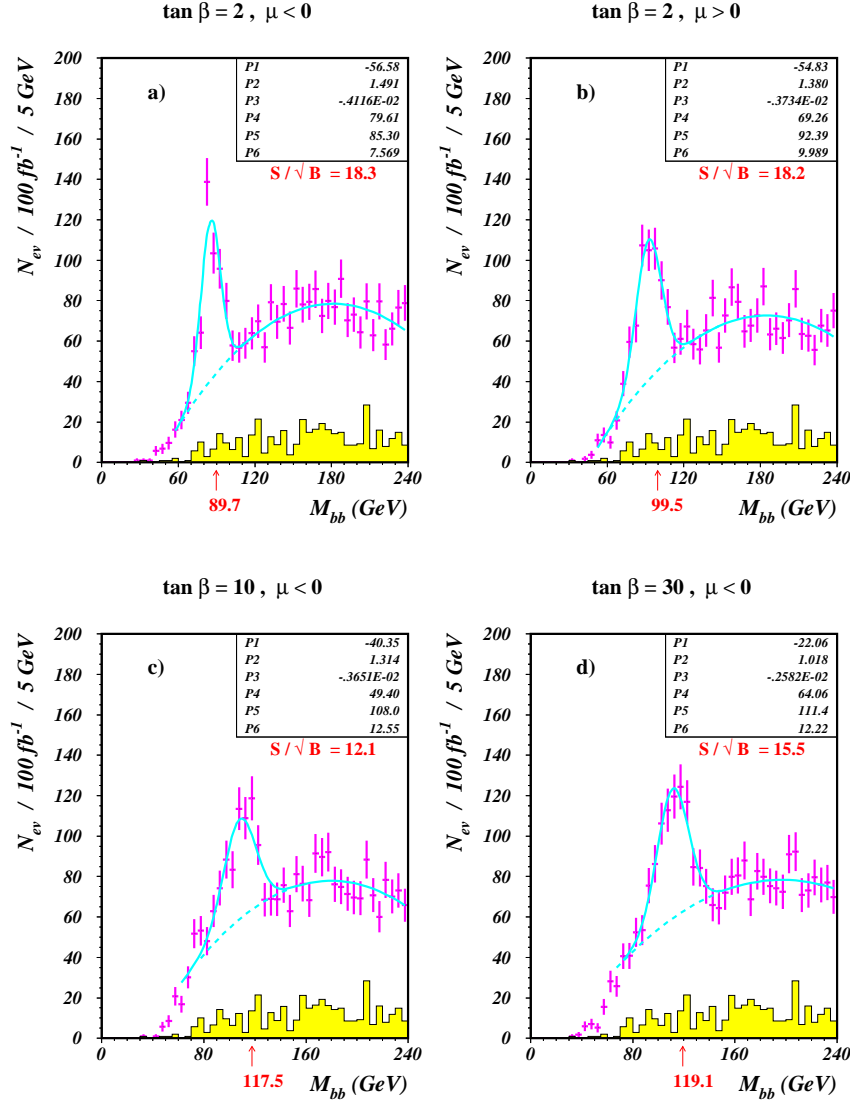


Figure 9.6: Dependence of the $h \rightarrow b\bar{b}$ signal visibility on m_h over the allowed range ~ 80 to 120 GeV, varying $\tan\beta$ and $sign(\mu)$ at a fixed $m_0 = m_{1/2} = 500$ GeV. Nominal CMS instrumental performance, 100 fb^{-1} integrated luminosity.

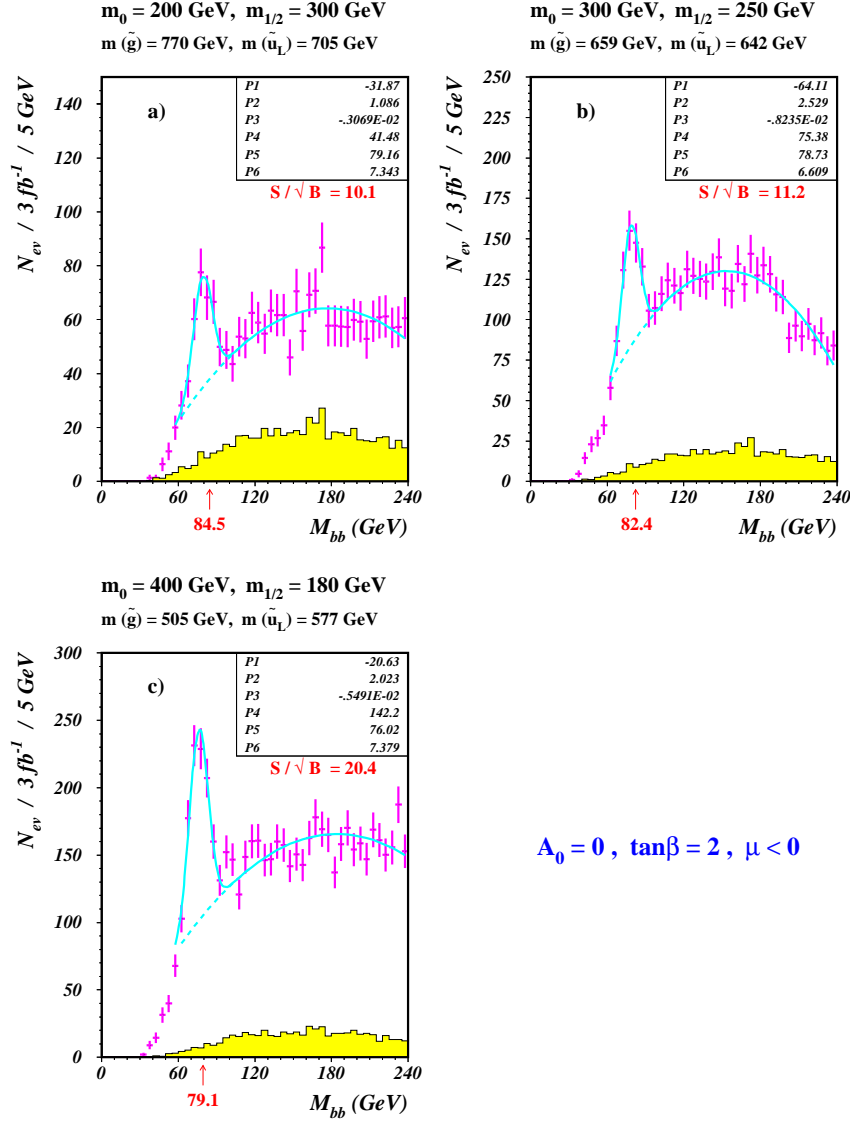


Figure 9.7: Some points in parameter space accessible already with 3 fb^{-1} . Nominal b -tagging performance of CMS is assumed.

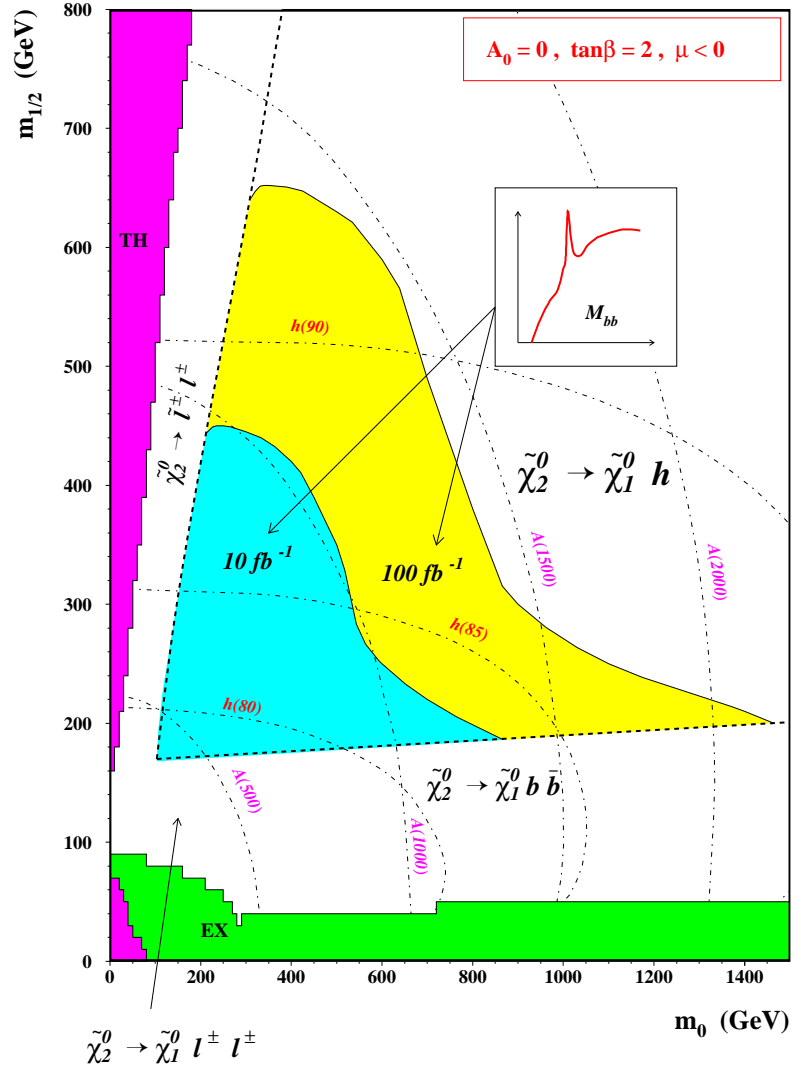


Figure 9.8: 5σ visibility contours of $h \rightarrow b\bar{b}$ for $\tan\beta = 2$, $A_0 = 0$ and $\mu < 0$ with 10 and 100 fb^{-1} . See also comments in text.

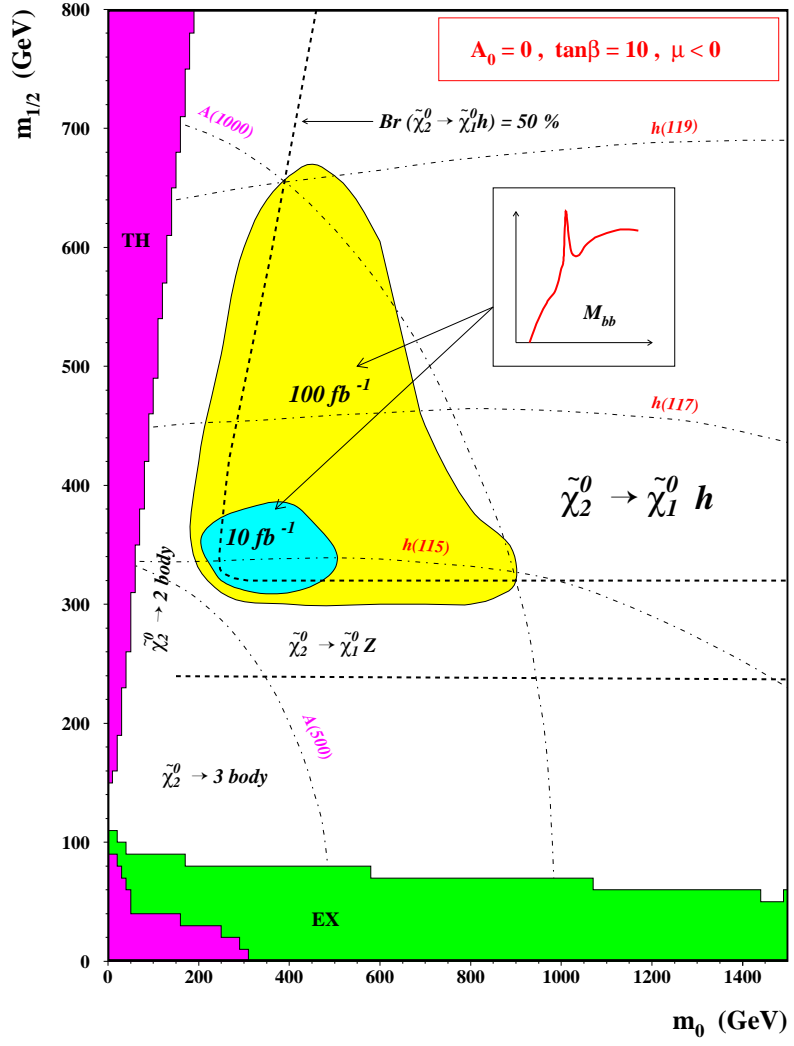


Figure 9.9: 5σ visibility contours of $h \rightarrow b\bar{b}$ for $\tan\beta = 10$, $A_0 = 0$ and $\mu < 0$ with 10 and 100 fb^{-1} . See also comments in text.

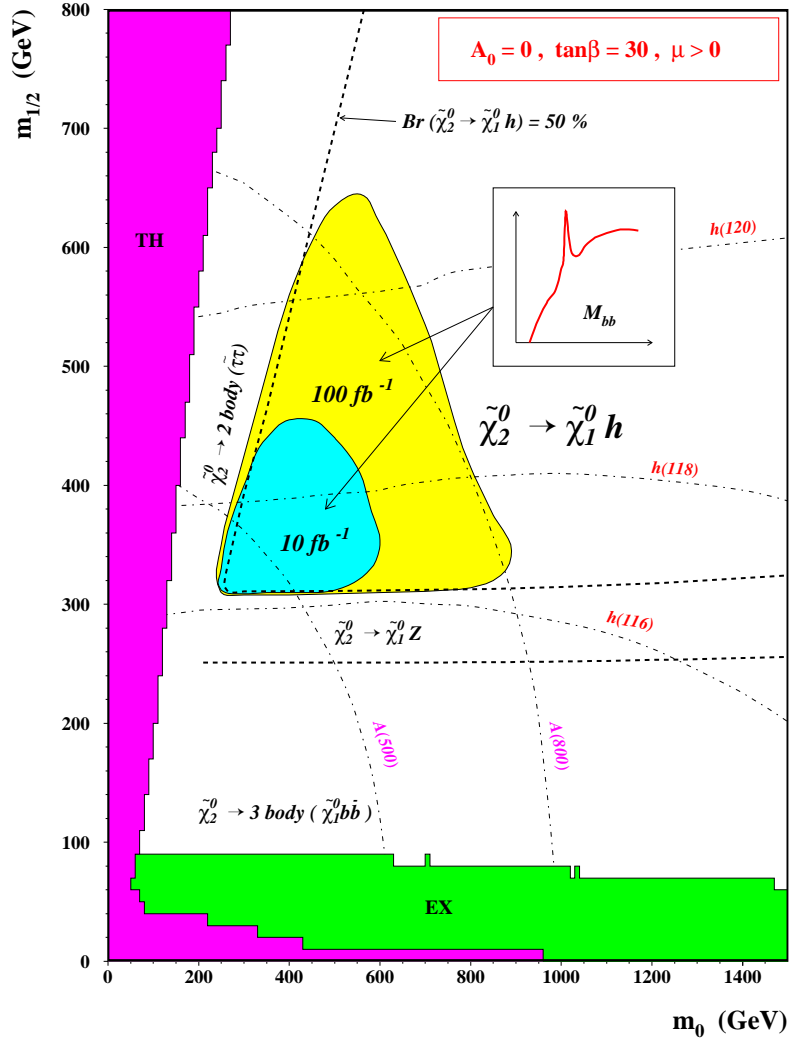


Figure 9.10: 5σ visibility contours of $h \rightarrow b\bar{b}$ for $\tan\beta = 30$, $A_0 = 0$ and $\mu < 0$ with 10 and 100 fb^{-1} . See also comments in text.

10 Sensitivity to sparticle masses and model parameters

10.1 Establishing the SUSY mass scale

Once a deviation from the SM expectations is established in a number of final states indicating the presence of SUSY, the determination of the “SUSY mass scale” would become the first objective. The production and decay of high mass strongly interacting particles, as would be the case for gluinos and squarks, would lead to hard event kinematics, with a number of hard central jets in the final state accompanied by significant missing transverse energy due to escaping LSPs and neutrinos. As suggested in [48], we can characterize the “hardness” of an event by the scalar sum of transverse energies of the four hardest jets and the missing transverse energy:

$$E_T^{sum} = E_T^1 + E_T^2 + E_T^3 + E_T^4 + E_T^{miss} \quad (10)$$

This variable is rather insensitive to the transverse energy flow induced by event pile-up since it takes into account only the calorimetric cells which are attached to a jet.

The following SM processes have been considered as a background to SUSY strong production: $t\bar{t}$, W/Z + jets and QCD jet production (PYTHIA 2 \rightarrow 2 processes including $b\bar{b}$). Events are selected by requiring:

- $E_T^{miss} > \max(100 \text{ GeV}, 0.2E_T^{sum})$;
- ≥ 4 jets with $E_T > 50 \text{ GeV}$, the hardest with $E_T > 100 \text{ GeV}$ in $|\eta| < 5$;
- Lepton veto: events are rejected if they contain an isolated lepton with $p_T > 10 \text{ GeV}$.

Figure 10.1 shows the E_T^{sum} distributions for a representative mSUGRA point (with $m_0 = 300 \text{ GeV}$, $m_{1/2} = 150 \text{ GeV}$, $A_0 = -600 \text{ GeV}$, $\tan\beta = 2$, $\mu > 0$) and the SM background. The background, which is dominated by $t\bar{t}$ and W/Z + jets productions, is small compared to the SUSY signal.

The peak value of the E_T^{sum} spectrum for the inclusive SUSY signal provides a good estimate of the SUSY mass scale, defined as in [48]:

$$M_{SUSY} = \min(M_{\tilde{g}}, M_{\tilde{q}}) \quad (11)$$

and where $M_{\tilde{q}}$ is the mass of squarks from the first two generations. Figure 10.2 shows the relationship between the peak value of the E_T^{sum} spectrum and M_{SUSY} for 100 mSUGRA models chosen at random with $100 < m_0 < 500 \text{ GeV}$, $100 < m_{1/2} < 500 \text{ GeV}$, $-1000 < A_0 < 1000 \text{ GeV}$, $1 < \tan\beta < 12$ and $\text{sign}(\mu) = \pm 1$ [49]. At each point the peak value of E_T^{sum} was found by a Gaussian fit. The very strong correlation between the peak value of E_T^{sum} and M_{SUSY} as can be seen in Fig. 10.2 could provide a first estimate of the relevant SUSY mass scale.

10.2 Constraints from $\tilde{\chi}_2^0$ leptonic decays

Establishing the sparticle spectrum, the measurement of sparticle masses and the model parameters will be the next step in uncovering SUSY, once its existence and its mass scale

have been established. In R -parity conserving models undetectable LSP's make this task nontrivial.

As mentioned previously, some specific SUSY decays are particularly useful for the determination of sparticle masses. The $\tilde{\chi}_2^0$ leptonic decays may not only provide the first indication for SUSY in significant regions of mSUGRA parameter space, but also allow us to obtain information on some sparticle masses by measuring the endpoint of the dilepton invariant mass spectrum and exploiting its specific kinematics. Before discussing how to exploit this feature in inclusive two- and three-lepton final states, which is a recent development, let us first review the l^+l^- invariant mass spectrum in the exclusive $\tilde{\chi}_1^\pm \tilde{\chi}_2^0 \rightarrow 3l^\pm + \text{no jets} + E_T^{\text{miss}}$ final state, first described in [40] for three-body decays $\tilde{\chi}_2^0 \rightarrow l^+l^- \tilde{\chi}_1^0$. In this case the upper limit of dilepton invariant mass spectrum is:

$$M_{l^+l^-}^{\text{max}} = M_{\tilde{\chi}_2^0} - M_{\tilde{\chi}_1^0} \quad (12)$$

Figure 10.3 shows the expected l^+l^- mass spectrum for mSUGRA “Point 1” (see Table 1.1) in the exclusive $\tilde{\chi}_1^\pm \tilde{\chi}_2^0 \rightarrow 3l^\pm + \text{no jets} + (E_T^{\text{miss}})$ channel arising from direct (Electroweak) $\tilde{\chi}_1^\pm \tilde{\chi}_2^0$ production. The SM and internal SUSY backgrounds are also shown, all for $L_{\text{int}} = 10^4 \text{ pb}^{-1}$ [10]. The edge is at 52 GeV and with these statistics it could be measured with a precision better than 1 GeV. This measurement of $M_{l^+l^-}^{\text{max}} = M_{\tilde{\chi}_2^0} - M_{\tilde{\chi}_1^0} = 52 \text{ GeV}$ should allow, within mSUGRA, estimation of $M_{\tilde{\chi}_1^0}$, $M_{\tilde{\chi}_2^0}$, $M_{\tilde{\chi}_1^\pm}$, $M_{\tilde{g}}$ and $m_{1/2}$ through eqs. (2) – (4) as discussed in section 2.1.

Even more information can be extracted from the $\tilde{\chi}_2^0$ two-body (cascade) decays $\tilde{\chi}_2^0 \rightarrow l^\pm \tilde{l}_{L,R}^\mp \rightarrow l^+l^- \tilde{\chi}_1^0$. The kinematical upper limit in this case is:

$$M_{l^+l^-}^{\text{max}} = \frac{\sqrt{(M_{\tilde{\chi}_2^0}^2 - M_l^2)(M_l^2 - M_{\tilde{\chi}_1^0}^2)}}{M_{\tilde{l}}} \quad (13)$$

i.e. it is sensitive also to the intermediate slepton mass. In this case, however, the measurement of only the edge position does not provide information on the masses of all the involved particles unambiguously. Nonetheless, as discussed in the following, through analyses of some kinematical distributions, the masses of $\tilde{\chi}_1^0$, $\tilde{\chi}_2^0$ and of the slepton can be determined with reasonable precision [9]. Therefore, with two-body decays one can constrain $m_{1/2}$ and m_0 through eqs. (2), (3) and (5)/(6), if the information on $\tan\beta$ is available, for example from the Higgs sector of the model.

Direct leptonic decays of the $\tilde{\chi}_2^0$ dominate below $m_{1/2} \lesssim 200 \text{ GeV}$ for nearly all values of m_0 ; there is also a small region of high $m_{1/2}$ where direct three-body decays are open, as can be seen from Fig. 2.3a. Cascade leptonic decays of $\tilde{\chi}_2^0$ via \tilde{l}_L (Fig. 2.3b) or \tilde{l}_R (Fig. 2.3c) occur at almost any $m_{1/2}$ as soon as $m_0 \lesssim 0.5m_{1/2}$, where $\tilde{\chi}_2^0$ is heavier than the sleptons.

The expected position of the edge as a function of $m_{1/2}$ is given in Fig. 10.4 for two different values of the common scalar mass: $m_0 = 400 \text{ GeV}$ and 100 GeV . The box size in the Figure is proportional to the branching ratio $B(\tilde{\chi}_2^0 \rightarrow l^+l^- + \text{invisible})$. At $m_0 = 400 \text{ GeV}$ the $\tilde{\chi}_2^0$ has only direct three-body decays for all values of $m_{1/2}$ up to $m_{1/2} \sim 180 \text{ GeV}$, where “spoiler” modes open up. Measurement of $M_{l^+l^-}^{\text{max}}$ thus yields the common gaugino mass parameter $m_{1/2}$ unambiguously in this region. For $m_0 = 100 \text{ GeV}$ the situation is more complicated. Here at different values of $m_{1/2}$ different leptonic decay modes of $\tilde{\chi}_2^0$ dominate: direct decays up to $m_{1/2} \lesssim 130 \text{ GeV}$; cascade decays via \tilde{l}_R at 130 GeV

$\lesssim m_{1/2} \lesssim 250$ GeV and, finally, cascade decays via \tilde{l}_L at $m_{1/2} \gtrsim 250$ GeV. In some regions two $\tilde{\chi}_2^0$ decay channels coexist.

The essential issue, for the exploitation of an observed edge, is knowing whether the $\tilde{\chi}_2^0$ decay chain is three-body or two-body. In general, the p_T spectra of leptons from $\tilde{\chi}_2^0$ two-body decays are more asymmetric compared to the three-body decays. To characterize the asymmetry we introduce the variable [9]:

$$\mathcal{A} = \frac{p_T^{max} - p_T^{min}}{p_T^{max} + p_T^{min}} \quad (14)$$

where p_T^{max} (p_T^{min}) corresponds to the lepton of maximum (minimum) transverse momentum.

An example of decay type determination is discussed for the mSUGRA point $m_0 = 100$ GeV, $m_{1/2} = 150$ GeV. The sparticle masses are $M_{\tilde{\chi}_2^0} = 135$ GeV, $M_{\tilde{\chi}_1^0} = 65$ GeV $M_{\tilde{l}_R} = 120$ GeV and $\tilde{\chi}_2^0$ decays via $\tilde{\chi}_2^0 \rightarrow l^\pm \tilde{l}_R^\mp \rightarrow l^+ l^- + \tilde{\chi}_1^0$ with a probability of 0.54. Figure 10.5 shows the dilepton mass spectrum for this parameter space point in the inclusive 3 *lepton* events for an integrated luminosity of $L_{int} = 5 \times 10^3$ pb $^{-1}$. The expected SM background is also shown. Of the three leptons with $p_T > 15$ GeV only the two of opposite charge and same flavor, which enter the invariant mass distribution, are required to be isolated. A very spectacular edge is situated at $\simeq 52$ GeV. There is a second and much weaker edge at $\simeq 69$ GeV which is due to direct three-body decays with $B(\tilde{\chi}_2^0 \rightarrow l^+ l^- + \tilde{\chi}_1^0) = 0.05$. Thus at this mSUGRA point there are two leptonic decay modes with very different branching ratios. To identify the decay chain responsible for the first edge, we look at the asymmetry \mathcal{A} distribution of the lepton pairs with $M_{l^+ l^-} < 52$ GeV. Figure 10.6 (full line) shows the \mathcal{A} distribution for these events. The pronounced asymmetry in p_T indicates the cascade nature of decays. If we now pick up the lepton pairs from the mass interval $55 < M_{l^+ l^-} < 69$ GeV below the second edge, then the corresponding \mathcal{A} distribution peaks near zero, as seen in Fig. 10.6 (dashed-dotted line), indicating the three-body decay type of these events. To illustrate the generality of this approach, two more examples of \mathcal{A} distributions are also shown in Fig. 10.6 for mSUGRA parameter space points $m_0 = 100$ GeV, $m_{1/2} = 400$ GeV with pure 2-body decays (dashed line) and $m_0 = 400$ GeV, $m_{1/2} = 150$ GeV with pure 3-body decays (dotted line), respectively.

Once the decay type is determined, the next step is to extract the masses of the particles involved, the $\tilde{\chi}_2^0$, $\tilde{\chi}_1^0$ and \tilde{l} . In our example case of two-body decay the $l^+ l^-$ kinematical upper limit is

$$M_{l^+ l^-}^{max} = \frac{\sqrt{(M_{\tilde{\chi}_2^0}^2 - M_l^2)(M_l^2 - M_{\tilde{\chi}_1^0}^2)}}{M_{\tilde{l}}} = 52 \text{ GeV}. \quad (15)$$

This equation can be satisfied by an infinite number of $M_{\tilde{\chi}_1^0}$, $M_{\tilde{\chi}_2^0}$ and $M_{\tilde{l}}$ mass combinations. To find a solution, we assume $M_{\tilde{\chi}_2^0} = 2M_{\tilde{\chi}_1^0}$ and generate $\tilde{\chi}_2^0 \rightarrow l^\pm \tilde{l}^\mp \rightarrow l^+ l^- \tilde{\chi}_1^0$ two-body sequential decays for various assumptions on $M_{\tilde{l}}$ ($M_{\tilde{\chi}_1^0}$), e.g. from 70 GeV to 150 GeV in 10 GeV steps, with the $\tilde{\chi}_1^0$ mass constrained to provide the “observed” position of the edge. For each value of $M_{\tilde{l}}$, one obtains two series of solutions for equation (15). Some of them are shown in Fig 10.7 in terms of dilepton invariant mass and p_T -asymmetry distributions, in Figs. 10.7a,c for “low mass” solutions and Figs. 10.7b,d for “high mass” solutions [9]. The solid lines in Figs. 10.7a-c correspond to the “observed” spectra and the

dotted histograms are the results obtained from eq. (15). Clearly, the “observed” l^+l^- invariant mass spectrum itself and the p_T -asymmetry distributions allow us to eliminate the “high mass” solutions of eq. (15). To find the best combination of $M_{\tilde{\chi}_1^0}$, $M_{\tilde{\chi}_2^0}$ and $M_{\tilde{l}}$ among the “low mass” solutions, we perform a χ^2 -test on the p_T -asymmetry distributions, taking into account only the difference in shapes, but not the normalization. The result is shown in Fig. 10.8. The horizontal line in this Figure corresponds to the expected uncertainty of simulations due to the detector resolution, background estimates, initial/final state radiations, etc. We obtain the following precisions on masses: $\delta M_{\tilde{\chi}_1^0} \lesssim 5$ GeV, $\delta M_{\tilde{l}} \lesssim 10$ GeV. The use of the total number of observed events, as well as the dilepton invariant mass spectrum itself in a combined χ^2 -test would further improve these results.

As shown above for the mSUGRA point under consideration, the second edge in the dilepton mass spectrum at $M_{l^+l^-}^{max} = 69$ GeV (see Fig. 10.6) is due to direct three-body decays of $\tilde{\chi}_2^0$. Using now two measured edge position values and assuming again $M_{\tilde{\chi}_2^0} = 2M_{\tilde{\chi}_1^0}$, two solutions for the slepton mass can be directly obtained $M_{\tilde{l}} = 120$ GeV and $M_{\tilde{l}} = 77$ GeV. The corresponding dilepton mass spectra for these two solutions are shown in Fig. 10.9. The clear difference in the predicted spectra (the first edge in Fig. 10.5 which proceeds through \tilde{l} vs. Fig. 10.9) allows us to eliminate the $M_{\tilde{l}} = 77$ GeV solution. At this particular mSUGRA point the use of two observable edges provides a precision of $\delta M_{\tilde{\chi}_1^0, \tilde{l}} \lesssim 1$ GeV [41, 9].

Another example of a double edge is given in Fig. 10.10 for the mSUGRA point (50 GeV, 125 GeV). Here the sparticle masses are $M_{\tilde{\chi}_2^0} = 116$ GeV, $M_{\tilde{\chi}_1^0} = 55$ GeV, $M_{\tilde{l}_L} = 110$ GeV, $M_{\tilde{l}_R} = 78$ GeV. In this case two two-body decays, via left and right sleptons coexist with the comparable branching ratios $B(\tilde{\chi}_2^0 \rightarrow l^\pm \tilde{l}_L^\mp \rightarrow l^+l^- \tilde{\chi}_1^0) = 0.037$ and $B(\tilde{\chi}_2^0 \rightarrow l^\pm \tilde{l}_R^\mp \rightarrow l^+l^- \tilde{\chi}_1^0) = 0.013$ and their analysis could proceed as indicated above providing a strong constraint on the underlying model.

10.3 Determination of the squark mass

The observation of an edge in the dilepton mass spectrum, resulting from $\tilde{\chi}_2^0$ leptonic decays allows not only the determination of $\tilde{\chi}_1^0$, $\tilde{\chi}_2^0$, (\tilde{l}) masses, but also enables the momenta to be fixed. At the upper limit of the l^+l^- spectrum in direct three-body decays $\tilde{\chi}_2^0 \rightarrow l^+l^- \tilde{\chi}_1^0$, the $\tilde{\chi}_1^0$ is produced at rest in the $\tilde{\chi}_2^0$ rest frame. Assuming knowledge of the $\tilde{\chi}_1^0$ mass (or, equivalently, knowledge of a relation between $\tilde{\chi}_1^0$ and $\tilde{\chi}_2^0$ masses), one can then, for events at the l^+l^- edge, reconstruct the $\tilde{\chi}_2^0$ momentum vector in the laboratory frame:

$$p_{\tilde{\chi}_2^0} = (1 + M_{\tilde{\chi}_1^0}/M_{l^+l^-}) \times p_{l^+l^-} \quad (16)$$

Once the four-momentum vector of the $\tilde{\chi}_2^0$ is determined, one can search for a resonance structure in, e.g. the $\tilde{\chi}_2^0 + \text{jet(s)}$ invariant mass distributions. This technique can be put to a good use to reconstruct \tilde{g}/\tilde{q} masses [48] as the next-to-lightest neutralinos are abundantly produced in gluino and squark decays, see e.g. Figs. 2.5a,b.

An example of the \tilde{q} mass reconstruction is given for mSUGRA point with $m_0 = 300$ GeV, $m_{1/2} = 150$ GeV, $A_0 = -600$ GeV, $\tan\beta = 2$ and $\mu > 0$, discussed in section 10.1. The masses of relevant sparticles are 463 GeV, 495 GeV, 151 GeV, 425 GeV, 112 GeV and 57 GeV for $\tilde{q}_{L,R}$ (squarks of the first two generations), \tilde{t}_2 , \tilde{t}_1 , \tilde{g} , $\tilde{\chi}_2^0$ and $\tilde{\chi}_1^0$, respectively, and the total SUSY cross-section (452 pb) is largely dominated by $\sigma_{\tilde{t}_1\tilde{t}_1} = 195$ pb, $\sigma_{\tilde{g}\tilde{q}_{L,R}} = 109$

pb, $\sigma_{\tilde{g}\tilde{g}} = 77$ pb productions. Gluinos are lighter than squarks of the first two generations, but their decays to stop and sbottom are kinematically allowed, giving several b -jets at the end of the decay chain. Right squarks \tilde{q}_R predominantly decay to $\tilde{\chi}_1^0 + q$ or to $\tilde{g} + q$. Finally, the Left squarks \tilde{q}_L have the interesting for us decay mode to $\tilde{\chi}_2^0 + q$ with a branching ratio of 0.27. To extract this latter decay chain from internal SUSY and SM backgrounds we have adopted the following procedure [49].

- Require two isolated leptons with $p_T > 10$ GeV; and an angular separation $\Delta R_{l+l-} = \sqrt{\Delta\eta^2 + \Delta\phi^2} < 1$.
- The scalar sum of calorimeter cell transverse energies and of muon transverse momenta, $\Sigma E_T^{calo} + p_T^\mu > 600$ GeV to ensure production of hard events. Require $E_T^{miss} > 100$ GeV.
- The l^+l^- invariant mass has been reconstructed and the edge position at $\simeq 54$ GeV has been observed. The p_T -asymmetry distribution of dilepton pairs indicates it is due to a the three-body decay of type $\tilde{\chi}_2^0 \rightarrow l^+l^-\tilde{\chi}_1^0$.
- Events with a dilepton mass close to the kinematical limit, i.e. $49 \text{ GeV} < M_{l+l-} < 54 \text{ GeV}$, have been selected for further analysis; the $\tilde{\chi}_2^0$ momentum has been determined using eq. (16).
- The invariant mass of the $\tilde{\chi}_2^0$ and each non- b -jet with $E_T^{jet} > 300$ GeV has then been reconstructed. Such a hard jet is unlikely to originate from a QCD radiation. Furthermore, due to the large mass difference $M_{\tilde{q}_L} - M_{\tilde{\chi}_2^0} = 351$ GeV the E_T -spectrum of quark-jets from the \tilde{q}_L decay is harder than both the inclusive SUSY and SM jet spectra. Hence this requirement enhances the \tilde{q}_L signal.

Figure 10.11 shows the reconstructed $\tilde{\chi}_2^0 + \text{jet}$ mass spectrum for SUSY and SM events for an integrated luminosity of $L_{int} = 10^4 \text{ pb}^{-1}$. As a source of the SM backgrounds we have considered $t\bar{t}$, $W/Z + \text{jets}$, WW , ZZ , ZW and $b\bar{b}$ processes. Their contribution is negligible compared to the internal SUSY background. A peak at ~ 450 GeV is clearly visible and a Gaussian plus polynomial fit yields a value of 447 ± 4 GeV (statistical error) for the reconstructed \tilde{q}_L mass. Significant systematic uncertainties are associated with this measurement due to the jet reconstruction algorithm, energy scale, approximations in determining the $\tilde{\chi}_2^0$ four-momentum, in particular the dilepton mass interval which has been chosen for analysis, etc. The overall systematic uncertainty is estimated to be about $\pm 5\%$. A much more detailed analysis is needed to understand fully the achievable precision [49].

As a concluding remark, the observation of a resonance peak in the $\tilde{\chi}_2^0 + \text{jet}$ invariant mass spectrum would be interpreted as a squark undergoing a two-body decay to $\tilde{\chi}_2^0$ and a quark. The technique described here is also applicable for gluino mass reconstruction, for example in $\tilde{g} \rightarrow q\bar{q}\tilde{\chi}_2^0$ with subsequent decay of $\tilde{\chi}_2^0 \rightarrow \tilde{\chi}_1^0$.

10.4 Sensitivity to model parameters in $3l + \text{no jets} + E_T^{miss}$ final states

Since information on $m_{1/2}$ can be obtained from the l^+l^- edge position in regions of parameter space where it is visible, one can then attempt to constrain the m_0 parameter

Table 10.1: SUSY cross-sections (in fb) after selection. Events are counted below “observed” edge at 54 GeV.

Point	$\tilde{\chi}_1^\pm \tilde{\chi}_2^0$	$\tilde{g}\tilde{g} \tilde{g}\tilde{q} \tilde{q}\tilde{q}$	$\tilde{g}\tilde{\chi} \tilde{q}\tilde{\chi}$	$\tilde{\chi}\tilde{\chi}$	$l\bar{l} \tilde{l}\tilde{\nu} \tilde{\nu}\tilde{\nu}$
(100,100)	71.6	14.1	11.3	5.9	14.5
(150,100)	53.8	15.9	5.3	2.6	5.3
(200,100)	45.6	11.9	6.0	4.0	0.0
(300,100)	29.7	0.5	1.0	0.5	0.0
(400,100)	23.0	0.0	0.0	0.0	0.0
(1000,100)	15.7	0.0	0.0	0.0	0.0
(1800,100)	12.3	0.0	0.0	0.0	0.0

Table 10.2: SM cross-sections (in fb) after selection. Events are counted below “observed” edge at 54 GeV.

WZ	ZZ	$t\bar{t}$	Wtb	Zbb	bb
1.42	0.48	1.07	0.46	0.27	< 0.15

from the event rates. Let us first discuss the case of $3l + no\ jets + E_T^{miss}$ events [10]. For a fixed $m_{1/2}$ the $\sigma \cdot B(\tilde{\chi}_1^\pm \tilde{\chi}_2^0 \rightarrow 3l + invisible)$ decreases monotonically with increasing m_0 in the region where $\tilde{\chi}_2^0$ has direct three-body decays. Table 10.1 gives the expected SUSY event rates for a series of points with different m_0 but with fixed $m_{1/2} = 100$ GeV, i.e. corresponding to approximately the same M_{l+l-}^{max} . The remaining parameters are $\tan\beta = 2$, $A_0 = 0$, $\mu < 0$. All expected SUSY sources of such events are included. The applied cuts are (Set 1 in section 8):

- $3l$ with $p_T^l > 15$ GeV in $|\eta^l| < 2.4(2.5)$ for muons (electrons);
- Isolation: no track with $p_T > 1.5$ GeV in a cone $R = 0.3$ about the lepton direction, for all leptons;
- Jet veto: no jet with $E_T^{jet} > 25$ GeV in $|\eta^{jet}| < 3.5$;
- Z -mass cut: no lepton pair with $M_{l+l-} > 81$ GeV.

Table 10.3: statistical ($L_{int} = 10^4 \text{ pb}^{-1}$) and systematic errors on m_0 measurement for $m_{1/2} \sim 100$ GeV.

Source	$m_0 \in [100 \text{ GeV}; 300 \text{ GeV}]$	$m_0 \in [300 \text{ GeV}; 400 \text{ GeV}]$
statistical error	$8 \div 20 \text{ GeV}$	$20 \div 55 \text{ GeV}$
edge measurement precision	$4 \div 8 \text{ GeV}$	$8 \div 25 \text{ GeV}$
uncertainty on SM background	$2.5 \div 9 \text{ GeV}$	$9 \div 30 \text{ GeV}$
uncertainty on luminosity	$27 \div 35 \text{ GeV}$	$35 \div 85 \text{ GeV}$
statistical \oplus systematic error	$30 \div 45 \text{ GeV}$	$45 \div 105 \text{ GeV}$

Table 10.4: SUSY cross-sections (in fb) after selection. Events are counted below the “observed” edge at 72 GeV.

Point	$\tilde{\chi}_1^\pm \tilde{\chi}_2^0$	$\tilde{g}\tilde{g} \tilde{g}\tilde{q} \tilde{q}\tilde{q}$	$\tilde{g}\tilde{\chi} \tilde{q}\tilde{\chi}$	$\tilde{\chi}\tilde{\chi}$	$\tilde{l}\tilde{l} \tilde{l}\tilde{\nu} \tilde{\nu}\tilde{\nu}$
(150,150)	26.3	0.3	1.5	1.3	2.9
(200,150)	19.9	0.7	0.8	0.8	0.8
(300,150)	10.7	0.5	0.1	0.1	0.0
(400,150)	6.4	0.0	0.0	0.1	0.0
(1000,150)	3.6	0.0	0.0	0.0	0.0
(1800,150)	3.3	0.0	0.0	0.0	0.0

Table 10.5: SM cross-sections (in fb) after selection. Events are counted below the “observed” edge at 72 GeV.

WZ	ZZ	$t\bar{t}$	Wtb	Zbb	bb
1.53	0.42	1.66	0.50	0.33	< 0.15

From the selected events we count the ones with $M_{l+l^-} < M_{l+l^-}^{max} = 54$ GeV. Contributions from different SUSY sources – $\tilde{\chi}_1^\pm \tilde{\chi}_2^0$ direct production, strong production, gluino/squark associated production, gaugino pair and slepton pair productions – are given separately. The main contribution is always due to $\tilde{\chi}_1^\pm \tilde{\chi}_2^0$ direct production, but below $m_0 \sim 300$ GeV other SUSY processes also contribute significantly.

The expected SM event rates after selection cuts are given in Table 10.2. All SM processes together amount 3.85 fb, which is always smaller than the $\tilde{\chi}_1^\pm \tilde{\chi}_2^0$ direct production rate at $m_{1/2} = 100$ GeV, and much smaller than that for $m_0 \lesssim 300$ GeV (Table 10.1).

Table 10.1 shows that the data selection does not wash out significantly the event rate sensitivity to m_0 expected from the behavior of $\sigma \cdot B$ for $\tilde{\chi}_1^\pm \tilde{\chi}_2^0$ direct production (Fig. 2.4). Figure 10.12a shows N_{SUSY} versus m_0 for $m_{1/2} = 100$ GeV, where N_{SUSY} is the SM-background-subtracted number of $3l + no\ jets + E_T^{miss}$ events surviving cuts for an integrated luminosity of $L_{int} = 10^4 pb^{-1}$. The error band includes both statistical and systematic uncertainties; The systematic uncertainties include effects due to the edge measurement precision, the uncertainty on the rate of SM processes and a 10% uncertainty

Table 10.6: statistical ($L_{int} = 10^5 pb^{-1}$) and systematic errors on m_0 measurement for $m_{1/2} \sim 150$ GeV.

Source	$m_0 \in [150 \text{ GeV}; 300 \text{ GeV}]$	$m_0 \in [300 \text{ GeV}; 400 \text{ GeV}]$
statistical error	5 ÷ 10 GeV	10 ÷ 18 GeV
edge measurement precision	2 ÷ 8 GeV	5 ÷ 8 GeV
uncertainty on SM background	9 ÷ 24 GeV	24 ÷ 55 GeV
uncertainty on luminosity	28 ÷ 30 GeV	30 ÷ 40 GeV
statistical \oplus systematic error	32 ÷ 40 GeV	40 ÷ 75 GeV

on the luminosity measurement. The resulting error on m_0 is 30 to 45 GeV for $100 \text{ GeV} \lesssim m_0 \lesssim 300 \text{ GeV}$ and 45 to 105 GeV for $300 \text{ GeV} \lesssim m_0 \lesssim 400 \text{ GeV}$. Above $m_0 \simeq 400 \text{ GeV}$ sensitivity to m_0 is lost (see also Fig. 2.4). Table 10.3 gives the statistical and the various systematic uncertainty contributions to the m_0 measurement error; the error on the integrated luminosity is the dominant contribution [10].

For $m_{1/2} = 150 \text{ GeV}$ the expected event rate is much lower than for $m_{1/2} = 100 \text{ GeV}$, and $L_{int} = 10^5 \text{ pb}^{-1}$ is needed to obtain a reasonable precision on m_0 . The cuts applied are the same as for the $m_{1/2} = 100 \text{ GeV}$ points, except for a relaxed jet veto requirement (Set 2 in section 8): no jet with $E_T^{jet} > 30 \text{ GeV}$ in $|\eta^{jet}| < 3$. Selected events are counted below the l^+l^- edge at 72 GeV. The event rates for the mSUGRA points and the SM background processes are given in Tables 10.4 and 10.5. After cuts the sum of SM processes is 4.6 fb. The SUSY/SM ratio exceeds 1.4 for $m_0 \lesssim 400 \text{ GeV}$. Figure 10.12b shows N_{SUSY} versus m_0 for $m_{1/2} = 150 \text{ GeV}$ assuming $L_{int} = 10^5 \text{ pb}^{-1}$. The sensitivity to m_0 is 32 to 40 GeV for $150 \text{ GeV} \lesssim m_0 \lesssim 300 \text{ GeV}$ and 40 to 75 GeV for $300 \text{ GeV} \lesssim m_0 \lesssim 400 \text{ GeV}$. Contributions from the different sources of uncertainty are given in Table 10.6. The error on the luminosity is still the main source of uncertainty, although the error on the SM background now has a significant influence due to the lower signal/background ratio compared to the $m_0=100 \text{ GeV}$ case.

10.5 Sensitivity to model parameters in inclusive $l^+l^- + E_T^{miss} + jets$ final states

More generally, information on event rates from the observation of an edge in inclusive studies can also be used to constraint the model parameters. Let us discuss the case of $l^+l^- + E_T^{miss} (+ jets)$ final states [7]. Within mSUGRA the expected edge position $M_{l^+l^-}^{max}$ in the dilepton mass distribution can be obtained from equations (12), (13). Figure 10.13 shows the contours of expected values of $M_{l^+l^-}^{max}$ in the $(m_0, m_{1/2})$ parameter plane. Different lines with same values of $M_{l^+l^-}^{max}$ belong to domains I, II and III which correspond to the three possible decay modes of $\tilde{\chi}_2^0$ to $l^+l^- \tilde{\chi}_1^0$ final states. The regions of $M_{l^+l^-}^{max}$ accessible at LHC are:

for	$\tilde{\chi}_2^0 \rightarrow \tilde{\chi}_1^0 l^+ l^-$	–	$50 \text{ GeV} \lesssim M_{l^+l^-}^{max} \lesssim 90 \text{ GeV}$	(I)
	$\tilde{\chi}_2^0 \rightarrow \tilde{l}_R l$	–	$M_{l^+l^-}^{max} \gtrsim 10 \text{ GeV}$	(II)
	$\tilde{\chi}_2^0 \rightarrow \tilde{l}_L l$	–	$M_{l^+l^-}^{max} \gtrsim 20 \text{ GeV}$	(III)

The first case is limited by the appearance of the spoiler modes $\tilde{\chi}_2^0 \rightarrow h^0(Z^0)\tilde{\chi}_1^0$. In the last two cases the upper limit on accessible $M_{l^+l^-}^{max}$ is determined only by the available statistics. A measurement of $M_{l^+l^-}^{max}$ in the inclusive dilepton mass distribution, with a single edge, thus constrains the model parameters in general to three lines in the $(m_0, m_{1/2})$ parameter plane. In the case of $M_{l^+l^-}^{max} \gtrsim 90 \text{ GeV}$ the constraint is stronger, as there are just two possible lines. The most favorable case is when the measured $M_{l^+l^-}^{max}$ value is large, $M_{l^+l^-}^{max} \gtrsim 180 \text{ GeV}$. Then one is left with a single line in the $(m_0, m_{1/2})$ parameter plane. The observation of two edges due to the simultaneous presence of two types of $\tilde{\chi}_2^0$ decay modes to $l^+l^- \tilde{\chi}_1^0$ would give even stronger constraints, see Refs. [7, 9, 41].

The proper line in the $(m_0, m_{1/2})$ plane can be determined by the method discussed in [7]. When the correct $M_{l^+l^-}^{max}$ line is identified, the next step is to find the point $(m_0, m_{1/2})$ on this line. In general the cross section decreases with increasing $m_{1/2}$ and m_0 , thus

Table 10.7: $M_{l^+l^-}^{max}$ values (in GeV) at the investigated $(m_0, m_{1/2})$ points from domain I,
 $\tilde{\chi}_2^0 \rightarrow \tilde{\chi}_1^0 + l^+ + l^-$.

	(120,160)	(130,160)	(180,160)	(200,160)	(220,160)	(240,160)	(290,160)	(350,160)
$M_{l^+l^-}^{max}$	74	74	74	74	74	74	74	73.7

Table 10.8: $M_{l^+l^-}^{max}$ values (in GeV) at the investigated $(m_0, m_{1/2})$ points from domain II,
 $\tilde{\chi}_2^0 \rightarrow \tilde{l}_R^\pm + l^\mp \rightarrow \tilde{\chi}_1^0 + l^+ + l^-$.

$(m_0, m_{1/2}) \rightarrow$	(80,162)	(90,170)	(105,180)	(110,187)	(120,195)
$M_{l^+l^-}^{max}$	74	74	73	75	73

Table 10.9: $M_{l^+l^-}^{max}$ values (in GeV) at the investigated $(m_0, m_{1/2})$ points from domain III, $\tilde{\chi}_2^0 \rightarrow \tilde{l}_L^\pm + l^\mp \rightarrow \tilde{\chi}_1^0 + l^+ + l^-$.

$(m_0, m_{1/2}) \rightarrow$	(20,195)	(40,210)	(60,230)	(80,255)
$M_{l^+l^-}^{max}$	73	73	73	73

the study of the event rate along the corresponding $M_{l^+l^-}^{max}$ lines will determine the point in parameter space. As an example of the general situation let us discuss the case of $M_{l^+l^-}^{max} = 74 \pm 1$ GeV, with three lines corresponding to domains I,II and III, respectively. The $(m_0, m_{1/2})$ points analysed are given in tables 10.7-10.9.

As this is an inclusive analysis, we assume a low luminosity of $L_{int} = 10^3 \text{ pb}^{-1}$. We discuss first domain III, where the situation is simplest. To minimize the uncertainties due to background, we require $p_T^{l_{1,2}} > 15$ GeV and $E_T^{miss} > 130$ GeV. The dependence of the resulting event rate on m_0 is shown in Fig. 10.14. The errors are calculated taking into account the statistical error and assuming a systematic error of 30 % for the background uncertainty; a systematic error due to the precision of the edge position measurement is also taken into account. From the observed event rate m_0 can be determined with good precision, $\delta m_0 \simeq 4$ GeV. The parameter $m_{1/2}$ is then given by the $M_{l^+l^-}^{max}$ -line in the $(m_0, m_{1/2})$ plane (Fig. 10.13). The precision obtained in such a way is $\delta m_{1/2} \simeq 4$ GeV.

In domain II, the event rate along a line of definite $M_{l^+l^-}^{max}$ first increases and then decreases with increasing m_0 , Fig. 10.15. This is mainly due to the change in the branching ratios. The event rate thus does not determine m_0 uniquely: a given event rate corresponds in general to two m_0 values. The ambiguity can, however, be solved at high luminosity $L_{int} = 10^5 \text{ pb}^{-1}$, when two edges in the $M_{l^+l^-}$ distribution can be observed [7].

For domain I, the m_0 dependence of the event rate is shown in Fig. 10.16a, again for $M_{l^+l^-}^{max} \simeq 74 \pm 1$ GeV. There is a steep increase of the rate at $m_0 \simeq 120 - 130$ GeV. This is due to the decay channel $\tilde{\chi}_2^0 \rightarrow l^+l^- \tilde{\chi}_1^0$ just opening up in this region. As can be seen from Fig. 10.16a, there is an ambiguity in the determination of m_0 if the event rate is in the region $3700 \lesssim N_{EV} \lesssim 5600$ or $120 \text{ GeV} \lesssim m_0 \lesssim 240 \text{ GeV}$. Additional information can however be obtained from the average number of jets $\langle N_{jet} \rangle$ in the events. Figure 10.16b shows $\langle N_{jet} \rangle$ as a function of m_0 . $\langle N_{jet} \rangle$ is increasing with m_0 as more jets are produced with increasing squark-mass. With the measured $\langle N_{jet} \rangle$ we can resolve the ambiguity in the region $120 \text{ GeV} \lesssim m_0 \lesssim 240 \text{ GeV}$ and determine m_0 with $\delta m_0 \simeq 7\text{-}3$ GeV.

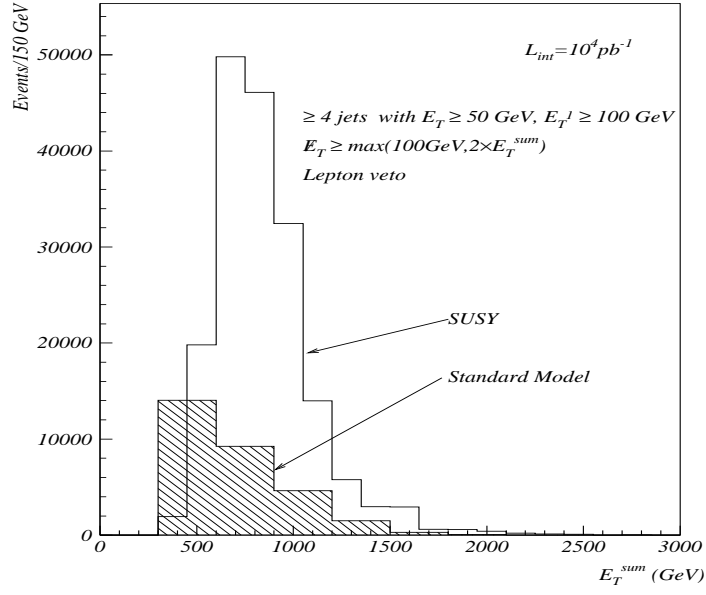


Figure 10.1: E_T^{sum} distribution for both the inclusive SUSY and the SM backgrounds after the event selection cuts have been applied.

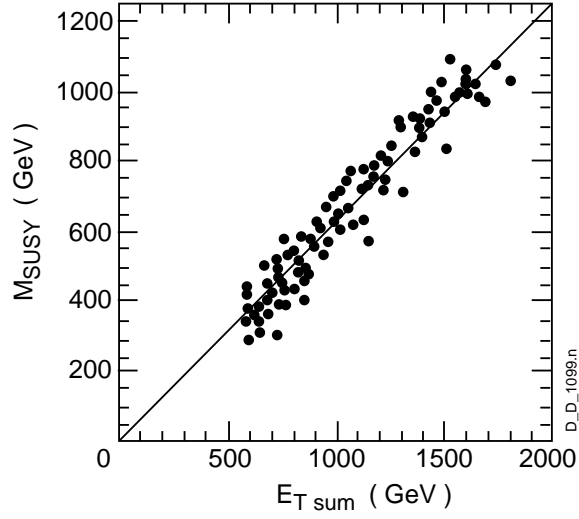


Figure 10.2: The relationship between the peak value of the E_T^{sum} distribution and the SUSY mass scale, as defined in the text.

$\tilde{\chi}_1^0$ mass determination in $3\ell^\pm + \text{no jets} + E_t^{\text{miss}}$
 final state from $\tilde{\chi}_1^\pm \tilde{\chi}_2^0$ production

$m_0 = 200 \text{ GeV}, m_{1/2} = 100 \text{ GeV}, \tan\beta = 2, A_0 = 0, \mu < 0$

$M(\tilde{\chi}_2^0) - M(\tilde{\chi}_1^0) \approx M(\tilde{\chi}_1^0) \approx 52 \text{ GeV}$

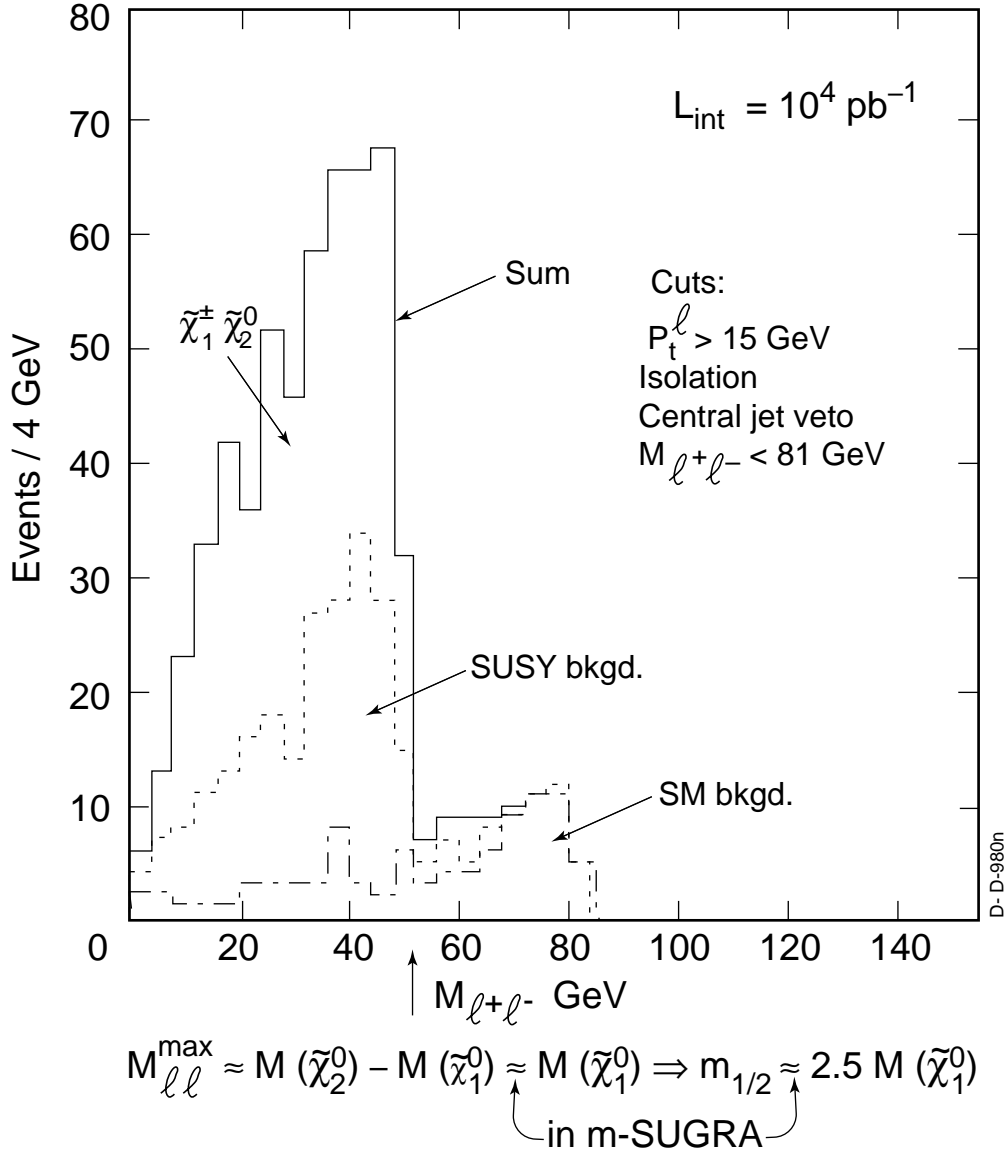


Figure 10.3: Dilepton invariant masses distribution for mSUGRA point ($m_0=200 \text{ GeV}$, $m_{1/2}=100 \text{ GeV}$) with $L_{\text{int}} = 10^4 \text{ pb}^{-1}$ in the $3\ell + \text{no jets} + (E_T^{\text{miss}})$ events. Contributions from SM and SUSY backgrounds are also shown.

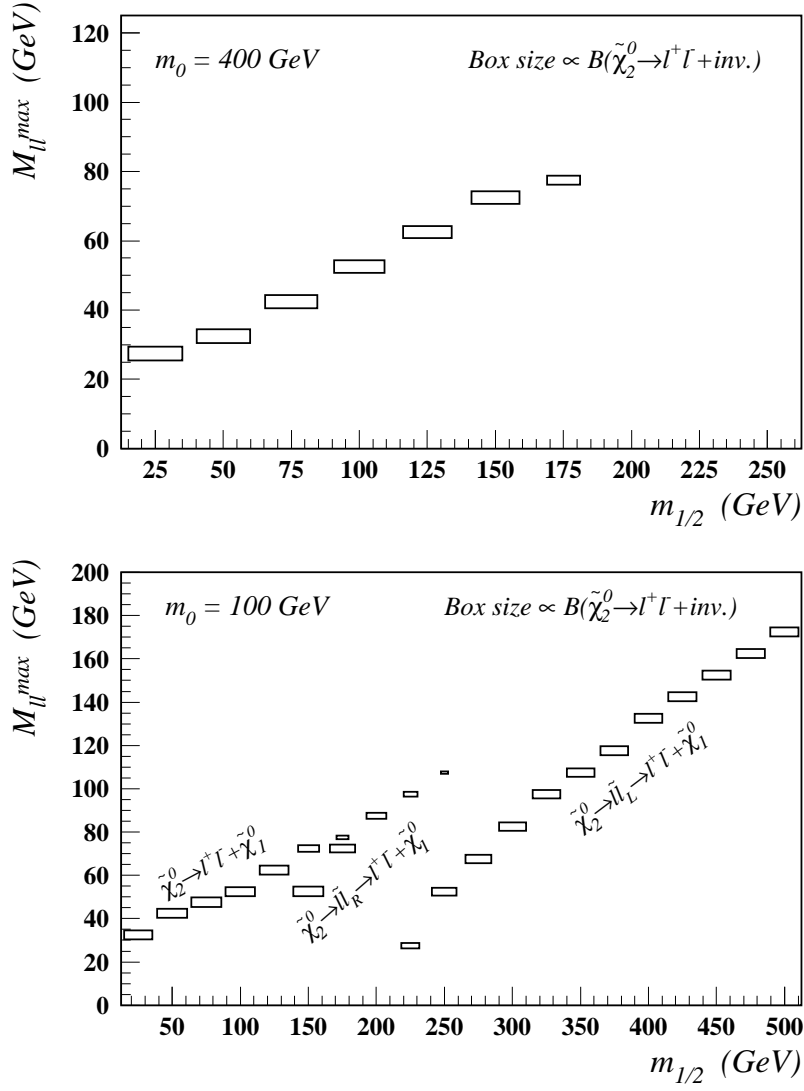


Figure 10.4: Correlation between M_{l+l-}^{max} and $m_{1/2}$ for fixed $m_0 = 400$ GeV and $m_0 = 100$ GeV. The other mSUGRA parameters are: $\tan\beta=2$, $A_0 = 0$ and $\mu < 0$.

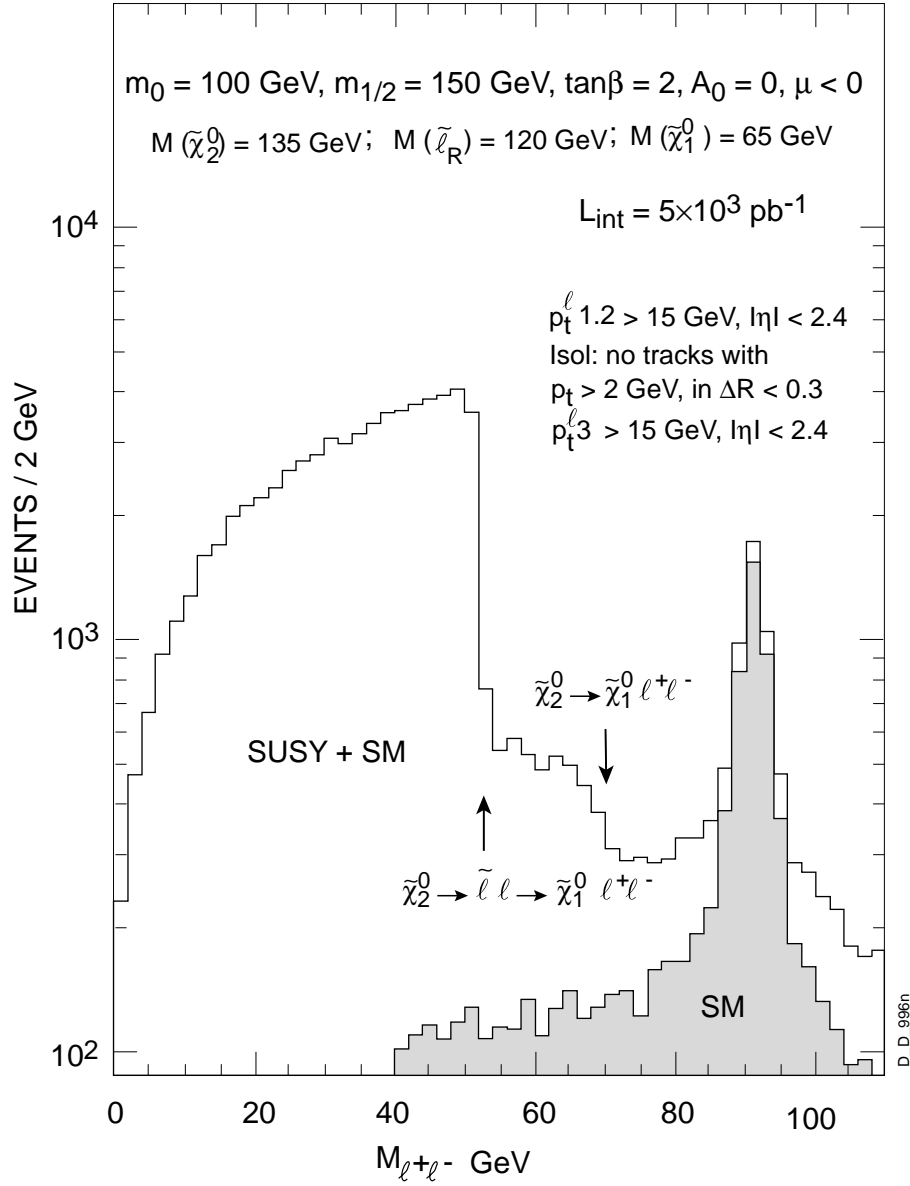


Figure 10.5: l^+l^- mass distribution for mSUGRA point ($m_0 = 100 \text{ GeV}$, $m_{1/2} = 150 \text{ GeV}$); the other mSUGRA parameters are: $\tan\beta=2$, $A_0 = 0$ and $\mu < 0$. The shaded histogram corresponds to the SM background.

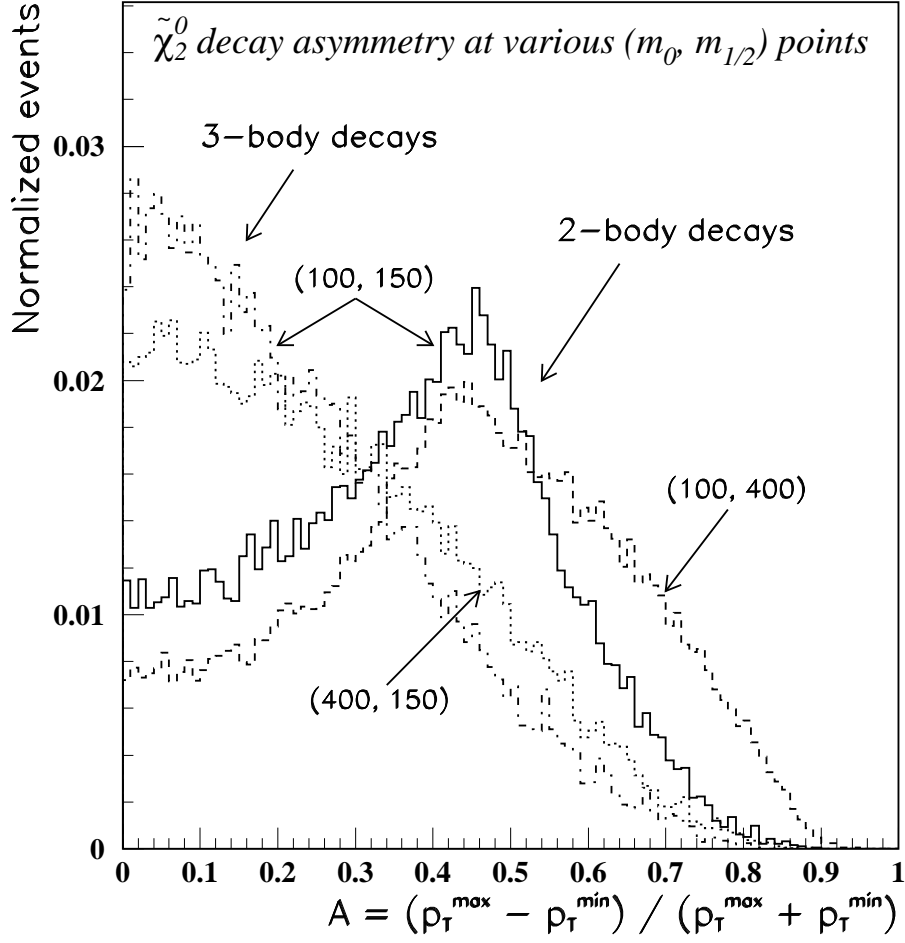


Figure 10.6: Lepton transverse momentum asymmetry distributions in $\tilde{\chi}_2^0$ decays. mSUGRA parameters $(m_0, m_{1/2})$ are the following: 100 GeV, 150 GeV (full and dashed-dotted lines); 100 GeV, 400 GeV (dashed line) and 400 GeV, 150 GeV (dotted line).

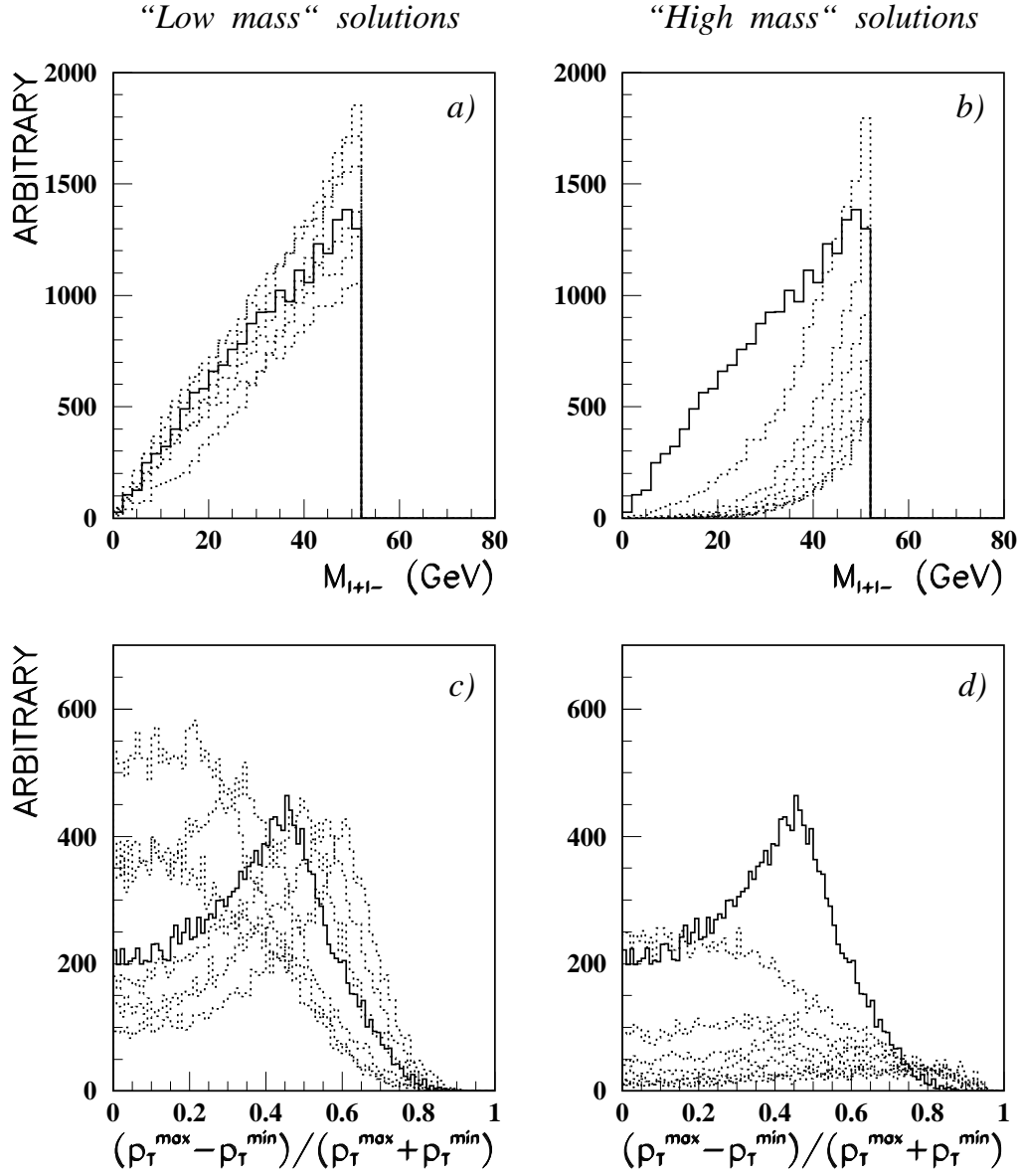


Figure 10.7: The dotted lines correspond to the invariant mass spectra and transverse momentum asymmetry distributions in $\tilde{\chi}_2^0$ two-body decays for several “low mass” and “high mass” solutions of eq. (10). The full line corresponds to the initial (observed) spectrum.

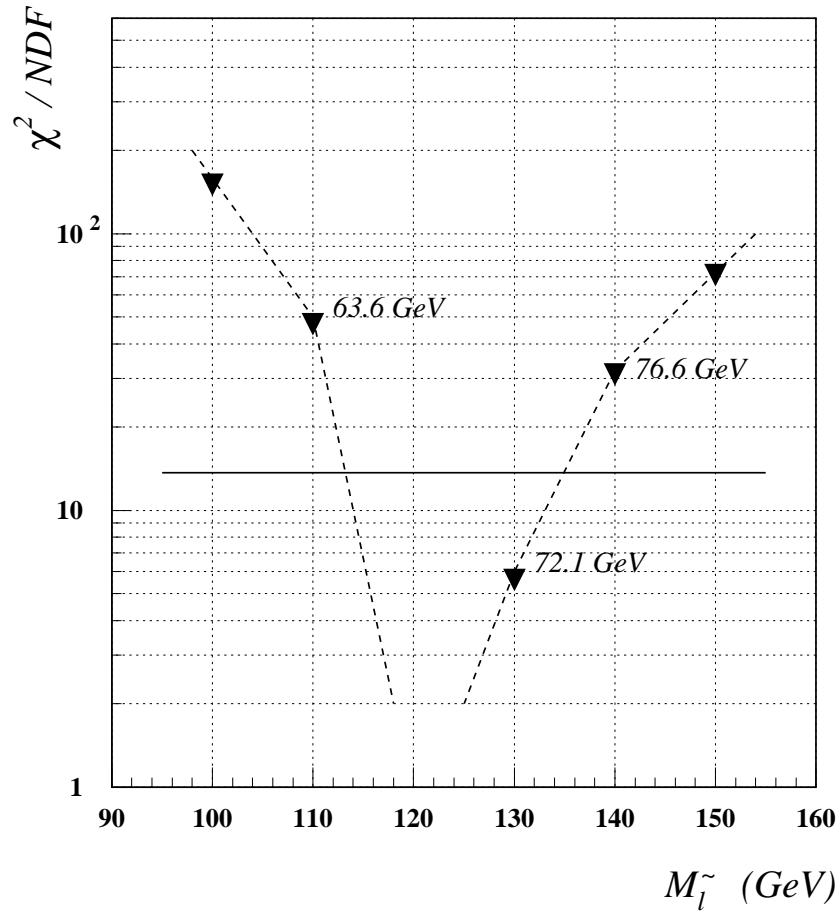


Figure 10.8: Results of the χ^2 test of the shape of p_T -asymmetry distributions as a function of slepton mass. The corresponding values of $M_{\tilde{\chi}_1^0}$ are also indicated.

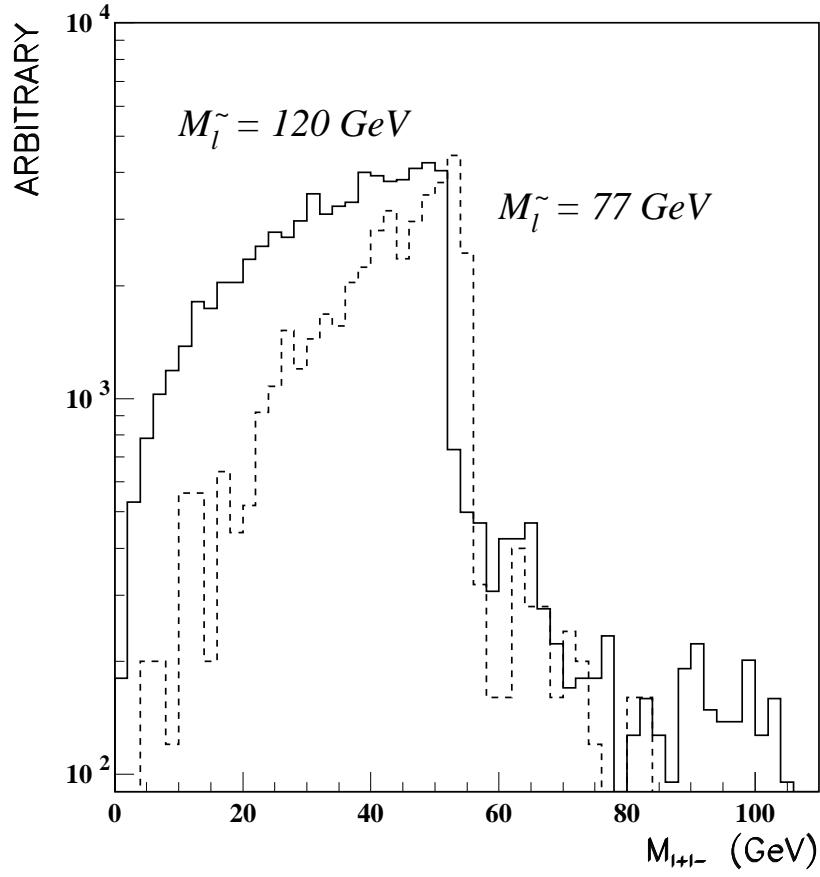


Figure 10.9: Predicted l^+l^- invariant mass spectra for two values of slepton masses: $M_{\tilde{l}} = 120$ GeV (full line) and $M_{\tilde{l}} = 77$ GeV (dashed line); mSUGRA parameters as in Fig. 10.6.

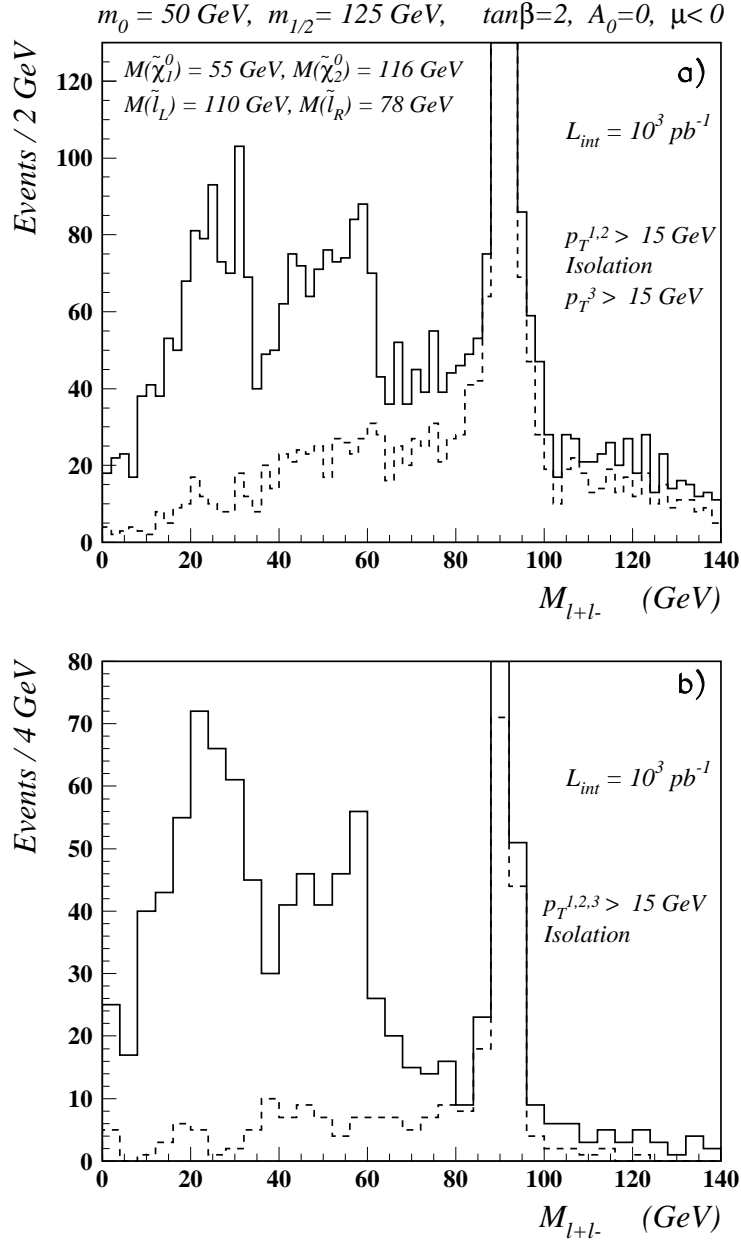


Figure 10.10: Expected l^+l^- mass spectrum for mSUGRA Point: $m_0 = 50 \text{ GeV}$, $m_{1/2} = 125 \text{ GeV}$, $\tan\beta=2$, $A_0 = 0$ and $\mu < 0$. a) Leptons with $p_T > 15 \text{ GeV}$ in $|\eta| < 2.4$ are considered. Two leptons which enter invariant mass spectrum are required to be isolated; b) as in previous case, but all three leptons are isolated. The dotted histogram corresponds to the SM background.

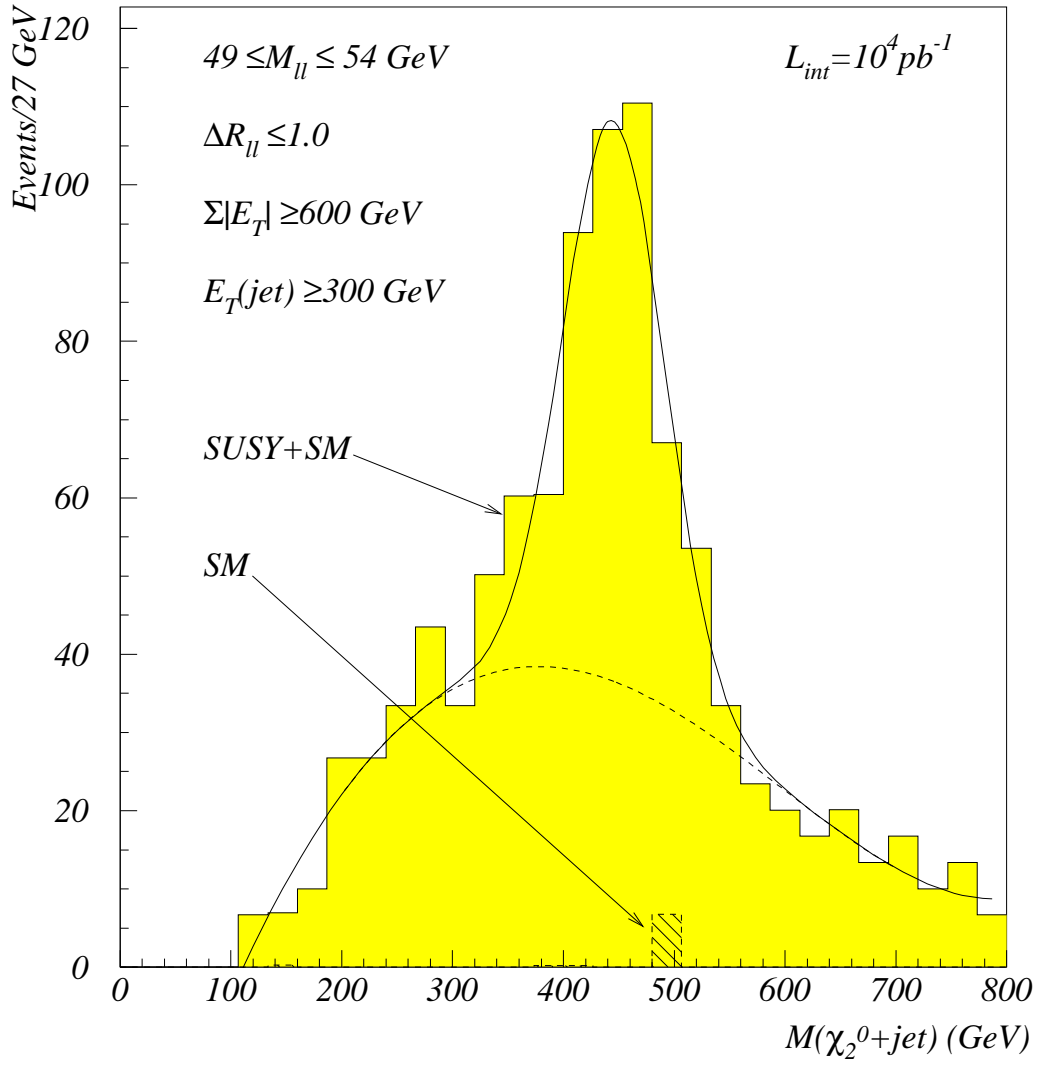


Figure 10.11: The reconstructed $\tilde{\chi}_2^0 + \text{jet}$ mass spectrum for the SUSY + SM events.

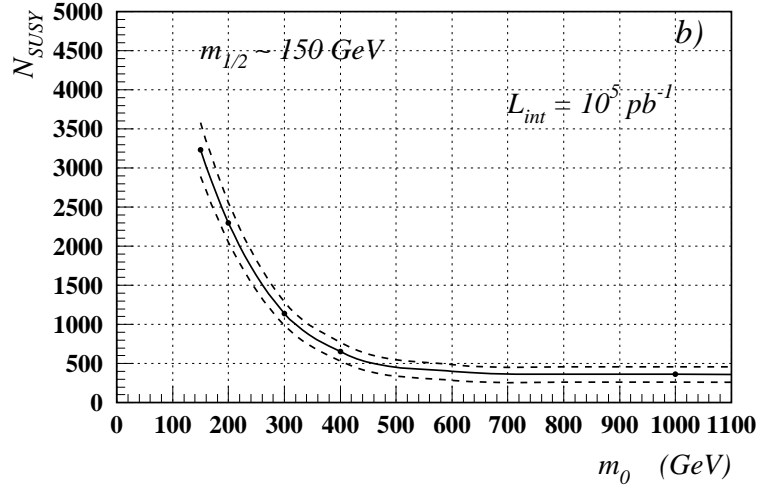
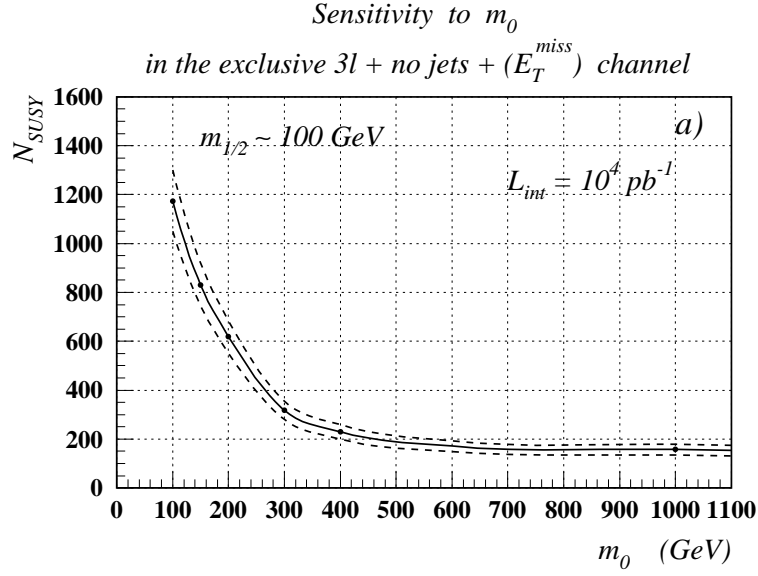


Figure 10.12: a) Number of SUSY $3l + no\ jets + (E_T^{miss})$ events with $L_{int} = 10^4 pb^{-1}$ as a function of common scalar mass m_0 for $m_{1/2} \sim 100\ GeV$. b) Number of SUSY $3l + no\ jets + (E_T^{miss})$ events with $L_{int} = 10^5 pb^{-1}$ as a function of common scalar mass m_0 for $m_{1/2} \sim 150\ GeV$.

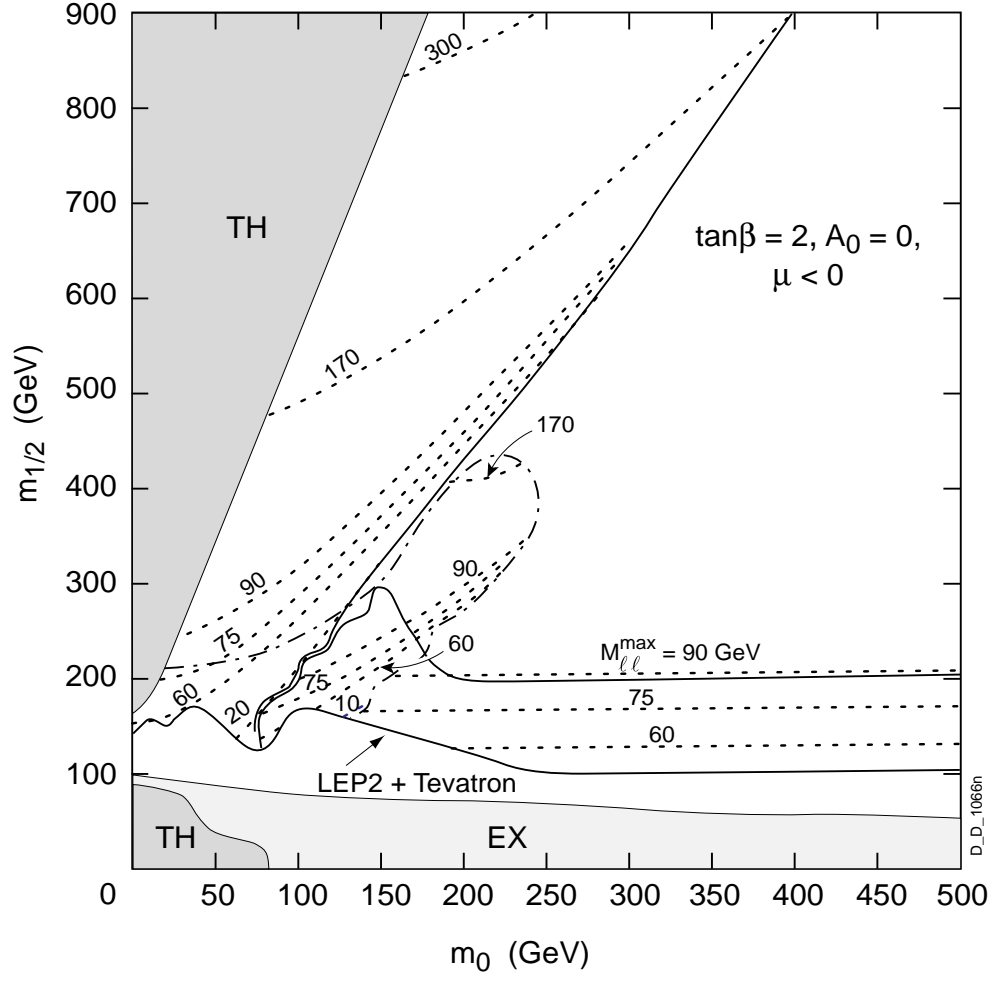


Figure 10.13: Contour lines of expected M_{l+l-}^{max} values (in GeV) in the invariant dilepton mass distribution corresponding to the three different $\tilde{\chi}_2^0$ decay modes in the region of the $(m_0, m_{1/2})$ parameter plane accessible with 10^5 pb^{-1} .

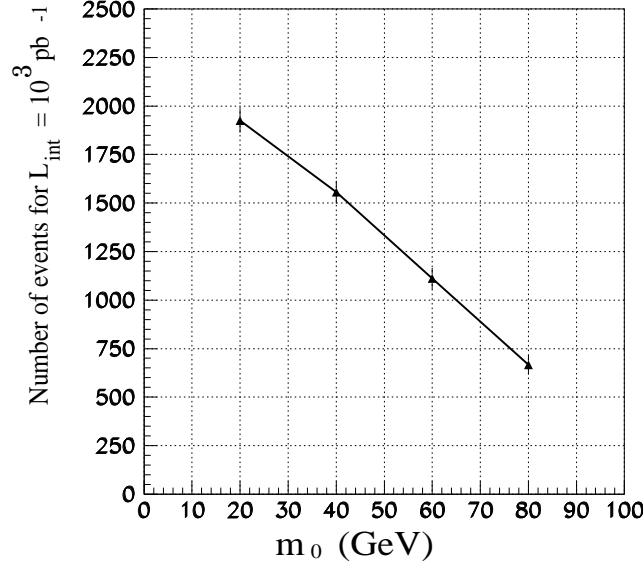


Figure 10.14: Expected $2l + E_T^{miss}$ event rate with $L_{int} = 10^3 \text{ pb}^{-1}$ along $M_{l+l^-}^{max} = 74 \pm 1$ GeV contour line in domain III ($\tilde{\chi}_2^0 \rightarrow \tilde{l}_L^\pm l^\mp \rightarrow \tilde{\chi}_1^0 l^+ l^-$) as a function of m_0 . Event selection criteria are: $p_T^{l_{1,2}} > 15$ GeV, $E_T^{miss} > 130$ GeV and $M_{l+l^-} < M_{l+l^-}^{max}$ at corresponding points.

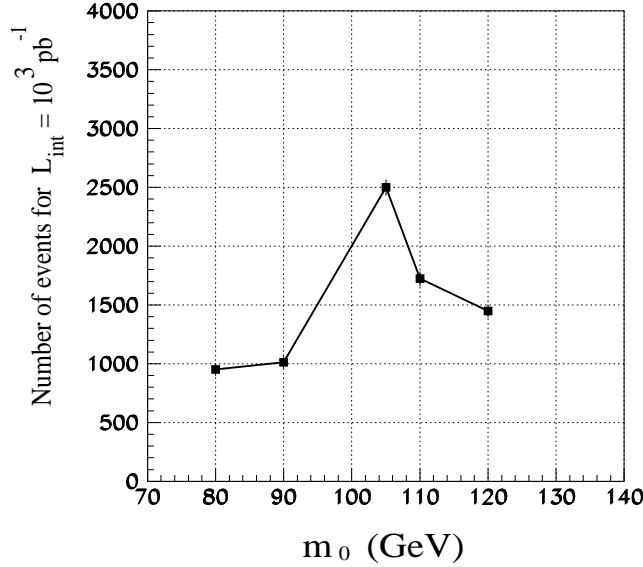


Figure 10.15: Expected $2l + E_T^{miss}$ event rate with $L_{int} = 10^3 \text{ pb}^{-1}$ along $M_{l+l^-}^{max} = 74 \pm 1$ GeV contour line in domain II ($\tilde{\chi}_2^0 \rightarrow \tilde{l}_R^\pm l^\mp \rightarrow \tilde{\chi}_1^0 l^+ l^-$) as a function of m_0 . Event selection criteria are: $p_T^{l_{1,2}} > 15$ GeV, $E_T^{miss} > 130$ GeV and $M_{l+l^-} < M_{l+l^-}^{max}$ at corresponding points.

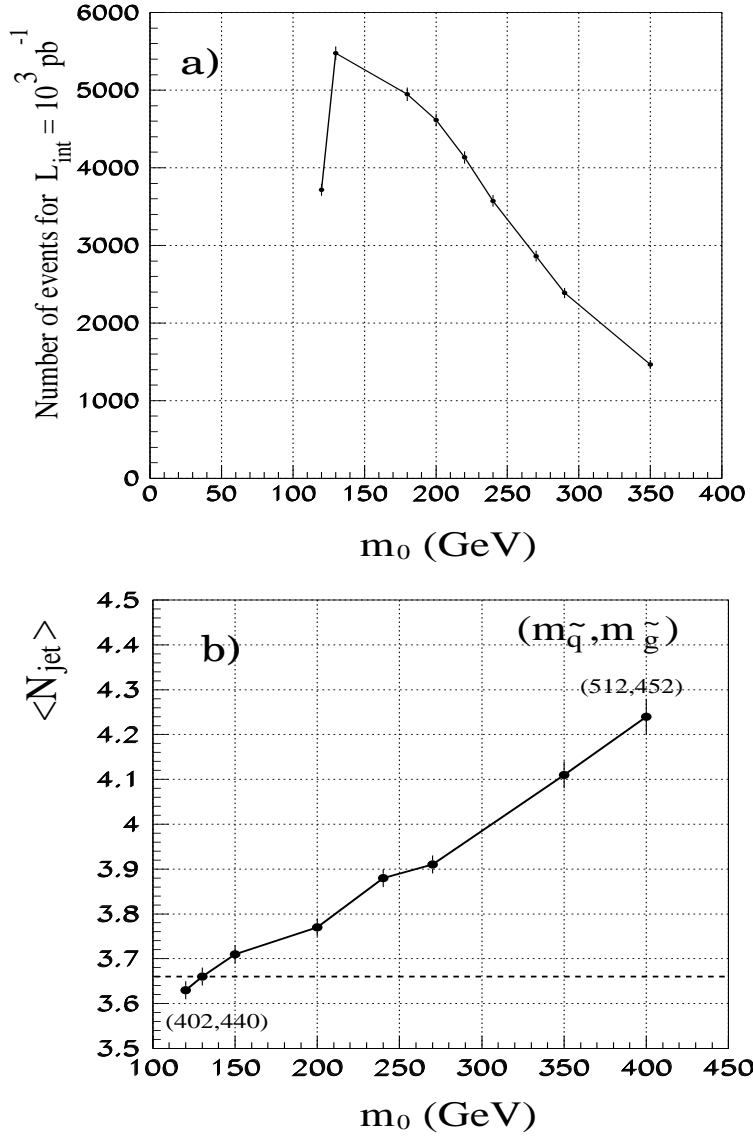


Figure 10.16: a) Expected $2l + E_T^{miss}$ event rate with $L_{int} = 10^3 \text{ pb}^{-1}$ along $M_{l+l^-}^{max} = 74 \pm 1 \text{ GeV}$ contour line in domain I ($\tilde{\chi}_2^0 \rightarrow \tilde{\chi}_1^0 l^+ l^-$) as a function of m_0 . Event selection criteria are: $p_T^{l_{1,2}} > 15 \text{ GeV}$, $E_T^{miss} > 130 \text{ GeV}$ and $M_{l+l^-} < M_{l+l^-}^{max}$ at corresponding points; b) Average number of jets ($E_T^{jet} > 30 \text{ GeV}$, $|\eta_{jet}| < 3$) at investigated points from domain I. The numbers in parenthesis show the masses of squarks and gluinos (in GeV) at corresponding points.

11 Summary and conclusions

We have investigated the ability of the CMS detector at the Large Hadron Collider to discover and characterise supersymmetry. As a benchmark model, we used the minimal supergravity-inspired supersymmetric standard model (mSUGRA). In the investigated scenarios the lightest supersymmetric particle (LSP) is stable and is the $\tilde{\chi}_1^0$.

Discovery of supersymmetry at the LHC will be relatively straightforward. It would be revealed by large excesses of events over the standard model expectations in a number of characteristic signatures – for example missing E_T plus jets, with one or more isolated leptons; an excess of trilepton events; a very characteristic signature in the l^+l^- invariant mass distribution.

Because of the importance of missing E_T signatures, considerable effort has been expended in optimising the performance of the CMS detector for E_T^{miss} measurements. In particular we have tried to minimize sources of non-Gaussian tails in the calorimeter response due to cracks and dead materials.

For the cases we have studied in detail and for 10^5 pb^{-1} integrated luminosity,

- Squarks and gluinos can be discovered up to masses well in excess of 2 TeV, i.e. for a parameter space region $m_0 \lesssim 2 - 3 \text{ TeV}$ and $m_{1/2} \lesssim 1 \text{ TeV}$ (see Fig. 11.1). This covers the entire parameter space over which supersymmetry can plausibly be relevant to electroweak symmetry breaking without excessive fine-tuning. Over the lifetime of LHC experiments these searches would probe the $\simeq 3 \text{ TeV}$ region.
- Charginos and neutralinos can be discovered from an excess of events in dilepton or trilepton final states. Inclusive searches could give early indications from their copious production in squark and gluino cascade decays just from the l^+l^- spectrum shapes. With 10^5 pb^{-1} the dilepton edge due to the $\tilde{\chi}_2^0$ leptonic decays can be seen up to $m_{1/2} \sim 900 \text{ GeV}$ for $m_0 \lesssim 400 \text{ GeV}$ (see Fig. 11.2). Applying isolation requirements and a jet veto would enable direct chargino/neutralino production to be selected; the mass reach in this case covers up to $\sim 170 \text{ GeV}$ for $\tilde{\chi}_1^\pm$, $\tilde{\chi}_2^0$ and $\sim 90 \text{ GeV}$ for $\tilde{\chi}_1^0$. The region of sensitivity (Fig. 11.1) is entirely determined by the production cross section and decay branching ratios rather than by any detector limitations.
- Directly-produced sleptons can be detected up to masses of $\sim 350 \text{ GeV}$ using dilepton signatures. Again, the use of a jet veto is crucial, and the lepton opening angle can be used to discriminate between the slepton signal and other SUSY backgrounds. The region of sensitivity (Fig. 11.1) is once again largely determined by the production cross section and decay branching ratios. It is also interesting to remark that the domain of parameter space explorable through direct slepton production searches matches closely the $\tilde{\chi}_1^0$ cosmological dark matter favored region of parameter space. This is due to relic $\tilde{\chi}_1^0$ densities being largely determined by slepton masses. Observation of a dilepton edge up to $m_{1/2} \sim 900 \text{ GeV}$ gives indirect access to slepton production for masses up to $M_{\tilde{l}} \sim 700 \text{ GeV}$.
- Squark and gluino production may in addition be a copious source of Higgs bosons through the cascade decays of the SUSY intermediate particles. In this case it will be relatively simple to reconstruct the lightest SUSY Higgs from its decay $h \rightarrow b\bar{b}$

by requiring two b -tagged jets. Unlike the case of the Standard Model Higgs in this decay mode, good signal to background ratios of order 1 can be obtained selecting SUSY events using a hard cut on E_T^{miss} thanks to the escaping LSP's (Fig. 11.2).

Once supersymmetry has been discovered, the challenge will be to determine the sparticle spectrum and to pin down model parameters. Over much of the parameter space, we have shown that, within this model, neutralino masses can be determined using the dilepton invariant mass distribution. Details of the $\tilde{\chi}_2^0$ decay scheme may be extracted from the lepton p_T -asymmetry, for example. What can exactly be measured and with what precision depends on the region in $m_0, m_{1/2}$ space Nature has chosen, and what topology/final state we use. As visible from Fig. 11.1 some regions of parameter space can be explored through several channels allowing for example simultaneous observation of \tilde{q}, \tilde{g} and of $\tilde{\chi}_1^\pm, \tilde{\chi}_2^0$ and \tilde{l} direct production giving thus access to a larger spectrum and providing more constraints on the supersymmetric models.

One of the attractive features of R -parity conserving SUSY models is that the $\tilde{\chi}_1^0$ – lightest supersymmetric particle is a plausible candidate for the cosmological dark matter. The region of parameter space where this is true for $\tan\beta = 2$ is shown in Fig. 11.1; as already mentioned, it is covered by both the squark and gluino searches and the slepton search, and overlaps the region where inclusive charginos and neutralino signals are visible (Fig. 11.2). Specifically, in \tilde{q}/\tilde{g} searches even with 10^4 pb^{-1} the $\tilde{\chi}_1^0$ (WIMP) is probed up to $\sim 350 \text{ GeV}$ for any m_0 , up to $\sim 450 \text{ GeV}$ for $m_0 \lesssim 400 \text{ GeV}$, i.e. well beyond the cosmologically plausible domain. The cosmologically favored region (hatched area in Fig. 11.1) is embedded deeply within the explorable domain of parameter space, implying that, if SUSY is responsible for cosmological dark matter, this could hardly escape discovery at the LHC, at least for $\tan\beta$ values investigated. This result is probably valid much more generally than implied by this specific model since there is a large safety margin, and a variety of experimental signatures/final states with different sensitivities, backgrounds and systematics. In this respect a detailed investigation of large $\tan\beta$ values would certainly be of interest.

We have not yet explored other supersymmetry scenarios in detail, but some general comments may be made. Generator-level studies [50] have shown that even if the lightest neutralino decays hadronically, the missing E_T plus jets and isolated leptons signature will remain sensitive to squark and gluino production. We also expect that the inclusive multilepton signature would be robust against changes in the SUSY decays. Gauge-mediated SUSY breaking models, which predict decays of the lightest neutralino into a photon plus a gravitino, would give in our detector striking signatures of diphotons plus missing E_T that would be easily detected [51].

We therefore believe that it will be very hard for electroweak-scale supersymmetry, if it exists, to escape detection at the LHC. If supersymmetry is still not found after the LHC has accumulated few times 10^5 pb^{-1} of data then it is essentially excluded at the electroweak scale, and some other new physics is presumably at work. On the other hand if supersymmetry is discovered at LEP or the Tevatron, there will be a rich program of SUSY studies to be carried out at the LHC since so much more of the Higgs and sparticle spectrum will be accessible.

Expected reach in various channels

m SUGRA; $\tan \beta = 2$, $A_0 = 0$, $\mu < 0$
 5σ contours, $N_\sigma = N_{\text{sig}} / \sqrt{N_{\text{sig}} + N_{\text{bkgd}}}$ for 10^5pb^{-1}

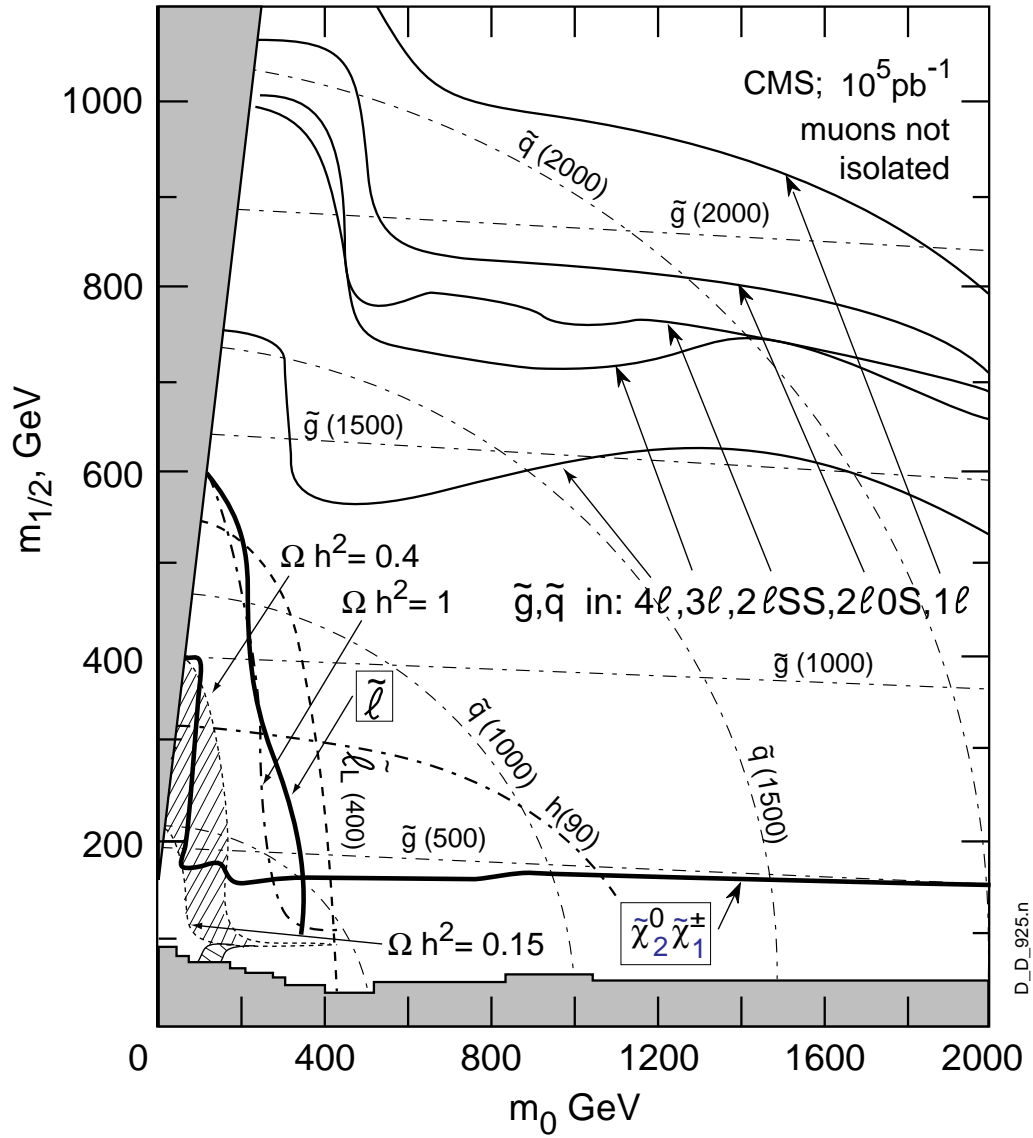


Figure 11.1: 5σ significance contours at $L_{\text{int}} = 10^5 \text{pb}^{-1}$ for different SUSY channels.

mSUGRA parameters: $\tan\beta=2$, $A_0=0$, $\mu<0$

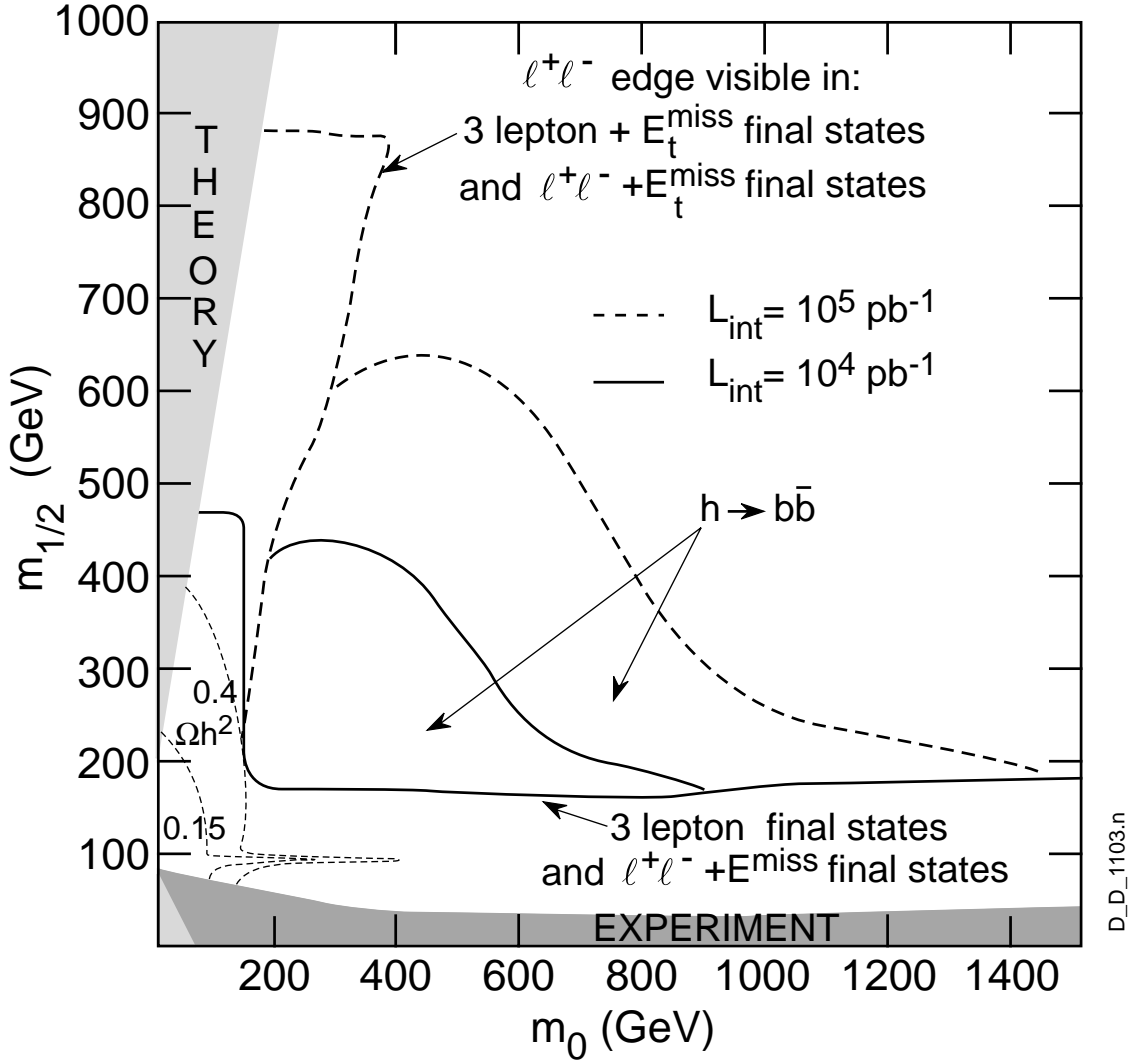


Figure 11.2: mSUGRA parameter reach in $h \rightarrow b\bar{b}$ decays at 10^4 pb^{-1} and 10^5 pb^{-1} integrated luminosities. The reach in $\tilde{\chi}_2^0$ via observation of edge(s) in dilepton mass distribution is also shown.

Acknowledgements

Over the past few years we have benefited from numerous discussions with our colleagues, from their suggestions and criticism. It is a pleasure for us to thank in first place H. Baer who has spent many hours in discussions with us and in following our studies. We are also grateful to A. Bartl, W. Majerotto, F. Pauss, C. Seez, M. Spira, T. Virdee for useful discussions and comments.

References

- [1] D. Abbaneo et al. (LEP Electroweak Working Group, SLD Heavy Flavour Group), preprint CERN-PPE/97-154.
- [2] H. Baer, C. Chen, F. Paige and X. Tata, Phys. Rev. **D49**, (1994) 3283.
- [3] *SUSY Studies in CMS*, in: LHCC SUSY Workshop, CERN, October 29–30, 1996, CMS Document 1996-149; Copies of transparencies are available on WEB under <http://www.cern.ch/Committees/LHCC/SUSY96.html>.
- [4] S. Abdullin, *Squark and gluino searches in leptons + jets + E_T^{miss} final state*, CMS TN/96-095.
- [5] S. Abdullin, Ž. Antunović and M. Dželalija, *Squarks and gluino searches in multilepton final states: $A_0 = 0$, $\tan\beta = 2$, $\mu > 0$ case*, CMS Note 1997/016.
- [6] D. Denegri, L. Rurua and N. Stepanov, *Detection of sleptons in CMS, mass reach*, CMS TN/96-59.
- [7] D. Denegri, W. Majerotto and L. Rurua, *Determining the parameters of the minimal supergravity model from $2l + E_T^{miss} + (jets)$ final states at LHC*, CMS Note 1997/094 and references therein; HEPHY-Pub 678/97; hep-ph/9711357.
- [8] I. Iashvili, A. Kharchilava and K. Mazumdar, *Study of $\tilde{\chi}_1^\pm \tilde{\chi}_2^0$ pair production with the CMS detector at LHC*, CMS Note 1997/007.
- [9] I. Iashvili and A. Kharchilava, *Search for the Next-To-Lightest Neutralino*, CMS Note 1997/065; hep-ph/9712393.
- [10] I. Iashvili, A. Kharchilava and C. Racca, *Sensitivity to sparticle masses and model parameters in direct $\tilde{\chi}_1^\pm \tilde{\chi}_2^0$ production*, CMS Note 1997/069.
- [11] D. Denegri, *SUSY and dark matter searches at the LHC*, in Proc. of Int. Workshop on Dark Matter in Astro and Particle Physics, Heidelberg, Germany, Sept. 96, World Scientific, eds. H. V. Klapdor and Y. Ramachers, pp 583-604; CMS CR 1997/009.
- [12] S. Abdullin and D. Denegri, *On the possibility to observe $h \rightarrow b\bar{b}$ with $S/B \sim 1$ in SUSY ($mSUGRA$), and implications for tracker and HCAL*, CMS Note 1997/070.
- [13] D. Denegri and V. Genchev, *Study of the CMS hadron calorimeter barrel/endcap transition region*, CMS Note 1996/020;
 D. Green, *HCAL "tailcatcher" decision*, CMS TN/96-008;
 S. Banerjee et al., *Towards a design of the CMS barrel hadron outer calorimeter*, TIFR/CMS-96-01, Nov. 1996;
 J. Womersley, *Study of E_T^{miss} resolution in CMS*, presentation at the CMS/Physics working group meeting, March 1996;
 I. Gaines et al., *Missing E_T + jets signals for supersymmetry in the CMS detector at the LHC*, CMS TN/96-058.

- [14] R. Kinnunen et al., *Expected SM/SUSY Higgs observability in CMS*, CMS Note 1997/057 and references therein;
R. Kinnunen and A. Nikitenko, *Study of $H_{SUSY} \rightarrow \tau\tau \rightarrow l^\pm + \tau \text{ jet} + E_T^{miss}$ in CMS*, CMS Note 1997/106;
S. Lehti, R. Kinnunen and J. Tuominiemi, *Study of $h^0, H^0, A^0 \rightarrow \tau\tau \rightarrow e\mu$ in the CMS detector*, CMS Note 1998/019.
- [15] J. F. Gunion et al., UCD-95-28, ILL-(TH)-95-28;
M. Carena, Phys. Lett. B355 (1994) 209.
- [16] For a review, see e.g., H. P. Nilles, Phys. Rep. 110 (1984) 1;
P. Nath, R. Arnowitt and A. Chamseddine, *Applied N=1 Supergravity*, ICTP series in Theoretical Physics (World Scientific, Singapore, 1984);
M. Drees and S. P. Martin, hep-ph/9504324.
- [17] H. Baer, F. Paige, S. Protopopescu and X. Tata, in: Proceedings of the Workshop on Physics at Current Accelerators and Supercolliders, eds. J. Hewett, A. White and D. Zeppenfeld (Argonne National Laboratory, Argonne, Illinois, 1993).
- [18] K. Inoue, A. Kakuto, H. Komatsu and S. Takeshita, Prog. Theor. Phys. 68 (1982) 927.
- [19] T. Sjöstrand, Comp. Phys. Comm. 82 (1994) 74.
- [20] H. L. Lai et al., Phys. Rev. **D51** (1995) 4763.
- [21] CMS Collaboration, Technical Proposal, CERN/LHCC 94-38, December 1994;
Meeting with CMS LHCC Referees, CMS Document 1996-132, Aug. 1996.
- [22] CMS, The Magnet Project, TDR, CERN/LHCC 97-10.
- [23] CMS, The Muon Project, TDR, CERN/LHCC 97-32;
F. Gasparini et al., Nucl. Instrum. Methods A336 (1993) 91;
R. Cardarelli et al., Nucl. Instrum. Methods A340 (1994) 466.
- [24] F. Angelini et al., Nucl. Instrum. Methods A343 (1994) 441;
CMS Meeting with LHCC Referees/Tracking, CMS Document 96-59, March 1996.
- [25] CMS, The Electromagnetic Calorimeter Project, TDR, CERN/LHCC 97-33;
P. Lecoq et al., *Lead Tungstate ($PbWO_4$) scintillators for LHC EM-Calorimetry*, CMS TN/94-308.
- [26] CMS ECAL group, *CMS Lead Tungstate ECAL: Test Beam Results 1995. Report to the CMS Referees*, CMS TN/96-004;
J. P. Peigneux et al., *Results from tests on matrices of lead tungstate crystals using high energy beams*, CMS TN/95-166.
- [27] CMS, The Hadron Calorimeter Project, TDR, CERN/LHCC 97-31.

- [28] For example: HPMT from DEP (Delft Electronische Producten, Netherlands), or HPD from Hamamatsu;
P. Cushman et al., Multi-Pixel Hybrid Photodiode Tubes for CMS Hadron Calorimeter, in Proc. of the Conf. on New Developments in Photodetection, Beaune 1996, NIM, to be published.
- [29] D. Green, Hadron calorimeter performance with a PbWO_4 EM compartment, FNAL, TM-1958, Dec. 1995;
D. Green, A. Skuja and J. Freeman, HCAL test beam results, CMS/HCAL working group meetings 1996 and 1997.
- [30] A. Ferrando et al., *Designing a compensating quartz fibre calorimeter for the CMS low angle calorimetry*, CMS TN/96-82;
S. Doulas et al., *Beam test results from a fine sampling quartz fibre calorimeter for lepton, hadron and jet detection*, CMS TN/95-144;
VFCAL General Meeting, CMS Document 1996-212, Dec. 10-11, 1996.
- [31] D. Green, *HCAL "tailcatcher" decision*, CMS TN/96-08;
S. Banerjee et al., *Towards a design of the CMS barrel hadron outer calorimeter*, TIFR/CMS-96-01, Nov. 1996.
- [32] M. Murbach and A. Skuja, presentation at the CMS/HCAL working group meetings, 1996.
- [33] D. Green, S. Kunori and A. Skuja, presentations at the CMS/HCAL/Physics working group meetings, 1996.
- [34] D. Denegri et al., *Justifications for a Microvertex Detector in CMS*, CMS TN/94-258;
R. Kinnunen and D. Denegri, *B-tagging with impact parameter in the CMS tracker*, CMS TN/96-045.
- [35] V. Genchev and L. Litov, *Study of the CMS TP calorimetry system*, CMS TN/94-272.
- [36] S. Abdullin, A. Khanov and N. Stepanov, *CMSJET*, CMS TN/94-180.
- [37] H. Baer and M. Brhlik, Phys. Rev. **D53** (1996) 597.
- [38] S. Abdullin, Ž. Antunović and M. Dželalija, *Squarks and gluino searches in four lepton final states*, CMS Note 1997/015.
- [39] F. Paige, *Search for SUSY at LHC: precision measurements*, talk given at International Europhysics Conference on High Energy Physics, 19-26 August 1997, Jerusalem, Israel.
- [40] H. Baer, C.-H. Chen, F. Paige and X. Tata, Phys. Rev. **D50** (1994) 4508 and references therein.
- [41] A. Kharchilava, *Search for next-to-lightest neutralino*, in: LHCC SUSY Workshop, CERN, October 29–30, 1996; Copies of transparencies available under <http://www.cern.ch/Committees/LHCC/SUSY96.html>; CMS Document 1996-149.

- [42] L. Rurua, presentation to CMS Physics Meeting, CMS Week, March 1998, CMS Document 1998-042.
- [43] C. Seez and T. S. Virdee, *The Higgs two photon decay in CMS: an update*, CMS TN/94-289;
D. J. Graham, *An algorithm using tracks to locate the two photon vertex at high luminosity*, CMS TN/95-115;
K. Lassila-Perini, *Reconstruction of $Higgs \rightarrow \gamma\gamma$ in CMS*, in Proc. of VI Int. Conf. on Calorimetry in HEP, Frascati, June 8-14, 1996, p 487; CMS CR 1997/006.
- [44] S. Abdullin, A. Starodumov and N. Stepanov, *Search for heavy Higgs via the $H \rightarrow ll\nu\nu$ channel*, CMS TN/93-087;
M. Dželalija et al., *Study of the associated production modes Wh , $t\bar{t}h$ in the Minimal Supersymmetric Standard Model in CMS*, CMS TN/96-091.
- [45] D. Drollinger, T. Muller, R. Kinnunen, presentation at CMS Week Physics meeting, June, 27, 1997, CMS Note 1998 (in preparation);
D. Froidevaux and E. Richter-Was, *Is the channel $H \rightarrow b\bar{b}$ observable at LHC?*, ATLAS Internal Note Phys-No-043 (1994).
- [46] L. Didenko and B. Lund-Jensen, *B-tagging of light Higgs boson in cascade decays of gluino*, ATLAS Internal Note Phys-No-42 (1994);
I. Hinchliffe et al., Phys. Rev. **D55** (1997) 5520.
- [47] A. Khanov and N. Stepanov, *Full pattern recognition and track reconstruction in CMS tracker*, CMS Note 1998 (in preparation);
N. Stepanov, *b-tagging with full pattern recognition*, presentation at the CMS/Physics meeting, June 27, 1997;
A. Caner, *CMS tracker optimisation study*, presentation at the CMS Collaboration meeting, March 1998.
- [48] F. Paige, *Determining SUSY particle masses at LHC*, Proc. of the 1996 DPF/DPB Summer Study on High-Energy Physics “New Directions for High-Energy Physics”, Snowmass, Colorado, 1996.
- [49] D. J. Graham, Ph. D. Thesis, Imperial College, University of London, London, 1997.
- [50] H. Baer, C. Chen and X. Tata, Phys. Rev. **D55** (1997) 1466.
- [51] F. Charles, *Inclusive search for light gravitino with the CMS detector*, CMS Note 1997/079;
M. Kazana and P. Zalewski, *Measurement of the stau mass in the GMSB model via time of flight determination in the CMS*, presentation at CMS Physics Meeting, CMS Week, December 1997, CMS Document 1997-169;
G. Wrochna and P. Zalewski, *Proposal for detecting $\tilde{\chi}_1^0 \rightarrow \tilde{G}\gamma$ and $\tilde{\tau}_1 \rightarrow \tilde{G}\tau$ decays in the CMS muon detector*, presentation at the CMS/Physics working group meeting, February 1998, CMS Note 1998 (in preparation).